Electrolyte solutions and simple fluids at curved walls

Von der Fakultät für Mathematik und Physik der Universität Stuttgart
zur Erlangung der Würde eines Doktors der Naturwissenschaften
(Dr. rer. nat.) genehmigte Abhandlung

Vorgelegt von

Andreas Stephan Josef Johann Reindl

aus Nabburg

Hauptberichter: Prof. Dr. Siegfried Dietrich
Mitberichter: Prof. Dr. Christian Holm

Tag der mündlichen Prüfung: 06.02.2018

Institut für Theoretische Physik IV der Universität Stuttgart und
Max-Planck-Institut für Intelligente Systeme, Stuttgart

2018

Erklärung

Hiermit erkläre ich, Andreas Reindl, dass ich abgesehen von den ausdrücklich bezeichneten Hilfsmitteln die Dissertation selbständig verfasst habe.

Stuttgart, den 23.10.2017

Contents

List of abbreviations

CIV	civilized or civilized model
DCF	direct correlation function
DFT	density functional theory
EDL	electric double layer
ELE	Euler-Lagrange equation
FMT	fundamental measure theory
HNC	hypernetted chain
MPB	modified Poisson-Boltzmann
MSA	mean spherical approximation
MT	morphometric thermodynamics
PB	Poisson-Boltzmann
PM	primitive model
RPA	random phase approximation
RPM	restricted primitive model
RTIL	room-temperature ionic liquid
SPM	solvent primitive model

Chapter 1

Introduction

An interface is the contact area between two different phases. The type of the interface can be specified corresponding to the combination of thermodynamic states (solid, liquid, or gaseous) of the adjacent phases: solid-gaseous, solid-liquid, solid-solid, liquid-gaseous, and liquid-liquid. For convenience, in the following the term fluid denotes a state which is not solid. Gases have the characteristic to mix, which is why there is no interface of the type gaseous-gaseous. The concept of a surface is also used frequently but it is less general. Strictly speaking the surface corresponds to a situation where a solid or a liquid is bounded by vacuum. Moreover it is common to denote the interfaces solid-gaseous and liquid-gaseous as surfaces [1, 2]. The definition of the interface as a surface in the mathematical sense agrees with our experience in daily life. There we often encounter macroscopic phases of large volumes which are separated from each other by (infinitesimally) small domains, e.g., the water-air interface of a lake or the wall-air interface of a building. However this picture only withstands a macroscopic treatment and is too vague on a microscopic scale.

In a more precise picture the interface is a domain of molecular dimensions. Within this domain the particles, e.g., atoms or molecules, i.e., the building blocks of the adjacent phases, are surrounded by less particles as compared to the bulk far away from the interface. That is, the isotropy of the surroundings of the particles, which is given in the bulk, is disturbed close to the interface and specific properties deviate from properties in the volume phase. Interfacial properties may be quantified by means of the interfacial tension γ. Consider, for instance, a two-phase system of total volume $\mathcal{V}$ and bulk pressure p. The phases are assumed to be separated by a planar interface of area $\mathcal{A}$. The grand canonical potential Ω_{eq} of this system reads [3]

$$\Omega_{\mathrm{eq}} = -p\mathcal{V} + \gamma\mathcal{A}. \tag{1.1}$$

The grand canonical potential of this assembled system is not equivalent to the sum of only the volume terms $(-p\mathcal{V})$. This would be the case, if the properties close to the

interface would not differ from the ones in the volume phases. However, in Eq. (1.1) additionally a contribution of the interface, $\gamma\mathcal{A}$, has to be taken into account. $\mathcal{A}$ is the size of a surface in the mathematical sense. The physical properties of the interfacial domain are included in γ.

The interfacial tension acts in any interface such that the interfacial area is minimized. The shapes of fluid-fluid interfaces result, among others, from this mechanism. This is different if at least one of the adjacent phases is solid; systems of this kind are in the focus of the present dissertation. According to the definition of a solid, the shape of such an interface is rigid, i.e., it remains in the predefined state. Nevertheless an interfacial tension can be formally defined also for these systems [4]. For the sake of comparability with other studies the discussions in Chaps. 2 and 3 are based on γ. Another common quantity, which describes interfacial phenomena, is the excess adsorption. The latter indicates the positive or negative excess number of particles in comparison with the bulk due to the presence of the interface. It is therefore a measure for accumulation or dilution of matter at interfaces [4]. Interfaces in the context of ionic solutions are usually accompanied by electric double layers (EDLs). The latter can be conveniently quantified by means of the differential capacitance C, which is in the focus of the discussion in Chaps. 4 and 5 (see below).

The concept of an interfacial tension enables to explain various interfacial phenomena, for instance, wetting phenomena. The latter are usually discussed by means of a generic setup: a limited amount of liquid is situated on a solid surface and is surrounded by a gas. The liquid can either completely wet the solid surface or it can form a drop. In the latter case a contact angle θ is established at the contact line where all three phases merge; θ is measured between the liquid-gaseous and solid-liquid interfaces. Young's equation

$$\gamma_{sg} = \gamma_{sl} + \gamma_{lg}\cos\theta \tag{1.2}$$

relates the contact angle with the interfacial tensions between the involved phases: the interfacial tension of the solid-gaseous (γ_{sg}), the solid-liquid (γ_{sl}), and the liquid-gaseous (γ_{lg}) interface, respectively. That is, the wettability of the solid surface, quantified by the value of the contact angle, corresponds to an interplay of the different interfacial tensions. An increase of the contact angle is equivalent to a reduction of wettability [1–3].

If two fluid phases are separated by a curved interface, then there is a pressure difference Δp across that interface due to the interfacial tension γ. The pressure difference can be quantified by means of the Young-Laplace or Laplace equation

$$\Delta p = \gamma\left(\frac{1}{R_1} + \frac{1}{R_2}\right), \tag{1.3}$$

where R_1 and R_2 denote principal radii of curvature. For example, Eq. (1.3) states that

the pressure inside of a spherical liquid drop is higher than the pressure of the surrounding gas. Capillary phenomena result from a balance between body forces due to gravity and interfacial forces. The latter combine wetting phenomena with geometric constraints and can be estimated by a combination of Eqs. (1.2) and (1.3) [2–4].

Both Young's equation (1.2) and the Young-Laplace equation (1.3) reveal that interfacial phenomena are determined by the composition of the adjacent phases. This includes the properties of the bulk phases and the geometry of the interface. However, even though the curvature of the interface explicitly enters the Young-Laplace equation, the underlying description of the interfacial geometry is a macroscopic one; usually the interfacial tension of a planar interface is taken into account although curved interfaces are under consideration. Such an approach neglects that the interfacial tension of a curved interface differs in general from that of a planar interface. Presumably Tolman has been the first to derive an explicit expression for the interfacial tension of a spherical droplet in equilibrium with its vapour. In Ref. [5] it is reported, among others, that for a droplet diameter of 10^{-6} cm the value of the interfacial tension deviates by 4% from its planar limit; the deviation becomes larger for smaller values of the droplet diameter. The influence of geometry on thermodynamic quantities like the interfacial tension is still causing debates. In particular the concept of morphometric thermodynamics, which is discussed below, is a divisive issue. The numerical example in Tolman's study indicates that, from a macroscopic point of view, the dependence of the interfacial tension on the shape of the interface becomes significant only for small radii. That is, the dependence of the interfacial tension on the geometry is likely to be negligible, if large volume phases separated by weakly curved interfaces are under consideration. However, in the converse limit, this cannot be assumed from the start. If the interfacial area is relatively large, which usually is tantamount with a highly curved interface, it must be assumed that interfacial properties have an impact of significant magnitude on the system. Systems of such kind exhibit a large specific interfacial area, which is given by the ratio (interfacial area)/volume. The following list of examples corresponds to systems, in which interfacial phenomena play an important role and which are likely to be encountered in daily life. (i) Interfacial phenomena are closely related to colloidal dispersions. The latter seem to be uniform on a macroscopic but actually are non-uniform on a microscopic scale. The highly dispersed colloids exhibit a large specific interfacial area which brings about that their behavior is strongly influenced by interfacial properties. Examples for colloidal systems are paints, pollen, smoke, smog, styrofoam, fire extinguishers, (inhalable) pharmaceuticals, butter, milk, ... [2,6]. (ii) In geology one is interested in the swelling behavior of clay or soil in combination with water. (iii) Due to interfacial forces water accumulates around small dust particles which leads to the formation of clouds and rain [2]. (iv) Proteins are large molecules consisting of a huge amount of atoms. In biological systems they are situated in an aqueous environment. The three-dimensional structure of a protein is related with

its biological function which is why there is a particular interest in understanding the underlying complex folding mechanism [7]. (v) The interface between an electrode and an electrolyte solution is usually accompanied by an electric double layer. In particular the fluid behavior close to the electrode can be conveniently manipulated by means of external electric fields. In a supercapacitor the double layer evolving between an electrode of high specific interfacial area and an ionic solution is used for energy storage (see Sec. 4.1).

The interfaces in the aforementioned examples are in general complex entities. A simple but yet precise theoretical description of the same would be valuable both from a scientific and a technological point of view. A model of this kind would be transferable to diverse geometries. It would be able to predict the behavior of the underlying interfaces without the need for cumbersome realizations in experiments. A step in this direction has been taken in Ref. [8]. The study focuses on the dependence of the grand canonical potential on the shape of the container which bounds the thermodynamic system. According to the approach of morphometric thermodynamics (MT), which is introduced in Ref. [8], the grand canonical potential depends on the geometry of the surroundings only by four morphometric measures [see also Eq. (2.1)]. All other quantities are independent of the geometry; they have to be determined only once for a specific wall-fluid combination. This information is sufficient in order to evaluate the grand canonical potential in arbitrary geometries by means of the expression in Eq. (2.1). Other thermodynamic quantities like the interfacial tension or the differential capacitance, which follow from the grand canonical potential, inherit the simple dependence on the geometry in line with MT.

The initial agenda of the present dissertation has been to explore the limitations of the morphometric approach in more detail. Limits of its applicability have been attested from the start. The approach has been introduced in combination with the restriction that it cannot be used with respect to systems with large intrinsic length scales [8]. However, insights gained in the same study as well as in several examples in literature, where MT either has been applied or where results have been found to be in agreement with MT, inspired confidence that MT is valid in simple fluids like hard sphere systems [8–18]. On the other hand several studies question the completeness of the MT approach even in the case of hard sphere systems [19–24]. In agreement with the latter studies also the calculations carried out in the course of this dissertation cannot confirm that MT is exactly valid.

Some interfaces are accompanied by electric double layers (EDLs). That is, at such interfaces oppositely charged layers are facing each other. EDLs essentially arise as a consequence of the following processes: charge carriers may transfer from one phase to another, ions may specifically adsorb at the interface, and external electric fields may cause an accumulation of charge [1]. In electrostatics two plates carrying opposite charges are known as a capacitor. Also the adjacent layers of EDLs exhibit a capacitive behavior. The

corresponding differential capacitance can be determined experimentally, for example, as a function of the electrode potential [25–29]. Measurements like these can be used to evaluate theoretical models of EDLs which in turn allow for a deeper insight into the underlying structure.

Studies with the objective of understanding the structure of EDLs go back to, at least, the year 1879. At that time Helmholtz considered an electric double layer ("electrische Doppelschicht") at the interface between a liquid and the wall of a vessel. He assumed the liquid part of the EDL to be of a very small, but finite thickness (see p. 349 in Ref. [30]). The structure of this EDL may be interpreted in terms of a molecular capacitor, where the surface charge of the solid wall is facing the same amount of opposite charge concentrated in a thin liquid layer parallel to the solid wall. If the (molecularly small) distance between the plates is known, the capacitance of this plate capacitor can be estimated [31]. However, the capacitance of a plate capacitor does not depend on the applied voltage. For that reason this model fails to explain experimentally found differential capacitance curves which exhibit a dependence on the voltage [25–29].

Several years later Gouy and Chapman have approached an EDL at the interface between an electrolyte solution and an electrode by means of the Poisson-Boltzmann (PB) equation. As compared to the Helmholtz model the charge in the liquid phase is spatially distributed which is why the double layer within the Gouy-Chapman approach is sometimes referred to as a diffuse double layer. The corresponding differential capacitance C depends on the electrode potential; the Gouy-Chapman model predicts a minimum at the potential of zero charge (see below). For monovalent ions, small ionic strengths, and surface charge densities the differential capacitance agrees with measurements [2, 32–34].

In 1924 Stern has drawn attention to certain limitations of the Gouy-Chapman theory. The latter allows for charge accumulation very close to the electrode. This explains the tendency of the Gouy-Chapman approach to predict too large values for the capacitance. Stern suggested to combine the Helmholtz and the Gouy-Chapman approach. Accordingly, the charge in the liquid phase is partly situated on a Helmholtz plane, which is located at a distance of about the ionic radius from the electrode surface. In this way the adsorption of ions at the electrode surface is taken into account. The remaining charge beyond the Helmholtz plane is treated as a diffuse layer in agreement with the Poisson-Boltzmann equation [31].

As compared to Stern's approach the model for an EDL according to Grahame describes the adsorption of the ions in more detail. Ions are considered as adsorbed, if they are held by the electrode not only due to coulombic forces but also due to covalent bonds or van der Waals forces or both. The term specific adsorption is used when the binding is specific to the various ions. In Grahame's model the adsorbed ions are situated closest to the electrode surface. Their electrical centers lie in the so-called inner Helmholtz plane. This description takes into account that adsorbed ions are not separated from the

electrode surface by solvent molecules in contrast to unadsorbed ions. As solvated ions the latter are accompanied by a solvent sheath which prevents that their electrical centers approach the electrode surface closer than the so-called outer Helmholtz plane [35].

The presented evolution of approaches, from Helmholtz until Grahame, shows that, over time, the description of an EDL has become more and more sophisticated. The introduction of Helmholtz layers takes into account that particles have a nonvanishing size. This concept has led to better agreements with experiments which suggests that the particle size is relevant for the structure of an EDL. However, in the approaches mentioned so far the particle size is only regarded close to the interface. In more recent models it is possible to take into account the molecular extent also further away. Such models are often denoted with respect to the underlying microscopic description of the present species, e.g., solvent particles, cations, and anions. For example, in the so-called "primitive model" (PM) ions are taken into account as charged hard spheres surrounded by a solvent which is regarded only implicitly by the corresponding permittivity. In the so-called "solvent primitive model" or "molecular solvent model" additionally the solvent molecules are treated as uncharged hard spheres. If the latter carry an embedded electric dipole, the corresponding model sometimes is referred to as "civilized model". In conjunction with the attribute "restricted" these models refer to hard spheres of the same radius, e.g., the restricted primitive model (RPM). In the following the term "molecular model" corresponds to any kind of these models in which particle sizes are explicitly taken into account, i.e., the PM, RPM, solvent primitive model, and civilized model.

Molecular models have been implemented in various ways. Theoretical approaches like modified Poisson-Boltzmann equations, integral equation approaches or density functional theories (see below) are usually based on mathematical approximations. The latter can be conveniently verified with help of computer simulations. Both Monte Carlo and molecular dynamics simulations have been applied in order to examine the structure of ionic systems within, e.g., the PM, RPM, or the solvent primitive model in the bulk [36–38] as well as in EDLs [39–41].

One possibility for the theoretical consideration of, inter alia, volume effects in electrolyte solutions is to evaluate the corresponding corrections to the Poisson-Boltzmann equation [42, 43]; in its original form the latter treats the ions as pointlike particles. The resulting improvements of the Poisson-Boltzmann equation are often referred to as modified Poisson-Boltzmann (MPB) equations [44, 45]. Various versions, e.g., MPB1 – MPB5, corresponding to different approximations have been suggested [46–48].

Mainly before density functional theory has been established molecular models have been implemented by means of integral equation approaches which are based on the Ornstein-Zernike equation. The latter relates the total correlation function h with the direct correlation function c. The Ornstein-Zernike equation can be solved for h and c, if it is combined with a so-called closure relation, i.e., a second independent relation

between h and c. In general closure relations are approximations with respect to which the various integral equation approaches are distinguished. For instance, the hypernetted chain (HNC) equation and the mean spherical approximation (MSA) have been commonly used [49–51]. A noteworthy feature of the MSA is the availability of an analytic solution for the PM which has been derived by Waisman and Lebowitz [52, 53]. For example, in Refs. [54–57] different integral equation approaches have been applied to model the structure of EDLs.

Alternatively EDLs in terms of molecular models can be considered by means of the density functional theory (DFT) [58], which is the approach of choice in the present dissertation. Therein the properties of the system under consideration are comprised in a density functional, i.e., a functional of the number density profiles of the various particle species. The density functional contains an external potential which conveys the interaction between the electrode and the electrolyte solution. In order to describe an EDL between a solid electrode and an electrolyte solution, the external potential is kept fixed and the corresponding equilibrium number density profiles are determined. The latter are defined as the number density profiles which minimize the density functional. The equilibrium number density profiles can be functions of the location and of further degrees of freedom like the orientation. They give detailed insight into the structure of the EDL which may be mapped onto quantities like the differential capacitance. The mutual interactions of the particles in the solution are taken into account by the so-called excess functional, i.e., the part of the density functional, which comprises contributions in excess to the exactly known ideal gas term. In general the exact expression of the excess functional is unknown which renders DFT approximative. However, in particular for hard spherical interactions accurate weighted density implementations have been developed, e.g., in Refs. [13, 59–61], which are referred to as "fundamental measure theory" (FMT). These approaches are valuable, among others, in DFT implementations of molecular models. There the hard-spherical character of the particles in the solution can be taken into account as a reference system by means of FMT. Additional interactions, like Coulomb interactions, can be treated perturbatively, e.g., within the MSA or the random phase approximation (RPA). DFT implementations of molecular models have been found to be in agreement with simulations [41, 62–65] and have been applied to examine, i.a., the structure of EDLs in Refs. [41, 62–72].

Among the electrically conducting liquids one may distinguish two types: (i) electrolyte solutions consist of ions that are dissolved in a solvent, e.g., salt water. (ii) Ionic liquids are solvent-free and consist of ions only. Molten salts are examples for ionic liquids but usually high temperatures are necessary in order to melt a salt. In contrast there are ionic liquids which liquify already at temperatures below $100\,°C$; these are commonly referred to as room-temperature ionic liquids (RTILs) [73, 74]. As compared to ions of common salts RTIL ions are not roundish on the atomic scale and the charge is distributed

inhomogeneously across the molecule [74], so that molecular models with hard spherical ions would be a rather crude approximation. The EDL between an ionic liquid and a charged wall behaves different as compared to an electrolyte solution EDL. For the latter case already a description in agreement with the Poisson-Boltzmann equation leads to reasonable results. This treatment corresponds to the picture that, up to the Coulomb interaction, ions are ideal gas particles. In particular in dilute electrolyte solutions the neglect of the volumes of the ions in the theoretical approach leads to, at least, a qualitative agreement with measurements in terms of the differential capacitance. In contrast, in ionic liquids the ions are the only species present so that volume effects should be taken into account. For example, in Ref. [73] the so-called Poisson-Fermi equation, a kind of modified Poisson-Boltzmann equation, is derived from a lattice-gas model of concentrated electrolytes which takes into account that there is a maximal possible local concentration of ions. The approach allows to conveniently interpolate between two extreme cases by means of one parameter γ: the Gouy-Chapman theory corresponds to $\gamma = 0$, whereas $\gamma = 1$ means that all available sites are occupied. The differential capacitance C in dependence of the dimensionless electrode potential u_0 is given analytically. Within the Gouy-Chapman approach $C(u_0) \propto \cosh(u_0/2)$. Already for small but finite values of γ deviations from this behavior manifest: instead of growing exponentially the capacitance begins to decrease for large $|u_0|$ due to lattice saturation. In the limit of large $|u_0|$ the proportionality $C \propto (\gamma|u_0|)^{-1/2}$ is predicted; the resulting plot could be described as camel-shaped. For sufficiently large values of γ the graph of $C(u_0)$ exhibits a maximum at $u_0 = 0$ and decays for growing $|u_0|$. This bell-shaped graph clearly contradicts the Gouy-Chapman behavior with a minimum at $u_0 = 0$ and thus supports Kornyshev's argument that the theory of the EDL in ionic liquids must be built differently [73]. The appearance of a bell-shaped differential capacitance versus potential curve has been confirmed experimentally for various ionic liquids [29]. Further insight into the structure of ionic liquids EDLs is provided by an approach of the Landau-Ginzburg type in Refs. [75, 76] which is able to describe both crowding and overscreening. For increasing surface potential the counterions form a condensed layer at the interface which expands into the bulk; this behavior originates from lattice saturation and is referred to as crowding. Due to short range correlations the accumulated charge overscreens the electrode charge, i.e., more charge is located in the condensed layer than on the surface. The resulting net charge leads to a formation of an additional layer of coions. The latter, in turn, slightly overscreens the net charge, and so on. The approach in Refs. [75, 76] is in better agreement with simulations than a simpler approach without correlations which allows for the conclusion that correlations play an essential role in ionic liquids. For the interested reader reference is made to Refs. [74, 77] where ionic liquids at interfaces are reviewed.

   To sum up, for the theoretical description it is crucial whether a solvent in the ionic system is present or not, i.e., one has to make a decision about whether an electrolyte

solution or an ionic liquid is to be modelled. In the present dissertation EDLs between electrolyte solutions and curved solid electrodes are discussed (see Chaps. 4 and 5). On one hand the discussion of ionic systems is partly dedicated to the evaluation of the morphometric approach. Against this background electrolyte solutions have been the first choice because their intrinsic length scale can be easily adjusted. In comparison ionic liquids are accompanied by strong Coulomb correlations [74], which questions the applicability of the morphometric approach in the first place. On the other hand, as compared with ionic liquids, the ions of common electrolyte solutions exhibit a simpler geometry which reduces the complexity of the underlying description. Systems of this kind can be approached by means of the aforementioned models which have been confirmed many times. Numeric DFT implementations of molecular models, which are able to resolve microscopic details of the structure of the EDL, converge relatively fast. This allows to study extensively the dependence of the EDL on the geometry of the electrode and to assess the impact of various (microscopic) parameters.

The following Chaps. 2 – 5 contain the insights which have been gained in the course of this dissertation. The chapters address distinct theoretical models and comprise the corresponding results and discussions; technical details are to be found in appendices at the end of each chapter. A thematic classification within the specific literature as well as a short summary is given for each chapter separately. The dissertation can be roughly divided into two parts; one consisting of Chaps. 2 and 3 with the focus on simple fluids, and the other consisting of Chaps. 4 and 5 with the focus on electrolyte solutions. Within the parts the chapters are closely related and partially build upon each other.

Chapters 2 and 3 are mainly dedicated to the examination of the morphometric thermodynamics. To that end the interface between a solid wall and a fluid phase is considered. The latter is assumed to consist of a simple fluid. The entire wall-fluid system is taken into account by means of density functional theory (DFT). Such an approach ensures a consistent description of the fluid phase both in the bulk and close to the inhomogeneity. This is essential because the interfacial tension finally arises from subtracting the contribution proportional to the volume of the phase from the grand canonical potential of the entire system [see, e.g., Eq. (1.1)]. In addition, the different DFT approaches in use are microscopic models. They are capable of resolving the structure in interfaces of macroscopically small radii of curvature in which the shape dependence of the interfacial tension becomes significant. The wall is of planar, spherical, or cylindrical shape. The symmetry of these geometries enables an effectively one-dimensional description, which allows for precise numerics or even for the derivation of exact expressions. Moreover such kinds of walls exhibit a constant curvature across their surfaces. As a result the expression for the interfacial tension in agreement with MT simplifies; it can be written as a polynomial in the inverse wall radius [see Eq. (2.3)].

In Chap. 2 a density functional within the second-virial-approximation is applied. This

approach ensures high precision for low number densities which is confirmed by comparison with simulation results. It is used in order to calculate numerically the interfacial tension as a function of the wall radius. This result is expanded in powers of the wall curvature and compared with the corresponding expression in agreement with MT. For all considered cases, i.e., distinct interaction potentials for the fluid-fluid as well as for the fluid-wall interactions, MT turns out to be not exactly valid. Its quality as an approximation strongly depends on the interface convention which underlies the definition of the interfacial tension.

In Chap. 3 a modified version of the density functional of Chap. 2 is used in order to model a Yukawa fluid at curved walls. The resulting Euler Lagrange equations can be solved analytically for the geometries under consideration and exact expressions for the interfacial tension can be obtained. These are expanded in powers of the wall curvature which leads to analytically known curvature coefficients. The latter are discussed in detail. Among others, they demonstrate that the approach of MT is not complete for the model in use. The quality of the morphometric approach as an approximation depends on the shape of the wall.

After a detailed discussion concerning simple fluids in contact with solid walls in Chaps. 2 and 3, in the subsequent Chaps. 4 and 5 electrolyte solutions at curved electrodes come into focus. Systems of the latter kind offer more possibilities to manipulate the fluid behavior in particular close to the interface. For instance, the amount of ions in the system determines the Debye length, which is an intrinsic length scale corresponding to the decay behavior of the electrostatic interaction. The wall-fluid interaction potential can be adjusted by means of the charge on the electrode surface. Moreover the shape of the electrode itself can be conveniently varied within the theoretical models under consideration. Since the choice of wall geometries in Chaps. 2 and 3 has led to fruitful discussions, the same types of geometries are considered also in Chaps. 4 and 5. The above addressed and further impacts on the structure of the electric double layer are captured by means of the differential capacitance C. The latter is related to the interfacial tension so that, in principle, the predictions of MT should be applicable likewise; without the necessity to specify an interfacial convention, C turns out to be a convenient quantity to test the morphometric approach. However, MT has turned out to be a doubtful approach already with respect to simple fluids. Having this in mind, it hardly comes as a surprise, that also the more complex electrolyte solutions are not in line with MT. For that reason it is abstained from a too detailed discussion in terms of curvature expansions as in the preceding chapters. Instead in Chaps. 4 and 5 the focus is on the entire curvature dependence of the differential capacitance. The outcome of various models is compared with each other and the influences of parameters, such as surface charge density and ionic strength, are analyzed.

In Chap. 4 an electrolyte solution in contact with an electrode is taken into account

by means of the Poisson-Boltzmann theory. The differential capacitance is discussed as a function of the wall curvature in dependence of, e.g., the ionic strength and the surface charge density. The corresponding graphs reveal two curvature ranges with distinct behaviors: in the range of small curvatures the capacitance is largely affected by the surface charge density. For large curvatures the dependence on the surface charge density diminishes. Both curvature ranges are analyzed in detail.

In Chap. 5 an electrolyte solution in contact with an electrode is approached by a microscopic DFT. The underlying implementation of the so-called civilized model can be considered as an extension of the PB approach in the preceding chapter. For instance, it allows for the description of steric effects between the particles in the solution and of a spatially varying polarization due to the electric dipoles embedded in the solvent particles. As compared to the PB theory, the civilized model enables to analyze the influence of microscopic parameters, such as the particle radii or the dipole moment. Furthermore it is possible to compare its outcome with the predictions of simpler theories for double layers at curved electrodes.

Conclusions and outlook are given in Chap. 6.

Chapter 2

Implications of interface conventions for morphometric thermodynamics

The present Chap. 2 corresponds to a slightly modified and extended version of the study published in Ref. [22]. There several model fluids in contact with planar, spherical, and cylindrical walls are investigated for small number densities within density functional theory. The dependence of the solid-fluid interfacial tension on the curvature of spherical and cylindrical walls is examined and compared with the corresponding expression derived within the framework of morphometric thermodynamics. Particular attention is paid to the implications of the choice of the interface location, which underlies the definition of the interfacial tension. Morphometric thermodynamics is found to be never exact for the considered systems. It turns out that its quality as an approximation depends sensitively on the choice of the interface location.

2.1 Introduction

In recent years morphometric thermodynamics (MT) has been used to understand the influence of geometric constraints on the thermodynamic properties of fluids [8, 14–16, 18]. This approach has been motivated by a theorem of integral geometry which is often referred to as "Hadwiger's theorem" [78, 79]. For example, in Ref. [8] it has been applied to a fluid of hard spheres bounded by a hard wall. Based on the assumption of being an additive, motion-invariant, and continuous functional of the shape of the walls, the grand canonical potential Ω_{eq} of a confined fluid is given, in accordance with Hadwiger's theorem, by a linear combination of only four geometrical measures which characterize the shape S of the confining walls: volume $\mathcal{V}$, surface area $\mathcal{A}$, integrated mean curvature C, and Euler characteristic Y:

$$\Omega_{\mathrm{eq}}[S] = -p\mathcal{V}[S] + \gamma_0\mathcal{A}[S] + \kappa C[S] + \bar{\kappa}Y[S]. \tag{2.1}$$

According to Eq. (2.1) the pressure p, the interfacial tension for a *planar* wall γ_0, and the bending rigidities κ and $\bar{\kappa}$, unlike the geometrical measures, do not depend on the shape of the bounding container. This structure turns morphometric thermodynamics into a very attractive tool, because once the thermodynamic coefficients p, γ_0, κ, and $\bar{\kappa}$ have been determined, preferably by considering simple geometries S, the grand canonical potential can be readily calculated even for systems bounded by complex geometries the shape S of which enters Eq. (2.1) only via the measures $\mathcal{V}, \mathcal{A}, C$, and Y. This strategy has been used, e.g., in Refs. [14, 15, 18] in order to calculate solvation free energies of proteins with complex shapes.

As a thermodynamic quantity, which follows from the grand canonical potential, the interfacial tension γ acquires the simple morphometric form [8]

$$\gamma = \gamma_0 + \kappa \bar{H} + \bar{\kappa} \bar{K}, \qquad (2.2)$$

where $\bar{H} = C/\mathcal{A}$ and $\bar{K} = Y/\mathcal{A}$ denote the averaged mean and Gaussian curvatures, respectively, of the confining wall [8]. In the case of geometries with constant curvatures, i.e., spherical and cylindrical walls with radii of curvature R, Eq. (2.2) can be written as

$$\gamma = \begin{cases} \gamma_0 + \dfrac{\gamma_1}{R} + \dfrac{\gamma_2}{R^2}, & \text{spherical wall,} \\[2mm] \gamma_0 + \dfrac{\gamma_1}{R}, & \text{cylindrical wall,} \end{cases} \qquad (2.3)$$

where $\gamma_{1,2}$ denote coefficients independent of the curvature $1/R$ and where $\gamma_2 = 0$ in the case of cylindrical walls. Note that in Eq. (2.3) and below in Eq. (2.18) the coefficients $\gamma_{n>0}$ are not the same for spherical and cylindrical walls. For clarity in the following the considered geometry is explicitly noted. For the case that coefficients of different geometries are compared with each other, additional subscripts will be introduced.

On one hand morphometric thermodynamics has already been applied to several physical systems confined to geometries with complex shapes [14, 15, 18] and it has been found to be in agreement with certain data of hard spheres [8, 10, 16] and of hard rods [9] in contact with hard walls. On the other hand, in agreement with earlier studies using gradient expansion approaches [80, 81], recently evidences have been provided, that a description as in Eq. (2.3), where the curvature expansion of the interfacial tension for a spherical wall terminates after the quadratic and that of a cylindrical wall after the linear order in $1/R$, could be incomplete [19–21].

Here an explanation for the observation is proposed that for certain studies morphometric thermodynamics appears to be applicable, whereas it is not for others. To that end, several model fluids with small number densities in contact with curved walls are analyzed by means of density functional theory (DFT) within the second virial approximation (see Sec. 2.2). This technically simple approach allows one to study various kinds

of interactions among the fluid particles [Eqs. (2.4) – (2.6)] with *high* numerical precision for low densities (see, e.g., Fig. 2.3). For this reason fluids with high densities as they occur, e.g., at two-phase coexistence, are not considered. It turns out that those basic features of morphometric thermodynamics this study is aiming at reveal themselves already at low densities for which one can control the numerical accuracy sufficiently in order to address reliably the corresponding issues. Moreover exact results are presented for an ideal gas fluid confined by non-hard spherical and cylindrical walls. The focus is on the interfacial tension γ. Its curvature dependence is compared with the one predicted from morphometric thermodynamics [Eq. (2.3), see Sec. 2.3]. It turns out that the morphometric form of the interfacial tension is indeed not valid exactly and that its quality as an approximation depends on the choice of the location of the interface underlying the definition of the interfacial tension (see Sec. 2.4).

2.2 Model

Let us consider a simple fluid composed of particles which interact via an isotropic pair potential $U(r)$ which is characterized by an energy scale U_0, a length scale L, and, for technical convenience, a cut-off length L_c such that $U(r > L_c) = 0$. The focus is on three distinct types of pair potentials:

- the square-well ($U_0 < 0$) or square-shoulder ($U_0 > 0$) potential

$$\beta U(r \leq L_c) = \beta U_0 \tag{2.4}$$

  with $L = L_c$,

- the Yukawa potential ($U_0 > 0$)

$$\beta U(r \leq L_c) = \beta U_0 \frac{L}{r} \exp\left(-\frac{r}{L}\right), \tag{2.5}$$

- the Lennard-Jones potential ($U_0 > 0$)

$$\beta U(r \leq L_c) = \beta U_0 \left[\left(\frac{L}{r}\right)^{12} - \left(\frac{L}{r}\right)^{6}\right]. \tag{2.6}$$

In the following non-uniform number density profiles $\varrho(\boldsymbol{r})$ of the fluid in contact with walls are studied. To this end density functional theory [58] offers a particularly useful approach. Since the present investigation is focused on *low* densities, we use the density functional $\Omega[\varrho]$ within the second-virial approximation [49, 61, 82] (see Appendix 2.A for

a derivation of the excess functional):

$$\beta\Omega[\varrho] = \int d^3r \, \varrho(\boldsymbol{r}) \left\{ \ln\left[\varrho(\boldsymbol{r})L^3\right] - 1 - \beta\mu + \beta V^{\text{ext}}(\boldsymbol{r}) \right\}$$
$$+ \frac{1}{2} \int d^3r \int d^3r' \, \varrho(\boldsymbol{r})\varrho(\boldsymbol{r}') \left\{ 1 - \exp[-\beta U(|\boldsymbol{r} - \boldsymbol{r}'|)] \right\}, \tag{2.7}$$

where $\beta = 1/(k_B T)$ is the inverse temperature, $V^{\text{ext}}(\boldsymbol{r})$ is the external potential due to walls, and μ is the chemical potential $\tilde{\mu}$ shifted by a constant (with respect to $\boldsymbol{r}$ and ϱ) given by the thermal de Broglie wavelength Λ and the length scale L of the pair potential among the fluid particles:

$$\beta\mu := \beta\tilde{\mu} - 3\ln\left(\frac{\Lambda}{L}\right). \tag{2.8}$$

The geometrical properties of the walls enter the description only via the external potential V^{ext}. In order to determine the thermodynamic coefficients in Eq. (2.1) we consider the bulk fluid and the fluid in contact with planar, spherical, and cylindrical walls exhibiting constant curvatures. For these choices the densities in Eq. (2.7) depend on a single spatial variable only.

- The uniform *bulk* corresponds to a spatially constant external potential, which can be set to zero without loss of generality:

$$\beta V^{\text{ext}}(\boldsymbol{r}) = 0. \tag{2.9}$$

  As a consequence the equilibrium density $\varrho_{\text{eq}}(\boldsymbol{r}) = \varrho_{\text{eq}}^{\text{bulk}}$ is independent of the position $\boldsymbol{r}$.

- A *planar* wall leads to an external potential

$$\beta V^{\text{ext}}(\boldsymbol{r}) = \begin{cases} \infty, & z < 0, \\ \beta V(z), & z \geq 0. \end{cases} \tag{2.10}$$

  This potential implies that the equilibrium density $\varrho_{\text{eq}}(z)$ is identically zero for $z < 0$. Therefore it is not possible for the *centers* of the fluid particles to get closer to the wall than $z = 0$. In the following the set of accessible points of the *centers* of the fluid particles closest to the geometrical wall surface is called the *reference surface*. In Eq. (2.10) $V(z)$ represents the excess part of the wall potential [i.e., in excess of $V^{\text{ext}}(z < 0) = \infty$] as a function of the distance z from the reference surface. Depending on the wall-fluid interaction potential, the *geometrical* wall surface at position X_g in Fig. 2.1 and the reference surface at position X in Fig. 2.1 can be distinct.

- A *spherical* wall with radius R of the reference surface is characterized by an external potential

$$\beta V^{\text{ext}}(\boldsymbol{r}) = \begin{cases} \infty, & r < R, \\ \beta V(r), & r \geq R, \end{cases} \tag{2.11}$$

where $V(r)$ represents the excess part of the external potential as a function of the distance r to the center of the sphere.

- A *cylindrical* wall with radius R of the reference surface is characterized by an external potential of the same form as the one in Eq. (2.11); however, in this case, r and R measure distances from the symmetry axis of the cylinder.

In accordance with the variational principle underlying density functional theory [58] the equilibrium density $\varrho_{\text{eq}}(\boldsymbol{r})$ minimizes the functional in Eq. (2.7). The corresponding Euler Lagrange equation,

$$\frac{\delta \beta \Omega[\varrho]}{\delta \varrho(\boldsymbol{r})}\bigg|_{\varrho_{\text{eq}}} = \ln \left[\varrho_{\text{eq}}(\boldsymbol{r}) L^3\right] - \beta \mu + \beta V^{\text{ext}}(\boldsymbol{r}) + \int \mathrm{d}^3 r' \, \varrho_{\text{eq}}(\boldsymbol{r}')\{1 - \exp[-\beta U(|\boldsymbol{r} - \boldsymbol{r}'|)]\}$$
$$= 0, \tag{2.12}$$

is solved numerically by means of the Piccard iteration scheme (see Sec. 8.1 in Ref. [61]). From the equilibrium density profile $\varrho_{\text{eq}}(\boldsymbol{r})$, the grand canonical potential Ω_{eq} follows from [58] [Eq. (2.7)]

$$\Omega_{\text{eq}} = \Omega[\varrho = \varrho_{\text{eq}}]. \tag{2.13}$$

It has been verified that the hard wall sum rule (see, e.g., Ref. [10]) is fulfilled by the functional in Eq. (2.7).

2.3 Discussion

The interfacial tension γ is defined by

$$L^2 \beta \gamma = \frac{\beta \Omega_{\text{eq}} - \beta \Omega_{\text{eq}}^{\text{bulk}}}{\mathcal{A} L^{-2}} = \frac{\beta \Omega_{\text{eq}} + \beta p \, \mathcal{V}}{\mathcal{A} L^{-2}} \tag{2.14}$$

as the work $\Omega_{\text{eq}} - \Omega_{\text{eq}}^{\text{bulk}}$ per interfacial area $\mathcal{A}$ required to create the interface [3]. On the right hand side of Eq. (2.14) the relation

$$\beta \Omega_{\text{eq}}^{\text{bulk}} = -\beta p \, \mathcal{V} \tag{2.15}$$
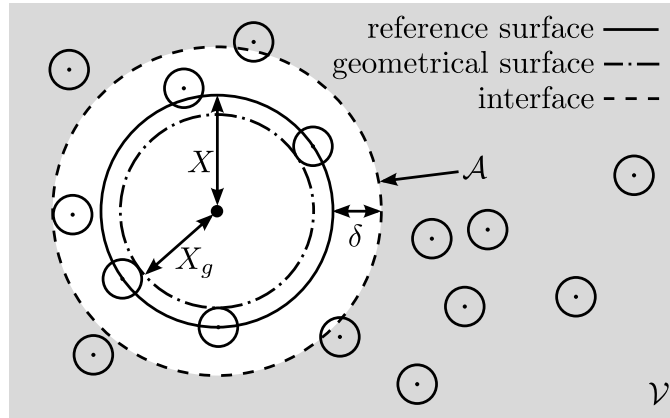
Figure 2.1: The reference surface (solid line) at position X is determined by the external potential. It consists of the set of all reachable locations of the *centers* of the fluid particles which are closest to the geometrical wall surface (dash-dotted line) at position X_g. Depending on the wall-fluid interaction potential, the geometrical wall surface and the reference surface can be distinct. The interface of area $\mathcal{A}$ (dashed line), with respect to which the interfacial tension γ in Eq. (2.16) is defined, may differ from the reference surface. The parameter δ measures the offset of the interface with respect to the reference surface. This sketch refers to the cases of spherical or cylindrical walls for which $X \equiv R$. However, the concept involving the parameter δ is valid also for other geometries, in particular for a planar wall with $X \equiv z = 0$. If the dashed line runs *within* the interior of the reference surface, δ is taken to be negative. The fluid volume $\mathcal{V}$, which refers to the set of all points being not closer to the geometrical wall surface than the interface, is shaded in grey.

between the grand canonical potential $\Omega_{\text{eq}}^{\text{bulk}}$, the fluid volume $\mathcal{V}$, and the bulk pressure p has been used [3].

The wall-fluid interfacial tension γ is not an observable because according to Eq. (2.14) its value depends, via $\mathcal{V}$ and $\mathcal{A}$, on the arbitrary choice of an interface position. In order to characterize various interface conventions we introduce a parameter δ which measures the offset of a chosen interface position with respect to the reference surface (see Fig. 2.1). In addition to the interfacial area $\mathcal{A}$ the choice of an interface position also determines what is called the fluid volume $\mathcal{V}$, which refers to the set of all points being not closer to the geometrical wall surface than the interface. As a consequence $\mathcal{A}$ and $\mathcal{V}$ are functions of $X + \delta$ where X characterizes the reference surface (see Fig. 2.1). On the other hand Ω_{eq} depends on X only, because due to Eq. (2.13) only the parameters of the substrate potential (i.e., X) enter Ω_{eq}. Accordingly, one has

$$L^2 \beta \gamma(X, \delta) = \frac{\beta \Omega_{\text{eq}}(X) + \beta p \, \mathcal{V}(X + \delta)}{\mathcal{A}(X + \delta) L^{-2}}. \tag{2.16}$$

In the following the data are calculated within the convention $\delta/L = 0$ as this choice
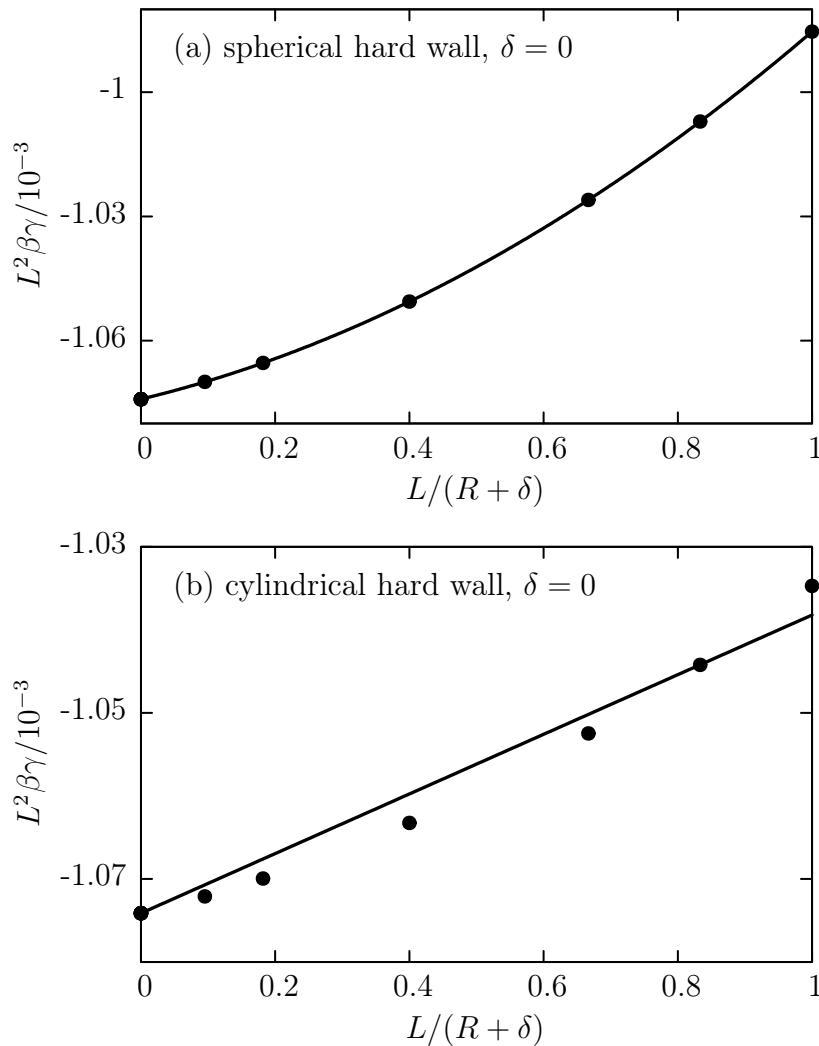
Figure 2.2: The interfacial tension γ of hard spheres with diameter L for the convention $\delta/L = 0$ as a function of the radius R of the reference surface forming the boundary of a spherical (a) and a cylindrical (b) hard body. Polynomials (lines) as predicted by morphometric thermodynamics [up to order $1/(R+\delta)^2$ for spherical walls and up to order $1/(R+\delta)$ for cylindrical walls] have been fitted to the numerical data (dots). In panel (a) the fit shows good agreement with the data, whereas panel (b) clearly shows deviations from the predicted behavior. This means that for the cylindrical wall the curvature expansion of γ Eq. (2.3) does not terminate after the first-order term, in contradiction to the prediction from morphometric thermodynamics. The hard spheres interact among each other via the square-shoulder potential $U(r)$ in Eq. (2.4) with $\beta U_0 = \infty$. The chemical potential is chosen as $\beta\mu = -2.768839$ which corresponds to the low packing fraction $\eta = \frac{\pi}{6}\varrho_{\mathrm{eq}}^{\mathrm{bulk}}L^3 \approx 0.02656$.

is convenient for various types of interactions U. Moreover, in certain studies (see, e.g., Ref. [83]) this choice has been argued to be "the natural one from the point of view of statistical mechanics". Figure 2.2 shows the interfacial tension γ for hard spheres in contact with spherical [Fig. 2.2(a)] and cylindrical [Fig. 2.2(b)] walls with various radii

R of the reference surface. The packing fraction $\eta = \pi \varrho_{\mathrm{eq}}^{\mathrm{bulk}} L^3/6$ is chosen sufficiently small such that the second virial approximation is valid. The plot for the cylindrical walls [Fig. 2.2(b)] reveals a non-linear increase, similar to the case of spherical walls [Fig. 2.2(a)]. This means that the curvature expansion of γ in terms of powers of $1/R$ does not terminate after the first-order term, in contradiction to the prediction from morphometric thermodynamics for cylindrical walls.

Evaluating Eq. (2.16) for $\delta = 0$ and arbitrary $\delta \neq 0$ and exploiting that Ω_{eq} does not depend on δ leads to

$$L^2 \beta \gamma(X, \delta) = \frac{\mathcal{A}(X)}{\mathcal{A}(X + \delta)} L^2 \beta \gamma(X, \delta = 0) + \frac{L^2 \beta p}{\mathcal{A}(X + \delta)} \left[\mathcal{V}(X + \delta) - \mathcal{V}(X) \right]. \qquad (2.17)$$

According to Eq. (2.17) the interfacial tension $\gamma(X, \delta = 0)$ calculated for the convention $\delta/L = 0$ can be translated to that for any other choice of the convention. For example the convention $\delta/L = -0.5$ is often used when discussing hard spheres confined by hard walls because this choice renders the interface to coincide with the geometrical wall surface at position X_g in Fig. 2.1, which, in this case, is separated from the reference surface at position X in Fig. 2.1 by a distance given by the particle radius $L/2$.

In Fig. 2.3 simulation results of Laird et al. [16] for hard spheres with packing fraction $\eta = 0.02656$, obtained for $\delta/L = -0.5$, are plotted together with the data of Fig. 2.2 which have been translated into the convention $\delta/L = -0.5$ according to Eq. (2.17). The agreement with the simulation data is very good. In particular, within this convention for δ, in the case of a cylindrical wall [Fig. 2.3(b)] the data points almost coincide with a straight line, in accordance with the prediction of morphometric thermodynamics. This finding has also been confirmed for the packing fractions $\eta \approx 0.053$ and 0.101, for which the respective plots are qualitatively similar to those in Fig. 2.3 except that, as expected, the results of the present virial expansion deviate more and more from the simulation data upon increasing the density.

Figures 2.2 and 2.3, which are based on the same microscopic system, show that the interfacial tension depends strongly on the choice of the convention for δ. Upon varying δ not only the sign of γ may change, as already noted in Ref. [10], but also the magnitude and even the qualitative functional form, which is revealed clearly in the case of cylindrical walls.

Figure 2.4 shows the behavior of the same microscopic system as above (hard spheres exposed to a hard cylindrical wall) described in terms of two conventions for $\eta \approx 0.01$. The data are presented in log-log plots which facilitate the identification of power laws in $1/(R + \delta)$. In this presentation the contribution $\gamma_0(\delta)$ of the planar wall is subtracted so that the plotted quantity vanishes for $R \to \infty$. Within the convention $\delta/L = 0$, at $R \approx 3L$ there is a crossover between two power laws. Thus the dependence of the interfacial tension on $1/R$ consists of more than the leading term $\sim 1/R$ which, according to morphometric
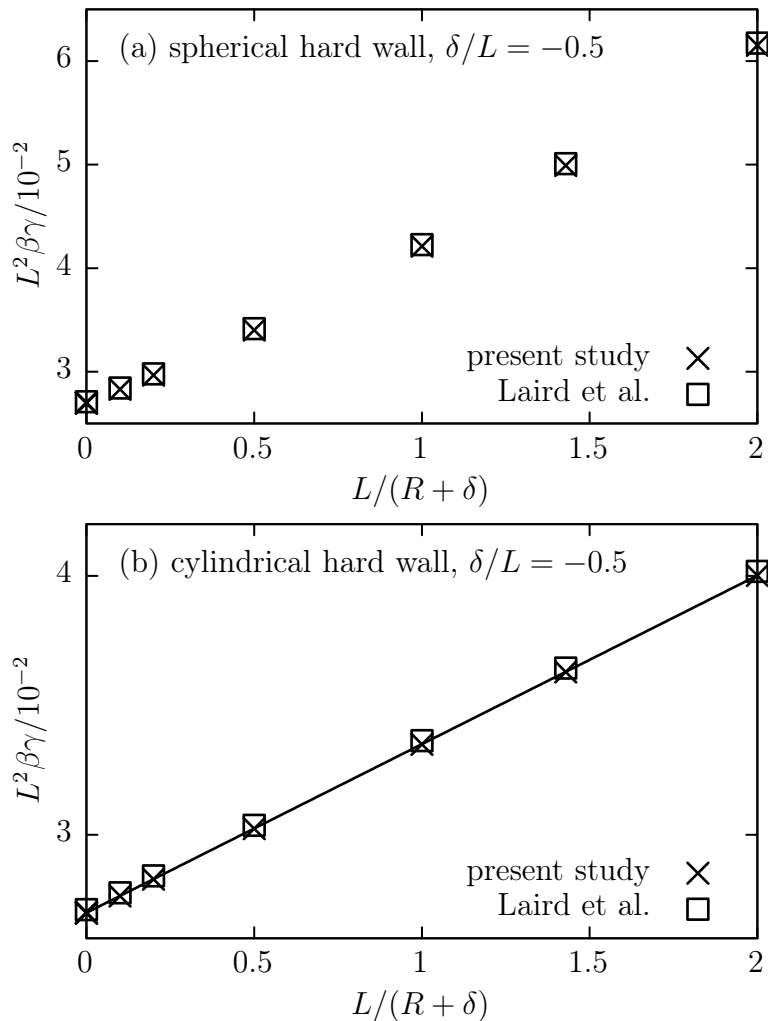
Figure 2.3: Comparison of the simulation results of Laird et al. [16] (squares $\square$) with the corresponding data of the present DFT study (crosses $\times$) for the packing fraction $\eta \approx 0.02656$. The latter have been obtained by translating the data displayed in Fig. 2.2 (for $\delta = 0$) into the convention $\delta/L = -0.5$ by using Eq. (2.17). In contrast to Fig. 2.2(b), the plot of the interfacial tension in the case of a cylindrical wall (b) almost coincides with a straight line.

thermodynamics, would be the only one allowed for the cylindrical configuration. The behavior is different within the convention $\delta/L = -0.5$. There, within this presentation, the interfacial tension is represented by an almost straight line throughout the whole range of $(R+\delta)/L$ shown. In order to analyze the curvature dependence of the interfacial tension more quantitatively, we assume that $\gamma(R, \delta)$ can be expanded in terms of a power series in $1/(R + \delta)$:

$$L^2 \beta \gamma(R, \delta) = L^2 \sum_{n=0}^{\infty} L^n \frac{\beta \gamma_n(\delta)}{(R + \delta)^n}. \tag{2.18}$$
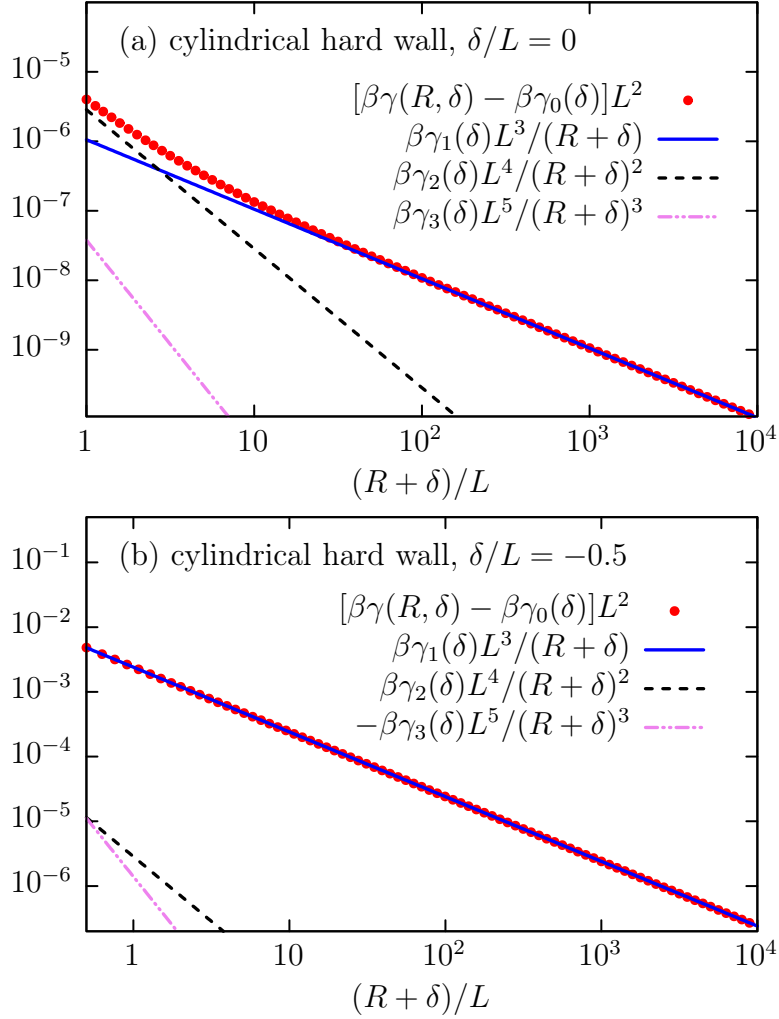
Figure 2.4: Dependence of the interfacial tension γ for hard spheres at a cylindrical hard wall on the radius R of the reference surface and on the shift parameter δ. The contribution of the planar wall $\gamma_0(\delta)$, which corresponds to the limit $R \to \infty$, has been subtracted. The numerical data (red dots) are obtained within the convention $\delta/L = 0$ (a) and translated to the convention $\delta/L = -0.5$ (b) via Eq. (2.17). The three straight lines represent the terms $n = 1, 2, 3$ of the curvature expansion in Eq. (2.18). In the case $\delta/L = 0$ the coefficient $\gamma_2(\delta)$ is the largest one, i.e., for small R the contribution $\beta\gamma_2(\delta)L^4/(R + \delta)^2$ is the dominant one so that a deviation from the leading behavior $\sim 1/(R + \delta)$ becomes obvious for $R/L \lesssim 3$. Within the convention $\delta/L = -0.5$ the leading coefficient $\gamma_1(\delta)$ is the largest one, i.e., the leading term $\beta\gamma_1(\delta)L^3/(R + \delta)$ is the dominant one. Here $U(r)$ is given by Eq. (2.4) with $U_0 \to \infty$ and $\beta\mu = -3.88$ so that $\eta \approx 0.01$. Note that at $(R + \delta)/L = 1$ the plots render the values of the dimensionless coefficients $\beta\gamma_n(\delta)L^2$.

For various radii R of the reference surface of the curved wall, the interfacial tension γ is calculated numerically (red dots in Fig. 2.4) and fitted to the curvature expansion Eq. (2.18) with $n \leq 10$. This way the coefficients $\gamma_n(\delta)$ have been determined. Only the coefficient $\gamma_0(\delta)$, which is the interfacial tension at a planar wall, can be obtained

independently without fitting. In Fig. 2.4 the terms $L^{n+2}\beta\gamma_n(\delta)/(R+\delta)^n$ corresponding to $n \in \{1, 2, 3\}$ in the curvature expansion of Eq. (2.18) are plotted as lines. Within the convention $\delta/L = 0$ the quadratic coefficient γ_2, which vanishes within morphometric thermodynamics, is even larger than the linear coefficient γ_1; this explains the crossover between two power laws describing the numerical data (red dots). However, within the convention $\delta/L = -0.5$ the first-order coefficient γ_1 is much larger than the higher order coefficients γ_n, $n \geq 2$, so that in this case morphometric thermodynamics is a very good approximation of the exact curvature dependence of the interfacial tension.

Within the class of systems with square-well-like or square-shoulder-like particle-particle interactions, a large variety of configurations within the convention $\delta/L = 0$ has been studied in the same way as shown in Fig. 2.4. Fluids with packing fractions $\eta \in \{0.01, 0.02, 0.05, 0.10\}$ and with interaction strengths $\beta U_0 \in \{-0.1, 0.1, 1, \infty\}$ have been examined near spherical and cylindrical hard walls. In addition to the interfacial tension γ, the dimensionless excess adsorption Γ [3],

$$L^2\Gamma(X, \delta) = \frac{N(X) - \varrho_{\text{eq}}^{\text{bulk}} \mathcal{V}(X+\delta)}{\mathcal{A}(X+\delta)L^{-2}}, \tag{2.19}$$

has been calculated for $U_0 > 0$ where $N(X) = \int_{\mathcal{V}(X)} \mathrm{d}^3r\, \varrho(\boldsymbol{r})$ denotes the number of fluid particles. The corresponding observations can be summarized as follows:

- Apart from opposite signs, both the excess adsorption Γ and the interfacial tension γ exhibit a similar dependence on the radius of curvature R.

- The functional form of $L^2 [\beta\gamma(R, 0) - \beta\gamma_0(0)]$ is similar when comparing fluids with the same bulk state near a spherical and a cylindrical hard wall. Because in all considered cases the third order coefficient γ_3 is smaller than γ_1 and γ_2, morphometric thermodynamics turns out to be a better approximation for spherical than for cylindrical walls.

- Decreasing packing fractions η or interaction strengths $U_0 > 0$ result in a shift of the crossover between the power laws describing $L^2[\beta\gamma(R, 0) - \beta\gamma_0(0)]$ towards larger radii R, i.e., the second coefficient γ_2 becomes larger in comparison to the first coefficient γ_1. Apart from that, the behavior of $L^2 [\beta\gamma(R, 0) - \beta\gamma_0(0)]$ is similar to the one shown in Fig. 2.4. For $U_0 < 0$, $L^2 [\beta\gamma(R, 0) - \beta\gamma_0(0)]$ exhibits a zero because the coefficients γ_1 and γ_2 have opposite signs.

- For some of the above systems the data have been translated to the convention $\delta/L = -0.5$ by using Eq. (2.17). In these cases, for the spherical wall configurations the third order coefficient γ_3 is much smaller than γ_1 and γ_2, and for the cylindrical wall configurations the leading coefficient γ_1 is much larger than the subleading

ones. Therefore, within this convention morphometric thermodynamics turns out to be a very good approximation.

The comparison of the plots in Figs. 2.4(a) and (b) shows that the coefficients $\gamma_n(\delta)$ in the curvature expansion [Eq. (2.18)] indeed depend on the chosen convention δ (see also, e.g., Refs. [10, 19, 21]). In order to examine the implications of shifting the position of the interface (see Fig. 2.1) this dependence is investigated more closely. The derivative of Eq. (2.16) with respect to δ for fixed R leads to

$$L\frac{\partial}{\partial\delta}L^2\beta\gamma(R,\delta) = -L^3\beta p - d\frac{L}{R+\delta}L^2\beta\gamma(R,\delta),$$

$$d = \begin{cases} 2, & \text{spherical wall,} \\ 1, & \text{cylindrical wall,} \end{cases} \tag{2.20}$$

where $\mathcal{V}'(R+\delta) = -\mathcal{A}(R+\delta)$ and $\mathcal{A}'(R+\delta)/\mathcal{A}(R+\delta) = d/(R+\delta)$ have been used. The derivative of Eq. (2.18) with respect to δ gives

$$L\frac{\partial}{\partial\delta}L^2\beta\gamma(R,\delta) = L^3\sum_{n=0}^{\infty}\left\{L^n\frac{\beta\gamma_n'(\delta)}{(R+\delta)^n} - L^n n\frac{\beta\gamma_n(\delta)}{(R+\delta)^{n+1}}\right\}. \tag{2.21}$$

Equating Eqs. (2.20) and (2.21) and using Eq. (2.18) leads to

$$-L^3\beta p = L^3\beta\gamma_0'(\delta) + \sum_{n=1}^{\infty}\frac{L^n}{(R+\delta)^n}\left\{L^3\beta\gamma_n'(\delta) + (d-n+1)L^2\beta\gamma_{n-1}(\delta)\right\} \tag{2.22}$$

for all R. Comparison order by order in $(R+\delta)^{-1}$ in Eq. (2.22) renders

$$O\left[(R+\delta)^0\right]: \quad -L^3\beta p = L^3\beta\gamma_0'(\delta) \tag{2.23}$$

and

$$O\left[(R+\delta)^{-n}\right], \ n \geq 1: \quad L^3\beta\gamma_n'(\delta) + (d-n+1)L^2\beta\gamma_{n-1}(\delta) = 0. \tag{2.24}$$

Integration of Eqs. (2.23) and (2.24) with respect to δ leads to the following iterative

Figure 2.5: Reduced coefficients $\gamma_n(\delta)$, $n \in \{0, 1, 2, 3\}$, characterizing the curvature expansion in Eq. (2.18) as function of the shift parameter δ and as obtained from Eq. (2.25). The data correspond to a hard sphere fluid at $\beta\mu = -3.88$, so that $\eta \approx 0.01$, exposed to hard spherical (a) or cylindrical (b) walls.

algorithm for determining the dependence of the coefficients $\gamma_n(\delta)$, $n \geq 0$, on δ:

$$n = 0: \quad L^2\beta\gamma_0(\delta) = L^2\beta\gamma_0(0) - L^3\beta p\frac{\delta}{L},$$

$$n \geq 1: \quad L^2\beta\gamma_n(\delta) = L^2\beta\gamma_n(0) + (n - d - 1)\int_0^\delta \frac{\mathrm{d}\tilde{\delta}}{L}L^2\beta\gamma_{n-1}(\tilde{\delta}),$$

$$d = \begin{cases} 2, & \text{spherical wall,} \\ 1, & \text{cylindrical wall.} \end{cases}$$

(2.25)

The dependence of the coefficients $\gamma_n(\delta)$ on δ is fully determined once in Eq. (2.25) the values of $\gamma_{n'}(0)$ for all $n' \leq n$ are known. Here the values $\gamma_n(0)$ are obtained by fitting
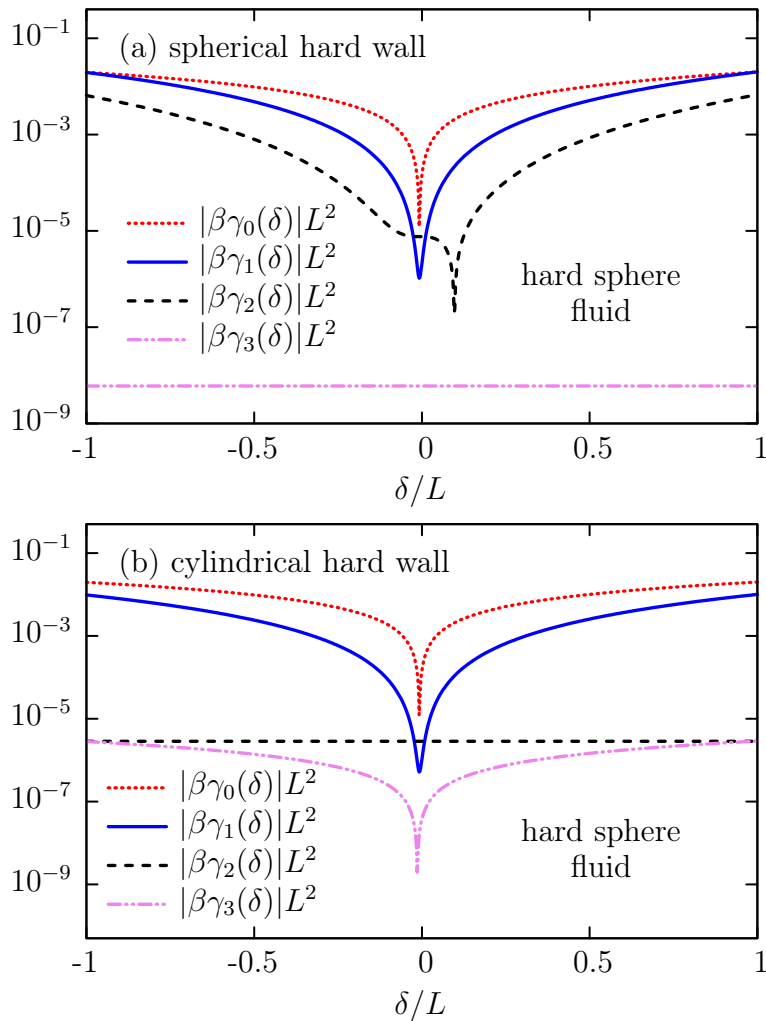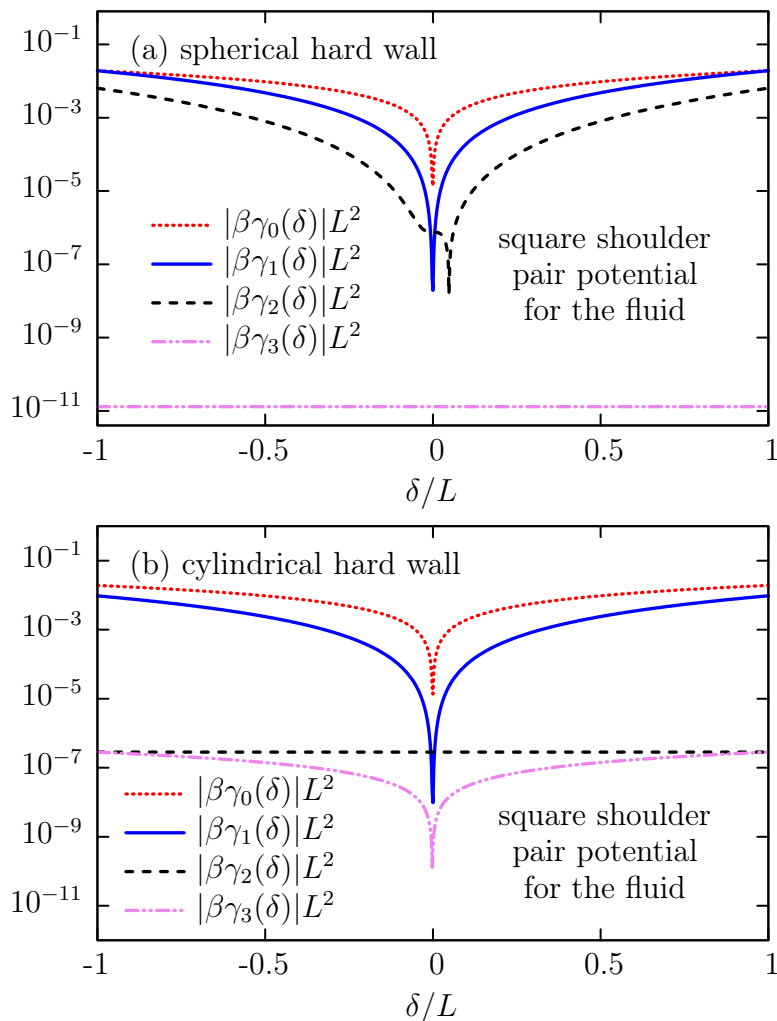
Figure 2.6: Reduced coefficients $\gamma_n(\delta)$, $n \in \{0, 1, 2, 3\}$, characterizing the curvature expansion in Eq. (2.18) as function of the shift parameter δ and as obtained from Eq. (2.25). The data correspond to a fluid with a square-shoulder pair potential $U(r)$ [Eq. (2.4)] with $\beta U_0 = 0.1$ and $\beta\mu = -3.95$ so that $\eta \approx 0.01$. The fluid is exposed to hard spheres (a) or hard cylinders (b).

Eq. (2.18) for $n \leq 10$ to the numerical data within the convention $\delta/L = 0$. Considering terms in Eq. (2.18) to such high orders was necessary in order to achieve a sufficiently high precision for the actually interesting coefficients $\gamma_1(\delta), \ldots, \gamma_3(\delta)$ (see Figs. 2.4 – 2.9); taking the additional terms of order $n \geq 4$ into account guarantees that these coefficients $\gamma_1(\delta), \ldots, \gamma_3(\delta)$ are not affected by the fast-decaying contributions of the full curvature expansion. Thereby it has been found that the ratio of the leading coefficients for the spherical wall, $\gamma_{s1}(0)$, and for the cylindrical wall, $\gamma_{c1}(0)$, takes the value $\gamma_{s1}(0)/\gamma_{c1}(0) = 2$ for all systems considered here, with a relative deviation of 10^{-7} or less. Comparison of that numerical result with the exact relation $\gamma_{s1}(\delta)/\gamma_{c1}(\delta) = 2$, which follows from the fact that the total curvatures $J = 1/R_1 + 1/R_2$ of a sphere, J^s, and of a cylinder, J^c, are related

by $J^s = 2J^c$ (see Refs. [8, 19]), validates the applied numerical approach. [See also the discussion in Sec. 3.3.4 with respect to Eq. (3.92).] The relationship between the leading coefficients has been the motivation for considering also the ratio of the next-to-leading coefficients. For small packing fractions $\gamma_{s2}(\delta)/\gamma_{c2}(\delta) \approx 8/3$ for $\delta = 0$, independently of the particle-particle interaction potential U. The value of this ratio does depend on the convention for δ because the spherical coefficient $\gamma_{s2}(\delta)$ varies with δ, whereas the cylindrical coefficient γ_{c2} is constant (see discussion below). Actually, the value $8/3$ can be obtained from the exact analytical expressions for the surface tension in the low-density limit for a fluid of *hard spheres* [21]. Moreover, the exact expression in Eq. (2.57) (see Appendix 2.B) describes the deviation of the ratio $\gamma_{s2}(0)/\gamma_{c2}(0)$ from $8/3$ for an ideal gas of particles as function of the strength βV_p^{yu} of a short-ranged excess external potential in addition to the hard wall potential. In Sec. 3.3.4 the discussion about the ratio $\gamma_{s2}(0)/\gamma_{c2}(0)$ is continued [see Eqs. (3.93) and (3.95) and the corresponding text].

It is interesting to pay special attention to the coefficient $\gamma_{n=d+1}$ in Eq. (2.25) which is the coefficient of the lowest order being not in accordance with morphometric thermodynamics. For this order $n = d + 1$ one has $n - d - 1 = 0$ and therefore γ_{d+1} is constant in δ [see Eq. (2.25) for $n \geq 1$, as well as, e.g., Refs. [19–21]]. This checks with Fig. 2.4 (corresponding to $d = 1$), where the values of the coefficients γ_2 can be read from the lines $\sim 1/(R+\delta)^2$ at $(R+\delta)/L = 1$. The value of γ_2 is not vanishing and it is the same in both conventions for δ. This implies that within morphometric thermodynamics the curvature expansion is not exact for any convention for δ. On the other hand, if, as a consequence of Eq. (2.25), the R-dependence of $\gamma(R, \delta)$ within morphometric thermodynamics would be exact for any single convention for δ, it would be exact for all conventions for δ. However, this statement is of no practical use, because, on the basis of numerical data, it is virtually impossible to prove that there is a convention for δ within which the morphometric form of the interfacial tension is *exact*. In contrast, Fig. 2.4 shows that even if the non-morphometric coefficients $\gamma_n(\delta)$ ($n \geq 2$ for a cylindrical wall) are numerically small for one convention for δ [see Fig. 2.4(b)] they may be large for another [see Fig. 2.4(a)]. The reason for this is that the operation of approximating the curvature-dependence of the interfacial tension by the form predicted within morphometric thermodynamics does not commute with the operation of shifting the interface.

Figure 2.5 shows the dependence of the coefficients $\gamma_n(\delta)$, $0 \leq n \leq 3$, of the curvature expansion Eq. (2.18) on the shift parameter δ. Except for the first non-morphometric coefficient (i.e., γ_3 for a sphere and γ_2 for a cylinder), which is constant in δ, the coefficients $\gamma_n(\delta)$ vary over several orders of magnitude upon changing δ. This is particularly pronounced near $\delta/L = 0$, where the morphometrically allowed coefficients are small; in the case of a cylindrical wall γ_1 is even smaller than the leading non-morphometric coefficient γ_2. However, apart from this region around $\delta/L = 0$, e.g., at $\delta/L = -0.5$, the morphometrically allowed coefficients exceed the leading non-morphometric coefficient by
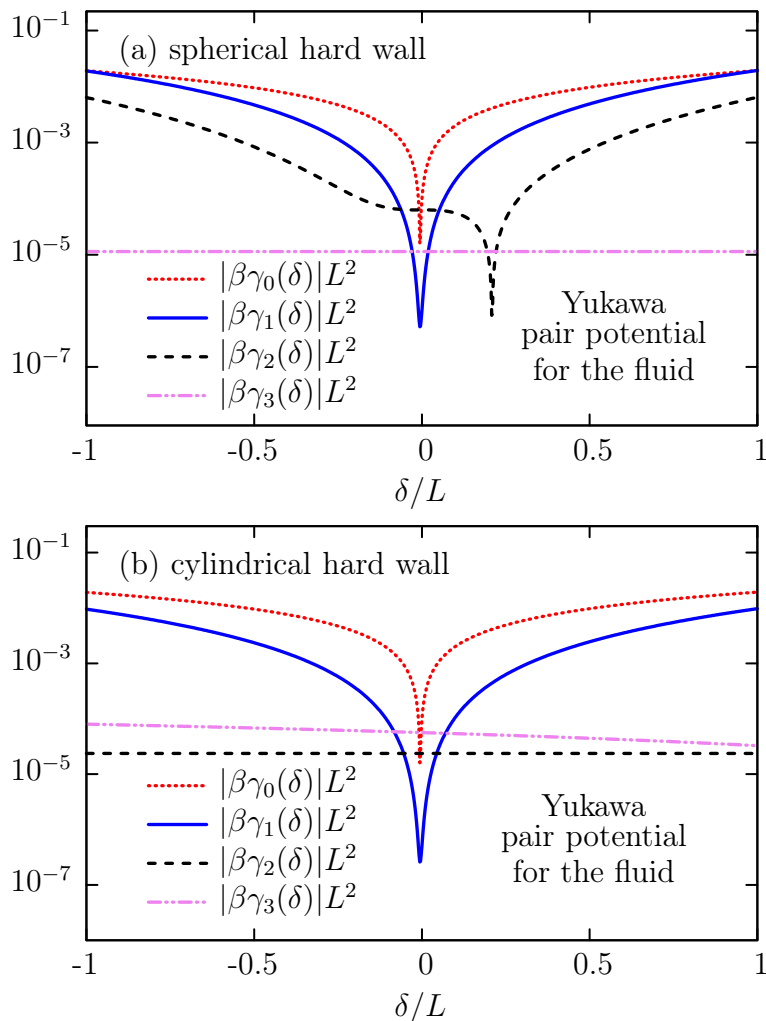
Figure 2.7: Same as Fig. 2.6 for a fluid with a Yukawa pair potential [Eq. (2.5)] with $\beta U_0 = 0.1$, $\beta\mu = -3.94$, and $L_c/L = 5$ so that $\eta \approx 0.01$.

several orders of magnitude. These observations are in agreement with the findings of Fig. 2.4 which is based on the same system and where for each convention for δ the coefficients, the values of which are rendered at $(R+\delta)/L = 1$, have been fitted independently. Figure 2.5 demonstrates that the interfacial tension cannot be represented exactly by the form obtained within morphometric thermodynamics, and that the quality of the approximation of the interfacial tension by the morphometric form depends on the position of the interface parameterized by the shift δ.

So far we have mainly focused on hard sphere fluids near hard walls. In the following we discuss to which extent the aforementioned observations can be extended to other systems. This will be discussed along the lines of Fig. 2.5.

Figure 2.6 displays the corresponding results for a fluid which is governed by a square-shoulder pair potential of finite strength βU_0, acting as a representative for interaction
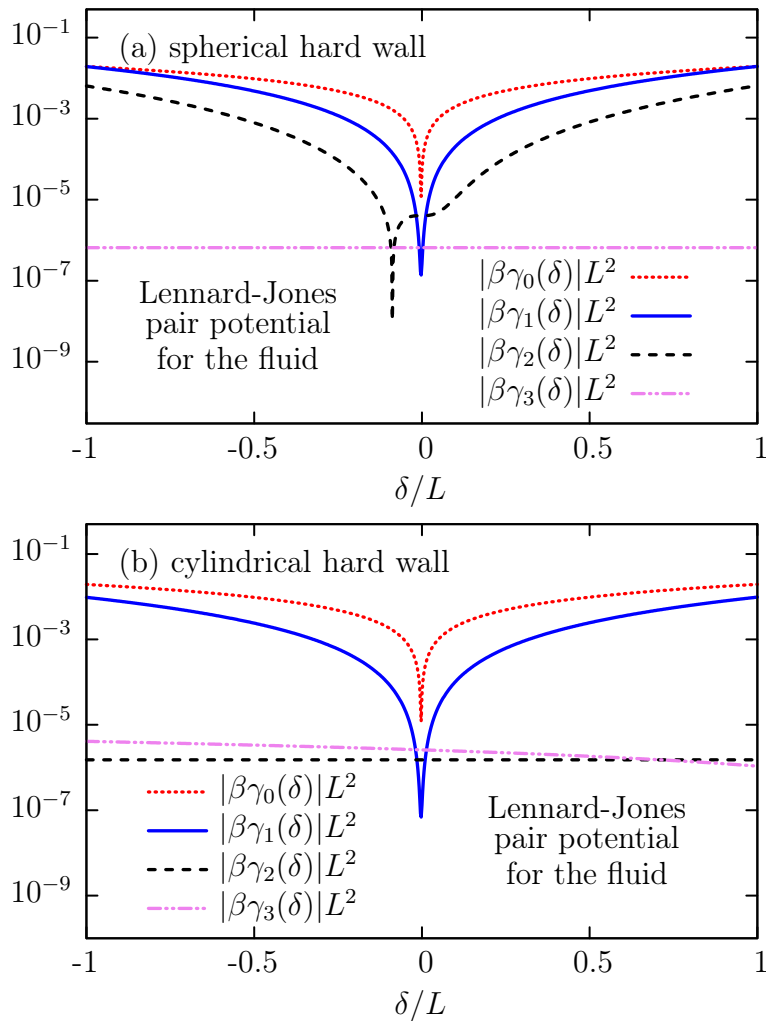
Figure 2.8: Same as Fig. 2.7 for a fluid with a Lennard-Jones pair potential [Eq. (2.6)] with $\beta U_0 = 0.1$, $\beta\mu = -3.92$, and $L_c/L = 5$ so that $\eta \approx 0.01$.

potentials of finite range. The comparison with Fig. 2.5 does not reveal qualitative changes. Figures 2.7 and 2.8, respectively, display the corresponding results for a fluid with a Yukawa pair potential, representing exponentially decaying interaction potentials, and for a Lennard-Jones pair potential, representing algebraically decaying pair potentials. Although comparing them with Figs. 2.5 and 2.6 reveals certain differences, the main conclusions remain the same: the coefficients $\gamma_n(\delta)$ are strongly affected by the choice of the convention for δ and, whereas for none of the systems considered here the curvature-dependence of the interfacial tension is exactly in agreement with morphometric thermodynamics, the morphometric form of the interfacial tension may be an excellent approximation for suitable conventions for δ.

In order to further assess to which extent the above findings are generic, an additional excess part V of the external potential V^{ext} is considered. This excess part V is obtained
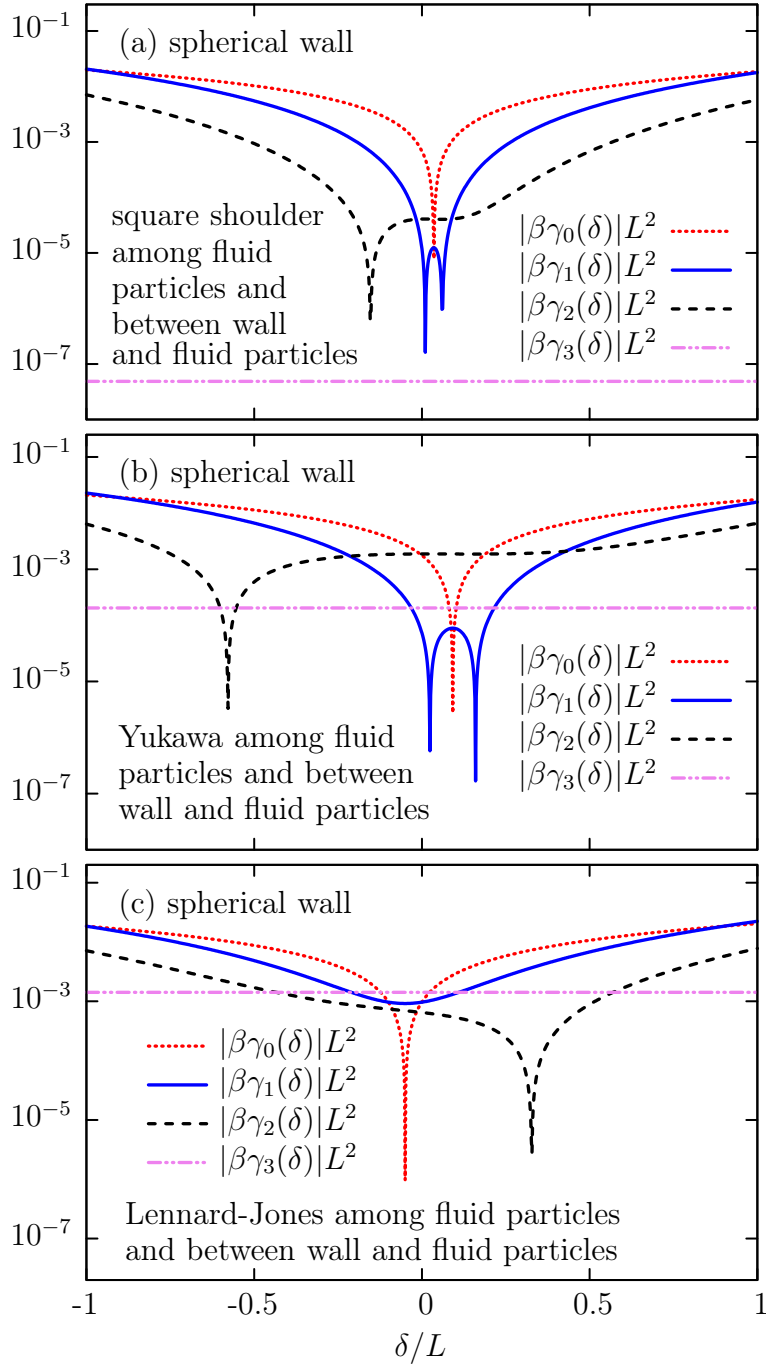
Figure 2.9: Reduced coefficients $\gamma_n(\delta)$, $n \in \{0, 1, 2, 3\}$, characterizing the curvature expansion in Eq. (2.18) as function of the shift parameter δ and as obtained from Eq. (2.25). Panels (a), (b), and (c) belong to the same systems as in Figs. 2.6(a), 2.7(a), and 2.8(a), respectively, with an additional soft part V of the external substrate potential: (a) V given by Eq. (2.59), (b) V given by Eq. (2.60), and (c) V given by Eq. (2.62). The data correspond to the following choice of system parameters: $\beta V_p^{sq} = \beta V_p^{yu} = \beta V_p^{LJ} = 0.1$ (see Appendix 2.C), $L_w/L = 1$, and $L_{cw}/L = 5$.

by integrating the pair potential $U_w(r)$ between a fluid particle and a wall particle over the volume $\tilde{\mathcal{V}}$ of the wall:

$$\beta V(\boldsymbol{r}) = \varrho_w \int_{\tilde{\mathcal{V}}} \mathrm{d}^3 r'\, \beta U_w(|\boldsymbol{r} - \boldsymbol{r}'|), \tag{2.26}$$

where in $\tilde{\mathcal{V}}$ the number density ϱ_w of the wall is taken to be constant. The particle-wall potentials $U_w(r)$ are chosen to be of a similar form as the pair potentials $U(r)$ between the fluid particles [Eqs. (2.4) – (2.6)], with the exception that the Yukawa-like wall-particle potential is not truncated and the repulsive part of a Lennard-Jones-like wall potential is replaced by a hard wall. The pair potentials are characterized by an energy scale U_{0w}, a length scale L_w and a cut-off length L_{cw} such that $U_w(r > L_{cw}) = 0$:

- the square-well ($U_{0w} < 0$) or square-shoulder ($U_{0w} > 0$) potential

$$\beta U_w(r \leq L_{cw}) = \beta U_{0w} \tag{2.27}$$

  with $L_w = L_{cw}$,

- the Yukawa potential ($U_{0w} > 0$, $L_{cw} = \infty$)

$$\beta U_w(r) = \beta U_{0w} \frac{L_w}{r} \exp\left(-\frac{r}{L_w}\right), \tag{2.28}$$

- the Lennard-Jones potential ($U_{0w} > 0$)

$$\beta U_w(r) = \begin{cases} \beta U_{0w} \left[\left(\dfrac{L_w}{r}\right)^{12} - \left(\dfrac{L_w}{r}\right)^{6}\right], & L_w \leq r \leq L_{cw}, \\[2mm] \infty, & r < L_w. \end{cases} \tag{2.29}$$

The resulting excess parts V of the substrate potentials as function of the radial distance z to a spherical reference surface of radius R are given in Eqs. (2.59), (2.60), and (2.62) in Appendix 2.C.

In Fig. 2.9 the results for systems with a non-vanishing excess part V of the external potential are shown. The parameters are chosen such that, apart from $V \neq 0$, the same systems as in Figs. 2.6(a), 2.7(a), and 2.8(a) are analyzed. It again turns out that the coefficients $\gamma_n(\delta)$ exhibit a strong dependence on δ so that the quality of morphometric thermodynamics as an approximation depends sensitively on the convention for δ. As a general trend, for all three examples shown in Fig. 2.9 the non-morphometric coefficient $|\beta\gamma_3(\delta)|L^2$ is not negligible in wider ranges of conventions for δ than in the cases without an excess substrate potential V. In this sense the quality of morphometric thermodynamics as an approximation deteriorates in the presence of excess parts V of the substrate potential.

2.4   Conclusions and Summary

By using density functional theory within the second virial approximation several model fluids with small number densities in contact with planar, spherical, or cylindrical walls have been analyzed. The curvature expansion [Eq. (2.18)] of the interfacial tension γ has been compared with the expression derived within morphometric thermodynamics [Eq. (2.3)]. Particular attention has been paid to the implications of the choice of the position of the interface, which underlies the definition of the interfacial tension [Eq. (2.16) and Fig. 2.1]. For none of the considered systems the expression for the interfacial tension in accordance with morphometric thermodynamics is exact, regardless of whether the particles interact with each other via a square-well or square-shoulder potential [Eq. (2.4)], a Yukawa potential [Eq. (2.5)], or a Lennard-Jones potential [Eq. (2.6)]. As shown in Figs. 2.5 – 2.8 the coefficients $\gamma_n(\delta)$ of the curvature expansion in Eq. (2.18) may depend sensitively on the chosen interface convention, which is expressed in terms of the shift parameter δ (Fig. 2.1). There are conventions for which the morphometrically allowed coefficients are much larger than the morphometrically forbidden ones so that within them morphometric thermodynamics is a reliable approximation of the interfacial tension. However, the opposite situation can occur for other interface conventions, in which case morphometric thermodynamics has to be used with caution. In particular the reliability of morphometric thermodynamics as an approximation deteriorates in the presence of excess contributions to the wall potential (Fig. 2.9). Based on these results, it turns out to be necessary in future applications of morphometric thermodynamics to clearly state which interface convention is chosen and why morphometric thermodynamics is expected to be a reliable approximation for that particular interface convention as compared with others.

2.A   Derivation of the excess functional

A grand canonical ensemble of particles is described within density functional theory by density functionals of the generic structure [58]

$$\beta\Omega[\varrho] = \int \mathrm{d}^3r \, \varrho(\boldsymbol{r}) \left\{ \ln\left[\varrho(\boldsymbol{r})\Lambda^3\right] - 1 - \beta\mu + \beta V^{\mathrm{ext}}(\boldsymbol{r}) \right\} + \beta\mathcal{F}^{\mathrm{ex}}[\varrho], \qquad (2.30)$$

with $\beta = 1/(k_B T)$, the Boltzmann constant k_B, the absolute temperature T, the number density ϱ, the de Broglie thermal wavelength Λ, the chemical potential μ, the external potential V^{ext}, and the excess functional $\mathcal{F}^{\mathrm{ex}}$. The latter takes into account interactions between the particles. With the choice $\mathcal{F}^{\mathrm{ex}} = 0$ Eq. (2.30) would correspond to a system of non-interacting ideal gas particles, i.e., $\mathcal{F}^{\mathrm{ex}}$ incorporates contributions *in excess* of the

ideal gas. In general the precise form of the excess functional is not known. However, since in the present case the focus is on systems with small number densities, $\mathcal{F}^{\text{ex}}$ can be approximated by a truncated expansion in powers of the number density, which is exact in the low density limit. This appendix is dedicated to explain the origin of the excess functional in use [see Eq. (2.7)] with respect to principles of statistical mechanics. The generic functional Eq. (2.30) gives rise to the Euler-Lagrange equation (ELE)

$$\left. \frac{\delta(\beta\Omega)}{\delta\varrho(\boldsymbol{r})} \right|_{\varrho_{\text{eq}}} = \ln\left[\varrho_{\text{eq}}(\boldsymbol{r})\Lambda^3\right] - \beta\mu + \beta V^{\text{ext}}(\boldsymbol{r}) - c^{(1)}(\boldsymbol{r}, [\varrho_{\text{eq}}]) = 0, \tag{2.31}$$

$$c^{(1)}(\boldsymbol{r}, [\varrho]) := -\frac{\delta\left(\beta\mathcal{F}^{\text{ex}}\right)}{\delta\varrho(\boldsymbol{r})}, \tag{2.32}$$

where the one-point direct correlation function $c^{(1)}$ has been introduced. In the following, at first an expression for $c^{(1)}$ is derived, which afterwards is used to determine the excess functional $\mathcal{F}^{\text{ex}}$ according to Eq. (2.32). The argument $(\boldsymbol{r}, [\varrho])$ indicates that the quantity in question is evaluated at the position $\boldsymbol{r}$ and that it is a functional of ϱ. For reasons of clarity this notation is only used with respect to $c^{(1)}$. The ELE (2.31) is fulfilled by the equilibrium number density ϱ_{eq}. With the abbreviation

$$z(\boldsymbol{r}) := \frac{\exp[\beta\mu - \beta V^{\text{ext}}(\boldsymbol{r})]}{\Lambda^3} \tag{2.33}$$

the ELE (2.31) can be written as

$$c^{(1)}(\boldsymbol{r}, [\varrho_{\text{eq}}]) = \ln\left[\frac{\varrho_{\text{eq}}(\boldsymbol{r})}{z(\boldsymbol{r})}\right]. \tag{2.34}$$

In density functional theory usually the ELE is an equation for the unknown equilibrium number density ϱ_{eq} whereas the quantities z and $c^{(1)}$ are given. However, within this appendix, an expression for $c^{(1)}$ is derived by calculating the right hand side of Eq. (2.34) by means of the grand partition function $\mathcal{Z}$. It will turn out that z and ϱ_{eq} cannot be chosen independently from each other. In the following the subscript "eq" of ϱ_{eq} indicates the equilibrium number density which corresponds to a certain choice of z. The grand partition function is given by [49, 58],

$$\mathcal{Z} = \sum_{N=0}^{\infty} \frac{1}{N!} \int \mathrm{d}^3 r_1 \ldots \int \mathrm{d}^3 r_N \prod_{i=1}^{N} z(\boldsymbol{r}_i) \exp[-\beta u(\boldsymbol{r}_1, \ldots, \boldsymbol{r}_N)], \tag{2.35}$$

where N denotes the number of particles in the system, $\boldsymbol{r}_i$ is the position of the ith particle, and where u is the potential energy due to mutual interactions of the particles. The equilibrium number density ϱ_{eq} is obtained by taking the average of the density

operator $\hat{\varrho}$ [58]

$$
\begin{aligned}
\varrho_{\mathrm{eq}}(\boldsymbol{r}) = \langle \hat{\varrho}(\boldsymbol{r}) \rangle &= \left\langle \sum_{i=1}^{N} \delta(\boldsymbol{r} - \boldsymbol{r}_i) \right\rangle \\
&= \frac{1}{\mathcal{Z}} \sum_{N=0}^{\infty} \frac{1}{N!} \int \mathrm{d}^3 r_1 \ldots \int \mathrm{d}^3 r_N \prod_{j=1}^{N} z(\boldsymbol{r}_j) \exp[-\beta u(\boldsymbol{r}_1, \ldots, \boldsymbol{r}_N)] \left[\sum_{i=1}^{N} \delta(\boldsymbol{r} - \boldsymbol{r}_i) \right].
\end{aligned}
\tag{2.36}
$$

The functional derivative of the grand partition function Eq. (2.35) with respect to z at position $\boldsymbol{r}$ is given by

$$
\frac{\delta \mathcal{Z}}{\delta z(\boldsymbol{r})} = \sum_{N=0}^{\infty} \frac{1}{N!} \int \mathrm{d}^3 r_1 \ldots \int \mathrm{d}^3 r_N \left\{ \sum_{i=1}^{N} \prod_{\substack{j=1 \\ j \neq i}}^{N} z(\boldsymbol{r}_j) \delta(\boldsymbol{r}_i - \boldsymbol{r}) \frac{z(\boldsymbol{r}_i)}{z(\boldsymbol{r})} \right\} \exp[-\beta u(\boldsymbol{r}_1, \ldots, \boldsymbol{r}_N)],
\tag{2.37}
$$

where the δ-function $\delta(\boldsymbol{r}_i - \boldsymbol{r})$ is the result of the functional derivative $\delta z(\boldsymbol{r}_i)/\delta z(\boldsymbol{r})$. Due to the presence of the δ-function the quotient $z(\boldsymbol{r}_i)/z(\boldsymbol{r})$ corresponds to a factor of 1, which is introduced in order to compare Eq. (2.37) with the expression Eq. (2.36) for the equilibrium number density. This results in

$$
\frac{\delta \mathcal{Z}}{\delta z(\boldsymbol{r})} = \frac{\mathcal{Z} \varrho_{\mathrm{eq}}(\boldsymbol{r})}{z(\boldsymbol{r})}
\tag{2.38}
$$

$$
\Leftrightarrow \frac{1}{\mathcal{Z}} \frac{\delta \mathcal{Z}}{\delta z(\boldsymbol{r})} = \frac{\varrho_{\mathrm{eq}}(\boldsymbol{r})}{z(\boldsymbol{r})},
\tag{2.39}
$$

that is, a relation between the grand partition function $\mathcal{Z}$ and the quantities which appear on the right hand side of Eq. (2.34). In the following it is assumed that the particles interact pairwisely with each other and that the particle-particle interaction potential U depends only on the distance between the particles,

$$
u(\boldsymbol{r}_1, \ldots, \boldsymbol{r}_N) = \frac{1}{2} \sum_{\substack{i,j=1 \\ i \neq j}}^{N} U(|\boldsymbol{r}_i - \boldsymbol{r}_j|).
\tag{2.40}
$$

The grand partition function Eq. (2.35) is functionally expanded in powers of z:

$$
\mathcal{Z} = 1 + \int \mathrm{d}^3 r_1\, z(\boldsymbol{r}_1) + \frac{1}{2} \int \mathrm{d}^3 r_1 \int \mathrm{d}^3 r_2\, z(\boldsymbol{r}_1) z(\boldsymbol{r}_2) \exp[-\beta U(|\boldsymbol{r}_1 - \boldsymbol{r}_2|)] + O\left(z^3\right).
\tag{2.41}
$$

This way the left hand side of Eq. (2.39) can be determined as

$$
\frac{1}{\mathcal{Z}} \frac{\delta \mathcal{Z}}{\delta z(\boldsymbol{r})} = 1 + \int \mathrm{d}^3 r_1\, z(\boldsymbol{r}_1) f(|\boldsymbol{r} - \boldsymbol{r}_1|) + O\left(z^2\right),
\tag{2.42}
$$

with the Mayer f-function [49]

$$f(x) := \exp[-\beta U(x)] - 1. \tag{2.43}$$

By combining Eqs. (2.39) and (2.42) z can be given in terms of ϱ_{eq}

$$z(\boldsymbol{r}) = \frac{\varrho_{\text{eq}}(\boldsymbol{r})}{\dfrac{1}{\mathcal{Z}}\dfrac{\delta\mathcal{Z}}{\delta z(\boldsymbol{r})}} = \varrho_{\text{eq}}(\boldsymbol{r})\left[1 - \int \mathrm{d}^3 r_1 \, z(\boldsymbol{r}_1) f(|\boldsymbol{r} - \boldsymbol{r}_1|) + O\left(z^2\right)\right] \tag{2.44}$$

$$= \varrho_{\text{eq}}(\boldsymbol{r})\left[1 - \int \mathrm{d}^3 r_1 \, \varrho_{\text{eq}}(\boldsymbol{r}_1) f(|\boldsymbol{r} - \boldsymbol{r}_1|) + O\left(\varrho_{\text{eq}}^2\right)\right]. \tag{2.45}$$

Equation (2.45) is obtained by applying the relation in Eq. (2.44) in order to replace the dependence on z on the right hand side of Eq. (2.44) with a dependence on ϱ_{eq}. Equation (2.45) relates z with the equilibrium number density ϱ_{eq} and shows that these quantities cannot be chosen independently from each other. With help of Eq. (2.45) the right hand side of Eq. (2.34) can be evaluated. The ratio $\varrho_{\text{eq}}(\boldsymbol{r})/z(\boldsymbol{r})$ exhibits only a dependence on the density; this dependence is inherited by $c^{(1)}$. That is, the expression for $c^{(1)}$ does not depend on the aforementioned relation between z and ϱ_{eq}, but it can be written in terms of an arbitrary number density ϱ. As a result, the low density approximation of the one-point direct correlation function [Eq. (2.34)] is given by

$$c^{(1)}(\boldsymbol{r}, [\varrho]) = \int \mathrm{d}^3 r_1 \, \varrho(\boldsymbol{r}_1) f(|\boldsymbol{r} - \boldsymbol{r}_1|) + O\left(\varrho^2\right). \tag{2.46}$$

Equation (2.46) gives the value of the one-point direct correlation function for any (small) number density ϱ. This relation can be used to obtain the expression for the excess functional by functional integration with respect to density; the procedure described here follows the one in Ref. [58]. For this purpose a path in the space of density functions is introduced

$$\varrho_\alpha(\boldsymbol{r}) := \alpha\varrho(\boldsymbol{r}), \tag{2.47}$$

where $\alpha \in [0, 1]$ parameterizes the path. $\alpha = 0$ corresponds to a density of zero $\varrho_0(\boldsymbol{r}) = 0$, whereas $\alpha = 1$ corresponds to the density $\varrho_1(\boldsymbol{r}) = \varrho(\boldsymbol{r})$ for which the value of the excess functional is of interest. The partial derivative of the excess functional, evaluated at ϱ_α, with respect to α,

$$\frac{\partial(\beta\mathcal{F}^{\text{ex}}[\varrho_\alpha])}{\partial\alpha} = \int \mathrm{d}^3 r \left.\frac{\delta(\beta\mathcal{F}^{\text{ex}})}{\delta\varrho(\boldsymbol{r})}\right|_{\varrho_\alpha(\boldsymbol{r})} \frac{\partial\varrho_\alpha(\boldsymbol{r})}{\partial\alpha} = -\int \mathrm{d}^3 r \, c^{(1)}(\boldsymbol{r}, [\varrho_\alpha])\varrho(\boldsymbol{r}), \tag{2.48}$$

can be written in terms of the one-point direct correlation function [Eq. (2.32)]. By

exploiting the fundamental theorem of calculus the excess functional is expressed as

$$\beta\mathcal{F}^{\text{ex}}[\varrho] = \beta\mathcal{F}^{\text{ex}}[\varrho] - \beta\mathcal{F}^{\text{ex}}[0] = \beta\mathcal{F}^{\text{ex}}[\varrho_1] - \beta\mathcal{F}^{\text{ex}}[\varrho_0] = \int_0^1 d\alpha \frac{\partial(\beta\mathcal{F}^{\text{ex}}[\varrho_\alpha])}{\partial\alpha}$$

$$= -\int d^3r \int_0^1 d\alpha \, c^{(1)}(\boldsymbol{r}, [\alpha\varrho])\varrho(\boldsymbol{r}). \tag{2.49}$$

In Eq. (2.49) it is assumed that in the limit of low densities the effect of interactions becomes negligible and thus $\beta\mathcal{F}^{\text{ex}}[0] = 0$ (see also Ref. [58]). With the explicit expression for the one-point direct correlation function Eq. (2.46) the excess functional is given by

$$\beta\mathcal{F}^{\text{ex}}[\varrho] = -\int d^3r \int d^3r' \int_0^1 d\alpha \, \alpha\varrho(\boldsymbol{r}')f(|\boldsymbol{r}-\boldsymbol{r}'|)\varrho(\boldsymbol{r}) + O\left(\varrho^3\right)$$

$$= -\frac{1}{2}\int d^3r \int d^3r' \varrho(\boldsymbol{r})\varrho(\boldsymbol{r}')f(|\boldsymbol{r}-\boldsymbol{r}'|) + O\left(\varrho^3\right) \tag{2.50}$$

$$= \frac{1}{2}\int d^3r \int d^3r' \, \varrho(\boldsymbol{r})\varrho(\boldsymbol{r}')\{1 - \exp[-\beta U(|\boldsymbol{r}-\boldsymbol{r}'|)]\} + O\left(\varrho^3\right).$$

The excess functional Eq. (2.50) is used in the density functional of the current chapter [see Eq. (2.7)]. Furthermore the random phase approximation in the next chapter [Eq. (3.2)] corresponds to the limit of low particle-particle interaction strength of the excess functional in Eq. (2.50).

2.B   Ideal Gas

In this appendix we analyze the exactly solvable case of non-interacting particles. The density functional in Eq. (2.7) with $U(r) = 0$ is minimized by the equilibrium number density

$$\varrho_{\text{eq}}(\boldsymbol{r}) = \varrho_{\text{eq}}^{\text{bulk}} \exp\left[-\beta V^{\text{ext}}(\boldsymbol{r})\right] \quad \text{with}$$

$$\varrho_{\text{eq}}^{\text{bulk}} = \Lambda^{-3}\exp(\beta\tilde{\mu}). \tag{2.51}$$

For pointlike ideal gas particles the convention $\delta = 0$ is convenient and will be used throughout this appendix. For this choice the interface of area $\mathcal{A}$, the reference surface, and the geometrical wall surface are the same and the interfacial tension γ is given by

$$\beta\gamma = -\frac{\varrho_{\text{eq}}^{\text{bulk}}}{\mathcal{A}}\int_\mathcal{V} d^3r \{\exp[-\beta V(\boldsymbol{r})] - 1\}, \ \delta = 0. \tag{2.52}$$

The integration volume $\mathcal{V}$ in Eq. (2.52) equals the volume accessible to the fluid particles. Therefore the integrand depends only on the excess part V of the external potential V^{ext}

[see Eqs. (2.10) and (2.11)].

In the case of a hard wall with $V = 0$ the interfacial tension of the ideal gas is zero, $\gamma = 0$, irrespective of the shape of the wall. Therefore the ideal gas is a useful choice for studying the influence of the excess part $V \neq 0$ of an external potential on the morphometric coefficients.

Here a *Yukawa-like* interaction U_w [Eq. (2.28)] between the fluid particles and the wall particles is analyzed. The excess part V follows from Eq. (2.26). For planar, spherical, and cylindrical walls, respectively, one finds

$$
\frac{V(z)}{V_p^{yu}} = \exp\left(-\frac{z}{L_w}\right), \quad \text{plane,}
$$

$$
\frac{V(r)}{V_p^{yu}} = \frac{L_w}{r} \exp\left(-\frac{r}{L_w}\right) \left[(S-1)\mathrm{e}^S + (S+1)\mathrm{e}^{-S}\right], \quad \text{sphere,} \tag{2.53}
$$

$$
\frac{V(r)}{V_p^{yu}} = 2S\, \mathrm{I}_1(S)\mathrm{K}_0\left(\frac{r}{L_w}\right), \quad \text{cylinder,}
$$

where $V_p^{yu} = 2\pi \varrho_w U_{0w} L_w^3$ denotes the strength of the excess part V at contact with a *p*lanar wall and $S = R/L_w$ with K_0 and I_1 as familiar modified Bessel functions [84]. The expressions in Eq. (2.53) for the excess parts V of the external potential facilitate to determine exactly the coefficients γ_n of the curvature expansion of the interfacial tension γ in Eq. (2.52). In the case of a spherical wall

$$
\beta\gamma = - \varrho_{\mathrm{eq}}^{\mathrm{bulk}} L_w \sum_{n=1}^{\infty} \frac{(-\beta V_p^{yu})^n}{n!\, n} \left\{ 1 + \frac{L_w}{R}\left[\frac{2}{n} - 1 - n\right] + \frac{L_w^2}{R^2}\left[\frac{n^2}{2} + \frac{n}{2} - 1 - \frac{3}{n} + \frac{2}{n^2}\right] \right.
$$
$$
\left. - \frac{L_w^3}{R^3}(2-n)(1-n)\left[\frac{1}{n^2} + \frac{1}{n} + \frac{1}{2} + \frac{n}{6}\right] + O\left(\frac{L_w^4}{R^4}\right) \right\} + O\left[\exp\left(-2\frac{R}{L_w}\right)\right], \quad \delta = 0,
\tag{2.54}
$$

and for the cylindrical wall the corresponding result is given by

$$
\beta\gamma = - \varrho_{\mathrm{eq}}^{\mathrm{bulk}} L_w \sum_{n=1}^{\infty} \frac{(-\beta V_p^{yu})^n}{n!\, n} \left\{ 1 + \frac{L_w}{R}\left[\frac{1}{n} - \frac{1}{2} - \frac{n}{2}\right] \right.
$$
$$
\left. + \frac{L_w^2}{R^2}\left[-\frac{1}{2n} - \frac{1}{8} + \frac{n}{8} + \frac{n^2}{8}\right] + O\left(\frac{L_w^3}{R^3}\right) \right\}, \quad \delta = 0.
\tag{2.55}
$$

The expression for the planar wall is included in the expressions for the curved walls [Eqs. (2.54) and (2.55)] as the term being independent of the radius R.

In Eqs. (2.54) and (2.55) the respective curvature expansions are presented up to and including the leading *non*-morphometric coefficients (belonging to R^{-3} in the case of spherical walls and to R^{-2} in the case of cylindrical walls) which in general are non-zero. Further interesting insight can be gained by studying ratios of particular coefficients:

- The ratio of the leading coefficients γ_1 (belonging to R^{-1}),

$$\frac{\gamma_{s1}}{\gamma_{c1}} = 2, \tag{2.56}$$

  i.e., a constant value independent of the strength βV_p^{yu} of the external potential.

- For small amplitudes βV_p^{yu} the ratio of the subdominant coefficients γ_2 (belonging to R^{-2}) is given by

$$\frac{\gamma_{s2}}{\gamma_{c2}} = \frac{8}{3} \left\{ 1 - \frac{1}{18} \left(\beta V_p^{yu} \right)^2 + O\left[\left(\beta V_p^{yu} \right)^3 \right] \right\}. \tag{2.57}$$

  For $\beta V_p^{yu} \ll 1$ this ratio reduces to the constant value 8/3 which has also been found in Ref. [21] and in the numerical calculations of Sec. 2.3.

- A comparison of the leading (γ_{c1}) and the subdominant (γ_{c2}) coefficients for cylindrical walls leads to

$$\frac{\gamma_{c1}}{\gamma_{c2}} = -\frac{2}{3}\beta V_p^{yu} + \frac{67}{162} \left(\beta V_p^{yu} \right)^2 + O\left[\left(\beta V_p^{yu} \right)^3 \right]. \tag{2.58}$$

  This implies that for $\beta V_p^{yu} \ll 1$ one has $|\gamma_{c2}| \gg |\gamma_{c1}|$ which contradicts the morphometric prediction according to which γ_{c2} should be zero.

These results for an ideal gas of non-interacting particles invalidate morphometric thermodynamics if there is a non-vanishing excess part $\beta V_p^{yu} \neq 0$ of the external potential.

2.C   Excess parts of the external potentials

The calculation of the excess parts V of the external potentials according to Eq. (2.26) results in lengthy expressions. Here these are presented for spherical walls as function of the distance $z \geq 0$ from the reference surface of radius R, i.e., the distance from the center of the spherical wall is $r = R + z$.

In the case of the square-well or square-shoulder potential [Eq. (2.27)] the excess part

V of the external potential is given by

$$\beta V(z \geq 0) = \beta V_p^{sq} \times \begin{cases} z \geq L_w: & 0, \\[2mm] z \leq L_w - 2R: & 2\dfrac{R^3}{L_w^3}, \\[4mm] L_w - 2R < z < L_w: & \dfrac{1}{8}\dfrac{L_w^3}{(R+z)^3}\left[\dfrac{z^6}{L_w^6} + 6\dfrac{z^5 R}{L_w^6} + \dfrac{z^4}{L_w^4}\left(9\dfrac{R^2}{L_w^2} - 6\right)\right. \\[4mm] & \quad + \dfrac{z^3}{L_w^3}\left(4\dfrac{R^3}{L_w^3} - 24\dfrac{R}{L_w} + 8\right) \\[4mm] & \quad + \dfrac{z^2}{L_w^2}\left(-30\dfrac{R^2}{L_w^2} + 24\dfrac{R}{L_w} - 3\right) \\[4mm] & \quad + \dfrac{z}{L_w}\left(-12\dfrac{R^3}{L_w^3} + 24\dfrac{R^2}{L_w^2} - 6\dfrac{R}{L_w}\right) \\[4mm] & \quad \left. + 8\dfrac{R^3}{L_w^3} - 3\dfrac{R^2}{L_w^2}\right], \end{cases}$$

$$\beta V_p^{sq} = \frac{2}{3}\pi L_w^3 \beta U_{0w}\varrho_w.$$

$$(2.59)$$

In the case of the Yukawa potential [Eq. (2.28)] the excess part V is given by

$$\beta V(z \geq 0) = \beta V_p^{yu}\exp\left(-\frac{z}{L_w}\right)\frac{L_w}{R+z}\left[\frac{R}{L_w} - 1 + \exp\left(-\frac{2R}{L_w}\right)\left(\frac{R}{L_w} + 1\right)\right],$$

$$\beta V_p^{yu} = 2\pi\varrho_w\beta U_{0w}L_w^3.$$

$$(2.60)$$

[Note that Eq. (2.60) and the sphere expression in Eq. (2.53) are identical.]

In the case of the Lennard-Jones-like potential [Eq. (2.29)] the reference surface and the *g*eometrical wall surface do not coincide: $R = R_g + L_w$ with R_g denoting the radius of the geometrical wall. Integration according to Eq. (2.26) results in an expression $\beta V_g(z_g, R_g)$ in which z_g measures the distance from the geometrical wall surface, i.e., the distance

from the center of the spherical wall is $r = R_g + z_g$:

$$\beta V_g(z_g, R_g) = \beta V_p^{LJ} \frac{\mathcal{I}_{12}(z_g, R_g) - \mathcal{I}_6(z_g, R_g)}{-2\pi L_w^3 \left\{ -\frac{1}{10}\left(\frac{10}{9}\frac{L_w^9}{L_{cw}^9} - \frac{L_w^{10}}{L_{cw}^{10}} - \frac{1}{9}\right) + \frac{1}{4}\left(\frac{4}{3}\frac{L_w^3}{L_{cw}^3} - \frac{L_w^4}{L_{cw}^4} - \frac{1}{3}\right)\right\}},$$

$$\beta V_p^{LJ} = -2\pi L_w^3 \varrho_w \beta U_{0w} \left\{ -\frac{1}{10}\left(\frac{10}{9}\frac{L_w^9}{L_{cw}^9} - \frac{L_w^{10}}{L_{cw}^{10}} - \frac{1}{9}\right) + \frac{1}{4}\left(\frac{4}{3}\frac{L_w^3}{L_{cw}^3} - \frac{L_w^4}{L_{cw}^4} - \frac{1}{3}\right)\right\},$$

$$\mathcal{I}_n(z_g, R_g) = \frac{2\pi}{n-2}L_w^{n-1}\frac{L_w}{R_g + z_g}\sum_{j=1}^{5} A_j^{(n)}(z_g, R_g),$$

$$A_1^{(n)}(z_g, R_g) = L_w^{4-n}\left\{ \frac{1}{n-3}\frac{R_g}{L_w}\left[\frac{z_g^{3-n}}{L_w^{3-n}} + \frac{(2R_g + z_g)^{3-n}}{L_w^{3-n}}\right]\right.$$
$$\left. + \frac{1}{(n-3)(n-4)}\left[-\frac{z_g^{4-n}}{L_w^{4-n}} + \frac{(2R_g + z_g)^{4-n}}{L_w^{4-n}}\right]\right\},$$

$$A_2^{(n)}(z_g, R_g) = L_w^{4-n}\Theta(R_g + z_g - L_{cw})\left\{ \frac{1}{3-n}\frac{R_g}{L_w}\frac{(2R_g + z_g)^{3-n}}{L_w^{3-n}} - \frac{1}{2}\frac{L_{cw}^{2-n}}{L_w^{2-n}}\frac{R_g^2}{L_w^2}\right.$$
$$\left. - \frac{1}{(4-n)(3-n)}\left[\frac{(2R_g + z_g)^{4-n}}{L_w^{4-n}} - \frac{(R_g + z_g)^{4-n}}{L_w^{4-n}}\right]\right\},$$

$$A_3^{(n)}(z_g, R_g) = L_w^{4-n}\Theta(2R_g + z_g - L_{cw})\Theta(L_{cw} - R_g - z_g)\left\{ \frac{1}{3-n}\frac{R_g}{L_w}\frac{(2R_g + z_g)^{3-n}}{L_w^{3-n}}\right.$$
$$- \frac{1}{2}\frac{L_{cw}^{2-n}}{L_w^{2-n}}\frac{R_g^2}{L_w^2} - \frac{1}{3-n}\frac{L_{cw}^{3-n}}{L_w^{3-n}}\frac{L_{cw} - R_g - z_g}{L_w}$$
$$\left. + \frac{1}{2}\frac{L_{cw}^{2-n}}{L_w^{2-n}}\frac{(L_{cw} - R_g - z_g)^2}{L_w^2} + \frac{L_{cw}^{4-n} - (2R_g + z_g)^{4-n}}{(3-n)(4-n)L_w^{4-n}}\right\},$$

$$A_4^{(n)}(z_g, R_g) = L_w^{4-n}\Theta(z_g - L_{cw})\left\{ \frac{1}{3-n}\frac{R_g}{L_w}\frac{z_g^{3-n}}{L_w^{3-n}} + \frac{1}{2}\frac{L_{cw}^{2-n}}{L_w^{2-n}}\frac{R_g^2}{L_w^2} + \frac{z_g^{4-n} - (R_g + z_g)^{4-n}}{(4-n)(3-n)L_w^{4-n}}\right\},$$

$$A_5^{(n)}(z_g, R_g) = L_w^{4-n}\Theta(R_g + z_g - L_{cw})\Theta(L_{cw} - z_g)\left\{ \frac{1}{3-n}\frac{L_{cw}^{3-n}}{L_w^{3-n}}\frac{R_g + z_g - L_{cw}}{L_w}\right.$$
$$\left. + \frac{1}{2}\frac{L_{cw}^{2-n}}{L_w^{2-n}}\frac{(R_g + z_g - L_{cw})^2}{L_w^2} + \frac{L_{cw}^{4-n} - (R_g + z_g)^{4-n}}{(4-n)(3-n)L_w^{4-n}}\right\}. \tag{2.61}$$

The excess part V of the external potential as function of the distance z from the reference surface of radius R is related to V_g in Eq. (2.61) via

$$\beta V(z \geq 0) = \beta V_g(z + L_w, R - L_w). \tag{2.62}$$

Chapter 3

Yukawa fluid at curved walls

In Chap. 3 density functional theory is used in order to investigate the interface between a Yukawa fluid and a convex wall of planar, spherical, or cylindrical shape. A modified version of the density functional in the preceding Chap. 2 (see also Ref. [22]) allows for exact solutions of the corresponding Euler Lagrange equations. The latter enable to derive closed expressions for the interfacial tension, which is the quantity of choice to analyze the dependence of the interface on the wall curvature. An expansion of the interfacial tension in small curvatures leads to the insight that an approach in agreement with morphometric thermodynamics is not complete. The question, whether the latter approach can be used as a good approximation instead, is addressed based on the analytically known curvature coefficients. The findings differ with respect to geometry: For cylindrical walls the morphometric approach proposes to truncate the exact curvature expansion such that terms of significant magnitude may be neglected. In the case of spherical walls, however, the curvature expansion truncated according to morphometric thermodynamics deviates from the exact one only by exponentially small terms.

3.1   Introduction

Within the preceding Chap. 2 (see also Ref. [22]), inter alia, the question has been discussed, why the quality of morphometric thermodynamics (MT) has been judged very differently in the literature. To that end density functional theory (DFT) has been used in order to discuss distinct types of fluids in contact with convex walls. Provided that small bulk densities have been under consideration the obtained results have been in good agreement with simulation results (see Fig. 2.3). The discussion has led to the insight that interface conventions, underlying the definition of the interfacial tension, have to be taken into account when the quality of MT is under consideration. Within certain conventions the DFT results clearly contradict the form of the curvature expansion, which is in accordance with MT [see, e.g., Eq. (2.3)], whereas in other conventions the numerical results show great agreement with the morphometric expression. However, because the

respective Euler Lagrange equations had to be solved numerically, various shortcomings
had to be accepted in that former discussion. (i) Interaction potentials of unlimited range,
i.e., the Yukawa potential or Lennard-Jones potential in the preceding chapter, could only
be considered in combination with a cutoff length, which, as it has turned out recently,
might have prevented interesting relations from emerging. In this context Ref. [23] reports
about qualitatively distinct dependences of the interfacial tension on the wall radius. For
the full 12-6 Lennard-Jones potential a logarithmic dependence occurs in the curvature
dependence which however vanishes in the case of the truncated version of the interaction
potential. Also for the so-called inverse power law potential logarithmic dependences ap-
pear [24]. (ii) Expansions of observables in terms of the wall curvature and the respective
coefficients have been determined by fitting to the numerical outcome. This procedure
is accompanied by inaccuracies which may lead to inconclusive results. For instance, the
question whether a comparatively small coefficient is zero or not is difficult to answer.
(iii) All results were obtained on a sample basis and discussions like the dependence of the
curvature coefficients on certain system parameters are (computation) time consuming.

In order to overcome these shortcomings, analytic expressions for the quantities under
consideration are desirable. For that purpose, within DFT an ansatz in terms of a gradient
expansion is, in principle, a promising candidate [58]. There the corresponding Euler
Lagrange equation (ELE) is a differential equation. This type of equation is typically
technically easier to handle than an integral equation. ELEs of the latter type result
from approaches with non-local excess functionals, see, e.g., Eq. (2.12) in the preceding
approach. However, the local gradient expansion ansatz is only recommendable, if the
number densities vary slowly compared with molecular correlations [58], i.e., if microscopic
details are not under consideration. The following discussion focuses on the dependence
of the interface between a fluid and a wall on the radius of the latter. Especially for the
case of (microscopically) small radii of curvature microscopic details can be expected to
be important and, in view of that, it seems to be a wise choice to not neglect microscopic
details, a priori, for larger radii. Moreover, in Ref. [85] it is pointed out that the gradient
expansion approximation is not valid, if there is a discontinuity in the density profile,
which is caused by the presence of an impenetrable wall. Therefore, as before, in the
present chapter a local gradient expansion model is omitted. Instead, the fluid is described
within a nonlocal theory which is accompanied by the consequence of having to deal with
equations of higher level of complexity.

In the present chapter the approved model of the preceding Chap. 2 (see also Ref. [22])
is modified in order to allow for analytic solutions. As a result, the approach under
consideration (see Sec. 3.2) is similar to a model, which in the literature is sometimes
referred to as Sullivan's model [85, 86]. The latter has originally been introduced to study
gas adsorption on planar surfaces. Subsequently also curved interfaces have come into
focus. For example, in Refs. [87, 88] Sullivan's model has been applied in order to study

interfacial properties and structures of liquid drops of various radii which are embedded in a vapour background. In Refs. [89–91] the wetting behavior of a spherical substrate surrounded by a fluid has been examined.

In Sec. 3.2 the model is explained in detail and amendments with respect to the preceding approach are pointed out. In Sec. 3.3 the equilibrium density profiles, i.e., the solutions of the ELE in various geometries, are given explicitly. These enable to calculate closed expressions for the interfacial tensions for the planar, spherical, and cylindrical wall. Finally, the exact expressions are expanded in terms of small wall curvatures which leads to analytically known curvature coefficients for the interfacial tension. In this way the aforementioned shortcomings can be overcome. (i) The present model takes into account the Yukawa interaction potential with its full range. Recently, untruncated algebraically decaying potentials have been shown to correspond to a curvature dependence of the interfacial tension which is not covered by a power series [23, 24]. Here, the exact expressions for the interfacial tension can be used to examine whether also the underlying Yukawa interaction potential leads to a dependence on the curvature which is not purely algebraic. (ii) Exact expressions for the curvature coefficients leave no doubt about whether MT is exactly valid or not. This is an advantage in comparison with numerical results the analysis of which has to rely on fitting procedures. Against the background of the influence of interface conventions (see Chap. 2 and Ref. [22]), the distinction between a comparatively small coefficient and a coefficient exactly equalling zero, can have huge consequences. (iii) With the help of exact expressions the parameter space can be scanned quickly. This way it is possible to put MT to the test in a wider range than within an approach which has to be addressed numerically. In particular, within the present model it is possible to take into account an external potential in excess to the hard fluid-wall interaction and therefore to examine the influence of a wall that is not purely hard. A summary is given in Sec. 3.4 and Appendix 3.A contains technical details.

3.2 Model

Let us consider a simple fluid composed of particles which interact via a Yukawa pair potential

$$U(r) = U_0 \frac{\exp(-r/L)}{r}. \tag{3.1}$$

In the preceding model [see Sec. 2.2] the cutoff length L_c in Eq. (2.5) has to be set to an infinitely large value in order to describe the same interaction potential as in Eq. (3.1). Interestingly, in the case of the preceding model, a larger cutoff length is accompanied by an increased computation time and letting $L_c \to \infty$ would prevent the numerical algorithm from finding a solution, whereas, within the present model, it is the properties of the pure

Yukawa in Eq. (3.1) that help to exactly solve the Euler Lagrange equation [see the following discussion and especially Eqs. (3.23) and (3.24)]. In Eq. (3.1) L sets the length scale of the exponential decay and U_0 parameterizes the strength of the interaction. Note that, unlike in the preceding chapter [Eq. (2.5)], the dimension of the latter parameter is $[U_0] = [\text{energy}] \times [\text{length}]$. The density functional Eq. (2.7) of the preceding chapter is modified and henceforth reads

$$\Omega[\varrho] = \int_{\mathcal{V}} \mathrm{d}^3 r \, \{f[\varrho(\boldsymbol{r})] + \varrho(\boldsymbol{r})[V^{\text{ext}}(\boldsymbol{r}) - \mu]\} + \frac{1}{2} \int_{\mathcal{V}} \mathrm{d}^3 r \int_{\mathcal{V}} \mathrm{d}^3 r' \, U(|\boldsymbol{r} - \boldsymbol{r}'|)\varrho(\boldsymbol{r})\varrho(\boldsymbol{r}').$$

(3.2)

In Eq. (3.2) μ and V^{ext} are the chemical and the external potential, respectively. $\mathcal{V}$ refers to all positions $\boldsymbol{r} \in \mathbb{R}^3$ which are accessible for the centers of the particles. In the following $|\mathcal{V}|$ labels the volume of this set of points. The series representation of the exponential function in the excess functional of Eq. (2.7) (see also Appendix 2.A) is taken into account up to linear order which leads to an excess functional in terms of the random phase approximation in Eq. (3.2) [58]. In the present chapter the free energy density of the ideal gas reference system in Eq. (2.7),

$$\tilde{f}(\varrho) := \frac{1}{\beta}\varrho \left[\ln\left(\Lambda^3 \varrho\right) - 1\right],$$

(3.3)

with the thermal wavelength Λ, $\beta = (k_B T)^{-1}$, the Boltzmann constant k_B, and with the absolute temperature T, is approximated by a truncated expansion f around an arbitrary but fixed number density ϱ^* up to quadratic order in $\varrho - \varrho^*$:

$$f(\varrho) := \tilde{f}(\varrho^*) + \tilde{f}'(\varrho^*)(\varrho - \varrho^*) + \frac{1}{2}\tilde{f}''(\varrho^*)(\varrho - \varrho^*)^2.$$

(3.4)

With the coefficients

$$a := \tilde{f}(\varrho^*) - \tilde{f}'(\varrho^*)\varrho^* + \frac{1}{2}\tilde{f}''(\varrho^*)\varrho^{*2} = -\frac{\varrho^*}{2\beta},$$

(3.5)

$$b := \tilde{f}'(\varrho^*) - \tilde{f}''(\varrho^*)\varrho^* = \frac{1}{\beta}\left[\ln\left(\Lambda^3 \varrho^*\right) - 1\right],$$

(3.6)

and

$$c := \tilde{f}''(\varrho^*) = \frac{1}{\beta\varrho^*}$$

(3.7)

the approximated reference free energy density f can be written as

$$f(\varrho) = a + b\varrho + \frac{c}{2}\varrho^2.$$

(3.8)

In combination with Eq. (3.8) the functional Eq. (3.2) reads

$$\Omega[\varrho] = \int_{\mathcal{V}} \mathrm{d}^3r \left\{ a + \varrho(\boldsymbol{r})[V^{\mathrm{ext}}(\boldsymbol{r}) - \mu^*] + \frac{c}{2}\varrho(\boldsymbol{r})^2 \right\} + \frac{1}{2} \int_{\mathcal{V}} \mathrm{d}^3r \int_{\mathcal{V}} \mathrm{d}^3r'\, U(|\boldsymbol{r} - \boldsymbol{r}'|)\varrho(\boldsymbol{r})\varrho(\boldsymbol{r}'),$$

(3.9)

$$\mu^* := \mu - b.$$

(3.10)

Note that only the difference Eq. (3.10) of μ and b contributes. Therefore the actual value of b and hence the value Λ of the thermal de Broglie wavelength is irrelevant. Altogether, in order to obtain Eq. (3.9), within the preceding model [Eq. (2.7)] both the free energy density of the reference system and the excess functional are approximated. In the limit of small deviations $\varrho - \varrho^*$ of the number density ϱ from ϱ^* and small amplitudes U_0 of the interaction potential Eq. (3.1) the simplified present model leads to similar results as the approved preceding one (see Fig. 3.2).

In the bulk, i.e., without the presence of an external potential $V^{\mathrm{ext}}(\boldsymbol{r}) = 0$, the number density is independent of the position: $\varrho^{\mathrm{b}} := \varrho(\boldsymbol{r})$ and $\mathcal{V} = \mathbb{R}^3$. In that case Eq. (3.9) becomes a *function* of the number density

$$\Omega^{\mathrm{b}}\left(\varrho^{\mathrm{b}}\right) = |\mathcal{V}| \left\{ a - \varrho^{\mathrm{b}}\mu^* + \frac{1}{2}\left(\varrho^{\mathrm{b}}\right)^2 \left[c + \hat{U}(0)\right] \right\},$$

(3.11)

$$\hat{U}(0) := \int_{\mathbb{R}^3} \mathrm{d}^3r\, U(|\boldsymbol{r}|) = 4\pi L^2 U_0.$$

(3.12)

The Euler Lagrange equation (ELE)

$$\left.\frac{\partial \Omega^{\mathrm{b}}}{\partial \varrho^{\mathrm{b}}}\right|_{\varrho^{\mathrm{b}}_{\mathrm{eq}}} = 0 \Leftrightarrow \mu^* = \left[c + \hat{U}(0)\right]\varrho^{\mathrm{b}}_{\mathrm{eq}}$$

(3.13)

relates the bulk equilibrium number density $\varrho^{\mathrm{b}}_{\mathrm{eq}}$ with the rescaled chemical potential μ^*. The bulk grand canonical potential $\Omega^{\mathrm{b}}_{\mathrm{eq}}$ is defined as the value of Ω^{b} when evaluated at the bulk equilibrium number density

$$\Omega^{\mathrm{b}}_{\mathrm{eq}} := \Omega^{\mathrm{b}}\left(\varrho^{\mathrm{b}}_{\mathrm{eq}}\right) = |\mathcal{V}| \left(a - \frac{1}{2}\varrho^{\mathrm{b}}_{\mathrm{eq}}\mu^*\right).$$

(3.14)

In order to ensure that the number density in accordance with Eq. (3.13) refers to a stable state, it has to correspond to a minimum in Ω^{b} Eq. (3.11), i.e., the parameters have to be chosen such that the inequality

$$\left.\frac{\partial^2 \Omega^{\mathrm{b}}}{(\partial \varrho^{\mathrm{b}})^2}\right|_{\varrho^{\mathrm{b}}_{\mathrm{eq}}} > 0 \Leftrightarrow c + \hat{U}(0) > 0$$

(3.15)

is fulfilled. Assuming that the reference density is positive $\varrho^* > 0$ it follows that $c > 0$ [Eq. (3.7)]. With this the stability criterion Eq. (3.15) is always fulfilled for the case of repulsive particle particle interactions, i.e., $U_0 > 0 \Rightarrow \hat{U}(0) > 0$ [Eq. (3.12)]. However, for $U_0 < 0$ the stability criterion Eq. (3.15) restricts the values that can be taken by c.

For spatially varying external potentials in general the number density is a spatially varying function. The equilibrium number density $\varrho_{\text{eq}}(\boldsymbol{r})$ fulfills the ELE which follows from the functional derivative of Eq. (3.9)

$$\left.\frac{\delta\Omega}{\delta\varrho(\boldsymbol{r})}\right|_{\varrho_{\text{eq}}} = 0 = V^{\text{ext}}(\boldsymbol{r}) - \mu^* + c\varrho_{\text{eq}}(\boldsymbol{r}) + \int_{\mathcal{V}} \mathrm{d}^3r'\, U(|\boldsymbol{r} - \boldsymbol{r}'|)\varrho_{\text{eq}}(\boldsymbol{r}'). \tag{3.16}$$

The grand canonical potential Ω_{eq} is given by the functional Eq. (3.9) evaluated at the equilibrium density ϱ_{eq}

$$\Omega_{\text{eq}} := \Omega[\varrho_{\text{eq}}] = |\mathcal{V}|a + \frac{1}{2}\int_{\mathcal{V}} \mathrm{d}^3r\, \varrho_{\text{eq}}(\boldsymbol{r})\left[V^{\text{ext}}(\boldsymbol{r}) - \mu^*\right]. \tag{3.17}$$

In the following the focus is on systems in three-dimensional space which consist of fluids surrounding a convex wall. The sketch in Fig. 3.1 illustrates the basic structure of these systems and how they are parameterized. The geometry of the wall enters the formalism via the external potential $V^{\text{ext}}(\boldsymbol{r})$ with $\boldsymbol{r} = (x, y, z) \in \mathbb{R}^3$:

- A *planar* wall occupies the half space beyond the xy-plane in a cartesian coordinate system

$$V^{\text{ext}}(\boldsymbol{r}) = \begin{cases} \infty, & r < 0, \\ V(r), & r \geq 0. \end{cases} \tag{3.18}$$

  $r := z$ is equal to the z-component of the position $\boldsymbol{r}$. The variable name "r" is chosen in order to have the same notation for all geometries. V represents the excess part of the external potential [i.e., in excess to the part $V(r < 0) = \infty$ which originates from the hard interaction between the fluid particles and the wall]. An equivalent notation is used in the cases of spherical Eq. (3.19) and cylindrical Eq. (3.20) walls.

- A *spherical* wall of radius R is given by

$$V^{\text{ext}}(\boldsymbol{r}) = \begin{cases} \infty, & r < R, \\ V(r), & r \geq R. \end{cases} \tag{3.19}$$

  $r := \sqrt{x^2 + y^2 + z^2}$ denotes the radial distance between the center of the spherical wall, which is chosen as the origin of the coordinate system, and the position $\boldsymbol{r}$.
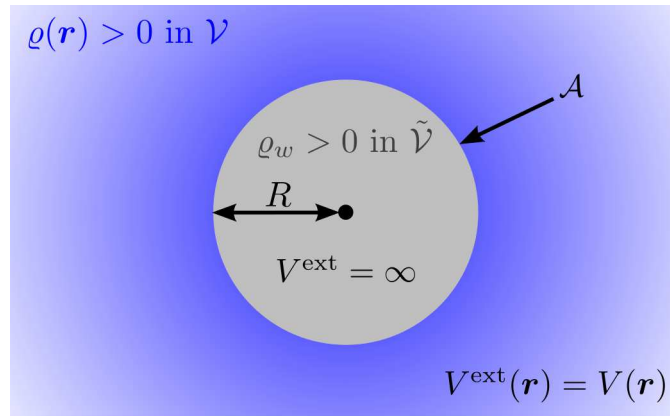
Figure 3.1: Sketch of the model system under consideration. The depicted case corresponds to a spherical [Eq. (3.19)] or a cylindrical [Eq. (3.20)] wall (gray circle) of radius R which is surrounded by a fluid. The wall consists of wall particles which are homogeneously distributed in the domain $\tilde{\mathcal{V}}$ with number density ϱ_w. The fluid particles cannot enter this domain because therein the external potential V^{ext} takes an infinitely large value [see Eqs. (3.18) – (3.20)]. Instead the former occupy the accessible domain $\mathcal{V}$ outside of the wall. Their number density ϱ is plotted in blue color; different shades of blue illustrate that, in general, $\varrho(\boldsymbol{r})$ is a spatially varying function. At all positions $\boldsymbol{r} \in \mathcal{V}$ the fluid particles interact with the wall by means of the excess external potential $V(\boldsymbol{r})$ [Eq. (3.22)]. Within the present chapter the reference surface, the geometrical surface, and the interface $\mathcal{A}$ (see Fig. 2.1) comprise the same set of points.

- A *cylindrical* wall of radius R is defined by

$$V^{\text{ext}}(\boldsymbol{r}) = \begin{cases} \infty, & r < R, \\ V(r), & r \geq R. \end{cases} \tag{3.20}$$

In this case $r := \sqrt{x^2 + y^2}$ measures the distance between the symmetry axis of the cylinder, i.e., the z-axis, and the position $\boldsymbol{r}$.

The excess external potential V in Eqs. (3.18) – (3.20) characterizes the interaction between fluid and wall particles apart from being in contact with each other. The latter are assumed to be homogeneously distributed in the wall $\tilde{\mathcal{V}}$, i.e., the positions that correspond to the hard part of the external potentials in Eqs. (3.18) – (3.20), with number density ϱ_w. In the present study the pair interaction potential U_w between fluid and wall particles adopts the same form as the potential U amongst fluid particles Eq. (3.1)

$$U_w(r) := U_{0w} \frac{\exp(-r/L_w)}{r}, \tag{3.21}$$

where the strength U_{0w} and the length scale L_w may be chosen independently of the fluid-fluid interaction parameters U_0 and L in Eq. (3.1). With this the excess external

potential can be calculated as

$$V(\boldsymbol{r}) = \varrho_w \int_{\tilde{\mathcal{V}}} \mathrm{d}^3 r' \, U_w(|\boldsymbol{r} - \boldsymbol{r}'|). \tag{3.22}$$

The ELE (3.16) is an integral equation because the required function $\varrho_{\mathrm{eq}}(\boldsymbol{r})$ is part of the integrand. In the present case it can be translated into a differential equation with corresponding boundary conditions by exploiting the properties of the interparticle potential U [Eq. (3.1)]. This approach has already been proposed earlier, e.g., in Refs. [85–92], in order to solve integral equations of similar form in planar and spherical geometry. Here a generalized notation is used which allows to conveniently apply this formalism with respect to various geometries. It is made use of the fact that the Yukawa potential U Eq. (3.1) is the Green's function of the Helmholtz operator $\Delta - L^{-2}$,

$$\Delta U(|\boldsymbol{r} - \boldsymbol{r}'|) - \frac{1}{L^2} U(|\boldsymbol{r} - \boldsymbol{r}'|) = -4\pi U_0 \, \delta(\boldsymbol{r} - \boldsymbol{r}'), \tag{3.23}$$

where Δ is acting on the unprimed coordinate $\boldsymbol{r}$. Together with Eq. (3.23) the Laplacian of the integration in Eq. (3.16) reads

$$
\begin{aligned}
\Delta \int_{\mathcal{V}} \mathrm{d}^3 r' \, U(|\boldsymbol{r} - \boldsymbol{r}'|) \varrho_{\mathrm{eq}}(\boldsymbol{r}') \\
= \frac{1}{L^2} \int_{\mathcal{V}} \mathrm{d}^3 r' \, U(|\boldsymbol{r} - \boldsymbol{r}'|) \varrho_{\mathrm{eq}}(\boldsymbol{r}') - 4\pi U_0 \int_{\mathcal{V}} \mathrm{d}^3 r' \, \delta(\boldsymbol{r} - \boldsymbol{r}') \varrho_{\mathrm{eq}}(\boldsymbol{r}') \\
= \frac{1}{L^2} \left[\mu^* - V(\boldsymbol{r}) - c\varrho_{\mathrm{eq}}(\boldsymbol{r}) \right] - 4\pi U_0 \varrho_{\mathrm{eq}}(\boldsymbol{r}).
\end{aligned}
\tag{3.24}
$$

The ELE (3.16) is used in order to replace the integral in the second line of Eq. (3.24). Finally, by applying the replacement of Eq. (3.24), the Laplacian of Eq. (3.16) leads to the ELE in the form

$$
\begin{aligned}
\Delta \varrho_{\mathrm{eq}}(\boldsymbol{r}) - \frac{1}{\xi^2} \varrho_{\mathrm{eq}}(\boldsymbol{r}) = F(\boldsymbol{r}), \\
\xi^2 := \left(\frac{1}{L^2} + \frac{4\pi U_0}{c} \right)^{-1}, \\
F(\boldsymbol{r}) := -\frac{1}{c} \left[\frac{\mu^* - V(\boldsymbol{r})}{L^2} + \Delta V(\boldsymbol{r}) \right],
\end{aligned}
\tag{3.25}
$$

which is a linear partial differential equation with inhomogeneity $F(\boldsymbol{r})$. Due to the symmetry of the considered geometries only the radial part of the Laplacian in Eq. (3.25) in one, two, or three dimensions contributes. In these cases Eq. (3.25) effectively turns into an ordinary differential equation [see Eqs. (3.39), (3.51), and (3.71)]. ξ can be identified as the bulk correlation length (see Appendix 3.A). The differential equation (3.25) describes

the fluid only within the domain $\mathcal{V}$. Additional boundary conditions are required in order to uniquely define the solution. Far away from the wall the solution has to fulfill the bulk ELE (3.13). There, no external potential is present and the number density is a constant, i.e., $V(\boldsymbol{r})|_{\text{bulk}} = 0$, $\Delta V(\boldsymbol{r})|_{\text{bulk}} = 0$, and $\Delta \varrho_{\text{eq}}(\boldsymbol{r})|_{\text{bulk}} = 0$. These special values reduce Eq. (3.25) to

$$\left(\frac{1}{L^2} + \frac{4\pi U_0}{c} \right) \varrho_{\text{eq}}(\boldsymbol{r})|_{\text{bulk}} = \frac{\mu^*}{cL^2} \tag{3.26}$$

$$\Leftrightarrow \left(c + 4\pi L^2 U_0 \right) \varrho_{\text{eq}}(\boldsymbol{r})|_{\text{bulk}} = \mu^* \tag{3.27}$$

$$\Leftrightarrow \left[c + \hat{U}(0) \right] \varrho_{\text{eq}}(\boldsymbol{r})|_{\text{bulk}} = \mu^*. \tag{3.28}$$

Thus, the intuitive choice $\varrho_{\text{eq}}(\boldsymbol{r})|_{\text{bulk}} := \varrho_{\text{eq}}^{\text{b}}$ readily fulfills this boundary condition [see the bulk ELE (3.13)]. The remaining boundary condition refers to the wall surface. The ELE (3.16) in integral form contains information about both the fluid within $\mathcal{V}$ and the connection with the boundaries of this domain. [Note that also the bulk Eq. (3.13) is covered by Eq. (3.16).] In order to conserve the consistent description of the integral equation, the boundary condition for the differential equation is obtained from the former. The corresponding procedure is now explained in terms of general expressions which are valid for all wall shapes under consideration. Subsequently, in Sec. 3.3.1, the procedure is demonstrated in detail with respect to the planar wall. In the case of the geometries considered in the present study [Eqs. (3.18) – (3.20)] the ELE (3.16) is effectively one-dimensional

$$\mathcal{I}(r) = \mu^* - V(r) - c\varrho_{\text{eq}}(r), \tag{3.29}$$

$$\mathcal{I}(r) := \int_{\mathcal{V}} \mathrm{d}^3 r' \, U(|\boldsymbol{r} - \boldsymbol{r}'|) \varrho_{\text{eq}}(r'). \tag{3.30}$$

The derivative of Eq. (3.29) with respect to r is evaluated at the wall surface

$$\mathcal{I}'(r)|_{r_w} = -V'(r)|_{r_w} - c\varrho'_{\text{eq}}(r)|_{r_w}, \tag{3.31}$$

where $r_w := 0$ for the planar geometry and $r_w := R$ for the curved geometries, respectively. It turns out that $\mathcal{I}'(r)|_{r_w}$ and $\mathcal{I}(r_w)$ are proportional to each other,

$$\mathcal{I}'(r)|_{r_w} = \zeta \, \mathcal{I}(r_w), \tag{3.32}$$

[see, e.g., Eq. (3.41)] and that the proportionality factor ζ depends on the wall geometry. This leads to a boundary condition of the general form

$$-V'(r)|_{r_w} - c\varrho'_{\text{eq}}(r)|_{r_w} = \zeta \left[\mu^* - V(r_w) - c\varrho_{\text{eq}}(r_w) \right], \tag{3.33}$$

which relates the number density at the wall $\varrho_{\mathrm{eq}}(r_w)$ with its derivative. The explicit expressions are given in the context of each geometry [see Eqs. (3.43), (3.53), and (3.73)].

3.3 Discussion

For the sake of clarity the subscript $_{\mathrm{eq}}$ is omitted in the case of the number densities and subsequently the focus is on equilibrium number densities. The interfacial tension

$$\gamma = \frac{\Omega_{\mathrm{eq}} - \Omega_{\mathrm{eq}}^{\mathrm{b}}}{|\mathcal{A}|} \tag{3.34}$$

measures the work $\Omega_{\mathrm{eq}} - \Omega_{\mathrm{eq}}^{\mathrm{b}}$ which is necessary in order to create the interface $\mathcal{A}$. In principle, $\mathcal{A}$ can be defined arbitrarily which is why Eq. (3.34) does not define γ uniquely (see Sec. 2.3). The pointlike particles in the present study are able to penetrate the whole space up to the wall. This is the reason why the accessible positions for the fluid particles $\mathcal{V}$ and the positions outside of the wall $\mathbb{R}^3 \backslash \tilde{\mathcal{V}}$ are *equal* $\mathcal{V} = \mathbb{R}^3 \backslash \tilde{\mathcal{V}}$. Or, to use the terminology of the preceding chapter, the reference surface and the geometrical surface are the same (see Fig. 2.1). It is therefore convenient to define the interface to consist of the same set of points as the reference and geometrical surface and, consequently, to determine the bulk contribution $\Omega_{\mathrm{eq}}^{\mathrm{b}}$ in Eq. (3.34) for the same domain $\mathcal{V}$ as the contribution Ω_{eq}. Speaking in terms of the preceding Chap. 2 (see also Ref. [22]) this choice corresponds to the convention $\delta = 0$, i.e., the following results will be quoted with respect to this convention. The interfacial tension is given by

$$\gamma = \frac{1}{2|\mathcal{A}|} \int_{\mathcal{V}} \mathrm{d}^3 r \, \left\{ \mu^* \left[\varrho^{\mathrm{b}} - \varrho(\boldsymbol{r}) \right] + V(\boldsymbol{r}) \varrho(\boldsymbol{r}) \right\}. \tag{3.35}$$

That is, the equilibrium number density profile $\varrho(\boldsymbol{r})$ is necessary in order to calculate the value of γ. To that end subsequently the ELE (3.16), or alternatively Eq. (3.25) with corresponding boundary conditions, is solved for various geometries.

3.3.1 Planar wall

Within this subsection the solution process is explained in detail for the planar geometry. In order to obtain expressions for the interfacial tension with respect to the curved geometries the following steps can be applied analogously (see Secs. 3.3.2 and 3.3.3). The

excess external potential V Eq. (3.22) in the case of the planar wall Eq. (3.18) is given by

$$V(r) = \int\limits_{-\infty}^{0} \mathrm{d}r' \int\limits_{-\infty}^{\infty} \mathrm{d}y' \int\limits_{-\infty}^{\infty} \mathrm{d}x'\, \varrho_w U_w(|\boldsymbol{r} - \boldsymbol{r}'|) = V_p \exp\left(-r/L_w\right), \qquad (3.36)$$

$$V_p := 2\pi\varrho_w U_{0w} L_w^2. \qquad (3.37)$$

V_p refers to the excess external potential evaluated at contact with the planar wall. It contains both the number density of wall particles ϱ_w and the amplitude of the wall-fluid interaction potential U_{0w} and will be used in the following in order to quote the strength of the excess external potential. Due to the symmetry of the system the number density $\varrho(r)$ is translationally invariant in any direction parallel to the wall surface and can only vary in normal direction with respect to the wall. Therefore the ELE (3.16) is effectively one-dimensional [see Eq. (3.29)]

$$\mathcal{I}(r) = 2\pi U_0 L \int\limits_{0}^{\infty} \mathrm{d}r'\, \varrho(r') \exp\left(-\frac{|r - r'|}{L}\right) = \mu^* - V(r) - c\varrho(r) \qquad (3.38)$$

and corresponds to a one-dimensional version of the differential equation (3.25)

$$\varrho''(r) - \frac{1}{\xi^2}\varrho(r) = -\frac{\mu^*}{cL^2} + B_p \exp\left(-\frac{r}{L_w}\right), \qquad (3.39)$$

$$B_p := \frac{V_p}{c}\left(\frac{1}{L^2} - \frac{1}{L_w^2}\right). \qquad (3.40)$$

The derivative of the integral expression in Eq. (3.38) with respect to r and evaluated at the wall surface $r = 0$,

$$\mathcal{I}'(r)|_{r=0} = 2\pi U_0 \int\limits_{0}^{\infty} \mathrm{d}r'\, \varrho(r') \exp\left(-\frac{r'}{L}\right) = \frac{1}{L}\mathcal{I}(0), \qquad (3.41)$$

is proportional to the integral expression in Eq. (3.38) evaluated at the wall surface with proportionality factor $\zeta = 1/L$ [see Eq. (3.32)]. The relation Eq. (3.41) between the derivative and the value of $\mathcal{I}(r)$ at the wall surface can be written in terms of the right hand side of Eq. (3.38) as

$$-V'(r)|_{r=0} - c\varrho'(r)|_{r=0} = \frac{1}{L}\left[\mu^* - V(0) - c\varrho(0)\right] \qquad (3.42)$$

which is equivalent to Eq. (3.33) in planar geometry. With the actual expression for the excess external potential [Eq. (3.36)] finally the boundary condition

$$\varrho'(0) - \frac{\varrho(0)}{L} = \frac{V_p}{cL_w} - \frac{\mu^* - V_p}{cL} \tag{3.43}$$

at the wall surface is obtained. The excess external potential Eq. (3.36) is an eigenfunction of the one-dimensional Laplacian $\Delta \equiv \partial_r^2$. Therefore the inhomogeneity F of Eq. (3.25) only consists of terms constant in r and of terms proportional to the eigenfunction of the Laplace operator [see the right hand side of Eq. (3.39)]. Since the differential operator of the differential equation (3.39) is the Laplacian, the particular solution can be determined straightforwardly. Note that analogous structures for the inhomogeneity also emerge for the curved geometries [see Eqs. (3.51) and (3.71)] which enables to solve the respective equations in a similar manner. The solution of the differential equation (3.39) is of the form

$$\varrho(r) = \varrho^{\mathrm{b}} + A_p \exp\left(-\frac{r}{L_w}\right) + D_p \exp\left(-\frac{r}{\xi}\right), \tag{3.44}$$

where the first two summands are an ansatz for the particular solution and the last summand solves the homogeneous differential equation, i.e., Eq. (3.39) with the right hand side set to zero. The constant term ϱ^{b} in Eq. (3.44) corresponds to the constant part of the inhomogeneity and fulfills the boundary condition in the bulk, i.e., for $r \to \infty$ [see Eqs. (3.26) – (3.28)]. The constant A_p is chosen such that the remaining part of the inhomogeneity is captured which leads to

$$A_p := B_p \left(\frac{1}{L_w^2} - \frac{1}{\xi^2}\right)^{-1}. \tag{3.45}$$

The constant

$$D_p := -\left[\left(\frac{1}{L_w} + \frac{1}{L}\right)\left(A_p + \frac{V_p}{c}\right) - \frac{\hat{U}(0)\varrho^{\mathrm{b}}}{cL}\right]\left(\frac{1}{\xi} + \frac{1}{L}\right)^{-1} \tag{3.46}$$

is determined in order to fulfill the boundary condition Eq. (3.43). It was checked that the number density profile Eq. (3.44) with Eqs. (3.45) and (3.46) solves the integral equation (3.38). Finally, the interfacial tension [Eq. (3.35)] may be determined as

$$\begin{aligned}
\gamma_p &= \frac{1}{2} \int_0^\infty \mathrm{d}r \left\{ \mu^* \left[\varrho^{\mathrm{b}} - \varrho(r)\right] + \varrho(r)V(r) \right\} \\
&= -\frac{\mu^*}{2}(A_p L_w + D_p \xi) + \frac{V_p}{2}\left(\varrho^{\mathrm{b}} L_w + \frac{1}{2}A_p L_w + \frac{D_p}{1/\xi + 1/L_w}\right).
\end{aligned} \tag{3.47}$$

3.3.2 Spherical wall

The excess external potential V Eq. (3.22) in the case of the spherical wall Eq. (3.19) is given by

$$V(r) = V_s \frac{\exp(-r/L_w)}{r/L_w}, \qquad (3.48)$$

$$V_s := V_p \left[\left(\frac{R}{L_w} - 1 \right) \exp\left(\frac{R}{L_w} \right) + \left(\frac{R}{L_w} + 1 \right) \exp\left(-\frac{R}{L_w} \right) \right], \qquad (3.49)$$

and the effectively one-dimensional ELE (3.29) reads

$$\frac{2\pi U_0 L}{r} \int_R^\infty dr' \, r' \varrho(r') \left\{ \exp\left[-\frac{|r - r'|}{L} \right] - \exp\left[-\frac{|r + r'|}{L} \right] \right\} = \mu^* - V(r) - c\varrho(r). \qquad (3.50)$$

The integral equation (3.50) translates into the differential equation [see Eq. (3.25)]

$$\varrho''(r) + \frac{2}{r}\varrho'(r) - \frac{1}{\xi^2}\varrho(r) = -\frac{\mu^*}{cL^2} + B_s \frac{\exp(-r/L_w)}{r}, \qquad (3.51)$$

$$B_s := \frac{V_s L_w}{c} \left(\frac{1}{L^2} - \frac{1}{L_w^2} \right), \qquad (3.52)$$

with the boundary condition

$$\varrho'(R) - \frac{1}{L}\mathcal{L}\left(\frac{R}{L} \right) \varrho(R)$$
$$= \left(\frac{1}{L_w} + \frac{1}{R} \right) \frac{V_s L_w}{c} \frac{\exp(-R/L_w)}{R} - \frac{1}{L}\mathcal{L}\left(\frac{R}{L} \right) \left[\frac{\mu^*}{c} - \frac{V_s L_w}{c} \frac{\exp(-R/L_w)}{R} \right] \qquad (3.53)$$

at the wall surface $r = R$. $\mathcal{L}(x) = \coth(x) - 1/x$ denotes the Langevin function. The proportionality Eq. (3.32) with

$$\zeta = \frac{1}{L}\mathcal{L}\left(\frac{R}{L} \right) \qquad (3.54)$$

is used in order to obtain the boundary condition Eq. (3.53). The differential equation (3.51) is solved by the ansatz

$$\varrho(r) = \varrho^b + A_s \frac{\exp(-r/L_w)}{r} + D_s \frac{\exp(-r/\xi)}{r} \qquad (3.55)$$

with the constants

$$A_s := B_s \left(\frac{1}{L_w^2} - \frac{1}{\xi^2} \right)^{-1} \qquad (3.56)$$

and

$$
\begin{aligned}
D_s := &- \exp\left(\frac{R}{\xi}\right) \left[\frac{1}{\xi} + \frac{1}{L}\coth\left(\frac{R}{L}\right)\right]^{-1} \\
&\times \left\{\exp\left(-\frac{R}{L_w}\right)\left(A_s + \frac{V_s L_w}{c}\right)\left[\frac{1}{L_w} + \frac{1}{L}\coth\left(\frac{R}{L}\right)\right] - \frac{R}{L}\mathcal{L}\left(\frac{R}{L}\right)\frac{\hat{U}(0)\varrho^{\mathrm{b}}}{c}\right\}.
\end{aligned}
$$
(3.57)

The interfacial tension for the spherical wall reads

$$
\begin{aligned}
\gamma_s = &- \frac{\mu^*}{2R^2}\left[A_s\exp\left(-\frac{R}{L_w}\right)(RL_w + L_w^2) + D_s\exp\left(-\frac{R}{\xi}\right)(R\xi + \xi^2)\right] \\
&+ \frac{V_s L_w}{2R^2}\left\{\varrho^{\mathrm{b}}\exp\left(-\frac{R}{L_w}\right)(RL_w + L_w^2) + \frac{1}{2}A_s L_w\exp\left(-\frac{2R}{L_w}\right)\right. \\
&\left. + D_s\left(\frac{1}{\xi} + \frac{1}{L_w}\right)^{-1}\exp\left[-R\left(\frac{1}{\xi} + \frac{1}{L_w}\right)\right]\right\}.
\end{aligned}
$$
(3.58)

In order to check the validity of the morphometric approach the expression for the interfacial tension γ_s is expanded in terms of large radii R of the wall. Note that the dependence of γ_s on R is also contained in the quantities A_s, D_s, and V_s. The latter can be written in terms of the following expansions

$$
V_s = V_p\left(\frac{R}{L_w} - 1\right)\exp\left(\frac{R}{L_w}\right) + O\left[\frac{R}{L_w}\exp\left(-\frac{R}{L_w}\right)\right],
$$
(3.59)

$$
B_s = B_p L_w\left(\frac{R}{L_w} - 1\right)\exp\left(\frac{R}{L_w}\right) + O\left[\frac{R}{L_w}\exp\left(-\frac{R}{L_w}\right)\right],
$$
(3.60)

$$
A_s = A_p L_w\left(\frac{R}{L_w} - 1\right)\exp\left(\frac{R}{L_w}\right) + O\left[\frac{R}{L_w}\exp\left(-\frac{R}{L_w}\right)\right],
$$
(3.61)

$$
D_s = R\exp\left(\frac{R}{\xi}\right)\left\{D_p + \frac{D_{s1}}{R} + O\left[\exp\left(-\frac{2R}{L}\right) + \exp\left(-\frac{2R}{L_w}\right)\right]\right\},
$$
(3.62)

with

$$
\coth\left(\frac{R}{L}\right) = 1 + O\left[\exp\left(-\frac{2R}{L}\right)\right],
$$
(3.63)

$$
D_{s1} := \left[L_w\left(A_p + \frac{V_p}{c}\right)\left(\frac{1}{L_w} + \frac{1}{L}\right) - \frac{\hat{U}(0)\varrho^{\mathrm{b}}}{c}\right]\left(\frac{1}{\xi} + \frac{1}{L}\right)^{-1}.
$$
(3.64)

For the interfacial tension these expansions lead to

$$
\gamma_s = \gamma_p + L\frac{\gamma_{s1}}{R} + L^2\frac{\gamma_{s2}}{R^2} + O\left[\exp\left(-\frac{2R}{L}\right) + \exp\left(-\frac{2R}{L_w}\right)\right]
$$
(3.65)

with the coefficients

$$L\gamma_{s1} := -\frac{\mu^*}{2}\left(D_p\xi^2 + D_{s1}\xi\right) + \frac{V_p}{2}\left[(D_{s1} - L_w D_p)\left(\frac{1}{\xi} + \frac{1}{L_w}\right)^{-1} - A_p L_w^2\right] \qquad (3.66)$$

and

$$L^2\gamma_{s2} := -\frac{\mu^*}{2}\left(D_{s1}\xi^2 - A_p L_w^3\right) + \frac{V_p}{2}\left[\frac{A_p L_w^3}{2} - \varrho^{\mathrm{b}} L_w^3 - D_{s1}L_w\left(\frac{1}{\xi} + \frac{1}{L_w}\right)^{-1}\right]. \qquad (3.67)$$

For the spherical wall the expansion Eq. (3.65) reveals that the morphometric expression Eq. (2.3) is not exactly valid because there are terms which are not constant, linear, and quadratic in the curvature. However, the deviation between the exact expression and the MT expression is exponentially small and thus, for not too small R, the deviation is essentially smaller than the algebraic terms in accordance with MT. In this geometry MT proposes to truncate the exact expression after the term $\propto R^{-2}$ which ensures an approximation of high quality.

3.3.3 Cylindrical wall

In the case of a cylindrical wall Eq. (3.20) the excess external potential Eq. (3.22) reads

$$V(r) = V_c \mathrm{K}_0\left(\frac{r}{L_w}\right), \qquad (3.68)$$

$$V_c := 2V_p \frac{R}{L_w} \mathrm{I}_1\left(\frac{R}{L_w}\right), \qquad (3.69)$$

with the modified Bessel functions K_ν and I_ν [84]. The cylindrical geometry enables to formulate an effectively one-dimensional ELE (3.29)

$$4\pi U_0 \left[\mathrm{K}_0\left(\frac{r}{L}\right) \int_R^r \mathrm{d}r'\, r' \varrho(r')\, \mathrm{I}_0\left(\frac{r'}{L}\right) + \mathrm{I}_0\left(\frac{r}{L}\right) \int_r^\infty \mathrm{d}r'\, r' \varrho(r')\, \mathrm{K}_0\left(\frac{r'}{L}\right) \right]$$
$$= \mu^* - V(r) - c\varrho(r), \qquad (3.70)$$

which is equivalent to the differential equation

$$\varrho''(r) + \frac{1}{r}\varrho'(r) - \frac{1}{\xi^2}\varrho(r) = -\frac{\mu^*}{cL^2} + B_c \mathrm{K}_0\left(\frac{r}{L_w}\right), \qquad (3.71)$$

$$B_c := \frac{V_c}{c}\left(\frac{1}{L^2} - \frac{1}{L_w^2}\right), \qquad (3.72)$$

with the boundary condition at the wall surface $r = R$

$$\varrho'(R) - \frac{\chi}{L}\varrho(R) = \frac{V_c}{cL_w}\,\mathrm{K}_1\left(\frac{R}{L_w}\right) - \frac{\chi}{cL}\left[\mu^* - V_c\,\mathrm{K}_0\left(\frac{R}{L_w}\right)\right], \tag{3.73}$$

$$\chi := \frac{\mathrm{I}_1(R/L)}{\mathrm{I}_0(R/L)}. \tag{3.74}$$

The proportionality Eq. (3.32) with $\zeta = \chi/L$ leads to the boundary condition Eq. (3.73). The number density profile

$$\varrho(r) = \varrho^{\mathrm{b}} + A_c\,\mathrm{K}_0\left(\frac{r}{L_w}\right) + D_c\,\mathrm{K}_0\left(\frac{r}{\xi}\right) \tag{3.75}$$

with

$$A_c := B_c\left(\frac{1}{L_w^2} - \frac{1}{\xi^2}\right)^{-1} \tag{3.76}$$

and

$$\begin{aligned}
D_c := &-\left[\frac{1}{\xi}\,\mathrm{K}_1\left(\frac{R}{\xi}\right) + \frac{\chi}{L}\,\mathrm{K}_0\left(\frac{R}{\xi}\right)\right]^{-1}\left\{A_c\left[\frac{1}{L_w}\,\mathrm{K}_1\left(\frac{R}{L_w}\right) + \frac{\chi}{L}\,\mathrm{K}_0\left(\frac{R}{L_w}\right)\right]\right.\\
&\left.+\frac{V_c}{c}\left[\frac{1}{L_w}\,\mathrm{K}_1\left(\frac{R}{L_w}\right) + \frac{\chi}{L}\,\mathrm{K}_0\left(\frac{R}{L_w}\right)\right] - \frac{\chi}{L}\frac{\hat{U}(0)\varrho^{\mathrm{b}}}{c}\right\}
\end{aligned} \tag{3.77}$$

solves the differential equation (3.71) and the associated boundary conditions. With this the interfacial tension reads

$$\begin{aligned}
\gamma_c = &-\frac{\mu^*}{2}\left[A_cL_w\,\mathrm{K}_1\left(\frac{R}{L_w}\right) + D_c\xi\,\mathrm{K}_1\left(\frac{R}{\xi}\right)\right]\\
&+\frac{V_c}{2}\left\{\varrho^{\mathrm{b}}L_w\,\mathrm{K}_1\left(\frac{R}{L_w}\right) + \frac{A_cR}{2}\left[\mathrm{K}_1\left(\frac{R}{L_w}\right)^2 - \mathrm{K}_0\left(\frac{R}{L_w}\right)^2\right]\right.\\
&\left.+ D_c\left[\frac{1}{\xi}\,\mathrm{K}_1\left(\frac{R}{\xi}\right)\mathrm{K}_0\left(\frac{R}{L_w}\right) - \frac{1}{L_w}\,\mathrm{K}_0\left(\frac{R}{\xi}\right)\mathrm{K}_1\left(\frac{R}{L_w}\right)\right]\left(\frac{1}{\xi^2} - \frac{1}{L_w^2}\right)^{-1}\right\}.
\end{aligned} \tag{3.78}$$

The dependence of the interfacial tension γ_c on the radius of the cylindrical wall turns out to be comparatively complex. In the case of the spherical wall Eq. (3.58) the R-dependence is covered by a combination of exponential and rational functions. For the cylindrical geometry Eq. (3.78) one has to deal with various combinations of modified Bessel functions. (Note that the latter are also contained in the abbreviations A_c, D_c, and V_c.) With the help of asymptotic expansions for large arguments of the modified

Bessel functions [84]

$$
I_\nu(z) \sim \frac{\exp(z)}{\sqrt{2\pi z}}
$$
$$
\times \left[1 - \frac{\mu - 1}{8z} + \frac{(\mu-1)(\mu-9)}{2!(8z)^2} - \frac{(\mu-1)(\mu-9)(\mu-25)}{3!(8z)^3} + O\left(z^{-4}\right) \right], \tag{3.79}
$$

$$
K_\nu(z) \sim \sqrt{\frac{\pi}{2z}} \exp(-z)
$$
$$
\times \left[1 + \frac{\mu - 1}{8z} + \frac{(\mu-1)(\mu-9)}{2!(8z)^2} + \frac{(\mu-1)(\mu-9)(\mu-25)}{3!(8z)^3} + O\left(z^{-4}\right) \right], \tag{3.80}
$$

$$
\mu = 4\nu^2, \quad \text{(3.81)}
$$

the exact expression for the interfacial tension γ_c in Eq. (3.78) can be discussed in terms of large radii of the cylinder. The expansions Eq. (3.79) and (3.80) lead to

$$
V_c = 2V_p \sqrt{\frac{R}{2\pi L_w}} \exp\left(\frac{R}{L_w}\right) \left[1 - \frac{3}{8}\frac{L_w}{R} - \frac{15}{128}\frac{L_w^2}{R^2} - \frac{105}{1024}\frac{L_w^3}{R^3} + O\left(R^{-4}\right) \right], \tag{3.82}
$$

$$
\chi = 1 - \frac{1}{2}\frac{L}{R} - \frac{1}{8}\frac{L^2}{R^2} - \frac{1}{8}\frac{L^3}{R^3} + O\left(R^{-4}\right), \tag{3.83}
$$

$$
D_c = \sqrt{\frac{2R}{\pi\xi}} \exp\left(\frac{R}{\xi}\right) \left[D_p + \frac{D_{c1}}{R} + \frac{D_{c2}}{R^2} + \frac{D_{c3}}{R^3} + O\left(R^{-4}\right) \right], \tag{3.84}
$$

with

$$
D_{c1} := -\frac{\xi}{8} \left[\left(\frac{1}{L_w} + \frac{1}{L}\right)\left(A_p + \frac{V_p}{c}\right) L_w \left(\frac{1}{L_w} - \frac{4}{\xi}\right) - \frac{\hat{U}(0)\varrho^{\mathrm{b}}}{c}\left(\frac{1}{L} - \frac{4}{\xi}\right) \right]
$$
$$
\times \left(\frac{1}{\xi} + \frac{1}{L}\right)^{-1} = \frac{\xi D_p}{8} + \frac{D_{s1}}{2}, \tag{3.85}
$$

$$
D_{c2} := -\frac{\xi^2 L}{128} \left[\left(\frac{1}{L_w} + \frac{1}{L}\right)\left(A_p + \frac{V_p}{c}\right) L_w \left(\frac{16}{\xi L_w} - \frac{7}{L L_w} - \frac{8}{\xi L} - \frac{16}{\xi^2}\right) \right.
$$
$$
\left. - \frac{\hat{U}(0)\varrho^{\mathrm{b}}}{c}\left(\frac{8}{\xi L} - \frac{7}{L^2} - \frac{16}{\xi^2}\right) \right] \left(\frac{1}{\xi} + \frac{1}{L}\right)^{-1}, \tag{3.86}
$$

and

$$
D_{c3} := -\frac{\xi^3 L^2}{1024} \left[\left(\frac{1}{L_w} + \frac{1}{L}\right)\left(A_p + \frac{V_p}{c}\right) L_w^3 \left(\frac{128}{\xi^2 L_w^3} - \frac{112}{\xi L L_w^3} + \frac{59}{L^2 L_w^3} - \frac{80}{\xi^2 L L_w^2} \right.\right.
$$
$$
\left. + \frac{28}{\xi L^2 L_w^2} - \frac{128}{\xi^3 L_w^2} + \frac{192}{\xi^3 L L_w} - \frac{192}{\xi^3 L^2}\right)
$$
$$
\left. - \frac{\hat{U}(0)\varrho^{\mathrm{b}}}{c}\left(\frac{48}{\xi^2 L} - \frac{84}{\xi L^2} + \frac{59}{L^3} - \frac{128}{\xi^3}\right) \right] \left(\frac{1}{\xi} + \frac{1}{L}\right)^{-1}. \tag{3.87}
$$

The expansion of γ_c in powers of the curvature $1/R$ of the cylinder is given by

$$\gamma_c = \gamma_p + L\frac{\gamma_{c1}}{R} + L^2\frac{\gamma_{c2}}{R^2} + L^3\frac{\gamma_{c3}}{R^3} + O\left(R^{-4}\right) \tag{3.88}$$

with

$$\begin{aligned}
L\gamma_{c1} := &- \frac{\mu^*\xi}{2}\left(\frac{3}{8}D_p\xi + D_{c1}\right) - \frac{1}{4}V_pA_pL_w^2 \\
&+ \frac{V_p}{2}\left(\frac{1}{\xi} + \frac{1}{L_w}\right)^{-1}\left[D_{c1} - \frac{1}{8}\xi L_w D_p\left(\frac{4}{\xi} + \frac{1}{L_w}\right)\right] = \frac{L}{2}\gamma_{s1},
\end{aligned} \tag{3.89}$$

$$\begin{aligned}
L^2\gamma_{c2} := &\frac{3}{16}\mu^* A_p L_w^3 - \frac{\mu^*\xi}{2}\left(-\frac{15}{128}D_p\xi^2 + \frac{3}{8}D_{c1}\xi + D_{c2}\right) - \frac{3}{16}V_p\varrho^{\mathrm{b}}L_w^3 + \frac{3}{32}V_pA_pL_w^3 \\
&+ \frac{V_p}{2}\left(\frac{1}{\xi} + \frac{1}{L_w}\right)^{-1}\left[D_{c2} - \frac{1}{8}\xi L_w D_{c1}\left(\frac{4}{\xi} + \frac{1}{L_w}\right) + \frac{\xi^2 L_w D_p}{128}\left(\frac{24}{\xi} + \frac{9}{L_w}\right)\right],
\end{aligned} \tag{3.90}$$

and

$$\begin{aligned}
L^3\gamma_{c3} := &- \frac{\mu^*\xi}{2}\left(\frac{105}{1024}D_p\xi^3 - \frac{15}{128}D_{c1}\xi^2 + \frac{3}{8}D_{c2}\xi + D_{c3}\right) - \frac{3}{16}V_pA_pL_w^4 \\
&+ \frac{V_p}{2}\left(\frac{1}{\xi} + \frac{1}{L_w}\right)^{-1}\left[D_{c3} - \frac{1}{8}\xi L_w D_{c2}\left(\frac{4}{\xi} + \frac{1}{L_w}\right) + \frac{\xi^2 L_w D_{c1}}{128}\left(\frac{24}{\xi} + \frac{9}{L_w}\right)\right. \\
&\left. - \frac{\xi^3 L_w^3 D_p}{1024}\left(\frac{192}{\xi^3} + \frac{192}{\xi^2 L_w} + \frac{180}{\xi L_w^2} + \frac{75}{L_w^3}\right)\right].
\end{aligned} \tag{3.91}$$

3.3.4   Interpretation of the results in Secs. 3.3.1 − 3.3.3

Recently, in Refs. [23, 24] systems have been examined in which the particles interact with each other via the $2k$-k Lennard-Jones potential and the inverse power law potential $\propto r^{-\nu}$, respectively. The first terms of curvature expansions of the interfacial tension in spherical and cylindrical geometry have been determined analytically. For $k = 6$ and $\nu = 6$ some of these terms comprise a logarithmic dependence on the wall radius. For faster decay behaviors, i.e., for larger values of k or ν, the dependence on the curvature is found to be algebraic. Moreover, the truncated version of the 12-6 Lennard-Jones potential does not lead to a logarithmic term, i.e., truncation of the potential leads to a significant change in the curvature dependence of the interfacial tension [23]. That is, in view of these results, it is not a priori clear, that the untruncated Yukawa potential Eq. (3.1) considered in the present study corresponds to an interfacial tension with algebraic curvature expansion. Indeed the closed expressions for both γ_s [Eq. (3.58)] and γ_c [Eq. (3.78)] reveal a transcendental dependence on the wall radius. With regard to small

curvatures, however, both expressions convert either into a polynomial in curvature up to an exponentially small remainder [see Eq. (3.65)] or into an expansion in powers of the curvature [see Eq. (3.88)]. Considering that, in the cylindrical case, even the *truncated* expansions of the modified Bessel functions correspond to transcendental dependences on the cylinder radius R [see, e.g., Eq. (3.82)], this finding is not clear from the start. However, the modified Bessel functions in Eq. (3.78) always occur in combinations such that the transcendental parts cancel. The expansion Eq. (3.83) of χ Eq. (3.74), which is a quotient of modified Bessel functions, illustrates this cancelation. That is, in terms of a curvature expansion, for which logarithmic terms have been reported to occur in Refs. [23, 24], we do not observe a comparable significant deviation from an algebraic dependence. Note that this finding nevertheless is in line with Refs. [23, 24] according to which potentials of shorter range give rise to algebraic curvature expansions. The Yukawa potential, which is regarded here, decays exponentially and hence faster than any of the ones considered in Refs. [23, 24].

For the cylindrical geometry morphometric thermodynamics predicts a curvature expansion of γ_c only up to linear order in the curvature. However, the curvature expansion Eq. (3.88) exhibits also higher orders and the coefficients γ_{c2} and γ_{c3}, which are given explicitly in Eqs. (3.90) and (3.91), are nonzero in general. Therefore this result contradicts the prediction from morphometric thermodynamics and disqualifies the approach from being exact. This finding is in line with other studies in which analytic expressions for the same or related coefficients have been shown to be nonzero [20, 21, 23, 24]. Incidentally the discussion about interface conventions within the preceding Chap. 2 (see also Ref. [22]) should be taken into account. There it has been worked out, that, if the R dependence of the interfacial tension in accordance with MT would be *exact* in one convention, it would remain exact for all conventions. The values of most of the coefficients depend on the chosen interface convention. If there are nonzero coefficients of larger order than allowed within MT, changing the convention can have the consequence, that a good approximation deteriorates (see, e.g., Fig. 2.4). From that point of view it makes a huge difference whether coefficients not in accordance with the MT approach are really zero or just small in comparison with coefficients in accordance with MT. Due to uncertainties within the fitting procedure this question can be difficult to answer on the basis of numerical results.

It is interesting to study ratios between curvature coefficients of different geometries. The quotient of the first order coefficients yields [see Eqs. (3.66) and (3.89)]

$$\frac{\gamma_{s1}}{\gamma_{c1}} = 2. \tag{3.92}$$

This result is in line with both the morphometric approach (see, e.g., Ref. [8]) and a more general curvature expansion which has been applied, e.g., in Refs. [19, 21, 23, 24] and which is ascribed to Ref. [93]. In both approaches the linear dependence of the interfacial

tension on the wall curvature is written in terms of the total curvature $J = 1/R_1 + 1/R_2$ where R_1 and R_2 are the principal radii of curvature. Note that the latter do not depend on the position on the wall surface for the geometries under consideration. The ratio of the total curvatures of a spherical J^s and a cylindrical wall J^c renders $J^s/J^c = 2$. In the present study the curvature expansions are written in terms of the inverse wall radius [see Eqs. (3.65) and (3.88)] and therefore the relation between the total curvatures is absorbed in the coefficients γ_{s1} and γ_{c1} [see Eq. (3.92)]. Note that Eq. (3.92) is valid for all parameter choices within the current model, in particular for any range L_w and strength V_p of the excess external potential. To a certain extent this finding might complement other studies where the fluid is confined by purely hard walls [19, 21, 23, 24].

Within MT the ratio γ_{s2}/γ_{c2} would not be defined because the morphometric approach predicts $\gamma_{c2} = 0$ and, in general, $\gamma_{s2} \neq 0$. However, in the previous study (see Ref. [22] and Chap. 2) it has been found that for small packing fractions this ratio is close to the constant value 8/3 for all fluid-fluid interaction potentials under consideration, i.e., for square-well, square-shoulder, Yukawa-like, and Lennard-Jones-like potentials. The generality of this relation has been further confirmed with help of analytic results for hard sphere systems which have been derived in Ref. [21]. Recently, in Refs. [23, 24] the quotient of second order coefficients has been analyzed with respect to systems interacting through a Lennard-Jones or an inverse-power law potential. In both studies the value $\gamma_{s2}/\gamma_{c2} = 8/3$ has been found again. The authors have pointed out that the origin of this relation is purely geometrical which explains the observed generality. Moreover, on the basis of this quotient, the author in Ref. [24] proposes, e.g., a so-called surface isotension condition as a tool in order to evaluate the accuracy of different approximations. Within the present model γ_{s2} and γ_{c2} [see Eqs. (3.67) and (3.90)] render

$$\frac{\gamma_{s2}}{\gamma_{c2}} = \frac{8\sqrt{1+x}}{2+x+\sqrt{1+x}}, \tag{3.93}$$

$$x := 4\pi\beta U_0 \varrho^* L^2, \tag{3.94}$$

where for simplicity the excess external potential is not considered, i.e., $V_p = 0$. States which fulfill the stability criterion Eq. (3.15) correspond to positive arguments in the square roots of Eq. (3.93). For $|x| \ll 1$ the exact expression Eq. (3.93) can be expanded which leads to

$$\frac{\gamma_{s2}}{\gamma_{c2}} = \frac{8}{3} - \frac{2}{9}x^2 + O\left(x^3\right), \tag{3.95}$$

that is, the meanwhile well-known ratio in zeroth order. Note that for the convenient choice $\varrho^* = \varrho^{\mathrm{b}}$ Eq. (3.95) corresponds to an expansion in the bulk number density. In Eq. (3.95) there is no term of linear order present and the coefficient of the term quadratic in x is comparatively small. Therefore the constant value 8/3 can be expected to be a
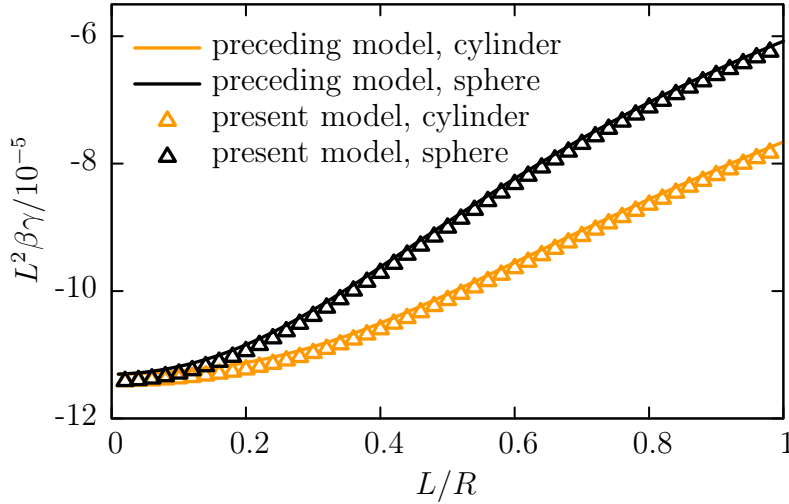
Figure 3.2: Reduced interfacial tension $L^2\beta\gamma$ for a fluid in contact with a cylindrical (orange plots) and with a spherical wall (black plots) in dependence of the dimensionless wall curvature L/R. The results of two models are compared with each other. Data labelled with *preceding model* refers to the approach in Chap. 2 and Ref. [22] in combination with the Yukawa-like interaction potential Eq. (2.5), $\beta\mu = -3.94$, $\beta U_0 = 0.1$, $L_c/L = 10$, and with $\beta V_p = 0$. Data labelled with *present model* refers to Eqs. (3.58) and (3.78) with $\eta \approx 0.01$, $\beta U_0/L = 0.1$, and with $\beta V_p = 0$. In the posed limit of small packing fraction, weak particle-particle interaction, and large cutoff parameter the two approaches exhibit a good agreement throughout the shown interval.

good estimate for the ratio γ_{s2}/γ_{c2} in the case of small $|x|$.

3.3.5   Illustration

The present approach enables to derive exact expressions for the observables of interest, i.e., the interfacial tension for fluids in contact with walls of different geometries [Eqs. (3.47), (3.58), and (3.78)] as well as the coefficients of the corresponding (truncated) curvature expansions [Eqs. (3.65) and (3.88)]. However, the expressions in question turn out to be rather complicated such that the further analysis is supported by plots. For that purpose lengths and energies are measured in units of the characteristic length scale L of the particle-particle interaction [see Eq. (3.1)] and the thermal energy $1/\beta$, respectively. The reference density is chosen to equal the bulk equilibrium density $\varrho^* = \varrho^{\mathrm{b}}$ which sets the value of the coefficient c [see Eq. (3.7)]. Furthermore some kind of packing fraction

$$\eta := \frac{\pi}{6}\varrho^{\mathrm{b}}L^3 \tag{3.96}$$

is introduced which might be a more intuitive quantity than the bulk density ϱ^{b}.

   In Fig. 3.2 the outcome of the present approach of a Yukawa fluid [Eq. (3.1)] is com-
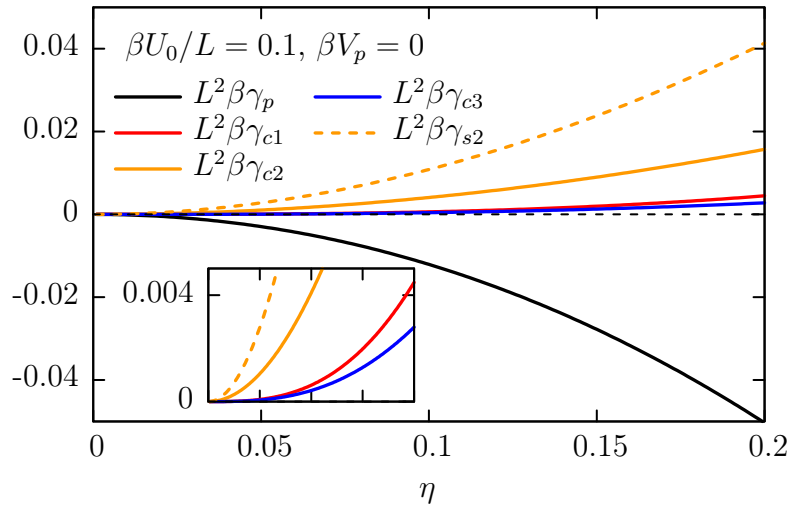
Figure 3.3: Reduced coefficients of the curvature expansions Eqs. (3.65) and (3.88) in dependence of the packing fraction η [Eq. (3.96)]. Every curve corresponds to the fixed values of $\beta U_0/L = 0.1$ and $\beta V_p = 0$. The coefficient γ_{s1} is not shown explicitly because the same essential information is already contained in γ_{c1} [see Eq. (3.89)]. The inset provides a zoomed in view with respect to the vertical axis in order to facilitate a distinction between the coefficients γ_{c1} and γ_{c3}. Note that morphometric thermodynamics would predict the coefficients γ_{c2} and γ_{c3} to be exactly zero.

pared with the results of the model with cut-off Yukawa-interaction Eq. (2.5) of the preceding Chap. 2 (see also Ref. [22]). The interfacial tension is plotted as a function of the wall curvature and the values of the fixed parameters correspond to a Yukawa(-like) fluid of small packing fraction with weak particle-particle interactions in the case of the present (preceding) approach. Within this limit the two approaches exhibit a good agreement throughout the shown interval. On one hand this finding may serve as a crosscheck for the solution processes of both models. On the other hand this finding implies that the present model is capable to reproduce results derived from the more sophisticated preceding approach, i.e., the simplified model leads to reasonable results. Compared with numerical solutions the exact expressions for the coefficients of the curvature expansions have the advantage that they do not suffer from inaccuracies during fitting procedures. Moreover, instead of being dependent on examining the coefficients on a sample basis due to computation time limitations, the dependence of the coefficients on various parameters can be scanned rapidly.

It is already known that MT in general is not an exact approach. However, it is still possible, that a truncation of the exact curvature expansion in line with MT leads to a good approximation. For *spherical* walls this is the case because the difference between the MT expression and the exact one is exponentially small [see Eq. (3.65)]. The question arises whether MT possibly works in a similar fashion also in the case of a *cylindrical*
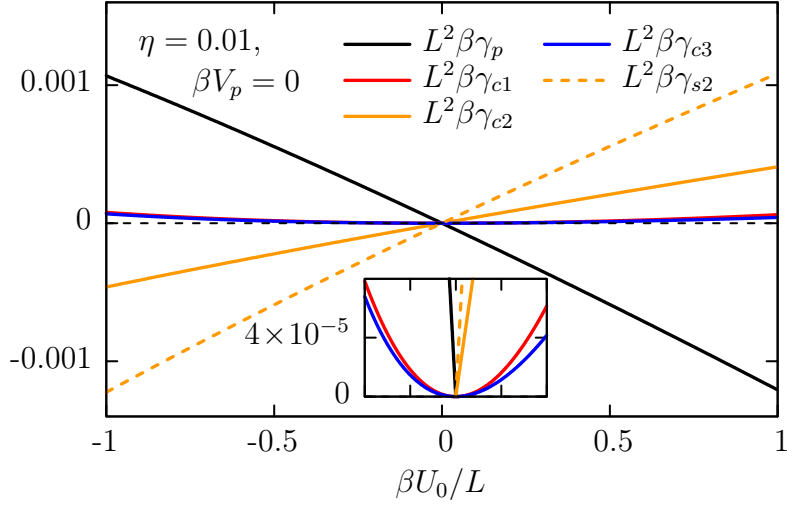
Figure 3.4: The same as Fig. 3.3 in dependence of the reduced strength $\beta U_0/L$ of the particle-particle interaction potential Eq. (3.1) and for the fixed parameters $\eta = 0.01$ and $\beta V_p = 0$.

wall. Therefore the remaining discussion focuses on the cylindrical geometry where the MT expression differs algebraically from the exact expression [see Eq. (3.88)], i.e., the precision of the MT approach can be expected to be of a poorer quality than in the case of the spherical wall. In order that a truncation of the exact curvature expansion in line with MT is a good approximation, the neglected coefficients should at least be smaller than the ones which are in accordance with MT, i.e., for the cylindrical geometry there should be $|\gamma_p|, |\gamma_{c1}| > |\gamma_{c2}|, |\gamma_{c3}|, \ldots$. Note that this criterion for a good approximation is an arbitrary choice which is introduced here as a basis for the subsequent discussion. For certain applications other criteria may be more appropriate and may lead to other conclusions. Furthermore note that in the preceding discussion (see Chap. 2 and Ref. [22]) it is revealed that the choice of the interface convention influences the values of the coefficients. Within the present chapter the expressions are given in the convention $\delta = 0$.

In Figs. 3.3 and 3.4 the coefficients are plotted in dependence of the bulk quantities η and $\beta U_0/L$, respectively. In both figures the excess external potential is exactly zero, i.e., the interaction between the wall and the fluid particles is purely hard. For many parameter choices the planar coefficient γ_p is the dominant one in both cases. However, the absolute value of the first order coefficient is smaller than the one of the second order coefficient $|\gamma_{c1}| < |\gamma_{c2}|$. For the parameter choices shown the quality of MT as an approximation is questionable because truncation in line with MT would demand to consider coefficients only up to $|\gamma_{c1}|$ and to neglect, e.g., the *larger* $|\gamma_{c2}|$.

Figures 3.5 and 3.6 show the curvature coefficients as functions of parameters which specify the strength βV_p and range L_w/L of the excess external potential. For many
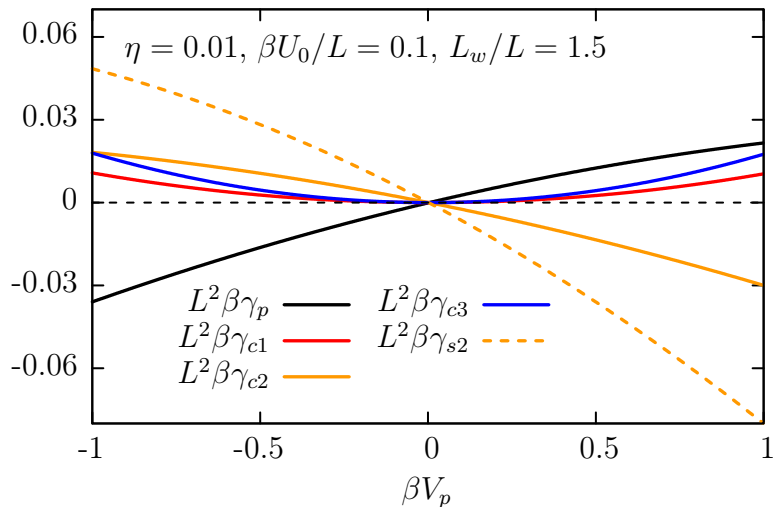
Figure 3.5: The same as Fig. 3.3 in dependence of the reduced strength βV_p [Eq. (3.37)] of the particle-wall interaction potential and for the fixed parameters $\eta = 0.01$, $\beta U_0/L = 0.1$, and $L_w/L = 1.5$.

parameter choices again $|\gamma_{c1}| < |\gamma_{c2}|$. Other relations, however, differ considerably from the behaviors observed so far. In the former Figs. 3.3 and 3.4 the third order coefficient γ_{c3} plays a minor role, i.e., its absolute value is the smallest of the coefficients shown. That is, in the former cases this parameter is not violating the criterion for a good approximation. In Figs. 3.5 and 3.6 its absolute value increases rapidly with growing $|\beta V_p|$ and L_w/L. For large values of $|\beta V_p|$ its value is larger than that of the first order coefficient $|\gamma_{c3}| > |\gamma_{c1}|$ (see Fig. 3.5). In Fig. 3.6, for large L_w/L, the absolute values of both the second and third order coefficients exceed the absolute values of zeroth and first order coefficients $|\gamma_{c2}|, |\gamma_{c3}| > |\gamma_p|, |\gamma_{c1}|$. Within the analytically quoted coefficients this is the exact opposite of the aforementioned criterion for a good approximation. This observation manifests that an excess external potential further deteriorates the applicability of MT as an approximation.

The evaluation of the analytically quoted coefficients in Figs. 3.3 – 3.6 renders that the criterion for a good approximation is violated for many parameter choices. Hence, by truncation of the exact curvature expansion for the cylindrical geometry according to the morphometric approach, terms of significant magnitude are neglected, in contrast to the spherical geometry.

3.4   Summary

The interface between a convex wall of planar, spherical, or cylindrical shape and a Yukawa fluid has been analyzed. To that end the fluid has been described within density functional
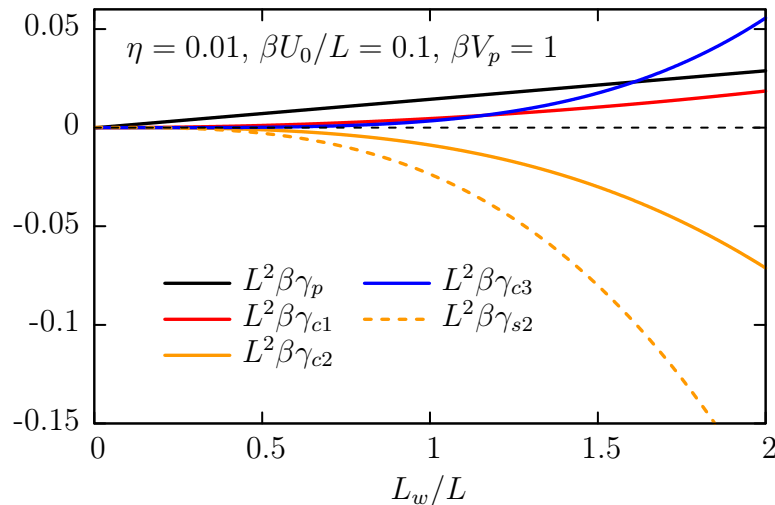
Figure 3.6: The same as Fig. 3.3 in dependence of the reduced decay length L_w/L of the particle-wall interaction potential [see Eq. (3.21)] and for the fixed parameters $\eta = 0.01$, $\beta U_0/L = 0.1$, and $\beta V_p = 1$.

theory by the functional in Eq. (3.9) which is a modified version of the functional Eq. (2.7) used in the preceding Chap. 2 (see also Ref. [22]). In order to analyze the dependence of the wall-fluid interface on the radius R of the wall, the interfacial tension [Eqs. (3.34) and (3.35)] has been chosen as an observable. The applied simplifications, which lead from the preceding model to the present one, enable one to obtain exact expressions for the interfacial tension at the planar [γ_p, Eq. (3.47)], spherical [γ_s, Eq. (3.58)], and at the cylindrical [γ_c, Eq. (3.78)] wall. In spite of the modifications, the results of the present model agree well with the ones corresponding to the preceding model (see Fig. 3.2). In contrast to the preceding approach the coefficients of the curvature expansions are available analytically for both cases, the spherical wall [with the expansion in Eq. (3.65) and corresponding coefficients γ_{s1} and γ_{s2} in Eqs. (3.66) and (3.67)] and the cylindrical wall [with the expansion in Eq. (3.88) and corresponding coefficients $\gamma_{c1} - \gamma_{c3}$ in Eqs. (3.89) – (3.91)]. With that it is possible to actually *prove*, that for the model under consideration the approach of morphometric thermodynamics (MT), stating that the dependence of the interfacial tension on the curvature is given exactly by a quadratic (linear) polynomial in the curvature in the case of a spherical (cylindrical) wall, is not complete. Therefore the morphometric approach has the status of an approximation. The quality of MT as an approximation has been discussed within the convention $\delta = 0$ [see Fig. 2.1 and Eq. (2.16) in the preceding chapter]. For the cylindrical geometry the arbitrary criterion for a good approximation $|\gamma_p|, |\gamma_{c1}| > |\gamma_{c2}|, |\gamma_{c3}|, \ldots$ has been introduced in order to judge the values of the coefficients relative to each other. With the aid of plots the dependence of the coefficients on various system parameters has been examined. In most cases the

criterion has turned out to be not fulfilled mainly because $|\gamma_{c2}| > |\gamma_{c1}|$. This can be observed, e.g., in Figs. 3.3 and 3.4, where the bulk parameters packing fraction and strength of the fluid-fluid interaction potential are varied. An additional excess external potential, parameterized by its strength and range in Figs. 3.5 and 3.6, further deteriorates the applicability of MT because there the criterion is as well violated with respect to γ_{c3}. The results for the two types of curved geometries reveal qualitative differences. In the case of *cylindrical* walls the morphometric approach proposes to truncate the curvature expansion such that terms of significant magnitude may be neglected. However, for *spherical* geometries the MT expression equals the exact one up to exponentially small terms and, thus, it corresponds to an approximation of comparatively high quality. Relations between curvature coefficients of different geometries [Eqs. (3.92) and (3.95)] agree well with those found in literature as well as in Chap. 2 and Ref. [22].

3.A   Determination of the bulk correlation length ξ

The bulk correlation length ξ provides information about the range over which fluctuations in the density are correlated [49]. Its value can be determined from the asymptotic decay of the density-density correlation function $\bar{G}$ evaluated in the bulk. $\bar{G}$ is a measure for the correlation of deviations of the number density from its equilibrium value ϱ_{eq} between two positions $\boldsymbol{r}$ and $\boldsymbol{r}'$. It is defined by the configuration average [58]

$$
\begin{aligned}
\bar{G}(\boldsymbol{r}, \boldsymbol{r}') &:= \langle [\tilde{\varrho}(\boldsymbol{r}) - \varrho_{\mathrm{eq}}(\boldsymbol{r})][\tilde{\varrho}(\boldsymbol{r}') - \varrho_{\mathrm{eq}}(\boldsymbol{r}')] \rangle \\
&= \varrho^{(2)}(\boldsymbol{r}, \boldsymbol{r}') + \varrho_{\mathrm{eq}}(\boldsymbol{r})\delta(\boldsymbol{r} - \boldsymbol{r}') - \varrho_{\mathrm{eq}}(\boldsymbol{r})\varrho_{\mathrm{eq}}(\boldsymbol{r}'),
\end{aligned}
\tag{3.97}
$$

with the density operator $\tilde{\varrho}$, the average of which renders the equilibrium number density $\langle \tilde{\varrho} \rangle = \varrho_{\mathrm{eq}}$, and the pairwise distribution function $\varrho^{(2)}$ (see below). In a uniform fluid, i.e., in the bulk, with equilibrium number density ϱ^{b} Eq. (3.97) simplifies to

$$
G(\boldsymbol{r} - \boldsymbol{r}') := \bar{G}(\boldsymbol{r}, \boldsymbol{r}')|_{\mathrm{bulk}} = \left(\varrho^{\mathrm{b}}\right)^2 g(|\boldsymbol{r} - \boldsymbol{r}'|) + \varrho^{\mathrm{b}}\delta(\boldsymbol{r} - \boldsymbol{r}') - \left(\varrho^{\mathrm{b}}\right)^2,
\tag{3.98}
$$

where use has been made of the relation $\varrho^{(2)}(\boldsymbol{r}, \boldsymbol{r}') = \left(\varrho^{\mathrm{b}}\right)^2 g(|\boldsymbol{r} - \boldsymbol{r}'|)$ between the pairwise distribution function $\varrho^{(2)}$ and the radial distribution function g [58]. In the following G denotes the *bulk* density-density correlation function. By means of the Fourier transform

$$
\hat{f}(\boldsymbol{q}) := \int\limits_{\mathbb{R}^3} \mathrm{d}^3 r\, f(\boldsymbol{r}) \exp(-\mathrm{i}\boldsymbol{q} \cdot \boldsymbol{r})
\tag{3.99}
$$

and the pair correlation function $h(r) := g(r) - 1$ Eq. (3.98) can be written in Fourier space as

$$\hat{G}(q) = \left(\varrho^{\mathrm{b}}\right)^2 \hat{h}(q) + \varrho^{\mathrm{b}}. \tag{3.100}$$

Next a relation between this quantity and density functional theory is obtained with help of the generic density functional $\beta\Omega[\varrho]$ in Eq. (2.30). Its second functional derivative with respect to number density and evaluated in the bulk reads

$$\left.\frac{\delta^2(\beta\Omega)}{\delta\varrho(\boldsymbol{r})\delta\varrho(\boldsymbol{r'})}\right|_{\varrho^{\mathrm{b}}} = \frac{\delta(\boldsymbol{r} - \boldsymbol{r'})}{\varrho^{\mathrm{b}}} - c^{(2)}(|\boldsymbol{r} - \boldsymbol{r'}|) =: K(\boldsymbol{r} - \boldsymbol{r'}), \tag{3.101}$$

where the bulk Ornstein-Zernike direct correlation function

$$c^{(2)}(|\boldsymbol{r} - \boldsymbol{r'}|) := -\left.\frac{\delta^2(\beta\mathcal{F}^{\mathrm{ex}})}{\delta\varrho(\boldsymbol{r})\delta\varrho(\boldsymbol{r'})}\right|_{\varrho^{\mathrm{b}}} \tag{3.102}$$

has been introduced [58]. The Fourier transform of Eq. (3.101) is given by

$$\hat{K}(q) = \frac{1}{\varrho^{\mathrm{b}}} - \hat{c}^{(2)}(q). \tag{3.103}$$

The product of $\hat{K}(q)$ and $\hat{G}(q)$ reduces to

$$\hat{K}(q)\hat{G}(q) = 1 + \varrho^{\mathrm{b}}\left[\hat{h}(q) - \hat{c}^{(2)}(q)\varrho^{\mathrm{b}}\hat{h}(q) - \hat{c}^{(2)}(q)\right] = 1 \tag{3.104}$$

$$\Leftrightarrow \hat{G}^{-1}(q) = \hat{K}(q), \tag{3.105}$$

where the term in brackets of Eq. (3.104) vanishes due to the Ornstein-Zernike equation for translationally invariant and isotropic systems in Fourier space [49],

$$\hat{h}(q) = \hat{c}^{(2)}(q) + \varrho^{\mathrm{b}}\hat{c}^{(2)}(q)\hat{h}(q). \tag{3.106}$$

Equation (3.105) states that, in Fourier space, the inverse of $\hat{G}$ is given by the second derivative of the density functional $\hat{K}$ [Eq. (3.101)]. The equivalent of Eq. (3.105) in real space is used in order to determine G^{-1} from the density functional of the present model Eq. (3.9) as

$$G^{-1}(\boldsymbol{r} - \boldsymbol{r'}) = \left.\frac{\delta^2(\beta\Omega)}{\delta\varrho(\boldsymbol{r})\delta\varrho(\boldsymbol{r'})}\right|_{\mathrm{bulk}} = \beta c\,\delta(\boldsymbol{r} - \boldsymbol{r'}) + \beta U(|\boldsymbol{r} - \boldsymbol{r'}|). \tag{3.107}$$

In Fourier space

$$\hat{G}^{-1}(q) = \frac{1}{\hat{G}(q)} = \frac{\beta c[1 + (qL)^2] + \beta\hat{U}(0)}{1 + (qL)^2}, \tag{3.108}$$

can be inverted and the Fourier transform of G reads

$$\hat{G}(q) = -\frac{\hat{U}(0)}{\beta c^2 L^2} \frac{1}{\frac{1}{L^2}\left[1 + \frac{\hat{U}(0)}{c}\right] + q^2} + \frac{1}{\beta c}. \tag{3.109}$$

The inverse Fourier transform

$$G(r) := \frac{1}{4\pi^2 i r} \int\limits_{-\infty}^{\infty} dq\, q\, \hat{G}(q) \exp(iqr), \tag{3.110}$$

gives the expression of $G(r)$ and the respective integration can be treated with the residue theorem. The asymptotic exponential decay of $G(r)$ is determined by the poles of $\hat{G}(q)$ and the longest decay length corresponds to the pole $q' + iq'' \in \mathbb{C}$ with smallest imaginary part. For our purpose it is not necessary to execute the integration in Eq. (3.110) because the value of the bulk correlation length can be read from the root of the denominator of the first term in Eq. (3.109) as

$$\xi = \frac{1}{|q''|} = \left\{\frac{1}{L^2}\left[1 + \frac{\hat{U}(0)}{c}\right]\right\}^{-1/2} = \left(\frac{1}{L^2} + \frac{4\pi U_0}{c}\right)^{-1/2}. \tag{3.111}$$

This result enables to identify the bulk correlation length ξ in the differential equation Eq. (3.25).

Chapter 4

Electrolyte solutions at curved electrodes. I. Mesoscopic approach

In Ref. [8] the idea of morphometric thermodynamics (MT) has been introduced in conjunction with the restriction, that the approach cannot be applied to systems with large intrinsic lengths, which comprises, e.g., critical phenomena or systems with long ranged fluid-fluid or fluid-wall interactions. For that reason, so far in Chaps. 2 and 3, simple flu-
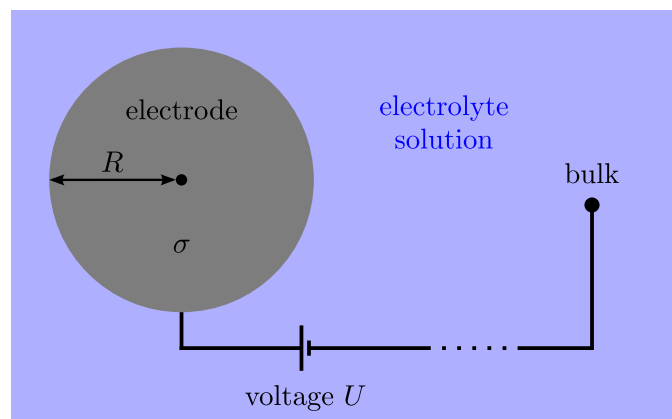
Figure 4.1: Idealized sketch of an experimental setup corresponding to the theoretical models which are discussed in Chaps. 4 and 5. An electrode (gray circle) of planar, spherical, or cylindrical shape is immersed in an electrolyte solution (blue background). The present sketch depicts a curved electrode, i.e., a sphere or cylinder of radius R. The electrode surface may be homogeneously charged with surface charge density σ by applying a voltage U between the electrode and the bulk far away from the electrode surface. Note that the voltage U is defined as the potential difference between two equipotential surfaces: one is equivalent to the electrode surface and the other one consists of points in the bulk which are at equal distance from the electrode surface. In the following, in particular the electrolyte solution is considered by various models. Figures 4.2 and 5.1 give a visual impression of the different levels of complexity of the latter.

ids with interaction potentials of limited or short range around curved walls have been in focus in order to check the morphometric approach within its original range of definition. It has turned out that MT is never exactly valid. However, depending on the convention for the interface, the morphometric expression for the interfacial tension can be a good approximation.

These former insights have given rise to systematically analyze also more complex fluids in contact with curved solid walls: electrolyte or ionic solutions at curved electrodes. In the following these systems are considered, because, on one hand, they are common in nature. Even pure water, for instance, is an ionic solution, because of the self-ionization of water. On the other hand, supercapacitors consisting of electrodes in contact with electrolyte solutions are of current interest in technological applications (see the references in Sec. 4.1) and findings with respect to the geometry dependence of the capacitance might be helpful for the development of energy storage systems. Last but not least electrolyte solutions are attractive from a scientific point of view. On one hand, they are more complex than the simple fluids under former consideration. For instance they consist of more than one particle species carrying different electrical charges which interact in distinct ways with each other and with the charged electrode; this makes their description comparatively difficult. On the other hand, these systems are endowed with more options to act upon them, both in theoretical models and in experimental setups. For example, the Debye length, which is an intrinsic length scale, can be tuned by means of the ionic strength. Furthermore the strength of the wall potential is set by the surface charge density of the electrode. It can be expected that these quantities, among others, have an effect on the structure of the electric double layer (EDL) whose dependence on the wall geometry is the focus of the following discussion. To that end the differential capacitance C, which is a measurable quantity, is chosen as an observable. Its definition does not underlie an interface convention as the interfacial tension, which is convenient, inter alia, for statements with respect to the validity of MT. Figure 4.1 depicts an idealized experimental setup corresponding to systems which are approached theoretically in the following. In an experiment one would set the surface charge density σ by applying a voltage between the electrode and, in the depicted case, the bulk. The differential capacitance is defined as the derivative of σ with respect to the voltage or the electrode potential. That is, the change of the surface charge density in response to a change of the electrode potential has to be known. In the following the underlying relation between σ and the electrode potential is determined theoretically by distinct approaches: a mesoscopic one in Chap. 4 and a microscopic one in Chap. 5. The analysis based on the differential capacitance, which contains integrated properties of the structure of the EDL, enables to investigate the influence of the electrode geometry on the EDL in dependence of, e.g., the surface charge density, the ionic strength, and other (microscopic) parameters which are introduced in the following. Furthermore the outcome of various models, some

of which are illustrated in Figs. 4.2 and 5.1, can be compared with each other.

Up to occasional modifications and add-ons the present Chap. 4 is equivalent to the study published in Ref. [94]. Therein the Poisson-Boltzmann (PB) approach is used in order to analyze systematically electrolytes in contact with planar, spherical, and cylindrical electrodes. The dependences of their capacitance C on the surface charge density σ and the ionic strength I are examined as a function of the wall curvature. The surface charge density has a strong effect on the capacitance for small curvatures, whereas for large curvatures the behavior becomes independent of σ. An expansion for small curvatures gives rise to capacitance coefficients which depend only on a single parameter, allowing for a convenient analysis. The universal behavior at large curvatures can be captured by an analytic expression.

4.1 Introduction

An electrical double layer capacitor or supercapacitor basically consists of electrodes which are insulated by a separator and which are in contact with an electrolyte. Supercapacitors are used as alternative electrical energy storage devices and combine the properties of conventional batteries, with high energy but low power densities, and conventional capacitors with the opposite characteristics [95]. They are used in electric vehicles and mobile phone equipments. Moreover, in search of sustainable energy systems there is still growing interest in double layer capacitors. The capacitive behavior is determined by the nature of the electrode material, e.g., its porosity and accessible surface area. Often carbon is the electrode material of choice and especially ordered carbon allotropes have received much attention because their micro-texture influences the electronic properties. Different kinds of carbon nanostructured materials, including carbon nanotubes, carbon nanorods, spherical fullerenes, and carbon nano-onions, have been used as electrodes [95,96]. Fiber-shaped supercapacitors exhibit low weight and high flexibility and thus are promising candidates for power sources in wearable electronics [97]. In contrast to conventional capacitors with smooth electrode morphologies, supercapacitors exhibit highly curved surfaces in order to obtain large specific areas, i.e., high porosity. This poses the problem of understanding the properties of electric double layers at curved geometries. A suitable method to model an electric double layer is given by the Poisson-Boltzmann (PB) theory. Within this mesoscopic approach the focus is on length scales larger than the ions or solvent molecules because electrolyte solutions are taken to consist of pointlike ions dissolved in a homogeneous solvent which is described by its electric permittivity only. The PB theory has been pioneered by Gouy [32] and Chapman [33] in the 1910s and sometimes it is referred to as the Gouy-Chapman theory. Although the model is simple, reliable predictions can be expected to hold for low ionic strengths (below $0.2\,\mathrm{M} = 0.2\,\mathrm{mol}/\ell$) and low electrode potentials (below $80\,\mathrm{mV}$), in the case of aqueous solutions and monovalent

salts [2]. For that reason and due to its simplicity the PB theory is used frequently. Under certain circumstances it even allows for exact solutions, e.g., for electrolyte solutions at planar electrodes [2, 34]. Recently, exact results have been presented for an electrolyte bounded by parallel plates or inside a cylindrical charged wall if only counterions are considered [98]. This setup might be used as a description for ions confined in a charged nanotube or pore. However, for the corresponding spherical system, so far a solution in closed form has not been found. In Ref. [99] the same authors presented an expansion for the solution of the PB equation in spherical and cylindrical geometries with large radii of curvature, which might resemble charged macromolecules surrounded by an electrolyte solution and which comes closest to an analytic solution of the full PB equation for these geometries. Within the framework of the linearized Gouy-Chapman-Stern theory in Ref. [100] a model for an arbitrary surface morphology was developed. This facilitates, for example, the calculation of capacitances of nanostructured electrodes, the study of which might contribute to the development of efficient energy generating and storage devices. But also for numerical studies the PB equation often is the model of choice because its simplicity allows for fast calculations: In order to understand the properties of the diffuse double layer at charged nanoelectrodes or carbon nanotubes the PB equation was solved in Refs. [101, 102] for spherical and cylindrical electrodes. The potential and capacitance were analyzed for various values of the electrode radius. The evolution of capacitance models for supercapacitors gave rise to the study in Ref. [103] in which cylindrical and slit pores were considered within the Gouy-Chapman-Stern model to address, inter alia, the issue of how the pore shape affects the capacitance.

However, so far the dependence of the capacitance on the geometry has only been addressed on a sample basis, i.e., for particular choices of system parameters. The intention of the present work is to study the curvature dependence of the capacitance systematically within the entire, relevant parameter space.

In the present study the PB equation is solved for electrolytes surrounding spherical and cylindrical electrodes (see Sec. 4.2). In addition to presenting results for a variety of parameter choices, a thorough overview of the spectrum of solutions is given. To that end the dependence of the differential capacitance on the various parameters is analyzed in detail within the PB theory for these geometries. The limiting behavior is discussed systematically, i.e., the dependence on only one parameter or analytically. This facilitates the understanding of the essential behavior of the data of interest which in the present case is the differential capacitance as a function of the wall curvature. In Sec. 4.3.1 a short overview of the exact results within the linearized theory is given before in Sec. 4.3.2 the full PB equation for various choices of the parameters is solved. In the subsequent Secs. 4.3.3 and 4.3.4 general trends for large and small radii of the electrodes are worked out. Corresponding technical details are discussed in Appendices 4.A and 4.B. Summary and outlook are given in Sec. 4.4.

4.2 Model

Consider an electrolyte composed of pointlike, monovalent ions, i.e., particles without volume carrying positive or negative elementary charge $\pm e$. Due to local charge neutrality the number densities of both ion species in the bulk are equal to the ionic strength I. The solvent is regarded as a dielectric continuum with homogeneous relative permittivity ϵ. The electrostatic potential Φ in this system obeys the Poisson-Boltzmann (PB) equation [2, 34]

$$\Delta\Phi(\boldsymbol{r}) = \frac{2eI}{\epsilon_0\epsilon}\sinh[\beta e\Phi(\boldsymbol{r})], \tag{4.1}$$

where Δ is the Laplace operator, $\boldsymbol{r} \in \mathbb{R}^3$ denotes a position in three-dimensional space, ϵ_0 is the vacuum permittivity, $\beta = (k_BT)^{-1}$ with the Boltzmann constant k_B and the absolute temperature T. The electrolyte is assumed to be in contact with a convex electrode of planar, spherical, or cylindrical shape. The electrode is described as a homogeneously charged hard wall with surface charge density σ. Under these assumptions the potential Φ in Eq. (4.1) depends on a single spatial variable $\Phi(r) := \Phi(\boldsymbol{r}) = \Phi(x, y, z)$ where the meaning of r depends on the geometry:

- A planar wall occupies the half space $z < 0$ which leads to a dependence of Φ on $r := z$,

- a spherical wall $x^2 + y^2 + z^2 < R^2$ of radius R gives rise to a dependence of the potential on $r := \sqrt{x^2 + y^2 + z^2}$, and for a

- cylindrical wall $x^2 + y^2 < R^2$ of radius R the potential depends on $r := \sqrt{x^2 + y^2}$.

The sketch in Fig. 4.2 illustrates the model under consideration. By introducing the parameter d in order to distinguish the three geometries the PB equation (4.1) may be formulated in a one-dimensional fashion:

$$\frac{1}{r^d}\frac{\partial}{\partial r}\left[r^d\frac{\partial\Phi(r)}{\partial r}\right] = \frac{2eI}{\epsilon_0\epsilon}\sinh[\beta e\Phi(r)],$$
$$d = \begin{cases} 0, & \text{planar wall,} \\ 1, & \text{cylindrical wall,} \\ 2, & \text{spherical wall.} \end{cases} \tag{4.2}$$
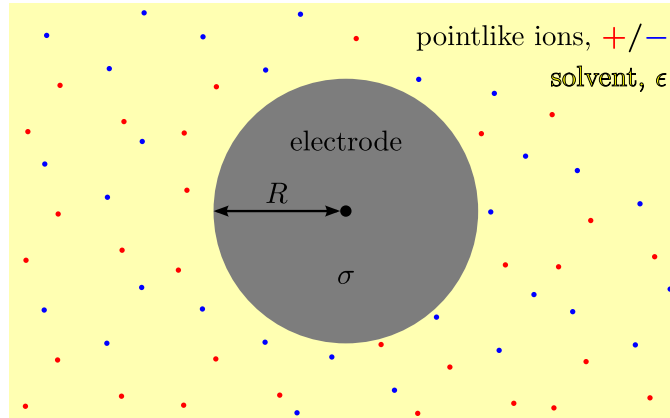
Figure 4.2: Sketch of the model system under consideration (see Sec. 4.2). The depicted case corresponds to a spherical or cylindrical electrode of radius R. The electrode, i.e., a homogeneously charged hard wall with surface charge density σ, is surrounded by an electrolyte solution which consists of pointlike, monovalent ions (red and blue dots) dissolved in a solvent with relative permittivity ϵ. Within the present model the solvent is taken into account as a structureless continuum which is represented by the yellowish background. The distribution of the ions depends, inter alia, on the geometry and the surface charge density of the electrode and gives rise to the electrostatic potential Φ which is determined by the Poisson-Boltzmann equation (4.1).

Solutions of Eq. (4.2) are subject to boundary conditions at the wall surface r_w and in the bulk $r \to \infty$:

$$\Phi'(r)\Big|_{r=r_w} = -\frac{\sigma}{\epsilon_0 \epsilon}, \quad r_w = \begin{cases} 0, & d = 0, \\ R, & d \in \{1,2\}, \end{cases} \tag{4.3}$$

$$\Phi'(r)\Big|_{r=\infty} = 0.$$

For the considered geometries the electric field exhibits only a component $E(r) = -\Phi'(r)$ in direction normal to the wall surface. The value of the component at the surface r_w is linked to the surface charge density σ by the first boundary condition. The second boundary condition ensures global charge neutrality. In the following we additionally demand $\Phi(\infty) = 0$ so that the lower boundary condition is fulfilled and the arbitrary integration constant of Φ is set.

For small values of the dimensionless potential $\beta e \Phi(r) \to 0$ it is sufficient to consider the expansion of the hyperbolic sine in the PB equation (4.2) only up to linear order in order to obtain the linearized PB equation

$$\frac{1}{r^d} \frac{\partial}{\partial r} \left[r^d \frac{\partial \Phi(r)}{\partial r} \right] = \kappa^2 \Phi(r), \quad \kappa := \sqrt{\frac{2e^2 I \beta}{\epsilon_0 \epsilon}}, \tag{4.4}$$

with the inverse Debye length κ.

4.3 Discussion

The differential capacitance is defined by [34]

$$C := \frac{\partial \sigma}{\partial \Phi(r_w)} \tag{4.5}$$

as the change of the surface charge density σ upon changing the potential at the wall $\Phi(r_w)$. Here the theoretical results are presented in terms of this measurable quantity in order to facilitate comparison with experiments. The examinations focus on the dependence of the capacitance C on the curvature $1/R$ of a spherical and a cylindrical wall.

4.3.1 Linearized PB equation

The linearized PB equation (4.4) can be solved analytically for the geometries under consideration:

- At a planar wall the potential at the electrode is

$$\Phi(0) = \frac{\sigma}{\epsilon_0 \epsilon \kappa}, \tag{4.6}$$

  and the capacitance is given by the double-layer capacitance $\epsilon_0 \epsilon \kappa$ [34]

$$\frac{C}{\epsilon_0 \epsilon \kappa} = 1. \tag{4.7}$$

  This quantity will be used as a reference in order to define dimensionless capacitances.

- For a spherical wall one has

$$\Phi(R) = \frac{\sigma}{\epsilon_0 \epsilon \kappa} \frac{\kappa R}{\kappa R + 1}, \tag{4.8}$$

  and

$$\frac{C}{\epsilon_0 \epsilon \kappa} = 1 + \frac{1}{\kappa R}, \tag{4.9}$$

  a polynomial of linear order in the dimensionless curvature $(\kappa R)^{-1}$.

- In the case of a cylindrical wall the electrode potential

$$\Phi(R) = \frac{\sigma}{\epsilon_0 \epsilon \kappa} \frac{K_0(\kappa R)}{K_1(\kappa R)}, \tag{4.10}$$

and the capacitance

$$\frac{C}{\epsilon_0 \epsilon \kappa} = \frac{K_1(\kappa R)}{K_0(\kappa R)} = 1 + \frac{1}{2}\frac{1}{\kappa R} - \frac{1}{8}\frac{1}{(\kappa R)^2} + O\left[\frac{1}{(\kappa R)^3}\right] \tag{4.11}$$

are given by a ratio of modified Bessel functions [84]. For large radii $\kappa R \gg 1$ the expression can be represented by an infinite power series in the curvature, the truncated version of which is shown in Eq. (4.11).

Already the linearized PB equation reveals interesting differences for the curvature dependencies of the capacitance. Whereas in the case of the spherical wall the entire curvature dependence is given by a linear polynomial, in the case of the cylindrical wall a transcendental expression is found. The leading curvature correction in the case of the spherical electrode [Eq. (4.9)] is twice of that in the cylindrical case [Eq. (4.11)]. In the following it turns out that this ratio also holds for systems in accordance with the nonlinear PB equation (see Sec. 4.3.3). The analysis based on the linearized PB equation becomes rather complex when arbitrary curved surfaces are considered, which was addressed in Refs. [100, 104, 105]. However, the linear theory is valid only in the limit $\Phi \to 0$ and the capacitances are independent of Φ or σ. Strictly speaking the full PB equation has to be considered as soon as systems with non-vanishing Φ or σ are of interest. This will be the focus in Secs. 4.3.2 – 4.3.4.

4.3.2   Full non-linear PB equation

The solution of the PB equation (4.2) at the planar wall is available in closed form and the capacitance is given by [34]

$$\frac{C}{\epsilon_0 \epsilon \kappa} = \cosh\left[\frac{1}{2}\beta e \Phi(0)\right], \tag{4.12}$$

where the potential at the wall $\Phi(0)$ depends on the surface charge density σ as

$$\Phi(0) = \frac{2}{\beta e}\text{arsinh}\left(\frac{\beta e \sigma}{2\epsilon_0 \epsilon \kappa}\right). \tag{4.13}$$

For spherical and cylindrical geometries the PB equation (4.2) is solved numerically; for this purpose an algorithm in the spirit of the Piccard iteration is used (see Sec. 8.1 in Ref. [61]). If lengths, charges, and energies are measured in units of the Debye length $1/\kappa$, the elementary charge e, and the thermal energy $1/\beta = k_B T$, respectively, the present

model of a monovalent salt solution is specified by the following three dimensionless, independent parameters: I/κ^3, κR, and $\sigma/(e\kappa^2)$. In Figs. 4.3 and 4.4 results for the reduced capacitance are shown for two cases A and B corresponding to the choices $I/\kappa^3 \approx$ 0.05329 and $I/\kappa^3 \approx 0.1685$, respectively. The parameters would, for example, refer to an aqueous electrolyte solution at room temperature $T = 300\,\mathrm{K}$ with relative permittivity $\epsilon = 77.7003$, Debye length $1/\kappa \approx 9.600\,\text{Å}$ [30.36 Å], and ionic strength $I = 0.1\,\mathrm{M}$ [0.01 M] in case A [B]. In Figs. 4.3 and 4.4 the reduced capacitance $C/(\epsilon_0 \epsilon \kappa)$ is plotted as function of the dimensionless wall curvature $1/(\kappa R)$ for various values of the reduced surface charge density $\sigma/(e\kappa^2)$. The value $1/(\kappa R) = 0$ corresponds to the planar wall result in Eq. (4.12). Larger values on the horizontal axes are equivalent to larger curvatures and hence to smaller radii of the wall. Since the PB equation originates from a classic theory the results for large curvatures should be treated with caution. In case A, for example, the Debye length is about $1/\kappa \approx 10\,\text{Å}$. This means that for $1/(\kappa R) > 10$ the wall radius is smaller than the atomic length scale of $1\,\text{Å}$. Within this range the particle size, which is not captured by the PB theory, should play a role. In the case of the spherical wall (Fig. 4.3) the curvature dependence of the capacitance for the smallest chosen value of σ almost coincides with a straight line. This is in accordance with the analytic result in Eq. (4.9) which renders a linear polynomial in $1/(\kappa R)$. For increasing σ the capacitance in the planar limit $1/(\kappa R) = 0$ increases, whereas for large curvatures the curves seem to converge from above to the graph for $\sigma \to 0$. This indicates that the linear theory becomes the more valid the larger the curvature is chosen. In between the limits of high and low curvatures the capacitance exhibits a minimum the position of which shifts with σ. Also the slope of the graph for small curvatures depends on σ. For $\sigma \to 0$ there is a positive slope, whereas larger surface charge densities give rise to a negative slope.

The curvature dependences in Fig. 4.4 of the capacitances for electrolytes in contact with cylindrical walls resemble the ones at spherical walls in Fig. 4.3. The results for cylinders look like the results for spheres stretched in horizontal direction. However, for $\sigma \to 0$ the capacitance at a cylindrical wall clearly deviates from a linear function [see Eq. (4.11)]. The potential $\Phi(R)$ at the cylindrical electrode agrees well with the expression for the surface potential in Ref. [106] [Eqs. (3) and (4) therein] within the specified range of validity, i.e., for not too small curvatures and line charge densities.

The linearized PB equation (4.4) corresponds to the lowest curves in Figs. 4.3 and 4.4. Thus important features, particularly in the range of small curvatures, are neglected, whereas for large curvatures a description based on the linear theory appears to be sufficient. In the solution of the full equation (4.2) the surface charge density affects the capacitance for small curvatures to a large extent whereas for large curvatures the behavior becomes more and more general and independent of σ. This phenomenon will be addressed in Secs. 4.3.3 and 4.3.4.
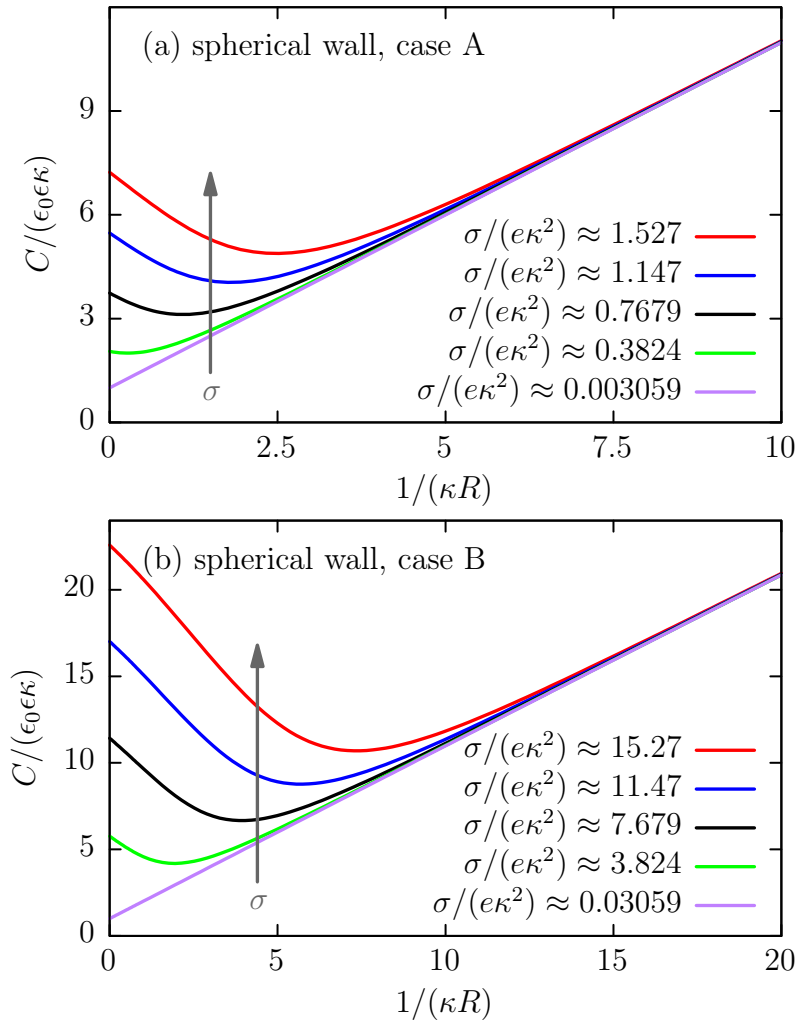
Figure 4.3: Reduced differential capacitance $C/(\epsilon_0\epsilon\kappa)$ as a function of the dimensionless curvature $1/(\kappa R)$ of spherical electrodes. The data are obtained by solving the PB equation (4.2) for two cases (A and B) of the bulk parameter choices (see the main text). Each curve corresponds to a constant value of the reduced surface charge density $\sigma/(e\kappa^2)$. The vertical arrow points in the direction of increasing σ.

4.3.3   Limit of large wall radii

Within this subsection we focus on walls with large radii $\kappa R \gg 1$ or small curvatures $1/(\kappa R) \ll 1$. It has been shown before that in this limit the capacitance as function of the curvature varies strongly with the surface charge density σ (see Figs. 4.3 and 4.4 and the discussion in the previous Sec. 4.3.2). In order to examine this observation in more detail, the capacitance is taken as a power series in terms of small curvatures $(\kappa R)^{-1} \ll 1$:

$$C = \epsilon_0\epsilon\kappa \sum_{n=0}^{\infty} \frac{C_n}{(\kappa R)^n}, \qquad (4.14)$$
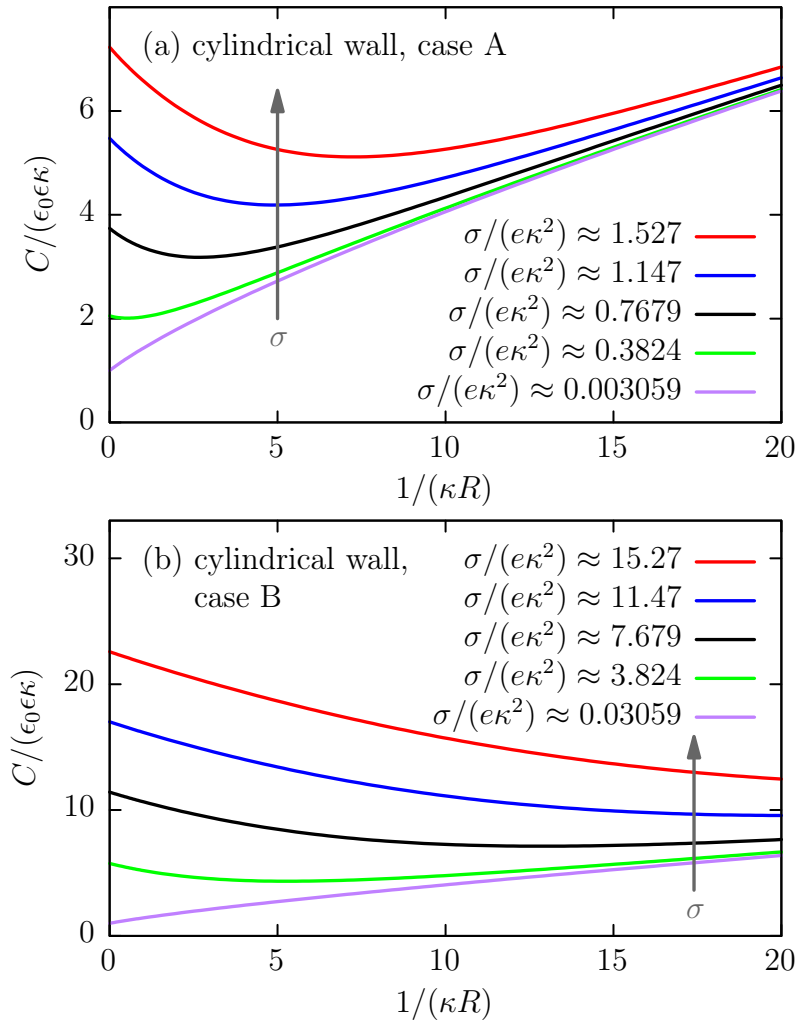
Figure 4.4: Same as Fig. 4.3 for cylindrical electrodes.

where $\epsilon_0\epsilon\kappa C_0$ is the capacitance of a planar wall [Eq. (4.12)]. In Appendix 4.A the calculation of the dimensionless coefficients C_n is explained in detail. In Fig. 4.5 the lowest order coefficients $C_{0,1,2}$ of the curvature expansion in Eq. (4.14) are plotted as function of the dimensionless parameter

$$t := \tanh\left[\frac{1}{2}\mathrm{arsinh}\left(\frac{\beta e\sigma}{2\epsilon_0\epsilon\kappa}\right)\right] \in [-1, 1], \qquad (4.15)$$

which is a combination of T, ϵ, I, and σ such that the sign of t agrees with the sign of σ [see also Eq. (4.28)]. Apart from the geometry captured by d, the coefficients C_n depend only on t. Thus within PB theory every parameter choice can be assigned to Fig. 4.5. Since the solutions $\Phi(r)$ of Eqs. (4.2) and (4.3) are odd functions of σ, the capacitance in Eq. (4.5) and hence the coefficients C_n are even functions of t, i.e., $C_n(t) = C_n(-t)$; it is therefore sufficient to only discuss the range $t \geq 0$. For the planar wall [Fig. 4.5(a)] the
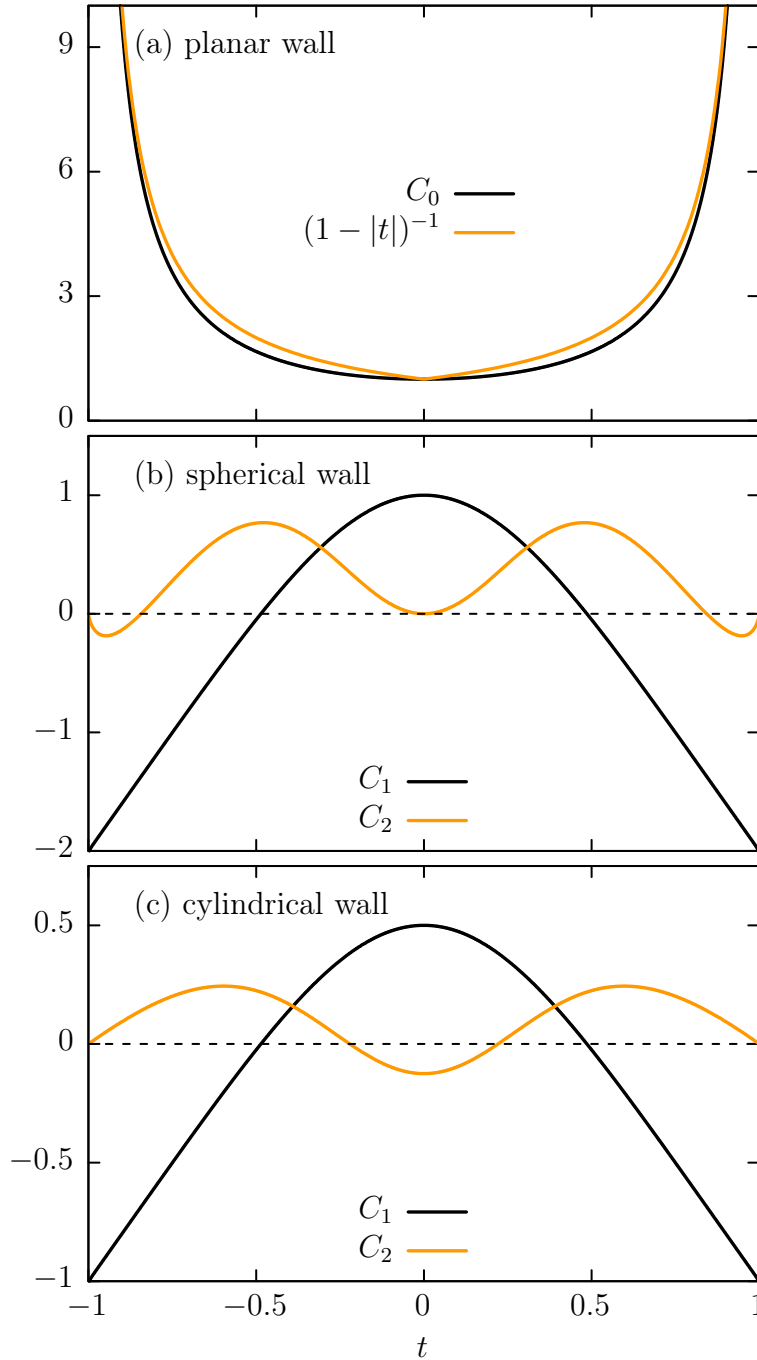
Figure 4.5: Lowest order coefficients $C_{0,1,2}$ of the curvature expansion [Eq. (4.14)] as function of the parameter t defined in Eqs. (4.15) and (4.28). The entire information about the influences of T, ϵ, I, and σ is contained in the dependence on $t \in [-1, 1]$ (see the discussion in Appendix 4.A). For clarity the coefficient C_0, describing the contribution of the planar wall to C [panel (a)], is displayed separately from the coefficients C_1 and C_2 for spherical (b) and cylindrical (c) walls.

formulation in terms of scaled variables is

$$C_0 = \frac{1 + t^2}{1 - t^2} \tag{4.16}$$

which diverges for $\sigma \to \pm\infty \Leftrightarrow t \to \pm 1$ as $(1 - |t|)^{-1}$. The coefficient C_1 [Figs. 4.5(b) and (c)] exhibits the same qualitative behavior for both curved walls: its value in the spherical case is twice of that in the cylindrical case. At $t = 0$, C_1 attains a positive maximum; for $t > 0$ the curve decreases monotonically and crosses the t-axis at $t = 0.4858(3)$. In Figs. 4.3 and 4.4, C_1 corresponds to the slope for small curvatures. Indeed the slope changes from positive to negative with increasing σ, i.e., increasing t. The roots of C_1 in Figs. 4.5(b) and (c) correspond to a special combination of parameters for which the initial slope in Figs. 4.3 and 4.4 would be exactly zero. For C_2 qualitative differences between the curved wall shapes occur. In the case of the spherical wall [Fig. 4.5(b)] C_2 is zero at $t = 0$ which is consistent with Fig. 4.3 showing a straight line for $\sigma \to 0$. Increasing t leads to a somewhat oscillatory behavior of C_2. Positive values of C_2 correspond to a convex function (from below) in Fig. 4.3 for small curvatures and intermediate values of σ whereas negative values of C_2 for $t \to 1$ indicate a concave behavior. The magnitude of negative values of C_2 is relatively small so that the concave behavior is less pronounced. However, the latter is visible in Fig. 4.3(b) for large σ. For the crossover value for t between convex and concave one obtains $t = 0.8428(3)$. In the case of the cylindrical wall [Fig. 4.5(c)] C_2 is negative at $t = 0$ and consequently in Fig. 4.4 the concave behavior for small curvatures and small σ is visible. Upon increasing t the coefficient C_2 changes sign from negative to positive and remains positive for values of t larger than the root at $t = 0.2208(3)$. In Fig. 4.4 the convex behavior can be observed for large σ. This analysis shows that even for very large σ no concave behavior can be expected as in the case of spherical walls. The coefficients [see Eqs. (4.9) and (4.11)] obtained within the linearized theory [Eq. (4.4)] are covered by the present analysis and correspond to the values at $t = 0 \Leftrightarrow \sigma = 0$.

At this stage an excursion to *morphometric thermodynamics* (MT) is appropriate. Within that approach the interfacial tension γ takes a very simple form with respect to the dependence on the geometry of the surrounding walls. For the geometries of the current study the dependences on the radius R can be formulated as [see also Eq. (2.3)]

$$\gamma = \begin{cases} \gamma_0 + \dfrac{\gamma_{s1}}{R} + \dfrac{\gamma_{s2}}{R^2}, & \text{spherical wall,} \\[2ex] \gamma_0 + \dfrac{\gamma_{c1}}{R}, & \text{cylindrical wall.} \end{cases} \tag{4.17}$$

Within MT there are no higher order terms and the coefficients γ_n are independent of the radius R. (For further details see, e.g., Refs. [8, 22] and Chap. 2.) The connection with the present study is given by the Lippmann equation [34]

$$\sigma = -\frac{\partial \gamma}{\partial \Phi(r_w)} \tag{4.18}$$

and hence

$$C = -\frac{\partial^2 \gamma}{\partial \Phi(r_w)^2}. \tag{4.19}$$

Since differentiation of Eq. (4.17) with respect to the electrode potential $\Phi(r_w)$ does not change the form of the equations, MT predicts the same truncated curvature dependence for the capacitance C. However, examinations in terms of the capacitance have the advantage that this quantity is uniquely defined contrary to the interfacial tension. In a previous study [22] (see also Chap. 2) the authors examined the implications of various interface conventions concerning the accuracy of MT in terms of the interfacial tension. They found that the quality of the approach as an approximation depends to a large extent on the interfacial position which in principle may be chosen arbitrarily. Following the prediction of MT in the case of cylindrical walls the coefficient C_2 should be zero. However, in agreement with earlier work on curved interfaces using gradient expansion approaches [80, 81, 107, 108], already the linear theory [Eq. (4.11)] exhibits a nonzero coefficient and the full solution Fig. 4.5(c) reveals that C_2 is nonzero for most choices of the parameters. Therefore MT is not an exact approach, which is not surprising because even for simple fluids its precision has been doubted recently (see, e.g., Refs. [19–22] as well as Chaps. 2 and 3). Therefore, MT has the status of an approximation. For example, when discussing cylindrical walls the necessary restriction $|C_2| \ll |C_1|$ might be adequate to truncate the curvature expansion in accordance with MT which is the case for values of t far away from the root of C_1. It is remarkable that this is the case for $|t| \to 1 \Leftrightarrow |\sigma| \to \infty$, i.e., for highly charged electrodes. In any case this quality criterion depends on t and therefore on the surface charge density. In general the curvature coefficients are properties of the fluid and the wall-fluid interaction [8]. As a consequence, for simple fluids, the coefficients are fixed once a certain wall-fluid system has been chosen. However, in the case of electrode-electrolyte systems, the wall-fluid interaction is typically not fixed but can be adjusted via the surface charge density. For such cases the dependence of the coefficients C_n on σ has to be known. This further complicates and reduces the applicability of MT.

4.3.4   Limit of small wall radii

For spherical walls and large curvatures a somewhat general behavior is observed (see Fig. 4.3): all curves shown approach the straight line which corresponds to the results for small σ and which is in accordance with the result of the linearized theory [Eq. (4.9)]. In the case of cylindrical walls (Fig. 4.4) a similar behavior is visible; however, the degree of convergence towards the curve corresponding to small σ is inferior to that for spherical walls, at least within the shown curvature interval.

Indeed, it is possible to show analytically that non-linear contributions to the solution

of the PB equation [Eq. (4.2)] are negligible for sufficiently large curvature, e.g., if

$$\frac{1}{\kappa R} \gg \sqrt{\frac{1}{\sqrt{6}} \frac{\beta e |\sigma|}{\epsilon_0 \epsilon \kappa}} \qquad (4.20)$$

for a spherical wall (see Appendix 4.B for details). This finding explains the general behavior encountered in Fig. 4.3 because for any finite σ there is a range of (large) curvatures for which the inequality in Eq. (4.20) holds. Cylindrical electrodes (Fig. 4.4) exhibit curvature dependent capacitances which resemble the spherical results (Fig. 4.3), stretched in horizontal direction. This finding is supported by the linearized theory. In the limit of small radii, $\kappa R \to 0$, Eqs. (4.8) and (4.10) read asymptotically [84]:

$$\text{spherical electrode:} \quad \Phi(R) = \frac{\sigma}{\epsilon_0 \epsilon \kappa} \frac{\kappa R}{\kappa R + 1} \sim \frac{\sigma}{\epsilon_0 \epsilon \kappa} \kappa R, \qquad (4.21)$$

$$\text{cylindrical electrode:} \quad \Phi(R) = \frac{\sigma}{\epsilon_0 \epsilon \kappa} \frac{\mathrm{K}_0(\kappa R)}{\mathrm{K}_1(\kappa R)} \sim -\frac{\sigma}{\epsilon_0 \epsilon \kappa} \kappa R \ln(\kappa R). \qquad (4.22)$$

That is, in this limit, the strengths $|\Phi(R)|$ of the electrode potentials are monotonically increasing functions of R and the one at the cylindrical electrode with the same R is larger than the corresponding one at the spherical wall. On one hand this means that in the case of cylindrical walls smaller radii or larger curvatures are necessary in order to get the same value of $\Phi(R)$ as in the spherical case; this also holds for the capacitance. On the other hand the linearized theory is based on small values of the dimensionless potential $\beta e |\Phi| \ll 1$. Thus, in the case of cylindrical walls the linearized theory turns into a reliable description at smaller radii or larger curvatures as compared to the spherical wall. From the comparison of Figs. 4.3 and 4.4 it follows that a corresponding estimate like the one in Eq. (4.20) would lead to wall radii below molecular sizes (see the discussion in Sec. 4.3.2) and which therefore would be of no practical use.

4.4 Summary and outlook

In terms of the Poisson-Boltzmann (PB) equation [Eq. (4.1)] electrolytes in contact with electrodes of planar ($d = 0$), cylindrical ($d = 1$), or spherical ($d = 2$) shape [Eq. (4.2)] have been analyzed. The differential capacitance C [Eq. (4.5)] was calculated for various ionic strengths I, surface charge densities σ, and electrode radii R. The focus was on examining the dependence of the capacitance on the curvature $1/R$ of the electrode as displayed in Figs. 4.3 and 4.4. In all cases the surface charge density has a strong effect on the capacitance for small curvatures whereas for large curvatures the behavior becomes independent of σ. These limits have been analyzed in detail. For small curvatures (see Sec. 4.3.3) a curvature expansion of the capacitance [Eq. (4.14)] reveals the behavior in a very convenient way because the corresponding expansion coefficients C_n depend on the

single parameter $t \in [-1, 1]$ [Eqs. (4.15) and (4.28)] and on the geometry $d \in \{0, 1, 2\}$ only. Therefore, within PB theory, the influence of any conceivable combination of system parameters on the lowest order coefficients C_n can be inferred from Fig. 4.5. For large curvatures (see Sec. 4.3.4) an analytic discussion provides the insight that the linearized PB theory becomes reliable, if the radius of the spherical wall is chosen to be small enough; this explains the general behavior visible in Fig. 4.3.

In the present study the mesoscopic structure of electrolyte solutions at curved electrodes has been discussed systematically in terms of the capacitance within PB theory (i) because this approach is widely used in various research fields, and (ii) because it offers to judge less integral, microscopic approaches such as the one presented in part II of this study (see Ref. [72] and Chap. 5).

4.A   Limit of large wall radii

Let us assume that for large radii $R \to \infty$ the solution of the PB equation (4.2) can be expanded in terms of powers of the curvature such that the dimensionless potential $y := \beta e \Phi$ takes the form

$$y(r = R + z) = \sum_{n=0}^{\infty} \frac{y_n(z)}{(\kappa R)^n}, \tag{4.23}$$

where $z \in [0, \infty)$ measures the distance from the wall. For all radii the boundary conditions in Eq. (4.3) translate into an inhomogeneous condition at the wall $z = 0$,

$$y_0'(z)\Big|_{z=0} = -\frac{\beta e \sigma}{\epsilon_0 \epsilon}, \quad y_{n>0}'(z)\Big|_{z=0} = 0, \tag{4.24}$$

and a homogeneous one at $z = \infty$:

$$y_{n \geq 0}(\infty) = 0. \tag{4.25}$$

The ansatz in Eq. (4.23) gives rise to a curvature expansion of the PB equation (4.2). In the following, we take into account orders up to and including $1/(\kappa R)^2$. The lowest order leads to

$$y_0''(z) = \kappa^2 \sinh[y_0(z)], \tag{4.26}$$

which is the PB equation (4.2) with $d = 0$ for the dimensionless potential $y_0(z)$ at the planar wall. The orders which are linear and quadratic in the curvature $1/(\kappa R)$ correspond

to differential equations for the spatially varying expansion coefficients $y_{1,2}(z)$:

$$\frac{y_n''(z)}{\kappa^2} - \cosh[y_0(z)]y_n(z) = \begin{cases} n = 1: & -d\dfrac{y_0'(z)}{\kappa}, \\[2mm] n = 2: & -d\dfrac{y_1'(z)}{\kappa} + zdy_0'(z) + \dfrac{1}{2}\sinh[y_0(z)]y_1(z)^2, \end{cases} \quad (4.27)$$

$d \in \{1, 2\}, \quad n \in \{1, 2\}.$

Within the curvature expansion given by Eq. (4.23) the contribution of the planar wall is entirely captured by the coefficient y_0. Higher order coefficients $y_{n>0}$ occur solely at curved walls ($d \neq 0$). The solution of Eq. (4.26) is given by (see Ref. [34])

$$y_0(z) = 4\,\mathrm{artanh}[t\exp(-\kappa z)],$$

$$t := \tanh\left[\frac{1}{2}\mathrm{arsinh}\left(\frac{\beta e\sigma}{2\epsilon_0\epsilon\kappa}\right)\right] = \frac{2\epsilon_0\epsilon\kappa}{\beta e\sigma}\left[\sqrt{1 + \left(\frac{\beta e\sigma}{2\epsilon_0\epsilon\kappa}\right)^2} - 1\right] \in [-1, 1]. \qquad (4.28)$$

In Eq. (4.28) the dependence on z maps onto the scaled spatial variable

$$x := t\exp(-\kappa z), \quad |x| \in [0, |t|], \quad \text{with}$$
$$f_n(x) := y_n(z(x)), \qquad (4.29)$$

such that, e.g., the planar wall result takes the simple form

$$f_0(x) = 4\,\mathrm{artanh}(x). \qquad (4.30)$$

The differential equations for $f_{1,2}(x)$ are given by

$$x^2 f_n''(x) + x f_n'(x) - \cosh[f_0(x)]f_n(x) = \begin{cases} n = 1: & xdf_0'(x), \\[2mm] n = 2: & xdf_1'(x) + d\ln\left(\dfrac{x}{t}\right)xf_0'(x) \\[2mm] & + \dfrac{1}{2}\sinh[f_0(x)]f_1(x)^2, \end{cases} \qquad (4.31)$$

$d \in \{1, 2\}, \quad n \in \{1, 2\},$

subject to the boundary conditions

$$f_{1,2}(x = 0) = 0,$$
$$f_{1,2}'(x)\Big|_{x=t} = 0. \qquad (4.32)$$

From Eqs. (4.31) and (4.32) it follows that the scaled potentials $f_{1,2}$ depend parametrically on $d \in \{1, 2\}$ and t. Moreover, the differential equations (4.31) are to be solved within a finite domain of values of x [Eq. (4.29)] so that the whole parameter space can be scanned

rapidly. Finally, the capacitance follows as

$$C = \left[\frac{\partial\Phi(r_w)}{\partial\sigma}\right]^{-1} = \left[\frac{1}{\beta e}\frac{\partial}{\partial\sigma}\sum_n\frac{y_n(z=0)}{(\kappa R)^n}\right]^{-1} = \left[\frac{1}{\beta e}\frac{\partial}{\partial\sigma}\sum_n\frac{f_n(x=t)}{(\kappa R)^n}\right]^{-1}$$

$$= \epsilon_0\epsilon\kappa\left[\sum_n\frac{1}{4}\frac{(1-t^2)^2}{1+t^2}\frac{\partial f_n(x=t)}{\partial t}\frac{1}{(\kappa R)^n}\right]^{-1} =: \epsilon_0\epsilon\kappa\sum_n\frac{C_n}{(\kappa R)^n},$$

(4.33)

which defines the dimensionless expansion coefficients C_n of the differential capacitance C. In Eq. (4.33) the expression $\partial f_n(x=t)/\partial t$ refers to the derivative of f_n with respect to t after evaluation at $x=t$; the dependence on d and t is transferred to the coefficients C_n.

Alternatively, the coefficients $C_{1,2}$ can be determined from the expressions for the surface potential of spherical and cylindrical surfaces which are given in Refs. [107, 108]: For the spherical electrode the coefficients are

$$C_1 = \frac{1 - 4t^2 - t^4}{1+t^2}$$

(4.34)

and

$$C_2 = \frac{1}{2}\frac{1-t^2}{(1+t^2)^3}\left(1 + 26t^2 + 16t^4 + 6t^6 - t^8\right) + \frac{1}{2}\frac{1-t^2}{t^2(1+t^2)}\ln\left(1-t^2\right)\left(1 + 6t^2 + t^4\right).$$

(4.35)

For the cylindrical electrode

$$C_2 = \frac{1}{8}\frac{1-t^2}{(1+t^2)^3}\left(-1 + 20t^2 + 10t^4 + 4t^6 - t^8\right)$$

(4.36)

and the coefficient C_1 is half of that in the spherical case [Eq. (4.34)]. With help of Eq. (4.34) the root of C_1 can be determined exactly. Its value, $t = \sqrt{\sqrt{5}-2} \approx 0.485868$, is in agreement with the numerically found one (see Sec. 4.3.3).

Apart from the influence of the geometry via d, the whole parameter space given by T, ϵ, I, and σ is contained in $t \in [-1, 1]$. Thus every parameter choice within PB theory can be assigned to Fig. 4.5.

4.B   Limit of small wall radii

Here we investigate under which conditions the non-linearities of the full PB equation (4.2) may be neglected. To this end, with the dimensionless potential $y := \beta e\Phi$ we consider

the equation

$$\frac{1}{r}\frac{\partial^2}{\partial r^2}[r\lambda y(r)] = \kappa^2 \sinh[\lambda y(r)] = \kappa^2 \left[\lambda y(r) + \frac{1}{6}\lambda^3 y(r)^3 + O\left(\lambda^5\right)\right] \tag{4.37}$$

in spherical geometry, where $\lambda \in \mathbb{C}$ is an arbitrary complex parameter. For $\lambda = 1$ the PB equation (4.2) is recovered, whereas for $|\lambda| \ll 1$ non-linearities on the right hand side are suppressed. In order to solve the truncated version of Eq. (4.37) we make the ansatz

$$y(r) = y_0(r) + \lambda^2 y_2(r) + O\left(\lambda^4\right). \tag{4.38}$$

In lowest order $O\left(\lambda^0\right)$ the linearized PB equation (4.4) with $d = 2$ is recovered for which the spatially varying potential $y_0(r)$ and the electrode potential $y_0(R)$ are given by

$$y_0(r) = A\frac{\exp(-\kappa r)}{r}, \qquad A := \frac{sR^2}{1+\kappa R}\exp(\kappa R), \qquad s := \frac{\beta e\sigma}{\epsilon_0 \epsilon}, \quad \text{and}$$
$$y_0(R) = \frac{sR}{1+\kappa R}, \tag{4.39}$$

respectively. The next higher order $O\left(\lambda^2\right)$ leads to a differential equation for the dominant non-linear contribution $y_2(r)$

$$\frac{1}{r}\frac{\partial^2}{\partial r^2}[ry_2(r)] = \kappa^2 y_2(r) + \frac{\kappa^2}{6}y_0(r)^3, \tag{4.40}$$

where the inhomogeneity is given by the solution of the linearized PB equation [Eq. (4.39)]. The solution of Eq. (4.40) takes the form

$$y_2(r) = B\frac{\exp(-\kappa r)}{r} + \frac{f(r)}{r}, \quad \text{where}$$
$$f(r) := -\frac{\kappa A^3}{12}\int_R^\infty dr' \exp(-\kappa|r-r'|)\frac{\exp(-3\kappa r')}{r'^2}, \tag{4.41}$$
$$B := f(R)\frac{\kappa R - 1}{\kappa R + 1}\exp(\kappa R).$$

The electrode potential $y_2(R)$ is given by

$$y_2(R) = -y_0(R)\frac{1}{6}\left(\frac{s}{\kappa}\right)^2 \frac{h(4\kappa R)}{\frac{1}{\kappa R}\left(1+\frac{1}{\kappa R}\right)^3}, \quad \text{with}$$
$$h(z) := z\exp(z)\int_z^\infty dx\,\frac{\exp(-x)}{x^2}. \tag{4.42}$$

From these results one infers that the contribution from the linearized PB equation is the dominant one if the leading non-linear term $y_2(R)$ is much smaller than the linear one $y_0(R)$. Since $h(z > 0) \leq 1$, one obtains

$$\left| \frac{y_2(R)}{y_0(R)} \right| \ll 1$$

$$\text{for} \quad \frac{1}{\kappa R} \gg \sqrt{\frac{1}{\sqrt{6}} \frac{|s|}{\kappa}} = \sqrt{\frac{1}{\sqrt{6}} \frac{\beta e |\sigma|}{\epsilon_0 \epsilon \kappa}}.$$

(4.43)

Hence for any finite σ the first non-linear term $y_2(R)$ becomes negligible if the curvature $(\kappa R)^{-1}$ is chosen large enough. For small radii R the linearized PB theory turns into a reliable description.

Chapter 5

Electrolyte solutions at curved electrodes. II. Microscopic approach

The present Chap. 5 consists of the occasionally amended study published in Ref. [72]. There density functional theory is used to describe electrolyte solutions in contact with electrodes of planar or spherical shape. The electrolyte solutions are considered by means of the so-called civilized model, in which all species present are treated on equal footing. The features of the electric double layer are discussed in terms of the differential capacitance. The model provides insight into the microscopic structure of the electric double layer, which goes beyond the mesoscopic approach addressed in part I of this study (see Ref. [94] and Chap. 4). This enables one to judge the relevance of microscopic details, such as the radii of the particles forming the electrolyte solutions or the dipolar character of the solvent particles, and to compare the predictions of various models. Similar to part I, a general behavior is observed for small radii of the electrode in that in this limit the results become independent of the surface charge density and of the particle radii. However, for large electrode radii non-trivial behaviors are observed. Especially the particle radii and the surface charge density strongly influence the capacitance. From the comparison with the Poisson-Boltzmann approach it becomes apparent that the shape of the electrode determines whether the microscopic details of the full civilized model have to be taken into account or whether already simpler models yield acceptable predictions.

5.1 Introduction

In the first part (Ref. [94] and Chap. 4) of this study electric double layers have been discussed in detail on mesoscopic scales within the Poisson-Boltzmann (PB) theory, which was pioneered by Gouy [32] and Chapman [33]. The focus of the analysis in Ref. [94] and Chap. 4 has been on electrodes of spherical or cylindrical shape surrounded by an electrolyte solution. Such kind of setups serve as models for certain parts of so-called double

layer capacitors, i.e., electrical energy storage devices which are promising candidates for supporting sustainable energy systems. In part I (Ref. [94] and Chap. 4) the differential capacitance C, which is the change of the surface charge density upon varying the electrostatic potential at the wall and thus is experimentally accessible, has been analyzed in particular concerning its dependence on the surface charge density and on the radius of the curved electrode. The focus has been, within the PB model, on a thorough discussion of the dependence of the capacitance on the geometry of the system.

Especially for large and small curvatures of the electrodes the behavior has been discussed systematically. On one hand, the simplifying assumptions underlying the PB approach facilitate such a detailed discussion, and, on the other hand, they are also the reason for the approach to be only reliable for weak ionic strengths (below $0.2\,\mathrm{M} = 0.2\,\mathrm{mol}/\ell$) and low electrode potentials (below $80\,\mathrm{mV}$) in the case of monovalent salts in aqueous solutions [2]. But already in these ranges deviations from experimental data are observable: the predicted differential capacitance is larger than the measured one [34].

Therefore Stern introduced a model which accounts for that shortcoming by combining the Gouy-Chapman description of the diffuse layer, i.e., the charge in the fluid is distributed continuously following the PB equation, with the model of a Helmholtz layer of counterions, i.e., the charge in the fluid is directly attached to the electrode surface within a molecular layer [31]. Accordingly, the pure Gouy-Chapman description, which does not consider the granular character of the fluid, has been improved by introducing a Stern layer in between the electrode and the diffuse layer, i.e., the actual nonzero particle volumes are taken into account only close to the wall. As a consequence the total capacitance of the system can be considered as a circuit of two capacitors (i.e., the Stern layer and the diffuse layer) in series [2,34] and, following the rules for electric circuits, the total capacitance is smaller than the Gouy-Chapman capacitance. Practically, one is left to fit the capacitance of the Stern layer to experimental results which, on one hand, might lead to good agreements with measurements, but which, on the other hand, provides only a coarse microscopic picture of the electrical double layer. One possible interpretation of the results of the Stern theory is that close to the wall the permittivity is reduced [2,34].

More sophisticated models have been developed in order to describe the structure of an electrical double layer more precisely than within the mesoscopic PB approach according to which the ions are treated as pointlike charges dissolved in a homogeneous background. Three classes of corresponding models are common in the literature. Within the so-called "primitive model" (PM) the ions are considered as charged hard spherical particles which are dissolved in a solvent which is taken into account only via the permittivity. In the so-called "solvent primitive model" (SPM) the solvent particles exhibit also a nonzero volume and are often described as hard spheres. Sometimes these models are labelled in conjunction with the attribute "restricted" which means that all particle radii are equal. Yet more elaborate theories incorporate the electrostatics between ions and solvent

particles by providing the latter with a dipole.

In 1980 Carnie and Chan used the so-called "civilized model" in order to model an electrolyte solution [54]. Therein, as opposed to a primitive model, "both the ions and the solvent are treated on an equal basis". The ions are represented by hard spheres with charges whereas the solvent is represented by hard spheres with an embedded dipole. In Ref. [54] exact and approximative results within the mean spherical approximation are presented for the structure of the electrolyte solution at a charged planar surface. For low ionic concentrations the surface potential has the Stern layer form, i.e., the expression of the surface potential is the sum of the diffuse part of the electrical double layer and an additional part which can be interpreted as the contribution of a Stern layer. Thus the result is regarded as a derivation of the Stern layer behavior. Analytic expressions reveal that both the nonzero ion size and the dipolar solvent alter the capacitance, which otherwise reduces to the double-layer capacitance of the linearized Gouy-Chapman theory. However, this change is not very large [54].

In Ref. [55] a similar approach is used in order to complement the results of Ref. [54]. Hard core and solvent effects, both of which are taken into account, lead to a reduction of the differential capacitance, i.e., the trend indicated by the Stern model is confirmed. However, the alignment of the dipoles close to the planar wall persists for several layers into the fluid. This ordering is not confined to a single Stern-like layer next to the electrode.

The so-called reference hypernetted-chain theory is used in Refs. [56, 57] in order to examine the double layer at the surface of large spherical macroions within a multipolar hard sphere model of electrolyte solutions, i.e., the ions are charged hard spheres and the solvent molecules are hard spheres carrying point multipoles. The structure of the double layer is discussed in terms of, e.g., the potential of mean force between the macroion and a counterion, ion or solvent number density profiles, and mean electrostatic potentials. The dependences of the structure on the surface charge density, the ionic concentration, and the (macro-)ionic radii are examined.

In Ref. [66] a possible realization of a microscopic model for electric double layers within density functional theory (DFT) is proposed. The functional is formulated for a mixture of spheres with embedded point charges or dipoles. Consequently, the excess part of the DFT functional splits into a Coulombic and into hard sphere parts where for the latter the fundamental measure theory (see Refs. [12, 13] in Ref. [66]) is adopted. Within this approach various density profiles near a charged planar wall are presented, which, due to the granular nature of the fluid, exhibit pronounced oscillations. The authors conclude by comparison that the primitive model is able to reproduce well ionic density profiles in low concentration regimes and beyond a certain distance from the wall. However, within the microscopic description and for higher concentrations the number density oscillations become increasingly pronounced such that a primitive model description turns out to be inadequate.

Within the microscopic model used in Ref. [67] the Coulombic interactions are taken into account in a mean-field-like kind while the excluded-volume effects are accounted for by the Percus Yevick approach. The radii of the various particle species, i.e., anions, cations, and solvent molecules, are chosen differently. This qualitatively affects the dependence of the differential capacitance C on the surface charge density σ of the planar electrode: within the Gouy-Chapman theory C is an even function of σ, whereas for unequal values of the particle radii this symmetry disappears.

Oleksy and Hansen have used DFT with an explicit solvent description in order to investigate the wetting and drying behavior of ionic solutions in contact with a charged solid substrate [68]. All particles are treated as hard spheres and the corresponding excluded-volume correlations are taken into account by fundamental measure theory. The other interactions, i.e., the electrostatic interaction and the cohesive Yukawa attraction, are treated within mean field theory in order to ensure full thermodynamic self-consistency. The key finding is the remarkable agreement between this version of a civilized model and a previous model in which the dipoles are not explicitly taken into account.

Henderson and coworkers proposed a nonprimitive model which differs from the aforementioned models with respect to the shape of the solvent particles [69]. Within DFT hard spherical ions are considered to be dissolved in a solvent which is composed of neutral dimers, i.e., touching positively and negatively charged hard spheres. The model predicts a larger electrode potential than in the case of an implicit model like the restricted primitive model. However, for technical reasons, results could only be obtained for comparatively low potential values.

Recently, electrolyte aqueous solutions near a planar wall have been discussed within a so-called polar-solvation DFT [71]. Therein all particles are considered as hard spheres via the fundamental measure theory and the mean spherical approximation is used in order to calculate the remaining part of the direct correlation functions. The comparison between the results of this polar-solvation DFT, within which the solvent particles are assumed to carry an embedded dipole, and the results of the unpolar-solvation DFT of Refs. [63, 64], within which the solvent particles are taken into account as hard spheres only, yields, e.g., a discrepancy in the density profiles which increases with increasing electrode potential. Due to technical reasons the model in Ref. [71] could not be used to study ion concentrations above $10 \, \mathrm{mM}$.

For many years a lot of efforts have been spent in order to understand the structure of electric double layers either at planar walls or around macroions. Therefore various realizations of microscopic approaches, which in general include an explicit description of dipolar solvents, have been proposed [54–57, 66–69, 71]. Here the case of a double layer at a spherical electrode of *arbitrary* radius R is studied. In the spirit of part I (Ref. [94] and Chap. 4) of this study, the structure of the electrolyte solution is captured in terms of the differential capacitance C, which facilitates to judge the relevance of various system

parameters. As compared to the mesoscopic PB approach used in part I (Ref. [94] and Chap. 4), in the present microscopic description the size of the spherical electrode affects the layering behavior of the particles due to steric effects. In addition, the charges or dipoles, embedded in the particles, interact with each other and with the charge on the electrode. Due to the interplay of various interactions, structural features, such as the spatially varying dipole orientation of the solvent particles, are expected to exhibit a comparatively complex dependence on the electrode radius. The model used within the present study is inspired by the work of Oleksy and Hansen [68]. It incorporates the aforementioned features (non-vanishing and distinct particle volumes as well as spatially varying dipole orientations), which contribute to the differential capacitance in ways that are, due to the influence of the electrode size, not yet well understood. Apart from dealing with the hard spheres the interactions are taken into account within a modified random phase description [58], the relatively simple structure of which allows one to conveniently generalize the planar geometry to the spherical one. Moreover, the concept of introducing an additional cohesive attraction amongst the particles corresponds to the intention to discuss an electrolyte solution in the liquid state under realistic conditions. To that end the respective model parameters are chosen to mimic liquid water as the solvent at room temperature and ambient pressure. The differential capacitance is discussed as function of the remaining inherent system parameters, in particular, the wall curvature. Here, especially the dependence on the latter contains mechanisms which are not revealed by more primitive models such that quantitative or even qualitative differences between the model under consideration and the more primitive ones can be expected to occur.

In Sec. 5.2.1 the present version of the density functional is discussed in detail. The corresponding Euler-Lagrange equations (ELE) are presented in Sec. 5.2.2. The method to account for the boundary conditions in the process of obtaining the numerical solution is described in Sec. 5.2.3. Section 5.2.4 summarizes the chosen parameters and the notation used here. Technical details are discussed in Appendices 5.A – 5.D. The results of the calculations are presented in Sec. 5.3 where the structures of the electric double layers are illustrated via spatially varying number density profiles. Subsequently the capacitance data obtained for the planar wall are shown for various choices of system parameters and models. Finally, the capacitance data of spherical electrodes are discussed as function of the electrode curvature and of the surface charge density. The influence of various choices of system parameters is discussed and various models are compared with each other.
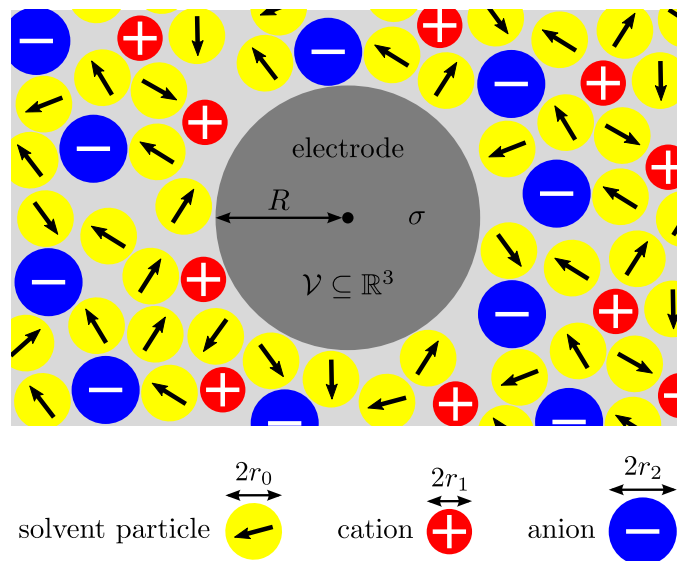
Figure 5.1: Sketch of the system under consideration. For clarity the sketch shows a two-dimensional cross-section (light gray background) of the system which actually occupies the three-dimensional space. The model (see Sec. 5.2) takes into account an electrolyte solution which is composed of three species: (i) Solvent particles (yellow circles) are considered as hard spheres with radius r_0. The arrows in the yellow circles illustrate embedded permanent dipoles. The orientational degrees of freedom of the latter are explicitly taken into account. For clarity the arrows are depicted parallel to the plane of the paper. Note, however, that the model incorporates the dipole orientations in *three* dimensions, i.e., the arrows may point into or out of the plane of the paper. (ii) Monovalent cations (red circles) are considered as hard spheres with radius r_1 carrying positive charge. (iii) Monovalent anions (blue circles) are considered as hard spheres with radius r_2 carrying negative charge. The spatial extent of the electrolyte solution is restricted due to the presence of an electrode (dark gray circle) occupying the volume $\mathcal{V} \subseteq \mathbb{R}^3$. In the present sketch the electrode is of spherical shape with radius R. Its surface may be homogeneously charged with a surface charge density σ. All particles interact with each other and with the electrode by means of steric effects, electrostatic interactions [Eq. (5.5)], and an attractive interaction [Eq. (5.7)]. For further details see Sec. 5.2. A comparison between the present sketch and the one in Fig. 4.2 gives a visual impression of the differences between the present *microscopic* civilized model and the *mesoscopic* Poisson-Boltzmann theory of Chap. 4.

5.2   Model

5.2.1   Density functional

The microscopic approach used here follows the one of Oleksy and Hansen in Ref. [68] which is sometimes referred to as the so-called *civilized model* [54] according to which both the ions and the solvent are treated on equal footing, in contrast to the primitive model. Let us consider an electrolyte solution composed of three species: solvent particles

(hard spheres with radius r_0 and an embedded dipole of strength m), monovalent cations (hard spheres with radius r_1 carrying a charge $q_1 = e > 0$, e denoting the absolute value of the elementary charge), and monovalent anions (hard spheres with radius r_2 carrying a charge $q_2 = -e < 0$). The spatial extent of the electrolyte solution is restricted due to the presence of an electrode occupying the volume $\mathcal{V} \subseteq \mathbb{R}^3$. In the present study the focus is on two types of electrodes or walls: planar electrodes correspond to the half-space $\mathcal{V} = \{(x, y, z) \in \mathbb{R}^3 \mid z < 0\}$ with surface $\mathcal{A} = \{(x, y, z) \in \mathbb{R}^3 \mid z = 0\}$ whereas spherical electrodes of radius R occupy the domain $\mathcal{V} = \{(x, y, z) \in \mathbb{R}^3 \mid x^2 + y^2 + z^2 < R^2\}$ with surface $\mathcal{A} = \{(x, y, z) \in \mathbb{R}^3 \mid x^2 + y^2 + z^2 = R^2\}$. The surfaces $\mathcal{A}$ of the walls may be homogeneously charged with a surface charge density σ. Figure 5.1 illustrates the system under consideration. The, in general inhomogeneous, distribution of solvent particles is given by the number density $\varrho_0(\boldsymbol{r}, \boldsymbol{\omega})$, i.e., the number of particles per volume with dipole orientation $\boldsymbol{\omega}$, $|\boldsymbol{\omega}| = 1$, at position $\boldsymbol{r} \in \mathbb{R}^3 \backslash \mathcal{V}$. In a fixed, but otherwise arbitrary, coordinate system the dipole orientation can be represented by

$$\boldsymbol{\omega} = \begin{pmatrix} \sin(\vartheta)\cos(\varphi) \\ \sin(\vartheta)\sin(\varphi) \\ \cos(\vartheta) \end{pmatrix} \tag{5.1}$$

with polar angle ϑ and azimuthal angle φ. The number density of all solvent particles at a point $\boldsymbol{r}$ irrespective of the orientation is given by

$$\bar{\varrho}_0(\boldsymbol{r}) := \int \mathrm{d}^2\omega\, \varrho_0(\boldsymbol{r}, \boldsymbol{\omega}) := \int\limits_0^\pi \mathrm{d}\vartheta\, \sin(\vartheta) \int\limits_0^{2\pi} \mathrm{d}\varphi\, \varrho_0(\boldsymbol{r}, \vartheta, \varphi). \tag{5.2}$$

In the following the integration over all orientations, i.e., over all possible values of the two angles ϑ and φ [see Eq. (5.1)], is denoted as $\int \mathrm{d}^2\omega$ [see, e.g., Eq. (5.2)]. The number density of ion species $i \in \{1, 2\}$ at position $\boldsymbol{r}$ is $\varrho_i(\boldsymbol{r})$.

Density functional theory (DFT) is a particularly useful approach to determine these density profiles and with them the structure of the electrolyte solution in contact with the wall [58]. To this end we consider the following approximation for the grand potential functional $\Omega[\varrho_0, \varrho_1, \varrho_2] =: \Omega[\varrho]$ of the number densities $\varrho_0(\boldsymbol{r}, \boldsymbol{\omega})$ and $\varrho_{1,2}(\boldsymbol{r})$:

$$\begin{aligned} \beta\Omega[\varrho] = &\int \mathrm{d}^3r \int \mathrm{d}^2\omega\, \varrho_0(\boldsymbol{r}, \boldsymbol{\omega}) \left[\beta V_0(\boldsymbol{r}) - \beta\mu_0\right] \\ &+ \sum_{i=1}^2 \int \mathrm{d}^3r\, \varrho_i(\boldsymbol{r}) \left[\beta V_i(\boldsymbol{r}) - \beta\mu_i\right] \\ &+ \beta\mathcal{F}^{\mathrm{id}}[\varrho] + \beta\mathcal{F}^{\mathrm{hs}}[\varrho] + \beta\mathcal{F}^{\mathrm{el}}[\varrho] + \beta\mathcal{F}^{\mathrm{att}}[\varrho]. \end{aligned} \tag{5.3}$$

In Eq. (5.3) one has $\beta = (k_B T)^{-1}$ with the Boltzmann constant k_B and the absolute

temperature T. V_i and μ_i denote the external and the chemical potential of species i, respectively. The external potential $V_0(\boldsymbol{r})$ acting on the solvent particles is taken to be independent of their dipolar orientations. Unless indicated differently, volume integrals $\int \mathrm{d}^3 r$ run over the space $\mathbb{R}^3 \backslash \mathcal{V}$. $\mathcal{F}^{\mathrm{id}}$ is the ideal gas contribution,

$$
\begin{aligned}
\beta \mathcal{F}^{\mathrm{id}}[\varrho] = & \int \mathrm{d}^3 r \int \mathrm{d}^2 \omega \, \varrho_0(\boldsymbol{r}, \boldsymbol{\omega}) \left\{ \ln \left[\Lambda_0^3 \varrho_0(\boldsymbol{r}, \boldsymbol{\omega}) \right] - 1 \right\} \\
& + \sum_{i=1}^2 \int \mathrm{d}^3 r \, \varrho_i(\boldsymbol{r}) \left\{ \ln \left[\Lambda_i^3 \varrho_i(\boldsymbol{r}) \right] - 1 \right\},
\end{aligned}
\tag{5.4}
$$

with the thermal wave lengths Λ_i.

The hard sphere interaction between the particles is taken into account by means of the functional $\mathcal{F}^{\mathrm{hs}}$ which, in the present case, is the White Bear version of the fundamental measure theory (see Ref. [60]). For the contribution $\mathcal{F}^{\mathrm{hs}}$ {and likewise $\mathcal{F}^{\mathrm{att}}$ [see Eq. (5.7) below]} the orientations $\boldsymbol{\omega}$ of the dipoles do not matter which is why it is a functional of $\bar{\varrho}_0(\boldsymbol{r})$ [see Eq. (5.2)].

The remaining terms of Eq. (5.3), $\mathcal{F}^{\mathrm{el}}$ [Eq. (5.5)] and $\mathcal{F}^{\mathrm{att}}$ [Eq. (5.7)], are taken into account by means of a modified random phase approximation. Appendix 5.A explains the assumptions underlying this approximation. Note that the discussion in Appendix 5.A concerns the excess functional $\mathcal{F}^{\mathrm{ex}}$. The latter takes into account mutual interactions of the particles in the electrolyte solution. In the strict sense, the surface terms contained in $\mathcal{F}^{\mathrm{el}}$ [Eq. (5.5)] are not part of $\mathcal{F}^{\mathrm{ex}}$ but formally act like external potentials.

The electrostatic interactions, both amongst the particles and between the particles and the wall, are captured by the functional

$$
\begin{aligned}
\beta \mathcal{F}^{\mathrm{el}}[\varrho] = & \frac{1}{2} \sum_{i,j=1}^2 \int \mathrm{d}^3 r \int \mathrm{d}^3 r' \frac{\beta}{4\pi\epsilon_0\epsilon_{\mathrm{ex}}} \frac{q_i q_j}{|\boldsymbol{d}|} \varrho_i(\boldsymbol{r}) \varrho_j(\boldsymbol{r}') \Theta[|\boldsymbol{d}| - (r_i + r_j)] \\
& + \sum_{i=1}^2 \int \mathrm{d}^3 r \int \mathrm{d}^3 r' \int \mathrm{d}^2 \omega' \frac{\beta}{4\pi\epsilon_0\epsilon_{\mathrm{ex}}} q_i \frac{m \boldsymbol{\omega}' \cdot \boldsymbol{d}}{|\boldsymbol{d}|^3} \varrho_i(\boldsymbol{r}) \varrho_0(\boldsymbol{r}', \boldsymbol{\omega}') \Theta[|\boldsymbol{d}| - (r_0 + r_i)] \\
& + \frac{1}{2} \int \mathrm{d}^3 r \int \mathrm{d}^2 \omega \int \mathrm{d}^3 r' \int \mathrm{d}^2 \omega' \frac{\beta}{4\pi\epsilon_0\epsilon_{\mathrm{ex}}} m^2 \left[\frac{\boldsymbol{\omega} \cdot \boldsymbol{\omega}'}{|\boldsymbol{d}|^3} - 3 \frac{(\boldsymbol{\omega} \cdot \boldsymbol{d})(\boldsymbol{\omega}' \cdot \boldsymbol{d})}{|\boldsymbol{d}|^5} \right] \\
& \quad \times \varrho_0(\boldsymbol{r}, \boldsymbol{\omega}) \varrho_0(\boldsymbol{r}', \boldsymbol{\omega}') \Theta(|\boldsymbol{d}| - 2r_0) \\
& + \sum_{i=1}^2 \int_{\boldsymbol{r} \in \mathcal{A}} \mathrm{d}^2 r \int \mathrm{d}^3 r' \frac{\beta}{4\pi\epsilon_0\epsilon_{\mathrm{ex}}} \frac{\sigma q_i}{|\boldsymbol{d}|} \varrho_i(\boldsymbol{r}') \Theta(|\boldsymbol{d}| - r_i) \\
& + \int_{\boldsymbol{r} \in \mathcal{A}} \mathrm{d}^2 r \int \mathrm{d}^3 r' \int \mathrm{d}^2 \omega' \frac{\beta}{4\pi\epsilon_0\epsilon_{\mathrm{ex}}} \sigma \frac{m \boldsymbol{\omega}' \cdot \boldsymbol{d}}{|\boldsymbol{d}|^3} \varrho_0(\boldsymbol{r}', \boldsymbol{\omega}') \Theta(|\boldsymbol{d}| - r_0),
\end{aligned}
\tag{5.5}
$$

where ϵ_0 is the vacuum permittivity,

$$\Theta(x) = \begin{cases} 0, & x < 0, \\ 1, & x > 0 \end{cases} \tag{5.6}$$

denotes the Heaviside step function, and $\boldsymbol{d} := \boldsymbol{r} - \boldsymbol{r}'$ is the spatial offset between positions $\boldsymbol{r}$ and $\boldsymbol{r}'$. Within the present approach, the dielectric properties of the solvent are described in terms of an explicit mean-field-like contribution due to the solvent particles with embedded dipole moments $\boldsymbol{p} := m\boldsymbol{\omega}$ and an implicit excess contribution given by the excess relative permittivity ϵ_{ex} which captures dielectric properties beyond the mean-field description [see also Sec. 5.2.3 and in particular Eq. (5.31)]. Alternatively, one could use descriptions based on the mean spherical approximation [71] or model the solvent molecules as dimers in the style of Ref. [69]. However, the present approach has technical advantages and, moreover, it has turned out that the explicit dipolar contribution affects the results only weakly.

The influence of Coulomb correlation contributions has been examined in Ref. [62], where semi-primitive model electrolytes have been described both in terms of a mean-field density functional, which neglects Coulomb correlations, and in terms of a more complex density functional including such correlations. The outcome of these different approaches has been compared with each other and with Monte Carlo simulations. The authors have found that Coulomb correlation corrections alter the mean-field results significantly only for high surface charges in the presence of divalent cations. Based on that finding, the model in the present study is expected to accurately describe electrolytes consisting of monovalent ions. In addition, the results of the present model for an ionic strength of 0.1 M have been compared with Figs. 5 and 6 in Ref. [41], which provide simulation results for a charged spherical macroparticle surrounded by an electrolyte solution within the molecular solvent model. All profiles show good agreement with the simulation data which supports the aforementioned argument that the present model is a reliable description for monovalent ions. Another consistency check has been carried out with respect to the bulk limit. To that end number density profiles around a spherical electrode, with the same size and charge as an ion, have been calculated. These density profiles, which correspond to pair distribution functions, have been compared with Fig. 2 in Ref. [38] where simulation data for an electrolyte within a solvent primitive model are presented. The results of the present model almost lie on top of the curves denoted by "HNC" and are in good agreement with the simulation data.

An attractive interaction between the particles is taken into account by the contribution $\mathcal{F}^{\mathrm{att}}$. This interaction is rationalized by a van der Waals attraction which enables the formation of a liquid state under realistic conditions, i.e., room temperature and ambient pressure. Amplitude and range of this potential, chosen to be square-well-like, are given

by u and r_c, respectively:

$$\beta\mathcal{F}^{\mathrm{att}}[\varrho] = \frac{1}{2}\sum_{i,j=0}^{2}\int \mathrm{d}^3r \int \mathrm{d}^3r'\, \beta u\Theta(r_c - |\boldsymbol{d}|)\varrho_i(\boldsymbol{r})\varrho_j(\boldsymbol{r}')\Theta[|\boldsymbol{d}| - (r_i + r_j)]. \qquad (5.7)$$

[Note that in Eq. (5.7) $\varrho_0(\boldsymbol{r},\boldsymbol{\omega})$ reduces to $\bar\varrho_0(\boldsymbol{r})$.] We make the simplifying assumption that this kind of attractive potential is the same for the interaction among the fluid particles and for their interaction with the wall particles. Thus for a homogeneous number density ϱ_w of the wall particles, the attractive van der Waals interaction gives rise to the substrate potential

$$\beta V^{\mathrm{att}}(\boldsymbol{r}) = \int_{\mathcal{V}} \mathrm{d}^3r'\, \varrho_w\beta u\Theta(r_c - |\boldsymbol{d}|). \qquad (5.8)$$

The attractive van der Waals potential V^{att} together with the hard repulsive interaction between wall and fluid particles comprise the external potentials V_i, $i \in \{0, 1, 2\}$:

$$\beta V_i(\boldsymbol{r}) = \begin{cases} \infty, & \exists\, \boldsymbol{r}' \in \mathcal{V} : |\boldsymbol{d}| < r_i, \\ \beta V^{\mathrm{att}}(\boldsymbol{r}), & \text{otherwise.} \end{cases} \qquad (5.9)$$

Further contributions, e.g., due to electrostatic image forces in the case of a dielectric contrast between wall and fluid, would have to be added to the second line of Eq. (5.9).

5.2.2   Euler-Lagrange equations

In accordance with the variational principle underlying density functional theory [58] the equilibrium densities ϱ_i^{eq} minimize the functional in Eq. (5.3) and thus fulfill the Euler-Lagrange equations (ELEs)

$$\left.\frac{\delta(\beta\Omega)}{\delta\varrho_0(\boldsymbol{r},\boldsymbol{\omega})}\right|_{\varrho_0^{\mathrm{eq}},\varrho_1^{\mathrm{eq}},\varrho_2^{\mathrm{eq}}} = 0, \quad \left.\frac{\delta(\beta\Omega)}{\delta\varrho_{1,2}(\boldsymbol{r})}\right|_{\varrho_0^{\mathrm{eq}},\varrho_1^{\mathrm{eq}},\varrho_2^{\mathrm{eq}}} = 0. \qquad (5.10)$$

Their forms will be discussed in more detail below (see also Ref. [68]). For clarity the superscript $^{\mathrm{eq}}$ is omitted and subsequently the focus is on equilibrium densities. In the bulk and thus in the absence of inhomogeneities, the density profiles entering the ELEs (5.10) are uniform and isotropic: $\varrho_0(\boldsymbol{r},\boldsymbol{\omega}) = \varrho_0^{\mathrm{b}}/(4\pi)$, $\varrho_1(\boldsymbol{r}) = \varrho_1^{\mathrm{b}} \equiv I$, and $\varrho_2(\boldsymbol{r}) = \varrho_2^{\mathrm{b}} \equiv I$ with the ionic strength I. Note that $\varrho_1^{\mathrm{b}} = \varrho_2^{\mathrm{b}}$ implies local charge neutrality. This also holds at points sufficiently far away from the wall. By subtracting from the ELEs (5.10) the respective expressions in the bulk, the chemical potentials μ_i and the lengths Λ_i drop out

of the equations:

$$\varrho_0(\boldsymbol{r}, \boldsymbol{\omega}) = \frac{\varrho_0^{\mathrm{b}}}{4\pi} \exp\Big\{ -\beta V_0(\boldsymbol{r}) + c_0^{\mathrm{hs}}(\boldsymbol{r}) - c_0^{\mathrm{hs,b}} + c_0^{\mathrm{att}}(\boldsymbol{r}) - c_0^{\mathrm{att,b}}$$
$$+ \beta m \boldsymbol{\omega} \cdot [\boldsymbol{E}(\boldsymbol{r}) - \boldsymbol{E}^{\mathrm{aux}}(\boldsymbol{r})] \Big\} \tag{5.11}$$

and, $i \in \{1, 2\}$,

$$\varrho_i(\boldsymbol{r}) = \varrho_i^{\mathrm{b}} \exp\Big\{ -\beta V_i(\boldsymbol{r}) + c_i^{\mathrm{hs}}(\boldsymbol{r}) - c_i^{\mathrm{hs,b}} + c_i^{\mathrm{att}}(\boldsymbol{r}) - c_i^{\mathrm{att,b}} - \beta q_i [\Phi(\boldsymbol{r}) - \Phi_i^{\mathrm{aux}}(\boldsymbol{r})] \Big\}. \tag{5.12}$$

Here the following quantities have been introduced: one-point direct correlation functions, $\mathrm{x} \in \{\mathrm{hs}, \mathrm{att}\}$,

$$c_i^{\mathrm{x}}(\boldsymbol{r}) := -\frac{\delta(\beta\mathcal{F}^{\mathrm{x}})}{\delta\varrho_i(\boldsymbol{r})}, \quad c_i^{\mathrm{x,b}} := -\frac{\delta(\beta\mathcal{F}^{\mathrm{x}})}{\delta\varrho_i(\boldsymbol{r})}\Big|_{\mathrm{bulk}}, \tag{5.13}$$

the polarization

$$\boldsymbol{P}(\boldsymbol{r}) := \int \mathrm{d}^2\omega \, m\boldsymbol{\omega}\varrho_0(\boldsymbol{r}, \boldsymbol{\omega}), \tag{5.14}$$

electric fields

$$\boldsymbol{E}(\boldsymbol{r}) := \sum_{i=1}^{2} \int \mathrm{d}^3 r' \frac{q_i}{4\pi\epsilon_0\epsilon_{\mathrm{ex}}} \frac{\boldsymbol{d}}{|\boldsymbol{d}|^3} \big[\varrho_i(\boldsymbol{r}') - \varrho_i^{\mathrm{b}}\big]$$
$$- \int \mathrm{d}^3 r' \frac{1}{4\pi\epsilon_0\epsilon_{\mathrm{ex}}} \left\{ \frac{\boldsymbol{P}(\boldsymbol{r}')}{|\boldsymbol{d}|^3} - \frac{3\boldsymbol{d}[\boldsymbol{P}(\boldsymbol{r}') \cdot \boldsymbol{d}]}{|\boldsymbol{d}|^5} \right\}$$
$$+ \int_{\boldsymbol{r}' \in \mathcal{A}} \mathrm{d}^2 r' \frac{\sigma}{4\pi\epsilon_0\epsilon_{\mathrm{ex}}} \frac{\boldsymbol{d}}{|\boldsymbol{d}|^3}, \tag{5.15}$$

and

$$\boldsymbol{E}^{\mathrm{aux}}(\boldsymbol{r}) := \sum_{i=1}^{2} \int \mathrm{d}^3 r' \frac{q_i}{4\pi\epsilon_0\epsilon_{\mathrm{ex}}} \frac{\boldsymbol{d}}{|\boldsymbol{d}|^3} \big[\varrho_i(\boldsymbol{r}') - \varrho_i^{\mathrm{b}}\big] \Theta(r_0 + r_i - |\boldsymbol{d}|)$$
$$- \int \mathrm{d}^3 r' \frac{1}{4\pi\epsilon_0\epsilon_{\mathrm{ex}}} \left\{ \frac{\boldsymbol{P}(\boldsymbol{r}')}{|\boldsymbol{d}|^3} - \frac{3\boldsymbol{d}[\boldsymbol{P}(\boldsymbol{r}') \cdot \boldsymbol{d}]}{|\boldsymbol{d}|^5} \right\} \Theta(2r_0 - |\boldsymbol{d}|)$$
$$+ \int_{\boldsymbol{r}' \in \mathcal{A}} \mathrm{d}^2 r' \frac{\sigma}{4\pi\epsilon_0\epsilon_{\mathrm{ex}}} \frac{\boldsymbol{d}}{|\boldsymbol{d}|^3} \Theta(r_0 - |\boldsymbol{d}|), \tag{5.16}$$

as well as electric potentials

$$
\begin{aligned}
\Phi(\boldsymbol{r}) := &\sum_{j=1}^{2} \int \mathrm{d}^3 r' \frac{1}{4\pi\epsilon_0\epsilon_{\mathrm{ex}}} \frac{q_j}{|\boldsymbol{d}|} \left[\varrho_j(\boldsymbol{r}') - \varrho_j^{\mathrm{b}} \right] \\
&+ \int \mathrm{d}^3 r' \frac{1}{4\pi\epsilon_0\epsilon_{\mathrm{ex}}} \frac{\boldsymbol{P}(\boldsymbol{r}') \cdot \boldsymbol{d}}{|\boldsymbol{d}|^3} \\
&+ \int\limits_{\boldsymbol{r}' \in \mathcal{A}} \mathrm{d}^2 r' \frac{1}{4\pi\epsilon_0\epsilon_{\mathrm{ex}}} \frac{\sigma}{|\boldsymbol{d}|}
\end{aligned}
\tag{5.17}
$$

and

$$
\begin{aligned}
\Phi_i^{\mathrm{aux}}(\boldsymbol{r}) := &\sum_{j=1}^{2} \int \mathrm{d}^3 r' \frac{1}{4\pi\epsilon_0\epsilon_{\mathrm{ex}}} \frac{q_j}{|\boldsymbol{d}|} \left[\varrho_j(\boldsymbol{r}') - \varrho_j^{\mathrm{b}} \right] \Theta(r_i + r_j - |\boldsymbol{d}|) \\
&+ \int \mathrm{d}^3 r' \frac{1}{4\pi\epsilon_0\epsilon_{\mathrm{ex}}} \frac{\boldsymbol{P}(\boldsymbol{r}') \cdot \boldsymbol{d}}{|\boldsymbol{d}|^3} \Theta(r_0 + r_i - |\boldsymbol{d}|) \\
&+ \int\limits_{\boldsymbol{r}' \in \mathcal{A}} \mathrm{d}^2 r' \frac{1}{4\pi\epsilon_0\epsilon_{\mathrm{ex}}} \frac{\sigma}{|\boldsymbol{d}|} \Theta(r_i - |\boldsymbol{d}|).
\end{aligned}
\tag{5.18}
$$

The original Heaviside functions inherited from the functional $\mathcal{F}^{\mathrm{el}}$ in Eq. (5.5) are split according to $\Theta(x) = 1 - \Theta(-x)$. This is the reason for the appearance of the auxiliary quantities, denoted with the superscript $^{\mathrm{aux}}$ [see Eqs. (5.16) and (5.18)]. Since these quantities act like electric fields or potentials, respectively, we use the same corresponding notions for them. The advantage of this separation is of technical nature: on one hand, the integration domains in $\boldsymbol{E}^{\mathrm{aux}}$ [Eq. (5.16)] and Φ_i^{aux} [Eq. (5.18)] are bounded and therefore numerically manageable. On the other hand, the *total* electric field $\boldsymbol{E} = -\boldsymbol{\nabla}\Phi$ [Eq. (5.15)] and the *total* electric potential Φ [Eq. (5.17)] are determined by electrostatics and fulfill Poisson's equation with Neumann boundary conditions:

$$
\begin{aligned}
\Delta\Phi(\boldsymbol{r}) &= -\frac{1}{\epsilon_0\epsilon_{\mathrm{ex}}} \sum_{j=1}^{2} q_j \varrho_j(\boldsymbol{r}) + \frac{1}{\epsilon_0\epsilon_{\mathrm{ex}}} \boldsymbol{\nabla} \cdot \boldsymbol{P}(\boldsymbol{r}), \\
\int\limits_{\boldsymbol{r} \in \mathcal{A}} \mathrm{d}^2 r\, \boldsymbol{n}(\boldsymbol{r}) \cdot \boldsymbol{E}(\boldsymbol{r}) &= \frac{\sigma}{\epsilon_0\epsilon_{\mathrm{ex}}} |\mathcal{A}|, \\
\lim_{\lambda \to \infty} \int\limits_{\boldsymbol{r} \in \mathcal{B}(\lambda)} \mathrm{d}^2 r\, \boldsymbol{n}(\boldsymbol{r}) \cdot \boldsymbol{E}(\boldsymbol{r}) &= 0, \\
\mathcal{B}(\lambda) := \big\{ \boldsymbol{r} + \lambda \boldsymbol{n}(\boldsymbol{r}) &\in \mathbb{R}^3 | \boldsymbol{r} \in \mathcal{A} \big\}.
\end{aligned}
\tag{5.19}
$$

Hence, $\boldsymbol{E}$ and Φ are the solution of the boundary value problem posed by Eq. (5.19). Since the differential equation (5.19) has to be evaluated only locally, this route is technically more convenient than to perform the integrals over the whole space in Eqs. (5.15) and (5.17). The unit vectors $\boldsymbol{n}$ in the second and in the last line of Eq. (5.19) point into

the radial direction away from the wall and are locally perpendicular to the respective surface. $|\mathcal{A}|$ denotes the area of the wall surface $\mathcal{A}$. Poisson's equation (5.19) determines the potential Φ up to an additive constant which is chosen such that $\lim_{r \to \infty} \Phi(r) = 0$, i.e., the potential $\Phi(r)$ at any position r corresponds to the voltage with respect to the bulk at large distances from the wall ($r \to \infty$). Note that the equations for the density profiles [see Eqs. (5.11) and (5.12)] depend only on the differences $E - E^{\mathrm{aux}}$ and $\Phi - \Phi_i^{\mathrm{aux}}$.

Due to the dependence of the ELE (5.11) on both the position r *and* the orientation ω, in general the problem has to be solved in a high-dimensional space which is difficult to handle. However, for certain geometries of the electrode, this dimension can be reduced to a large extent [68]. To this end the distribution function f of the dipole orientations is introduced and expanded in terms of spherical harmonics:

$$f(r, \omega) := \frac{\varrho_0(r, \omega)}{\bar{\varrho}_0(r)} = \sum_{l=0}^{\infty} \sum_{m=-l}^{l} f_{lm}(r) Y_{lm}(\vartheta, \varphi). \tag{5.20}$$

Due to the definition of the orientation independent number density $\bar{\varrho}_0(r)$ in Eq. (5.2), f is normalized, i.e.,

$$\int \mathrm{d}^2\omega \, f(r, \omega) = 1, \tag{5.21}$$

which determines the value of the coefficient $f_{00}(r) = (4\pi)^{-1/2}$. In principle, the expansion in Eq. (5.20) leads to a dependence of the polarization P [Eq. (5.14)] on the coefficients f_{lm} of order $l = 1$, i.e., on $f_{1,0}$, $f_{1,1}$, and $f_{1,-1}$. However, for planar and spherical electrodes the orientation of P is perpendicular to the electrode surface everywhere and to all corresponding parallel surfaces. The respective normal component P is

$$P(r) = \sqrt{\frac{4\pi}{3}} m \bar{\varrho}_0(r) f_{1,0}(r), \tag{5.22}$$

i.e., the polarization depends only on the coefficient $f_{1,0}$, provided that the polar axis of the spherical harmonics is chosen perpendicular to the electrode surface pointing away from the wall. Likewise the electric fields E and E^{aux} are perpendicular to the surface $\mathcal{A}$ with components E and E^{aux}, respectively. This facilitates integration over the orientations ω such that the ELE (5.11) for $\varrho_0(r, \omega)$ can be split into two equations (see Appendix 5.B): one for the orientation independent density

$$\bar{\varrho}_0(r) = \varrho_0^{\mathrm{b}} \Big\{ \exp \Big[-\beta V_0(r) + c_0^{\mathrm{hs}}(r) - c_0^{\mathrm{hs,b}} + c_0^{\mathrm{att}}(r) - c_0^{\mathrm{att,b}} \Big] \Big\}$$
$$\times \frac{\sinh\{\beta m [E(r) - E^{\mathrm{aux}}(r)]\}}{\beta m [E(r) - E^{\mathrm{aux}}(r)]}, \tag{5.23}$$

and another one for the coefficient

$$f_{1,0}(\boldsymbol{r}) = \sqrt{\frac{3}{4\pi}} \mathcal{L}\{\beta m[E(\boldsymbol{r}) - E^{\mathrm{aux}}(\boldsymbol{r})]\} \tag{5.24}$$

with the Langevin function $\mathcal{L}(x) = \coth(x) - 1/x$. Altogether the model is described by four equations: one for each of the number densities $\varrho_i(\boldsymbol{r})$ of the ion species $i \in \{1, 2\}$ [see Eq. (5.12)], one for the solvent number density $\bar{\varrho}_0(\boldsymbol{r})$ independent of the dipole orientation [see Eq. (5.23)], and one for the orientation coefficient $f_{1,0}(\boldsymbol{r})$ of the dipoles [see Eq. (5.24)]. The entire dependence on the orientation $\boldsymbol{\omega}$ is covered by the latter quantity. Therefore and because in the case of planar and spherical electrodes the four profiles $\bar{\varrho}_0$, ϱ_1, ϱ_2, and $f_{1,0}$ vary only along the direction perpendicular to the surface, the dimensionality of the original problem has been reduced considerably.

5.2.3   Behavior at large distances from the wall

Equations (5.12), (5.16), (5.18), (5.19), (5.22), (5.23), and (5.24) form a complicated system of coupled nonlinear integro-differential equations, which can be solved only numerically; here this is accomplished by means of the Piccard iteration scheme (see Sec. 8.1 in Ref. [61]). This requires discretization of the various profiles on a large but finite grid along the radial direction. This approach requires assumptions concerning the profiles outside the numerical grid at large distances from the wall. Here it is assumed that the one-point direct correlation functions $c_i^{\mathrm{hs}}(\boldsymbol{r})$ and $c_i^{\mathrm{att}}(\boldsymbol{r})$ decay rapidly towards their bulk values $c_i^{\mathrm{hs,b}}$ and $c_i^{\mathrm{att,b}}$, respectively, such that in Eqs. (5.11) and (5.12) the differences $c_i^{\mathrm{hs}}(\boldsymbol{r}) - c_i^{\mathrm{hs,b}}$ and $c_i^{\mathrm{att}}(\boldsymbol{r}) - c_i^{\mathrm{att,b}}$ can be neglected outside the numerical grid. (See Appendix 5.D for a detailed discussion of the decay behavior of these one-point direct correlation functions.) Global charge neutrality requires the vanishing of the electric field $\boldsymbol{E}$ infinitely far away from the wall [see the third line of Eq. (5.19)]. Since a numerical grid can span only a finite distance from the wall, the solution of Poisson's equation (5.19) in the asymptotic range outside the grid has to be determined, e.g., in terms of a linearized theory and matched with the numerical solution inside the grid. Therefore the electric fields $\boldsymbol{E}(\boldsymbol{r})$ and $\boldsymbol{E}^{\mathrm{aux}}(\boldsymbol{r})$ as well as the potentials $\Phi(\boldsymbol{r})$ and $\Phi_i^{\mathrm{aux}}(\boldsymbol{r})$ are not required to vanish outside the numerical grid. Instead it is assumed that at large distances from the wall the electric fields and potentials are sufficiently small to allow for a linearization of the exponential function in Eqs. (5.11) and (5.12) such that the ELEs are given by Eqs. (5.52) and (5.53) in Appendix 5.C. It can be shown by means of Eqs. (5.15) – (5.18) that for equally-sized ions and weakly charged walls the quantities $E_x - E_x^{\mathrm{aux}}$, $E_y - E_y^{\mathrm{aux}}$, $E_z - E_z^{\mathrm{aux}}$, $\Phi - \Phi_1^{\mathrm{aux}}$, and $\Phi - \Phi_2^{\mathrm{aux}}$ (i) exhibit the same asymptotic decay behavior at large distances from the wall ($\boldsymbol{r} \to \infty$) and (ii) are proportional to the surface charge density (see Appendix 5.C for details). We make use of this property by introducing *constants*

k^E, k_1^Φ, and k_2^Φ,

$$k_i^\Phi := -\lim_{\boldsymbol{r}\to\infty} \frac{\Phi_i^{\mathrm{aux}}(\boldsymbol{r})}{\Phi(\boldsymbol{r})}, \quad k^E := -\lim_{\boldsymbol{r}\to\infty} \frac{E^{\mathrm{aux}}(\boldsymbol{r})}{E(\boldsymbol{r})}, \tag{5.25}$$

for systems with weakly charged planar walls, where E and E^{aux} denote the radial components of the electric fields. Since both numerators and denominators in Eq. (5.25) exhibit the same decay behavior, as well as the asymptotic proportionality to σ in the limit $\sigma \to 0$, to leading order the constants do not vary spatially and do not depend on the surface charge density. It has turned out numerically that the constants k^E, k_1^Φ, and k_2^Φ as determined for a weakly charged planar wall are valid for all curvatures and surface charges used in the present study. Moreover, this procedure has been found to work also for small differences between the particle radii, which are at most as large as the ones considered in the following. By using Eq. (5.25) the asymptotically leading contribution to the auxiliary fields in Eqs. (5.52) and (5.53) in Appendix 5.C can be expressed in terms of the constants k^E, k_1^Φ, and k_2^Φ as well as the total electric potential Φ and the radial component E of the total electric field. [Note that the radial component of the electric field is the relevant one (see Appendix 5.B).] A treatment analogous to the one in Sec. 5.2.2 and in Appendix 5.B leads to the ELEs for the four relevant profiles

$$\varrho_i(\boldsymbol{r}) \simeq \varrho_i^{\mathrm{b}} \left[1 - \beta q_i \Phi(\boldsymbol{r}) \left(1 + k_i^\Phi \right) \right], \ i \in \{1, 2\}, \tag{5.26}$$

$$\bar{\varrho}_0(\boldsymbol{r}) \simeq \varrho_0^{\mathrm{b}}, \tag{5.27}$$

$$f_{1,0}(\boldsymbol{r}) \simeq \frac{1}{3}\sqrt{\frac{3}{4\pi}} \beta m \left(1 + k^E \right) E(\boldsymbol{r}), \tag{5.28}$$

which correspond to simplified versions of Eqs. (5.12), (5.23), and (5.24). Equations (5.26) – (5.28) together with Poisson's equation (5.19) lead to a linearized, modified Poisson-Boltzmann equation

$$\Delta\Phi(\boldsymbol{r}) \simeq \frac{\dfrac{e^2 I \beta}{\epsilon_0 \epsilon_{\mathrm{ex}}} \left(2 + k_1^\Phi + k_2^\Phi \right)}{1 + \dfrac{\varrho_0^{\mathrm{b}} \beta m^2}{3\epsilon_0 \epsilon_{\mathrm{ex}}} \left(1 + k^E \right)} \Phi(\boldsymbol{r}) = \kappa^2 \Phi(\boldsymbol{r}). \tag{5.29}$$

The requirement to recover the Debye length $1/\kappa$ in Eq. (5.29) with

$$\kappa := \sqrt{\frac{2e^2 I \beta}{\epsilon_0 \epsilon}}, \tag{5.30}$$

and with the *total* relative permittivity ϵ defines the excess relative permittivity

$$\epsilon_{\mathrm{ex}} = \epsilon \left[1 + \frac{1}{2} \left(k_1^\Phi + k_2^\Phi \right) \right] - \frac{\varrho_0^{\mathrm{b}} \beta m^2}{3\epsilon_0} \left(1 + k^E \right). \tag{5.31}$$

Parameter	Case A	Case B
κr_0	0.1617	0.05114
$\varrho_0^{\mathrm{b}}/\kappa^3$	29.36	931.8
I/κ^3	0.05329	0.1685
$\kappa m/e$	0.04012	0.01269
βu	-1.500	-1.500
κr_c	0.5821	0.1841
ϱ_w/κ^3	9.843	311.3

Table 5.1: Two sets of values for those independent, dimensionless parameters which are kept fixed for each case studied numerically (see Sec. 5.2.4). The choice of values for the remaining dimensionless parameters [κr_1, κr_2, κR, and $\sigma/(e\kappa^2)$] will be quoted for the corresponding numerical results. The choices of the values of the dimensionless parameters given in the table are guided by adopting realistic values for the corresponding dimensional quantities (see the main text). The values in case A assume the Debye length as $1/\kappa \approx 9.600\times 10^{-10}$ m and $1/\kappa \approx 3.036\times 10^{-9}$ m in case B. Both cases correspond to the energy scale $\beta \approx 2.414\times 10^{20}$ J^{-1}, i.e., $T = 300$ K. The parameter values for case B emerge from those of case A by multiplying the latter by $(1/\kappa_A)/(1/\kappa_B)$ and $[(1/\kappa_B)/(1/\kappa_A)]^3$, respectively, and by replacing I_A by $I_B = I_A/10$.

Note that in the case of vanishing particle volumes, i.e., $k_1^\Phi = k_2^\Phi = k^E = 0$, and vanishing dipole moment $m = 0$ the excess relative permittivity equals the total relative permittivity $\epsilon_{\mathrm{ex}} = \epsilon$. The linearized modified Poisson-Boltzmann equation (5.29) can be solved analytically within the geometries under consideration.

5.2.4   Choice of parameters

If lengths, charges, and energies are measured in units of the Debye length $1/\kappa$ [Eq. (5.30)], the elementary charge e, and the thermal energy $1/\beta = k_B T$, respectively, the present model of a monovalent salt solution is specified by the following eleven independent, dimensionless parameters: κr_0, κr_1, κr_2, $\varrho_0^{\mathrm{b}}/\kappa^3$, I/κ^3, $\kappa m/e$, βu, κr_c, κR, $\sigma/(e\kappa^2)$, and ϱ_w/κ^3. This implies that those systems are equivalent, which exhibit the same values for these dimensionless parameters. Note that for this choice of forming dimensionless ratios the relative permittivity ϵ is not an independent parameter but is absorbed in the expression of the Debye length [Eq. (5.30)]. The present study is focused on examining the influence of the electrode geometry. Therefore and for illustration purposes, in the following some of these parameters are fixed to certain, realistic values, i.e., they are chosen such that, at best, they describe a realistic system. Table 5.1 provides an overview of the corresponding dimensionless parameters for two cases A and B. The choices of the parameter values within each case and for the two cases relative to each other are guided

by adopting realistic values for the corresponding dimensional quantities. These would, for example, refer to an aqueous electrolyte solution at room temperature $T = 300\,\text{K}$ and ambient pressure $p \approx 1013\,\text{hPa}$. The dipole moment $m = 1.85\,\text{D} \approx 6.171 \times 10^{-30}\,\text{Cm}$ of the model solvent particles is chosen corresponding to the literature value of m for the water molecule [109, 110]. The relative permittivity of water in static fields takes the value of $\epsilon = 77.7003$ for the temperature chosen here [110]. The equation of state for the pure solvent is derived from the functional Eq. (5.3) in the bulk and is matched to the saturation properties of liquid water at $T = 300\,\text{K}$, i.e., its saturation number density and its pressure [111]. This fixes the particle radius of the solvent to $r_0 \approx 1.552 \times 10^{-10}\,\text{m}$. In addition the amplitude u and range r_c of the attractive interaction [Eq. (5.7)] are adjusted in order to obtain the best possible agreement between the first peak of the structure factor of the present model and the corresponding data for water determined by X-ray scattering (see p. 347 in Ref. [112]). This way one obtains the values $u \approx -1.500 \times k_B T$ and $r_c = 3.6 \times r_0$; recall that within the present approach the interaction potentials between the substrate particles and the fluid particles are chosen to be the same square well ones as the ones among the fluid particles. Finally, in the model under consideration the homogeneous number density ϱ_w of the particles forming the electrode enters into the strength of the attractive interaction [Eq. (5.8)] between the wall and the fluid particles. Its value is estimated from the number density profile of the pure solvent in contact with an uncharged planar wall. The choice $\varrho_w \approx 1.112 \times 10^{28}\,\text{m}^{-3}$ ensures that the number density peak closest to the wall matches that of water in contact with a single graphene layer [113]. Although the value of ϱ_w is expected to depend on the chosen electrode material, the aforementioned value leads to a surprisingly good agreement also with the data corresponding to an aqueous electrolyte solution at a charged Ag-surface (see Fig. 4a in Ref. [114]). Case A corresponds to an ionic strength $I = 0.1\,\text{M}$, i.e., to a Debye length $1/\kappa \approx 9.600 \times 10^{-10}\,\text{m}$, whereas case B corresponds to $I = 0.01\,\text{M}$, i.e., $1/\kappa \approx 3.036 \times 10^{-9}\,\text{m}$. The pressure p follows from the equation of state derived from the functional Eq. (5.3) in the bulk with the equilibrium number densities ϱ_0^b and I. The ELEs in the bulk relate the chemical potentials μ_i [Eq. (5.3)] and the thermal wave lengths Λ_i [Eq. (5.4)], $i \in \{0, 1, 2\}$, with bulk quantities which have already been quoted at the beginning of the current Subsec. 5.2.4. Therefore, in this sense μ_i and Λ_i are not independent variables. The solvent number density ϱ_0^b has to be adjusted in order to render the required value of the pressure p for all examined ionic configurations. However, these variations are marginal such that for given κ the numerical value of ϱ_0^b/κ^3 in Tab. 5.1 is valid with the precision of four significant digits. It is not claimed that the present model is able to accurately describe liquid water because it lacks crucial properties such as hydrogen bonds and the tetrahedral shape of the water molecules. Nevertheless, this procedure precludes one from choosing arbitrary parameter values which correspond to "exotic" or even unrealistic systems. In the following this type of system, corresponding

to the *civ*ilized model introduced in Secs. 5.2.1 – 5.2.3, is abbreviated by "CIV", possibly in conjunction with additional parameter specifications or modifications (e.g., a vanishing dipole moment, $m = 0$). In the following the remaining dimensionless parameters r_1/r_0, r_2/r_0, $\sigma/(e\kappa^2)$, and κR are varied and their influence on the structure of the electrolyte solution is studied. The radii r_1 and r_2 of the ions are given in units of the radius r_0 of the solvent particles, which is equivalent to providing them in units of $1/\kappa$, and we choose either $r_1 \leq r_0 \leq r_2$ or $r_2 \leq r_0 \leq r_1$. By choosing special values for some of the parameters, other well known models can be obtained within the described framework. For the *restricted primitive model* (RPM) one has $r_1 = r_2$, $m = 0$, $\beta u = 0$, and $\varrho_0^b = 0$, and for the *Poisson-Boltzmann* (PB) description one has $r_1 = r_2 = 0$, $m = 0$, $\beta u = 0$, and $\varrho_0^b = 0$.

5.3 Discussion

In Fig. 5.2 various profiles relevant for the electrostatics are displayed as functions of the distance z from a charged planar wall. The CIV model, within which all particles have the same radius, and PB (see Sec. 5.2.4) are compared with each other. The electrode is positively charged and consequently the electrostatic potential Φ [Fig. 5.2(a)] has a positive value at the wall. Qualitatively there are no significant differences in Φ between PB and CIV and even quantitatively both models lead to similar results. This is in contrast to the charge density [Fig. 5.2(b)]. Within the microscopic CIV the centers of the fluid particles cannot get closer to the wall than their own radius. Hence, there is a discontinuity at the distance of contact. Furthermore, again due to the non-vanishing particle volumes, the charge density exhibits a layered structure close to the wall. For clarity of the presentation the solvent profile $\bar{\varrho}_0(z)$ is not shown here. However, it is noteworthy that the high density of the solvent particles contributes considerably to the pronounced layering of the charge density. It is remarkable that the oscillating behavior of the charge density corresponds to a rather smooth potential Φ. In contrast, in the case of PB, within which the particle volumes are neglected, the charge density exhibits a monotonic behavior. The polarization, the component P of which in the direction normal to the wall [Eq. (5.22)] is shown in Fig. 5.2(c), is identically zero in PB. Within CIV also this profile has a layered structure close to the wall. Its positive value is in accordance with expectation because it corresponds to dipoles, which, on average, point away from the positively charged wall. The discontinuity at contact with the wall causes the slight kink in Φ at the same distance [see Eq. (5.19)]. At large distances from the wall both models exhibit a monotonic exponential decay on the scale of the Debye length $1/\kappa$.

Figure 5.3 shows results for the same models as in Fig. 5.2 but for a larger value of the reduced surface charge density. As expected, the larger surface charge density leads to an increase of the absolute values of the shown profiles. In addition nonlinear effects are more
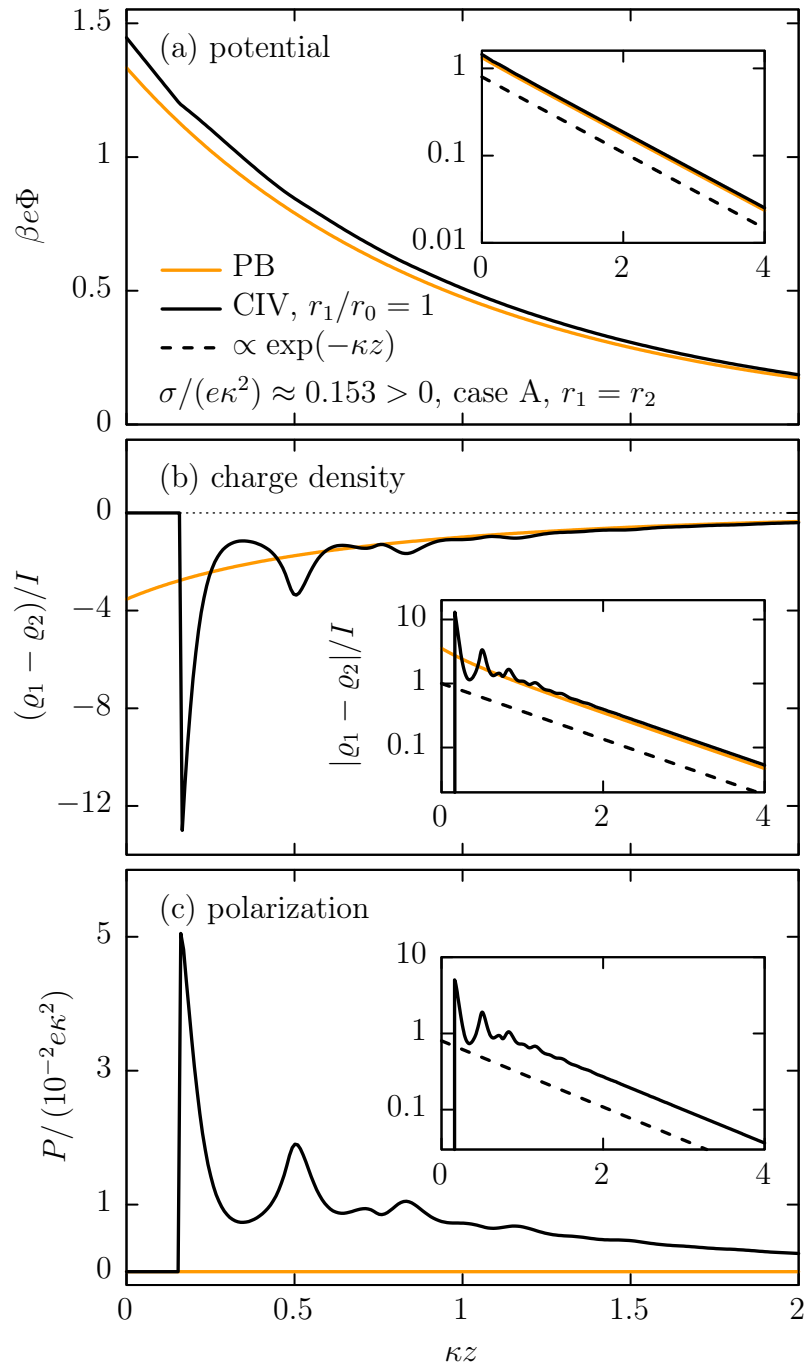
Figure 5.2: Reduced electrostatic potential $\beta e\Phi$ [panel (a)], reduced charge density $(\varrho_1 - \varrho_2)/I$ [panel (b)], and component $P/(10^{-2}e\kappa^2)$ of the reduced polarization in the direction normal to the wall [Eq. (5.22), panel (c)] as functions of the reduced distance κz from a planar electrode with reduced surface charge density $\sigma/(e\kappa^2) \approx 0.153$. The CIV model and PB corresponding to case A (see Sec. 5.2.4) are compared with each other. The insets reveal that at large distances from the wall the displayed profiles of both models exhibit an exponential decay on the scale of the Debye length $1/\kappa$. The specifications given in panel (a) apply for (b) and (c), too.
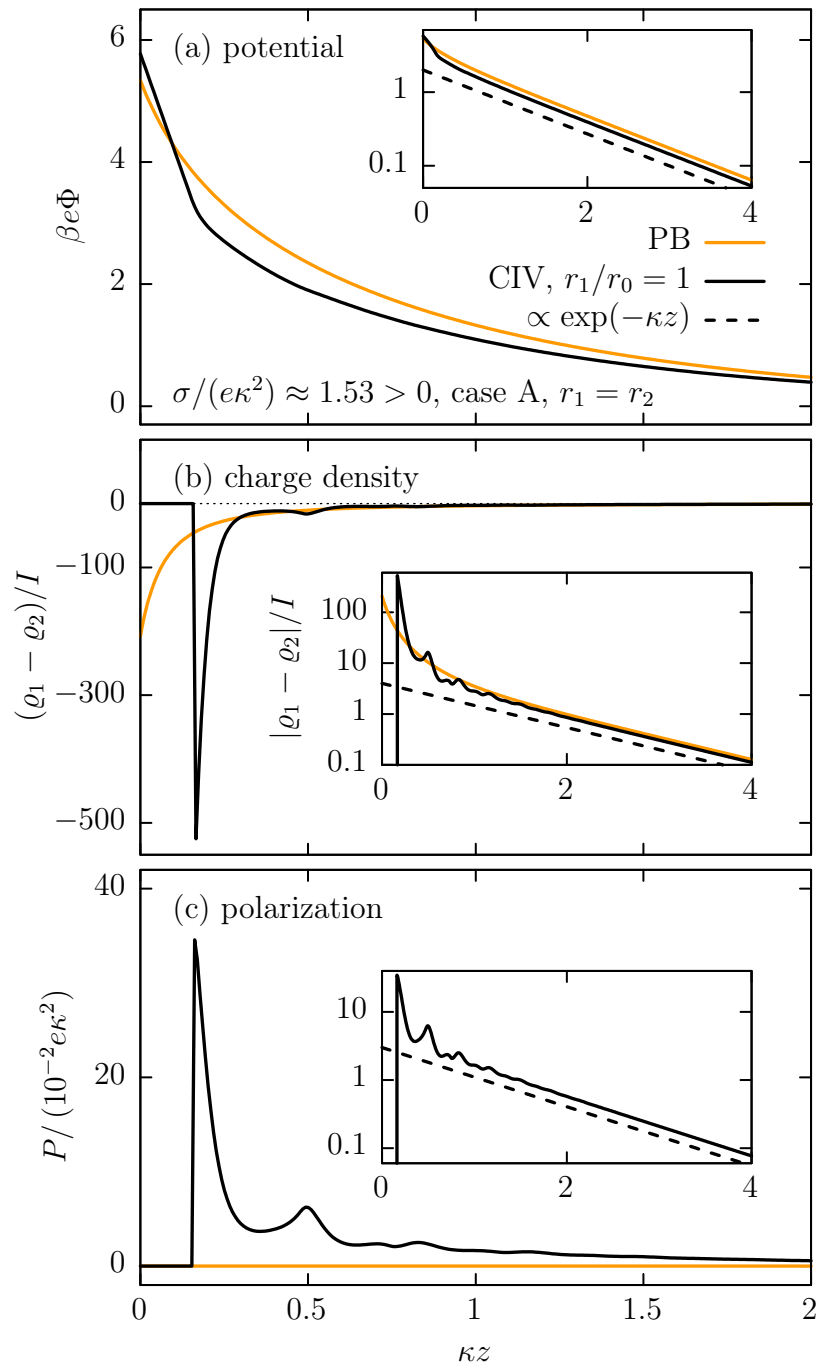
Figure 5.3: Same as Fig. 5.2 but for a larger value $\sigma/(e\kappa^2) \approx 1.53$ of the reduced surface charge density.

pronounced than in Fig. 5.2. This is clearly visible in the insets of panel (b): in Fig. 5.2 the PB result for the reduced charge density is almost a straight line which is in accordance with the linearized PB equation; in Fig. 5.3 deviations from an exponential behavior occur. The layering of the reduced charge density [Fig. 5.3(b)] and of the component of the reduced polarization in the direction normal to the wall [Fig. 5.3(c)] within the CIV
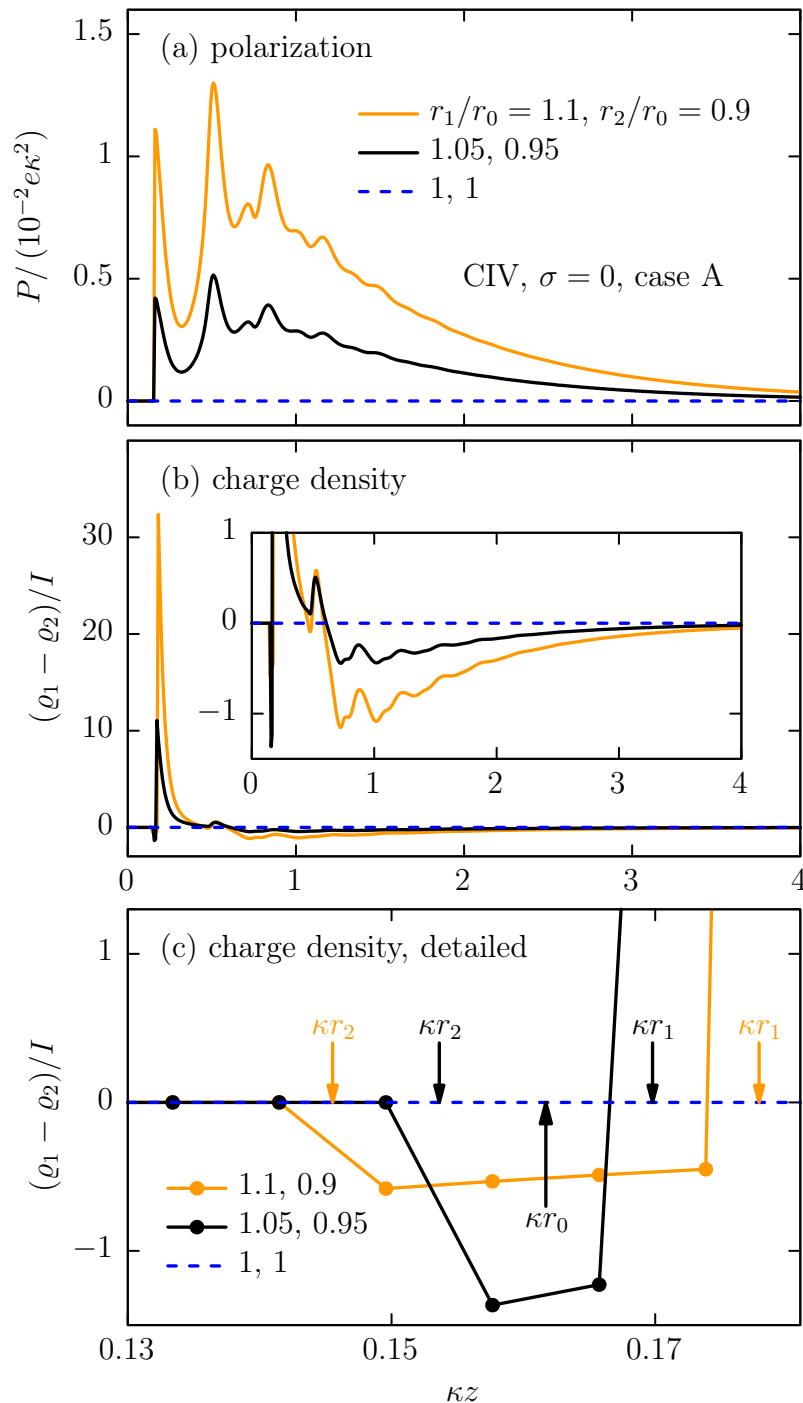
Figure 5.4: Component $P/(10^{-2}e\kappa^2)$ of the reduced polarization in normal direction [Eq. (5.22), panel (a)] and reduced charge density $(\varrho_1 - \varrho_2)/I$ [panels (b) and (c)] of an electrolyte solution as functions of the reduced distance κz from an uncharged planar electrode at $z = 0$. The system is described by case A in the CIV model (see Sec. 5.2.4). Unequal particle radii give rise to nonzero profiles of the charge density although the wall is not charged. Panel (c) provides an enlarged view of the charge density close to the wall. There the data are plotted in the form of circles on the numerical grid points only and the connecting straight lines are drawn to guide the eye. The specifications given in panel (a) apply for (b) and (c), too. For further discussions of the panels and in particular of the arrows in (c), see the main text.

model is less pronounced in the case of high surface charges. That is, in comparison with Fig. 5.2, the peak closest to the wall is large relative to the subsequent peaks. For large distances from the wall, PB predicts a larger value for both the potential [Fig. 5.3(a)] and the absolute value of the charge density [inset of Fig. 5.3(b)] than the CIV model does. However, at contact with the electrode the order is reversed.

Figure 5.4 shows results for the CIV model for various particle radii. The profiles are shown as functions of the distance z from an *uncharged* planar wall. If all radii are equal, i.e., $r_1/r_0 = r_2/r_0 = 1$, there is no electric field present and the profiles of the charge density and the polarization in Fig. 5.4 vanish identically due to symmetry reasons. This changes in the case of different values of the radii. Figure 5.4(c) provides an enlarged view of the charge density close to the wall. (Due to the large zoom factor there the points of the numerical grid become visible.) The arrows pointing downwards indicate the reduced positions of closest approach of the ions (κr_1 and κr_2). The colors of the arrows and their labels correspond to the colors of the keys. The arrow pointing upwards indicates the reduced position of closest approach of the solvent particles (κr_0) which is the same for all systems shown there. The space between the electrode surface $z = 0$ and the point of closest approach (κr_2) of the smaller ions (here negative) cannot be penetrated by any particle; in this region the charge density is identically zero. Subsequently, in the direction away from the wall the charge density is negative because only negative ions can approach that space. This holds up to the point beyond which the positive ions are able to penetrate that space (κr_1); there the charge density becomes positive. The further behavior is visible in Fig. 5.4(b) which shows a high but narrow positive peak. The inset of Fig. 5.4(b) reveals that this positive charge is compensated by the subsequent wide region of negative charge density such that global charge neutrality is fulfilled. The polarization [Fig. 5.4(a)] has a discontinuity at the position $z = r_0$, i.e., at the point of closest approach of the solvent particles. In Fig. 5.4(c), the arrow pointing upwards indicates this position κr_0. Because the value of the radius of the solvent particles is chosen to be in between the values of the radii of the ions, the discontinuity of the polarization (κr_0) is located to the right of the point of closest approach of the negative ions (κr_2) and to the left of the point of closest approach of the positive ions (κr_1).

In the following we discuss the properties of an electrolyte solution in contact with an electrode in terms of the differential capacitance [34]

$$C := \frac{\partial \sigma}{\partial \Phi(\boldsymbol{r})|_{\mathcal{A}}} \tag{5.32}$$

which is the change of the surface charge density σ upon varying the (constant) potential at the wall $\Phi(\boldsymbol{r})|_{\mathcal{A}}$ taken relative to its bulk value. Within the present study the ELEs in Sec. 5.2.2 are solved for various values of the surface charge density σ. Together with the solutions of the ELEs the electric potential Φ [Eq. (5.17)] is known. The relation between
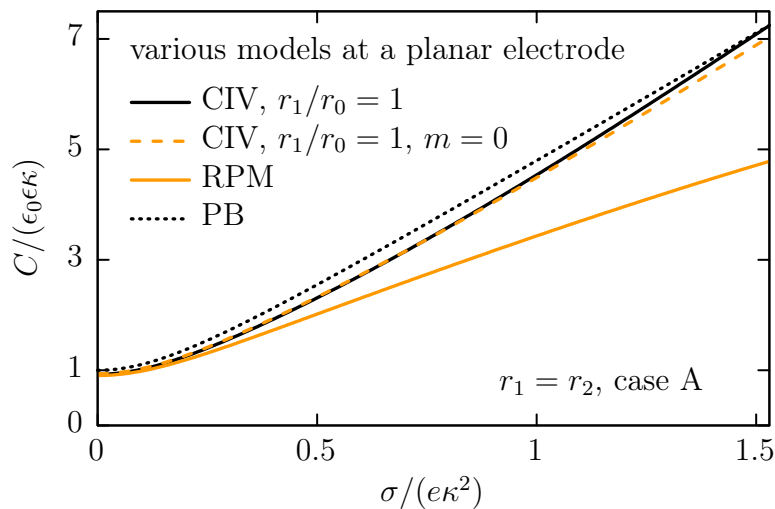
Figure 5.5: Reduced differential capacitance $C/(\epsilon_0\epsilon\kappa)$ as a function of the reduced surface charge density $\sigma/(e\kappa^2)$ of a planar electrode. The electrolyte solution corresponding to case A is described as indicated by various models in which the ionic radii are chosen to be equal ($r_1 = r_2$, see Sec. 5.2.4).

the potential at the wall and σ is used in order to determine C [Eq. (5.32)] numerically. The differential capacitance is experimentally accessible, e.g., via cyclic voltammetry, chronoamperometry, and impedance spectroscopy [2]. It contains integrated properties of the structure of the electrolyte solution (see, e.g., Figs. 5.2 – 5.4). This facilitates the comparison with other models and the analysis of the influence of the parameters r_1/r_0, r_2/r_0, $\sigma/(e\kappa^2)$, I/κ^3, and κR.

Figure 5.5 depicts results of various models in which the ionic radii are chosen to be equal ($r_1 = r_2$, see Sec. 5.2.4). The electrolyte solution is in contact with a planar electrode the rescaled surface charge density σ of which is the horizontal axis. Here and in the following, the differential capacitance is plotted in units of the double-layer capacitance $\epsilon_0\epsilon\kappa$ which facilitates comparison with Gouy-Chapman results (see also Ref. [94] and Chap. 4). Within the range shown, all displayed curves exhibit the same characteristics as the PB result: for small σ the differential capacitance attains a constant with zero slope. Upon increasing σ also the capacitance increases; the main differences between the models are borne out within this range. The two indicated CIV results differ with respect to the strength of the dipole moment m: in one case (black solid line) the latter is chosen according to Sec. 5.2.4 and in the other case (orange dashed line) it is set to zero. The two curves almost coincide and only for large values of σ a small deviation is visible. Hence, for these two systems the influence of the dipole moment is relatively weak. This finding is in accordance with previous studies of the differential capacitance [54,71] as well as of wetting phenomena [68] for which the explicit dipole description turned out to have a relatively small effect. The agreement between the simple PB and the comparatively complex CIV
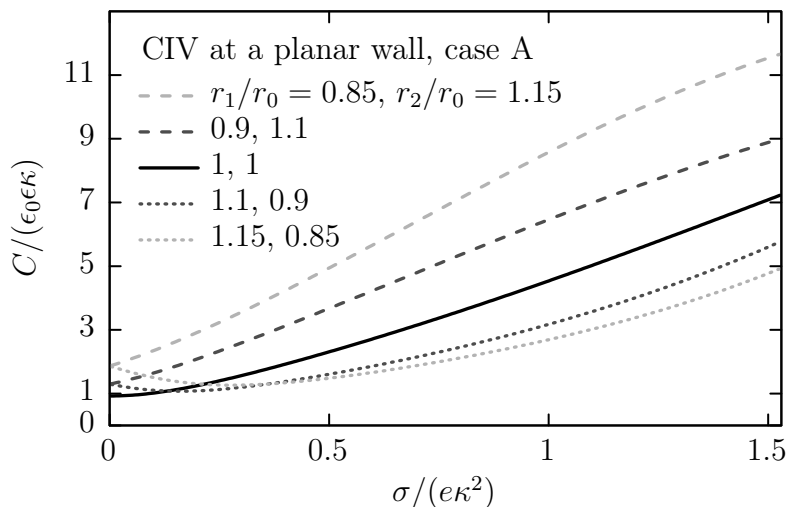
Figure 5.6: Reduced differential capacitance $C/(\epsilon_0\epsilon\kappa)$ as a function of the reduced surface charge density $\sigma/(e\kappa^2)$ of a planar electrode. The electrolyte solution is described within the CIV model in case A (see Sec. 5.2.4). Curves with the same shade of gray correspond to the same *set* of ion size ratios $\{r_1/r_0, r_2/r_0\}$ where the cations are the larger ions $(r_1/r_0 > r_2/r_0)$ for dotted curves whereas the anions are the larger ions $(r_1/r_0 < r_2/r_0)$ for dashed curves. The PB result turns out to be close to the solid black curve (see Fig. 5.5).

models throughout the studied range is remarkable, in particular when taking into account that RPM, endowed with an intermediate degree of complexity, clearly shows deviations from the otherwise common trend. An explanation for this observation could be that within CIV and PB all particles of the electrolyte solution are described consistently on the same footing whereas within RPM they are not: within PB all particles are pointlike and within the displayed cases of CIV the particles are treated as hard spheres of *equal* radii. In contrast, within RPM the solvent is a structureless continuum and the ions are described as hard spheres of finite size.

In Fig. 5.6 the influence of various choices for the ionic radii is examined within CIV: the solid curve corresponds to the case in which all radii are equal whereas they are unequal for the other curves. In the limit of an uncharged ($\sigma \to 0$) electrode the capacitance increases with increasing difference between the ionic radii. Curves with the same shade of gray correspond to the same *set* of ion size ratios $\{r_1/r_0, r_2/r_0\}$ where the cations are the larger ions $(r_1/r_0 > r_2/r_0)$ for dotted curves whereas the anions are the larger ions $(r_1/r_0 < r_2/r_0)$ for dashed curves. As expected, curves of the same shade concur at the vertical axis: For $\sigma \to 0$ swapping the ion radii is equivalent to flipping the sign of all charges and the latter does not change the differential capacitance C [see Eq. (5.32)]. However, for a charged electrode ($\sigma > 0$) this equivalence does not hold and for the differential capacitance two branches occur. If the positive ions are the smaller
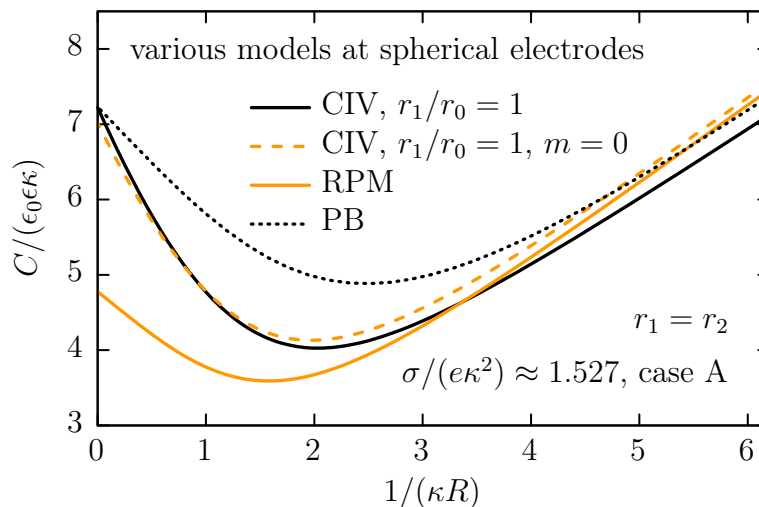
Figure 5.7: Reduced differential capacitance $C/(\epsilon_0\epsilon\kappa)$ as a function of the dimensionless curvature $1/(\kappa R)$ of spherical electrodes. The electrolyte solution corresponding to case A (see Sec. 5.2.4) is described by the same models as the ones used in Fig. 5.5. The value of the reduced surface charge density is $\sigma/(e\kappa^2) \approx 1.527$. The planar limit $[1/(\kappa R) = 0]$ corresponds to that planar electrode in Fig. 5.5 with the highest surface charge density.

(larger) particles, the capacitance curve exhibits (non-)monotonic behavior within the investigated interval of σ. Compared to the models in Fig. 5.5, where the ionic radii are chosen to be equal, the decrease of C for small values of σ is a new feature in Fig. 5.6 for $r_1/r_0 > 1$ and $r_2/r_0 < 1$. On the other hand, for $r_1/r_0 < 1$ and $r_2/r_0 > 1$ the capacitance increases rapidly thus leading to values of C larger than those for the cases shown in Fig. 5.5. Due to the symmetries of the present model the differential capacitance fulfills the relation $C(r_1, r_2, \sigma) = C(r_2, r_1, -\sigma)$, where the first, second, and third argument are the cation radius, the anion radius, and the surface charge density, respectively. That is, if the capacitance is known for a particular system, the same capacitance is obtained for a system in which the values of the ionic radii are swapped and the surface charge density is taken to be opposite. This explains why curves with the same shade of gray meet at $\sigma = 0$ in Fig. 5.6. Moreover the above relation enables one to extend the curves in Fig. 5.6 to negative values of σ. For unequal values of the ionic radii the resulting curve has a minimum at a certain nonzero value of σ and the curve is not symmetric with respect to this minimum. The shape of such a curve is in better qualitative agreement with experimental findings than the curve for $r_1 = r_2$ which is symmetric around the minimum at $\sigma = 0$ (see, e.g., Ref. [28]).

So far the focus has been on planar electrodes (see Figs. 5.2 – 5.6). In Fig. 5.7 the same models as in Fig. 5.5 are used in order to investigate electrolyte solutions in contact with spherical electrodes of various radii R. The surface charge density of $\sigma/(e\kappa^2) \approx 1.527$ is chosen such that the planar limit, i.e., for zero curvature $1/(\kappa R) = 0$, corresponds to that
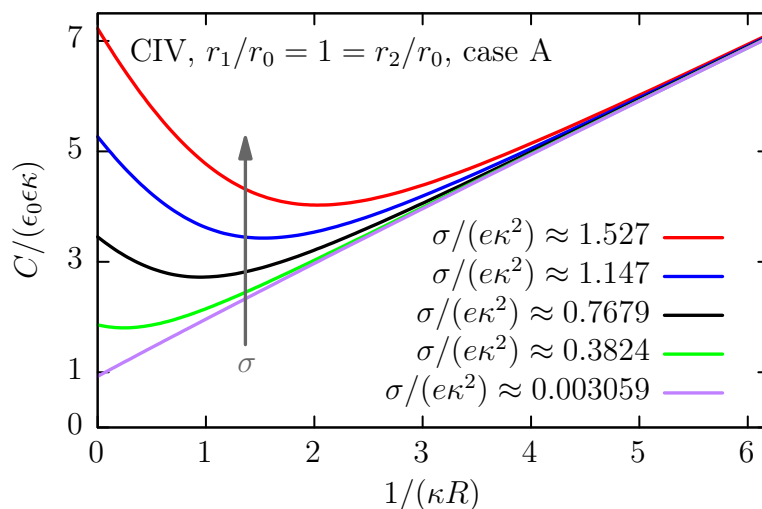
Figure 5.8: Reduced differential capacitance $C/(\epsilon_0\epsilon\kappa)$ as a function of the dimensionless curvature $1/(\kappa R)$ of spherical electrodes. The displayed data correspond to an electrolyte solution described by case A in the CIV model (see Sec. 5.2.4) with equal particle radii $r_1/r_0 = 1 = r_2/r_0$. Each curve corresponds to a certain value of the surface charge density σ. The vertical arrow indicates the direction of increasing σ.

planar electrode in Fig. 5.5 with the largest surface charge density. In this planar limit PB and CIV (dotted and solid black line in Fig. 5.5, respectively) yield almost the same value for the differential capacitance. However, in Fig. 5.7 differences between the two models appear for nonzero curvatures, i.e., finite electrode radii: PB predicts larger values for the capacitance than CIV. Hence, compared with the situation at planar electrodes, where PB is a surprisingly accurate approximation for CIV with equal particle radii, at curved electrodes larger deviations occur. It is likely that these differences originate from the hard-sphere character of the particles within CIV. As within PB, the charged electrode interacts with the charges of the ions and denies them access to a certain R-dependent volume. However, in the case of CIV in addition the layering of the particles is influenced by varying the radius of the electrode. A mechanism of such kind is not present within PB. This might explain, why between CIV and PB there are differences in the curvature dependences and why the importance of microscopic details hinges on the geometry of the electrode. Again (as in Fig. 5.5) the two CIV results shown in Fig. 5.7 are close to each other indicating that within CIV the dipole moment has no significant effect on the capacitance. Since already at a planar wall RPM exhibits clear deviations from the other models (see Fig. 5.5), it does not come as a surprise, that the curve predicted by it deviates considerably also at spherical electrodes (see Fig. 5.7). For small wall radii the various models seem to attain a linear dependence on curvature and, compared with intermediate values of the curvature, these lines are relatively close to each other.

Figures 5.8 – 5.14 display the differential capacitance C of spherical electrodes as a
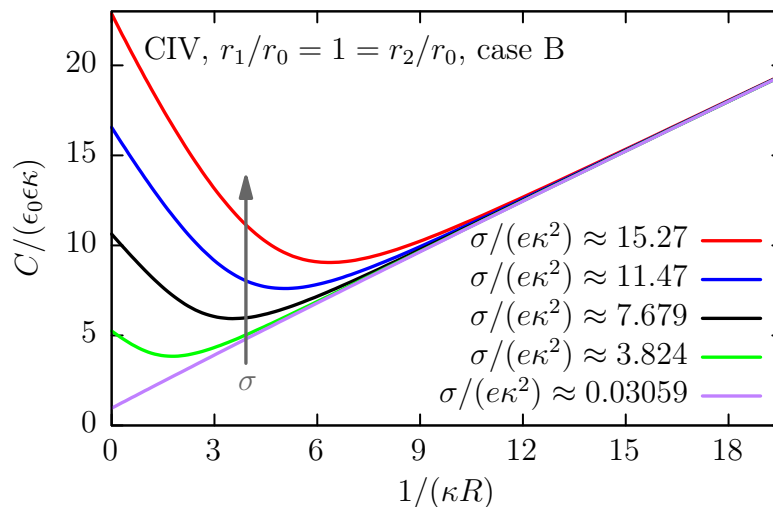
Figure 5.9: Same as Fig. 5.8 for case B (see Sec. 5.2.4).

function of their curvature $1/(\kappa R)$. The corresponding data are obtained within CIV (see Sec. 5.2.4) and each curve corresponds to a fixed value of the surface charge density σ. For $1/(\kappa R) = 0$ the capacitance values reduce to the corresponding ones for a planar wall. For the largest curvatures considered, the radius of the electrode approximately equals the radii of the fluid particles. It is remarkable that all systems studied exhibit a common behavior for *large* curvatures: irrespective of the value of σ all curves converge to the graph corresponding to $\sigma \to 0$. However, the dependence on σ becomes non-trivial for small curvatures. A similar general behavior for *large* curvatures has been observed in part I (Ref. [94] and Chap. 4) of this study, where the PB model is discussed in detail. There it is possible to show analytically, that for sufficiently small radii (i.e., large curvatures) of the electrode the linearized version of the PB equation is a reliable description. Within the linearized PB theory the electrode potential is proportional to the surface charge density and hence the differential capacitance is independent of σ. This explains within PB, why at large curvatures the dependence of the capacitance C on σ disappears. It is not possible to analytically analyze the CIV model as detailed as PB. However, the data from the CIV model in the present study reveal the same behavior as in the PB model, i.e., the dependence of C on σ weakens for large curvatures. Furthermore, Fig. 5.15 demonstrates that the capacitance C at large curvatures is also independent of the radii of the particles. Hence the capacitance exhibits a general behavior for *large* curvatures which is independent of σ and of the particle radii.

Figures 5.8 – 5.10 are related because in the cases studied there the radii of all particles are chosen to be equal. Compared with Fig. 5.8, in Fig. 5.9 the ionic strength is reduced, and in Fig. 5.10 the dipole moment is set to zero. Qualitatively these three systems exhibit similar curves and their shapes resemble the results obtained within the
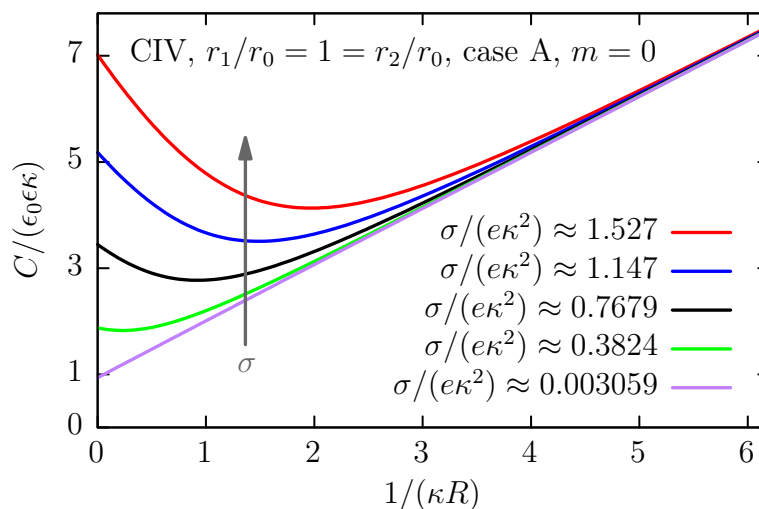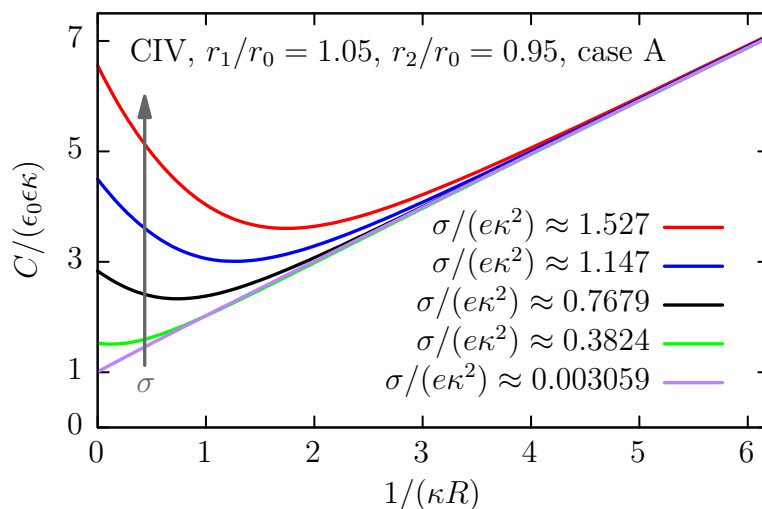
Figure 5.10: Same as Fig. 5.8 for $m = 0$.

pure PB approach in part I (Ref. [94] and Chap. 4) of this study. Quantitatively, however, the distinct models render deviations which are visible most clearly in Fig. 5.7, where various approaches are compared for one fixed value of the surface charge density. Again, the results are only weakly affected by the strength of the dipole moment: the graphs in Fig. 5.8 (with the dipole moment chosen as in Sec. 5.2.4) and Fig. 5.10 (no dipole moment) differ only slightly. Also in the case of planar walls (see Fig. 5.5 and Refs. [54, 68, 71]) the explicit dipole description turned out to have only a small effect. It would be interesting to counter-check this finding with alternative approaches such as computer simulations. Thereby it might be possible to clarify, whether the aforementioned small differences in the capacitance originate from an insufficient description of the dipoles or whether already simpler models are capable to capture sufficiently accurately the relevant structure of an electrolyte solution. In this case it might be justified to skip the comparatively sophisticated description of the dipoles. Simulations for models, which take dipoles explicitly into account, have already been carried out. In Ref. [115] results for mixtures of hard spherical ions and dipoles in contact with charged walls are presented in terms of spatially varying profiles. Reference [116] summarizes several simulation studies concerning the effective interaction between two charged surfaces separated by a solution described by ions dissolved in a Stockmayer fluid which is a Lennard-Jones fluid with an embedded point-dipole. However, computer simulations of ion-dipole mixtures are regarded to be technically difficult [115]. Possibly, this is the reason why numerical capacitance data derived from models with and without explicit dipole description had not yet been compared with each other, as it is done, e.g., in Fig. 5.5.

Unequal particle radii can give rise to qualitatively different behaviors which may be discussed according to the sizes of the ionic species. In the case that the positive ions are
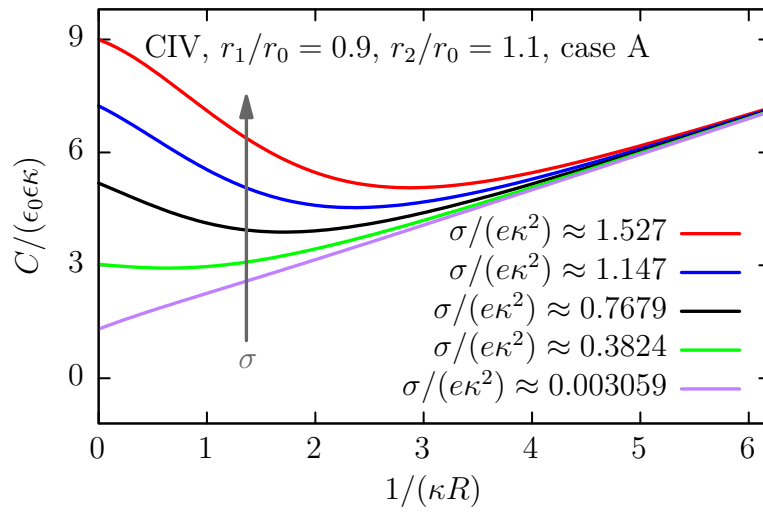
Figure 5.11: Same as Fig. 5.8 for $r_1/r_0 = 0.9$ and $r_2/r_0 = 1.1$.
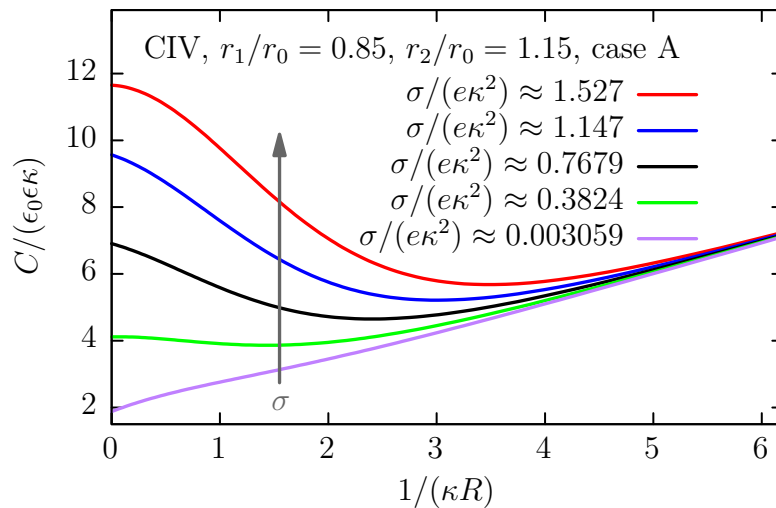
Figure 5.12: Same as Fig. 5.8 for $r_1/r_0 = 0.85$ and $r_2/r_0 = 1.15$.

the smaller particles (Figs. 5.11 and 5.12) the capacitance in the planar limit $1/(\kappa R) \to 0$ increases with increasing difference in the particle radii. Moreover the graphs become more concave (from below) for small curvatures and in particular for large surface charge densities. In the case that the positive ions are the largest particles (Figs. 5.13 and 5.14) the capacitance in the planar limit shows a more complex behavior (see also Fig. 5.6): for $\sigma \to 0$ the capacitance increases with increasing difference in the particle radii. However, for intermediate and large values of σ, the capacitance decreases upon increasing the particle size difference. As a consequence, some curves approach the graph for $\sigma \to 0$ from *below* (see, e.g., the (green) graph for $\sigma/(e\kappa^2) \approx 0.3824$ in Fig. 5.14), whereas in the

Figure 5.13: Same as Fig. 5.8 for $r_1/r_0 = 1.05$ and $r_2/r_0 = 0.95$.
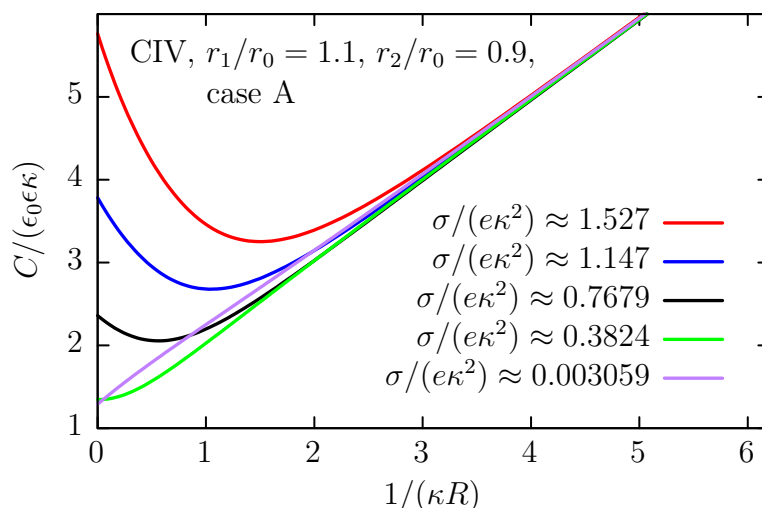
Figure 5.14: Same as Fig. 5.8 for $r_1/r_0 = 1.1$ and $r_2/r_0 = 0.9$. The only concave curve corresponds to the bottom entry of the key; the order of the vertical intercepts of the convex curves corresponds to the order of the remaining keys.

most other cases the convergence is from above (see Figs. 5.8 – 5.12).

Already in the case of planar electrodes it has become apparent that a variation of the particle radii has a relatively strong effect on the shape of capacitance data (see Figs. 5.5 and 5.6). This finding is confirmed for the case of spherical electrodes when comparing the data corresponding to unequal particle radii (Figs. 5.11 – 5.14) with the data corresponding to equal particle radii (Figs. 5.8 – 5.10), upon varying the ionic strength I or the dipole moment m. The difference in particle radii has a strong influence on the charge distribution because the smallest species can approach the wall closest. For a
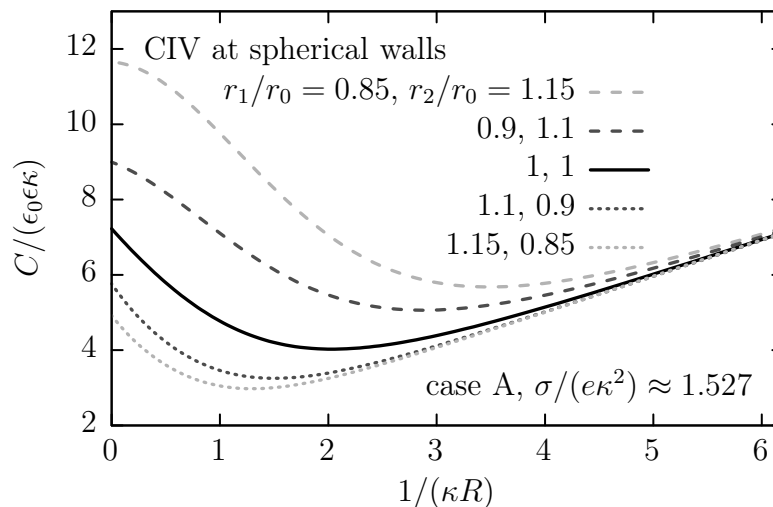
Figure 5.15: Reduced differential capacitance $C/(\epsilon_0\epsilon\kappa)$ as a function of the dimensionless curvature $1/(\kappa R)$ of spherical electrodes with rescaled surface charge density $\sigma/(e\kappa^2) \approx$ 1.527. The electrolyte solution corresponding to case A is described within the CIV model (see Sec. 5.2.4). Curves with the same shade of gray correspond to the same *set* of ion size ratios $\{r_1/r_0, r_2/r_0\}$ where the cations are the larger ions $(r_1/r_0 > r_2/r_0)$ for dotted curves and the anions are the larger ions $(r_1/r_0 < r_2/r_0)$ for dashed curves.

planar wall this behavior is captured in Fig. 5.4. For spherical electrodes the interplay of these steric effects with electrostatic interactions is influenced additionally by the radius R of the electrode which increases the complexity and gives rise to the various shapes of the presented capacitance data. Figure 5.15 facilitates the comparison of distinct data sets. The solid curve corresponds to the case in which all radii are equal whereas the radii are unequal for the cases corresponding to the other curves. For large curvatures the curves approach each other and exhibit a common behavior independent of the chosen particle radii. In view of the limiting behavior at large curvatures, as shown in Figs. 5.8 – 5.14, the common behavior at large curvatures is also independent of the surface charge density. At this stage it is already known that the simple PB model is a rather good approximation for CIV with equal particle radii in the limit of small electrode radii (see Fig. 5.7). Furthermore, in part I (Ref. [94] and Chap. 4) of this study it is shown that in the limit of large curvatures these results are in accordance with the *linearized* PB description. Combined with the insight obtained from Fig. 5.15 it seems that for $1/(\kappa R) \gg 1$ the linearized PB model might be an adequate approximation for all systems displayed in Fig. 5.15. This finding might be interesting for describing small electrodes or highly curved parts of electrodes.

5.4   Summary

The electric double layer (EDL) of an electrolyte solution in contact with electrodes of planar or spherical shape has been analyzed. Inspired by the study of Oleksy and Hansen [68] the electrolyte solution is described in terms of density functional theory (DFT) based on the functional given in Eq. (5.3). This approach, which is a certain version of the so-called *civ*ilized model (CIV, see Sec. 5.2.4), takes into account all particle species on equal footing. All particles are modelled as hard spheres with non-vanishing volumes, embedded charges (in the cases of the monovalent anions or cations) or point-dipoles (in the case of the solvent molecules), and with an attractive interaction amongst all particles which enables one to discuss an electrolyte solution in the liquid state under realistic ambient conditions. This microscopic model is a possible extension of the mesoscopic Poisson-Boltzmann (PB) approach, which was used in part I of the present study (Ref. [94] and Chap. 4) in order to discuss EDLs at curved electrodes. Close to the wall the microscopic description gives rise to a layering behavior of the charge density and of the polarization (see Figs. 5.2 – 5.4) whereas the PB approach renders monotonic profiles only. As in part I (Ref. [94] and Chap. 4) the structural features of the EDL enter into the differential capacitance C [Eq. (5.32)] which facilitates the comparison of various models with each other or to evaluate the influence of various system parameters such as particle radii, dipole moment of the solvent molecules, ionic strength, surface charge density, and electrode radius. At the planar wall and for equal radii of all particles, PB and CIV lead to similar values for the capacitance (see Fig. 5.5). Since compared with CIV (see Sec. 5.2.4) PB neglects many microscopic details, this finding is not obvious. Against this background, in its turn it is remarkable, that in the case of spherical electrodes of finite radii R the agreement between the predictions of the two models deteriorates (see Fig. 5.7), i.e., the relevance of microscopic details, captured by the CIV model, depends on the geometry of the electrode. The restricted primitive model (RPM), in which the particles are not treated on equal footing, clearly exhibits a different trend in comparison with the other models (see Figs. 5.5 and 5.7). In the case of spherical electrodes the capacitance data obtained within CIV for equal particle radii are qualitatively similar to the PB results of part I (Ref. [94] and Chap. 4) of this study (see Figs. 5.8 – 5.10). Nevertheless, there are quantitative differences (see Fig. 5.7). Considering the dipoles explicitly has no large effect (compare the two curves labelled with CIV in Figs. 5.5 and 5.7 or compare Fig. 5.8 with Fig. 5.10). Qualitative and relatively large quantitative differences occur if the particle radii are unequal. This is the case both for planar electrodes [see Fig. 5.6 where the PB result turns out to be close to the solid black curve (see Fig. 5.5)] and for spherical electrodes (compare Fig. 5.8 with Figs. 5.11 – 5.14). However, the differences are borne out only for small and intermediate curvatures $1/(\kappa R)$. For large curvatures the capacitance curves of all considered cases exhibit a common behavior and converge to

the limiting graph valid for small surface charge densities $\sigma \to 0$, i.e., in this limit the behavior becomes independent of σ (see Figs. 5.8 – 5.14). Moreover, this behavior becomes also independent of the choice of the particle radii (see Fig. 5.15). For $1/(\kappa R) \gg 1$ the simple linearized PB model appears to be an adequate approximation of the relatively complex CIV. In summary it can be stated that the geometry of the electrode determines the relevance of microscopic details. Apart from the limit of small electrode radii, for which a general behavior is observed, PB provides acceptable estimates in the case of equal particle sizes and large electrode radii.

5.A Derivation of the modified random phase approximation

The model in Sec. 5.2 takes into account the electrostatic [Eq. (5.5)] and attractive [Eq. (5.7)] interactions by means of a modified random phase approximation. Within this Appendix the assumptions underlying this approximation are explained. For clarity, in the following indices describing the particle species are suppressed and the dipole orientations are omitted. A generalization of the final result is straightforward. Starting point is a relation between the pairwise distribution function $\varrho^{(2)}$, the pairwise intermolecular potential U, and the excess functional $\mathcal{F}^{\text{ex}}$ [58]:

$$\varrho^{(2)}(\boldsymbol{r}, \boldsymbol{r}', [\varrho, U]) = 2 \frac{\delta \mathcal{F}^{\text{ex}}[\varrho, U]}{\delta U(\boldsymbol{r}, \boldsymbol{r}')}. \tag{5.33}$$

Here the notation $\varrho^{(2)}(\boldsymbol{r}, \boldsymbol{r}', [\varrho, U])$ means that $\varrho^{(2)}$ is a function of the positions $\boldsymbol{r}$ and $\boldsymbol{r}'$ and that it is a functional of the number density ϱ and of the interaction potential U. $\mathcal{F}^{\text{ex}}$ is the part of the density functional [Eq. (5.3)] which is in excess to the ideal gas contribution $\mathcal{F}^{\text{id}}$, i.e., in the present case, it is given by the sum $\mathcal{F}^{\text{ex}} = \mathcal{F}^{\text{hs}} + \mathcal{F}^{\text{el}} + \mathcal{F}^{\text{att}}$. $\mathcal{F}^{\text{ex}}$ takes into account the interaction potential U between the particles. In principle, the excess functional $\mathcal{F}^{\text{ex}}$ is set once the interaction potential U has been chosen. However, often the precise form of $\mathcal{F}^{\text{ex}}$ is not available and therefore approximative expressions have to be used (see below). Equation (5.33) can be functionally integrated [58]. For that purpose the integration path

$$U_\alpha(\boldsymbol{r}, \boldsymbol{r}') := U_{\text{ref}}(\boldsymbol{r}, \boldsymbol{r}') + \alpha \left[U(\boldsymbol{r}, \boldsymbol{r}') - U_{\text{ref}}(\boldsymbol{r}, \boldsymbol{r}') \right], \quad \alpha \in [0, 1], \tag{5.34}$$

is chosen. The path U_α interpolates between a reference interaction potential $U_{\text{ref}} = U_{\alpha=0}$ and the interaction potential $U = U_{\alpha=1}$. The partial derivative of the excess functional

with respect to the parameter α reads

$$
\begin{aligned}
\frac{\partial \mathcal{F}^{\text{ex}}[\varrho, U_\alpha]}{\partial \alpha} &= \int \mathrm{d}^3 r \int \mathrm{d}^3 r' \left. \frac{\delta \mathcal{F}^{\text{ex}}[\varrho, U]}{\delta U(\boldsymbol{r}, \boldsymbol{r}')} \right|_{U = U_\alpha} \frac{\partial U_\alpha(\boldsymbol{r}, \boldsymbol{r}')}{\partial \alpha} \\
&= \frac{1}{2} \int \mathrm{d}^3 r \int \mathrm{d}^3 r' \, \varrho^{(2)}(\boldsymbol{r}, \boldsymbol{r}', [\varrho, U_\alpha]) \left[U(\boldsymbol{r}, \boldsymbol{r}') - U_{\text{ref}}(\boldsymbol{r}, \boldsymbol{r}') \right],
\end{aligned}
\tag{5.35}
$$

where Eqs. (5.33) and (5.34) have been used. Integration of the left hand side of Eq. (5.35) with respect to α leads to

$$
\int_0^1 \mathrm{d}\alpha \, \frac{\partial \mathcal{F}^{\text{ex}}[\varrho, U_\alpha]}{\partial \alpha} = \mathcal{F}^{\text{ex}}[\varrho, U_1] - \mathcal{F}^{\text{ex}}[\varrho, U_0] = \mathcal{F}^{\text{ex}}[\varrho, U] - \mathcal{F}^{\text{ex}}[\varrho, U_{\text{ref}}] = \mathcal{F}^{\text{ex}}[\varrho] - \mathcal{F}^{\text{ex}}_{\text{ref}}[\varrho].
\tag{5.36}
$$

In agreement with the definition in Eq. (5.34), $\mathcal{F}^{\text{ex}}[\varrho, U_1]$ corresponds to the interaction potential U and therefore it is the excess functional $\mathcal{F}^{\text{ex}}[\varrho] := \mathcal{F}^{\text{ex}}[\varrho, U]$, whereas $\mathcal{F}^{\text{ex}}[\varrho, U_0]$ corresponds to the reference interaction potential U_{ref}, which is why it is denoted as the reference excess functional $\mathcal{F}^{\text{ex}}_{\text{ref}}[\varrho] := \mathcal{F}^{\text{ex}}[\varrho, U_{\text{ref}}]$. In Eq. (5.35) the pairwise distribution function can be replaced by (see Ref. [49])

$$
\varrho^{(2)}(\boldsymbol{r}, \boldsymbol{r}', [\varrho, U_\alpha]) = \varrho(\boldsymbol{r}) \varrho(\boldsymbol{r}') g(\boldsymbol{r}, \boldsymbol{r}', [\varrho, U_\alpha]),
\tag{5.37}
$$

that is, by a product of the number density ϱ evaluated at two positions $\boldsymbol{r}$ and $\boldsymbol{r}'$ and of the pair distribution function g. As a result the integration of Eq. (5.35) with respect to α can be written as (see also Ref. [58])

$$
\mathcal{F}^{\text{ex}}[\varrho] = \mathcal{F}^{\text{ex}}_{\text{ref}}[\varrho] + \frac{1}{2} \int_0^1 \mathrm{d}\alpha \int \mathrm{d}^3 r \int \mathrm{d}^3 r' \, \varrho(\boldsymbol{r}) \varrho(\boldsymbol{r}') g(\boldsymbol{r}, \boldsymbol{r}', [\varrho, U_\alpha]) \left[U(\boldsymbol{r}, \boldsymbol{r}') - U_{\text{ref}}(\boldsymbol{r}, \boldsymbol{r}') \right].
\tag{5.38}
$$

Equation (5.38) provides a prescription to obtain the excess functional $\mathcal{F}^{\text{ex}}$, corresponding to the interaction potential U, if the reference excess functional $\mathcal{F}^{\text{ex}}_{\text{ref}}$, corresponding to some reference interaction potential U_{ref}, and g for all U_α, $\alpha \in [0, 1]$, are known.

In the present model (see Sec. 5.2) the hard-spherical interaction, denoted by U_{hs} in this Appendix, is chosen as the reference interaction, $U_{\text{ref}} = U_{\text{hs}}$, and the reference excess functional is given by $\mathcal{F}^{\text{ex}}_{\text{ref}} = \mathcal{F}^{\text{hs}}$. Consequently, the difference in interactions in Eq. (5.38), $U - U_{\text{hs}}$, is given by the sum of the electrostatic and attractive interactions, which is abbreviated by $U_{\text{el,att}}$ within this Appendix. The pair distribution function g in Eq. (5.38) is not known. The approximation $g = 1$ is referred to as random phase approximation [58]. In order to go beyond this approximation the following *modified*

random phase approximation is used:

$$
g(\boldsymbol{r}, \boldsymbol{r}', [\varrho, U_\alpha]) \approx \begin{cases} 0, & \text{if hard spheres centered at } \boldsymbol{r} \text{ and } \boldsymbol{r}' \text{ would intersect,} \\ 1, & \text{otherwise.} \end{cases} \tag{5.39}
$$

The first line of Eq. (5.39) is exactly valid since the hard-spherical particles cannot overlap. The approximation in the second line neglects correlations. Finally, the approximation of Eq. (5.38) reads

$$
\begin{aligned}
\mathcal{F}^{\text{ex}}[\varrho] &= \mathcal{F}^{\text{hs}}[\varrho] + \mathcal{F}^{\text{el}}[\varrho] + \mathcal{F}^{\text{att}}[\varrho] \\
&\approx \mathcal{F}^{\text{hs}}[\varrho] + \frac{1}{2} \int \mathrm{d}^3 r \int \mathrm{d}^3 r' \, \varrho(\boldsymbol{r})\varrho(\boldsymbol{r}')U_{\text{el,att}}(\boldsymbol{r}, \boldsymbol{r}') \\
&\qquad\qquad\qquad \times \begin{cases} 0, & \text{if hard spheres centered at } \boldsymbol{r} \text{ and } \boldsymbol{r}' \text{ would intersect,} \\ 1, & \text{otherwise.} \end{cases}
\end{aligned} \tag{5.40}
$$

The term corresponding to $\mathcal{F}^{\text{el}}+\mathcal{F}^{\text{att}}$ in Eq. (5.40) is used in the present model in Eqs. (5.5) and (5.7). There the Heaviside step functions prevent that the hard-spherical particles intersect.

5.B   Derivation of the ELEs for the solvent in the form of Eqs. (5.23) and (5.24)

Equations (5.23) and (5.24) follow from the ELE (5.11) which contains all information needed about the solvent. It can be written as

$$
\begin{aligned}
\varrho_0(\boldsymbol{r}, \boldsymbol{\omega}) &= \zeta(\boldsymbol{r}) \exp\left\{\beta m\boldsymbol{\omega} \cdot [\boldsymbol{E}(\boldsymbol{r}) - \boldsymbol{E}^{\text{aux}}(\boldsymbol{r})]\right\}, \\
\zeta(\boldsymbol{r}) &:= \frac{\varrho_0^{\text{b}}}{4\pi} \exp\left[-\beta V_0(\boldsymbol{r}) + c_0^{\text{hs}}(\boldsymbol{r}) - c_0^{\text{hs,b}} + c_0^{\text{att}}(\boldsymbol{r}) - c_0^{\text{att,b}}\right].
\end{aligned} \tag{5.41}
$$

Due to the dependence of Eq. (5.41) on both the position $\boldsymbol{r}$ and the orientation $\boldsymbol{\omega}$, in general the equation has to be solved in a high-dimensional space. In order to reduce the dimensionality of the problem we focus only on the relevant information contained in Eq. (5.41). With Eq. (5.41) and the definition of the orientationally integrated number density $\bar{\varrho}_0(\boldsymbol{r})$ of the solvent [Eq. (5.2)] one has

$$
\bar{\varrho}_0(\boldsymbol{r}) = \zeta(\boldsymbol{r}) \int \mathrm{d}^2\omega \, \exp\left\{\beta m\boldsymbol{\omega} \cdot [\boldsymbol{E}(\boldsymbol{r}) - \boldsymbol{E}^{\text{aux}}(\boldsymbol{r})]\right\}. \tag{5.42}
$$

In order to carry out the angular integration in Eq. (5.42) the orientation vector $\boldsymbol{\omega}$ [Eq. (5.1)] is represented in a coordinate system the polar axis of which points into the radial direction away from the wall, i.e., the polar axis is parallel to the electric fields

$E(r)$ and $E^{\mathrm{aux}}(r)$. Therefore the scalar product in Eq. (5.42) reduces to

$$\beta m\boldsymbol{\omega} \cdot [E(r) - E^{\mathrm{aux}}(r)] = \beta m\, [E(r) - E^{\mathrm{aux}}(r)] \cos(\vartheta) = a(r) \cos(\vartheta),$$
$$a(r) := \beta m\, [E(r) - E^{\mathrm{aux}}(r)]\,, \tag{5.43}$$

so that

$$\bar{\varrho}_0(r) = \zeta(r) \int_0^{2\pi} \mathrm{d}\varphi \int_0^{\pi} \mathrm{d}\vartheta\, \sin(\vartheta) \exp\left[a(r)\cos(\vartheta)\right] = \zeta(r) 4\pi \frac{\sinh[a(r)]}{a(r)}, \tag{5.44}$$

which is equivalent to Eq. (5.23).

For this orientation of the coordinate system, the normal component P [Eq. (5.22)] of the polarization only depends on the coefficient $f_{1,0}(r)$ of the expansion in Eq. (5.20):

$$f_{1,0}(r) = \int \mathrm{d}^2\omega\, Y_{1,0}^*(\vartheta, \varphi) f(r, \boldsymbol{\omega}) = \sqrt{\frac{3}{4\pi}} \int \mathrm{d}^2\omega\, \cos(\vartheta) \frac{\varrho_0(r, \boldsymbol{\omega})}{\bar{\varrho}_0(r)}$$
$$= \sqrt{\frac{3}{4\pi}} \frac{a(r)}{4\pi \sinh[a(r)]} \int \mathrm{d}^2\omega\, \cos(\vartheta) \exp\left\{\beta m\boldsymbol{\omega} \cdot [E(r) - E^{\mathrm{aux}}(r)]\right\} \tag{5.45}$$

where the asterisk * denotes the complex conjugate. In order to carry out the angular integration in Eq. (5.45) the scalar product therein is treated like in Eq. (5.43) such that one obtains

$$f_{1,0}(r) = \sqrt{\frac{3}{4\pi}} \frac{a(r)}{4\pi \sinh[a(r)]} \int_0^{2\pi} \mathrm{d}\varphi \int_0^{\pi} \mathrm{d}\vartheta\, \sin(\vartheta) \cos(\vartheta) \exp\left[a(r)\cos(\vartheta)\right]$$
$$= \sqrt{\frac{3}{4\pi}} \left\{\coth[a(r)] - \frac{1}{a(r)}\right\} = \sqrt{\frac{3}{4\pi}} \mathcal{L}[a(r)], \tag{5.46}$$

which is equivalent to Eq. (5.24).

5.C   Asymptotic behavior at large distances from the wall

In Sec. 5.2.2 the *full* ELEs are presented in Eqs. (5.11) and (5.12) which provide the most general description of the model. From them the relevant reduced Eqs. (5.12), (5.23), and (5.24) are derived in Sec. 5.2.2. They have to be solved numerically on a large but finite grid along the radial direction. However, beyond the finite grid radial cutoff, the position of which is characterized by the length r_g in this Appendix, assumptions concerning the profiles have to be made. Here we focus on these assumptions and on the resulting behavior at large distances from the wall, where the external potentials [Eq. (5.9)] are

identically zero and where it can be assumed that the quantities

$$\Delta \boldsymbol{E}(\boldsymbol{r}) := \boldsymbol{E}(\boldsymbol{r}) - \boldsymbol{E}^{\mathrm{aux}}(\boldsymbol{r}), \tag{5.47}$$

$$\Delta \Phi_i(\boldsymbol{r}) := \Phi(\boldsymbol{r}) - \Phi_i^{\mathrm{aux}}(\boldsymbol{r}), \quad i \in \{1, 2\}, \tag{5.48}$$

and

$$\Delta c_i^{\mathrm{hs,att}}(\boldsymbol{r}) := c_i^{\mathrm{hs}}(\boldsymbol{r}) - c_i^{\mathrm{hs,b}} + c_i^{\mathrm{att}}(\boldsymbol{r}) - c_i^{\mathrm{att,b}}, \quad i \in \{0, 1, 2\}, \tag{5.49}$$

are sufficiently small to allow for linearization of the exponential functions in Eqs. (5.11) and (5.12). The following considerations focus on the general case of a spherical wall; the corresponding results for a planar wall can be obtained from taking the limit of infinite wall radius. With this, at large distances from the wall the ELEs (5.11) and (5.12) take the form

$$\varrho_0(\boldsymbol{r}, \boldsymbol{\omega}) \Big|_{|\boldsymbol{r}| > r_g} \simeq \frac{\varrho_0^{\mathrm{b}}}{4\pi} \left[1 + \Delta c_0^{\mathrm{hs,att}}(\boldsymbol{r}) + \beta m \boldsymbol{\omega} \cdot \Delta \boldsymbol{E}(\boldsymbol{r}) \right], \tag{5.50}$$

and

$$\varrho_i(\boldsymbol{r}) \Big|_{|\boldsymbol{r}| > r_g} \simeq \varrho_i^{\mathrm{b}} \left[1 + \Delta c_i^{\mathrm{hs,att}}(\boldsymbol{r}) - \beta q_i \Delta \Phi_i(\boldsymbol{r}) \right], \quad i \in \{1, 2\}. \tag{5.51}$$

Within this Appendix the focus is on the spatial decay of the electrostatic quantities $\Delta \Phi_i(\boldsymbol{r})$ and $\Delta \boldsymbol{E}(\boldsymbol{r})$ which follow from Eqs. (5.15) – (5.18). These expressions are independent of the contribution $\Delta c_0^{\mathrm{hs,att}}(\boldsymbol{r})$. The latter can enter $\Delta \Phi_i(\boldsymbol{r})$ and $\Delta \boldsymbol{E}(\boldsymbol{r})$ only via the polarization $\boldsymbol{P}(\boldsymbol{r})$. However, due to the angular integration in Eq. (5.14), terms in $\varrho_0(\boldsymbol{r}, \boldsymbol{\omega})$ which are independent of the orientation $\boldsymbol{\omega}$, such as $\Delta c_0^{\mathrm{hs,att}}(\boldsymbol{r})$ in Eq. (5.50), do not contribute to $\boldsymbol{P}(\boldsymbol{r})$. In the limit of equal radii of the ions, $r_1 = r_2$, the contributions $\Delta c_i^{\mathrm{hs,att}}(\boldsymbol{r})$, $i \in \{1, 2\}$, are equal and drop out of the sums in the first terms of Eqs. (5.15) – (5.18) due to the same absolute value of the ionic charges $q_1 = -q_2$. In this limit, as it will turn out in the following, the electrostatic contributions $\Delta \boldsymbol{E}(\boldsymbol{r})$ and $\Delta \Phi_i(\boldsymbol{r})$ exhibit the same decay behavior. The corresponding length scale is set by the Debye length $1/\kappa$ [Eqs. (5.29) and (5.30)]. In Appendix 5.D the asymptotic decay behavior of $\Delta c_i^{\mathrm{hs,att}}(\boldsymbol{r})$ is discussed. There it is shown that in the limit of equal particle radii the one-point direct correlation functions decay on the length scale of the bulk correlation length ξ emerging due to the presence of the hard spherical and attractive interactions. Except very close to critical points, at which ξ diverges, ξ is typically much smaller than $1/\kappa$ such that the contributions $\Delta c_i^{\mathrm{hs,att}}(\boldsymbol{r})$ decay rapidly towards zero and can be neglected in Eqs. (5.50) and (5.51) for large distances from the wall. This can be expected to hold also for small differences between the particle radii which is the limit we focus on in the present study.

Accordingly, our approximation for the ELEs at large distances from the wall reads

$$\varrho_0(\boldsymbol{r}, \boldsymbol{\omega})\Big|_{|\boldsymbol{r}|>r_g} \simeq \frac{\varrho_0^b}{4\pi}\left[1 + \beta m \boldsymbol{\omega} \cdot \Delta \boldsymbol{E}(\boldsymbol{r})\right] \tag{5.52}$$

and

$$\varrho_i(\boldsymbol{r})\Big|_{|\boldsymbol{r}|>r_g} \simeq \varrho_i^b\left[1 - \beta q_i \Delta \Phi_i(\boldsymbol{r})\right], \quad i \in \{1, 2\}. \tag{5.53}$$

Equations (5.15) – (5.18) are discussed in detail now. For this purpose the original integration domain $\mathbb{R}^3 \setminus \mathcal{V}$ is extended to $\mathbb{R}^3$. Note that within $\mathcal{V}$ the integrands are identically zero for $r_1 = r_2$. The extended domain $\mathbb{R}^3$ is split into a region $|\boldsymbol{r}| \leq r_g$ close to the wall, where the full solutions are known, and into a region $|\boldsymbol{r}| > r_g$ further away from the wall, where the number densities are approximated either as in Eqs. (5.50) and (5.51) in the limit of equal ionic radii, or as in Eqs. (5.52) and (5.53) under the assumption of negligible one-point direct correlation function differences. This leads to

$$\Delta E_\alpha(\boldsymbol{r}) \simeq h\Bigg[-\sum_{i=1}^2 \beta q_i^2 \varrho_i^b \int_{\mathbb{R}^3} \mathrm{d}^3 r' \, K_{\alpha i}^{(1)}(\boldsymbol{d}) \Delta \Phi_i(\boldsymbol{r}')$$
$$-\frac{\beta m^2 \varrho_0^b}{3} \sum_{\gamma=x}^z \int_{\mathbb{R}^3} \mathrm{d}^3 r' \, K_{\alpha\gamma}^{(2)}(\boldsymbol{d}) \Delta E_\gamma(\boldsymbol{r}') + S_\alpha^{(1)}(\boldsymbol{r})\Bigg], \quad \alpha \in \{x, y, z\}, \tag{5.54}$$

and

$$\Delta \Phi_i(\boldsymbol{r}) \simeq h\Bigg[-\sum_{j=1}^2 \beta q_j^2 \varrho_j^b \int_{\mathbb{R}^3} \mathrm{d}^3 r' \, K_{ij}^{(0)}(\boldsymbol{d}) \Delta \Phi_j(\boldsymbol{r}')$$
$$+\frac{\beta m^2 \varrho_0^b}{3} \sum_{\alpha=x}^z \int_{\mathbb{R}^3} \mathrm{d}^3 r' \, K_{\alpha i}^{(1)}(\boldsymbol{d}) \Delta E_\alpha(\boldsymbol{r}') + S_i^{(0)}(\boldsymbol{r})\Bigg], \quad i \in \{1, 2\}, \tag{5.55}$$

with

$$K_{ij}^{(0)}(\boldsymbol{r}) := \frac{1}{|\boldsymbol{r}|}\Theta[|\boldsymbol{r}| - (r_i + r_j)], \qquad\qquad i, j \in \{1, 2\}, \tag{5.56}$$

$$K_{\alpha i}^{(1)}(\boldsymbol{r}) := \frac{r_\alpha}{|\boldsymbol{r}|^3}\Theta[|\boldsymbol{r}| - (r_0 + r_i)], \qquad\qquad \alpha \in \{x, y, z\}, \ i \in \{1, 2\}, \tag{5.57}$$

$$K_{\alpha\gamma}^{(2)}(\boldsymbol{r}) := \left(\frac{\delta_{\alpha\gamma}}{|\boldsymbol{r}|^3} - \frac{3 r_\alpha r_\gamma}{|\boldsymbol{r}|^5}\right)\Theta(|\boldsymbol{r}| - 2r_0), \qquad \alpha, \gamma \in \{x, y, z\}, \tag{5.58}$$

$$S_i^{(0)}(\boldsymbol{r}) := \sum_{j=1}^{2} \int\limits_{|\boldsymbol{r}'| \leq r_g} \mathrm{d}^3 r' \frac{q_j}{|\boldsymbol{d}|} \left\{ \left[\varrho_j(\boldsymbol{r}') - \varrho_j^{\mathrm{b}} \right] + \beta q_j \varrho_j^{\mathrm{b}} \Delta \Phi_j(\boldsymbol{r}') \right\} \Theta[|\boldsymbol{d}| - (r_i + r_j)]$$

$$+ \int\limits_{|\boldsymbol{r}'| \leq r_g} \mathrm{d}^3 r' \left[\frac{\boldsymbol{P}(\boldsymbol{r}') \cdot \boldsymbol{d}}{|\boldsymbol{d}|^3} - \frac{1}{3} \varrho_0^{\mathrm{b}} \beta m^2 \frac{\Delta \boldsymbol{E}(\boldsymbol{r}') \cdot \boldsymbol{d}}{|\boldsymbol{d}|^3} \right] \Theta[|\boldsymbol{d}| - (r_0 + r_i)] \qquad (5.59)$$

$$+ \int\limits_{\mathcal{A}} \mathrm{d}^2 r' \frac{\sigma}{|\boldsymbol{d}|} \Theta(|\boldsymbol{d}| - r_i), \quad i \in \{1, 2\}, \quad \boldsymbol{d} = \boldsymbol{r} - \boldsymbol{r}',$$

$$S_\alpha^{(1)}(\boldsymbol{r}) := \sum_{i=1}^{2} \int\limits_{|\boldsymbol{r}'| \leq r_g} \mathrm{d}^3 r' \, q_i \frac{d_\alpha}{|\boldsymbol{d}|^3} \left\{ \left[\varrho_i(\boldsymbol{r}') - \varrho_i^{\mathrm{b}} \right] + \beta q_i \varrho_i^{\mathrm{b}} \Delta \Phi_i(\boldsymbol{r}') \right\} \Theta[|\boldsymbol{d}| - (r_0 + r_i)]$$

$$- \int\limits_{|\boldsymbol{r}'| \leq r_g} \mathrm{d}^3 r' \left\{ \left[\frac{P_\alpha(\boldsymbol{r}')}{|\boldsymbol{d}|^3} - \frac{3 d_\alpha \boldsymbol{P}(\boldsymbol{r}') \cdot \boldsymbol{d}}{|\boldsymbol{d}|^5} \right] \right.$$

$$\left. - \frac{1}{3} \varrho_0^{\mathrm{b}} \beta m^2 \left[\frac{\Delta E_\alpha(\boldsymbol{r}')}{|\boldsymbol{d}|^3} - \frac{3 d_\alpha \Delta \boldsymbol{E}(\boldsymbol{r}') \cdot \boldsymbol{d}}{|\boldsymbol{d}|^5} \right] \right\} \Theta(|\boldsymbol{d}| - 2 r_0) \qquad (5.60)$$

$$+ \int\limits_{\mathcal{A}} \mathrm{d}^2 r' \, \sigma \frac{d_\alpha}{|\boldsymbol{d}|^3} \Theta(|\boldsymbol{d}| - r_0), \quad \alpha \in \{x, y, z\},$$

and

$$h := \frac{1}{4\pi \epsilon_0 \epsilon_{\mathrm{ex}}}. \qquad (5.61)$$

In the limit $r_1 = r_2$ the expressions of $S_i^{(0)}$ and $S_\alpha^{(1)}$ are odd functions of σ. That is, for small surface charge densities $\sigma \to 0$ both contributions are of the order $O(\sigma)$. This property will be referred to at the end of this Appendix. Note that $\delta_{\alpha\gamma}$ is the Kronecker symbol and the abbreviation $\boldsymbol{d} = \boldsymbol{r} - \boldsymbol{r}'$ for the spatial offset is still valid. The Greek indices α, γ denote the vector components x, y, z whereas the Latin indices i, j denote the ion species $1, 2$. For example, the first term of Eq. (5.54) can be derived as follows: from Eqs. (5.15) and (5.16) one obtains

$$\boldsymbol{E}(\boldsymbol{r}) - \boldsymbol{E}^{\mathrm{aux}}(\boldsymbol{r}) = \Delta \boldsymbol{E}(\boldsymbol{r}) \qquad (5.62)$$

$$= \sum_{i=1}^{2} \int\limits_{\mathbb{R}^3} \mathrm{d}^3 r' \frac{q_i}{4\pi \epsilon_0 \epsilon_{\mathrm{ex}}} \frac{\boldsymbol{d}}{|\boldsymbol{d}|^3} \left[\varrho_i(\boldsymbol{r}') - \varrho_i^{\mathrm{b}} \right] \left[1 - \Theta(r_0 + r_i - |\boldsymbol{d}|) \right] + \dots$$

$$= \frac{1}{4\pi \epsilon_0 \epsilon_{\mathrm{ex}}} \sum_{i=1}^{2} \int\limits_{\mathbb{R}^3} \mathrm{d}^3 r' \, q_i \frac{\boldsymbol{d}}{|\boldsymbol{d}|^3} \left[\varrho_i(\boldsymbol{r}') - \varrho_i^{\mathrm{b}} \right] \Theta[|\boldsymbol{d}| - (r_0 + r_i)] + \dots \, .$$

In the next step, the asymptotic expressions for the density profiles at large distances $|\boldsymbol{r}| > r_g$ from the wall [Eq. (5.51) or (5.53)] are used. Note that $q_1 \varrho_1^{\mathrm{b}} + q_2 \varrho_2^{\mathrm{b}} = 0$ due to

local charge neutrality. The equation is written in terms of each component $\alpha \in \{x, y, z\}$ of the electric field:

$$
\Delta E_\alpha(\boldsymbol{r}) \simeq \frac{1}{4\pi\epsilon_0\epsilon_{\text{ex}}}
$$

$$
\times \left\{ \sum_{i=1}^{2} \int_{|\boldsymbol{r}'| \leq r_g} \mathrm{d}^3 r'\, q_i \frac{d_\alpha}{|\boldsymbol{d}|^3} \left\{ \left[\varrho_i(\boldsymbol{r}') - \varrho_i^{\text{b}}\right] - \varrho_i^{\text{b}} \left[\Delta c_i^{\text{hs,att}}(\boldsymbol{r}') - \beta q_i \Delta\Phi_i(\boldsymbol{r}')\right] \right\} \right.
$$

$$
\times \Theta[|\boldsymbol{d}| - (r_0 + r_i)]
$$

$$
\left. + \sum_{i=1}^{2} \int_{\mathbb{R}^3} \mathrm{d}^3 r'\, q_i \frac{d_\alpha}{|\boldsymbol{d}|^3} \varrho_i^{\text{b}} \left[\Delta c_i^{\text{hs,att}}(\boldsymbol{r}') - \beta q_i \Delta\Phi_i(\boldsymbol{r}')\right] \Theta[|\boldsymbol{d}| - (r_0 + r_i)] + \dots \right\}.
$$

(5.63)

In the limit of equal radii for the ions the contribution $\Delta c_i^{\text{hs,att}}(\boldsymbol{r}')$ drops out of the sum. The integrations with respect to positions $|\boldsymbol{r}'| \leq r_g$ close to the wall are collected in $S_\alpha^{(1)}$ [Eq. (5.60)] and will not be considered further in this example. Finally by using Eqs. (5.57) and (5.61) one has

$$
\Delta E_\alpha(\boldsymbol{r}) \simeq \frac{1}{4\pi\epsilon_0\epsilon_{\text{ex}}} \left[-\sum_{i=1}^{2} \beta q_i^2 \varrho_i^{\text{b}} \int_{\mathbb{R}^3} \mathrm{d}^3 r' \frac{d_\alpha}{|\boldsymbol{d}|^3} \Theta[|\boldsymbol{d}| - (r_0 + r_i)] \Delta\Phi_i(\boldsymbol{r}') + \dots \right]
$$

$$
= h\left[-\sum_{i=1}^{2} \beta q_i^2 \varrho_i^{\text{b}} \int_{\mathbb{R}^3} \mathrm{d}^3 r'\, K_{\alpha i}^{(1)}(\boldsymbol{d}) \Delta\Phi_i(\boldsymbol{r}') + \dots \right].
$$

(5.64)

In terms of the Fourier transform

$$
\hat{f}(\boldsymbol{q}) := \int_{\mathbb{R}^3} \mathrm{d}^3 r\, f(\boldsymbol{r}) \exp(-\mathrm{i}\boldsymbol{q} \cdot \boldsymbol{r})
$$

(5.65)

Eqs. (5.54) and (5.55) lead to a system of five linear equations for the components $\Delta\hat{E}_\alpha(\boldsymbol{q})$, $\alpha \in \{x, y, z\}$, of the vector $\Delta\hat{\boldsymbol{E}}(\boldsymbol{q})$ and for $\Delta\hat{\Phi}_i(\boldsymbol{q})$ with $i \in \{1, 2\}$:

$$
\Delta\hat{E}_\alpha(\boldsymbol{q}) = h\left[-\sum_{i=1}^{2} \beta q_i^2 \varrho_i^{\text{b}} \hat{K}_{\alpha i}^{(1)}(\boldsymbol{q}) \Delta\hat{\Phi}_i(\boldsymbol{q}) - \frac{\beta m^2 \varrho_0^{\text{b}}}{3} \sum_{\gamma=x}^{z} \hat{K}_{\alpha\gamma}^{(2)}(\boldsymbol{q}) \Delta\hat{E}_\gamma(\boldsymbol{q}) + \hat{S}_\alpha^{(1)}(\boldsymbol{q}) \right]
$$

(5.66)

and

$$
\Delta\hat{\Phi}_i(\boldsymbol{q}) = h\left[-\sum_{j=1}^{2} \beta q_j^2 \varrho_j^{\text{b}} \hat{K}_{ij}^{(0)}(\boldsymbol{q}) \Delta\hat{\Phi}_j(\boldsymbol{q}) + \frac{\beta m^2 \varrho_0^{\text{b}}}{3} \sum_{\alpha=x}^{z} \hat{K}_{\alpha i}^{(1)}(\boldsymbol{q}) \Delta\hat{E}_\alpha(\boldsymbol{q}) + \hat{S}_i^{(0)}(\boldsymbol{q}) \right].
$$

(5.67)

With the 5-component vectors $\boldsymbol{v}$ and $\boldsymbol{s}$ as well as the 5×5 matrix $\boldsymbol{M}$,

$$\boldsymbol{v} = \begin{pmatrix} v_x \\ v_y \\ v_z \\ v_1 \\ v_2 \end{pmatrix}, \quad \boldsymbol{s} = \begin{pmatrix} s_x \\ s_y \\ s_z \\ s_1 \\ s_2 \end{pmatrix}, \quad \boldsymbol{M} = \begin{pmatrix} M_{xx} & M_{xy} & M_{xz} & M_{x1} & M_{x2} \\ M_{yx} & M_{yy} & M_{yz} & M_{y1} & M_{y2} \\ M_{zx} & M_{zy} & M_{zz} & M_{z1} & M_{z2} \\ M_{1x} & M_{1y} & M_{1z} & M_{11} & M_{12} \\ M_{2x} & M_{2y} & M_{2z} & M_{21} & M_{22} \end{pmatrix}, \tag{5.68}$$

defined by

$$v_\alpha := \sqrt{\frac{\beta m^2 \varrho_0^{\mathrm{b}}}{3}} \, \Delta \hat{E}_\alpha(\boldsymbol{q}), \qquad\qquad \alpha \in \{x, y, z\}, \tag{5.69}$$

$$v_i := \sqrt{\beta q_i^2 \varrho_i^{\mathrm{b}}} \, \Delta \hat{\Phi}_i(\boldsymbol{q}), \qquad\qquad i \in \{1, 2\}, \tag{5.70}$$

$$s_\alpha := h \sqrt{\frac{\beta m^2 \varrho_0^{\mathrm{b}}}{3}} \, \hat{S}_\alpha^{(1)}(\boldsymbol{q}), \qquad\qquad \alpha \in \{x, y, z\}, \tag{5.71}$$

$$s_i := h \sqrt{\beta q_i^2 \varrho_i^{\mathrm{b}}} \, \hat{S}_i^{(0)}(\boldsymbol{q}), \qquad\qquad i \in \{1, 2\}, \tag{5.72}$$

$$M_{\alpha\gamma} := h \frac{\beta m^2 \varrho_0^{\mathrm{b}}}{3} \hat{K}_{\alpha\gamma}^{(2)}(\boldsymbol{q}), \qquad\qquad \alpha, \gamma \in \{x, y, z\}, \tag{5.73}$$

$$M_{\alpha i} := -M_{i\alpha} := h \sqrt{\frac{\beta m^2 \varrho_0^{\mathrm{b}}}{3} \beta q_i^2 \varrho_i^{\mathrm{b}}} \, \hat{K}_{\alpha i}^{(1)}(\boldsymbol{q}), \qquad \alpha \in \{x, y, z\}, \ i \in \{1, 2\}, \tag{5.74}$$

and

$$M_{ij} := h \sqrt{\beta q_i^2 \varrho_i^{\mathrm{b}} \beta q_j^2 \varrho_j^{\mathrm{b}}} \, \hat{K}_{ij}^{(0)}(\boldsymbol{q}), \qquad\qquad i, j \in \{1, 2\}, \tag{5.75}$$

the system of linear equations (5.66) and (5.67) has the form

$$(\boldsymbol{1} + \boldsymbol{M}) \cdot \boldsymbol{v} = \boldsymbol{s} \Leftrightarrow \boldsymbol{v} = (\boldsymbol{1} + \boldsymbol{M})^{-1} \cdot \boldsymbol{s} \tag{5.76}$$

with the identity matrix $\boldsymbol{1}$. With the abbreviations

$$k^2 := 8\pi \beta e^2 h I, \tag{5.77}$$

$$p^2 := \beta m^2 h \varrho_0^{\mathrm{b}}, \tag{5.78}$$

$$\bar{r}_i := \frac{r_i}{r_0}, \quad i \in \{1, 2\}, \tag{5.79}$$

$$\bar{k} := k r_0, \tag{5.80}$$

$$x := q r_0 := \sqrt{\boldsymbol{q} \cdot \boldsymbol{q}} \, r_0, \tag{5.81}$$

$$a := \frac{\pi}{6} p^2 \frac{\sin(2x) - 2x \cos(2x)}{x^3}, \tag{5.82}$$

$$b_j := -\mathrm{i} \sqrt{\frac{2\pi}{3}} p \bar{k} \frac{\sin[x(1 + \bar{r}_j)]}{x^2 (1 + \bar{r}_j)}, \quad j \in \{1, 2\}, \tag{5.83}$$

and

$$M_{ij} = \frac{\bar{k}^2}{2} \frac{\cos[x(\bar{r}_i + \bar{r}_j)]}{x^2}, \quad i, j \in \{1, 2\}, \tag{5.84}$$

one obtains

$$\mathbf{1} + \mathbf{M} = \begin{pmatrix} 1-a & 0 & 0 & 0 & 0 \\ 0 & 1-a & 0 & 0 & 0 \\ 0 & 0 & 1+2a & b_1 & b_2 \\ 0 & 0 & -b_1 & 1+M_{11} & M_{12} \\ 0 & 0 & -b_2 & M_{12} & 1+M_{22} \end{pmatrix}. \tag{5.85}$$

For various combinations of the indices α, i and α, γ the Fourier transforms $\hat{K}_{\alpha i}^{(1)}(\mathbf{q})$ and $\hat{K}_{\alpha\gamma}^{(2)}(\mathbf{q})$ are identically zero. Therefore the matrix $\mathbf{1} + \mathbf{M}$ exhibits this kind of block structure. Equation (5.76) relates the response of the fields $\mathbf{v}$ to an external perturbation $\mathbf{s}$, i.e., it is a multidimensional analogue of Yvon's equation in Fourier space [49]. Therefore, up to irrelevant factors, the matrix $\hat{\mathbf{G}}(q) := (\mathbf{1} + \mathbf{M})^{-1}$ is the Fourier transform of the bulk two-point direct correlation functions of the field components $\Delta E_{x,y,z}$ and of the potential differences $\Delta\Phi_{1,2}$. With the inverse Fourier transform

$$\mathbf{G}(r) := \frac{1}{4\pi^2 \mathrm{i} r} \int_{-\infty}^{\infty} \mathrm{d}q \, q \, \hat{\mathbf{G}}(q) \exp(\mathrm{i}qr), \quad r := |\mathbf{r}|, \tag{5.86}$$

one obtains $\mathbf{G}(r)$, which determines the asymptotic spatial dependence of $\Delta E_{x,y,z}(\mathbf{r})$ and $\Delta\Phi_{1,2}(\mathbf{r})$. The integral in Eq. (5.86) can be studied by using the residue theorem. As a consequence the exponential decay of $\mathbf{G}(r)$ is determined by the poles of $\hat{\mathbf{G}}(q)$ [117, 118]. The pole $q' + \mathrm{i}q'' \in \mathbb{C}$, with $q', q'' \in \mathbb{R}$, of $\hat{\mathbf{G}}(q)$ with the smallest imaginary part $|q''|$ determines the asymptotic decays of $\Delta E_{x,y,z}(\mathbf{r})$ and $\Delta\Phi_{1,2}(\mathbf{r})$ on the length scale $1/|q''|$ away from the charged wall. Since, according to Cramer's rule, the inverse matrix $(\mathbf{1} + \mathbf{M})^{-1} = \hat{\mathbf{G}}(q) \propto 1/\det(\mathbf{1} + \mathbf{M})$ is proportional to the reciprocal of $\det(\mathbf{1} + \mathbf{M})$, the poles of $\hat{\mathbf{G}}(q)$ are given by the roots of the determinant $\det(\mathbf{1} + \mathbf{M})$:

$$\det(\mathbf{1} + \mathbf{M}) = (1-a)^2[(1+2a)(1+M_{11})(1+M_{22}) - 2b_1 b_2 M_{12} + b_2^2(1+M_{11})$$
$$-M_{12}^2(1+2a) + b_1^2(1+M_{22})] = 0. \tag{5.87}$$

Equation (5.87) can be solved numerically. The parameter choices of the present study (see Sec. 5.2.4) correspond to purely imaginary roots $\mathrm{i}q''$, i.e., the asymptotic decay of $\Delta E_{x,y,z}(\mathbf{r})$ and of $\Delta\Phi_{1,2}(\mathbf{r})$ is monotonic. However, the important finding is that all electric field components and electric potentials decay on the *same* length scale $1/|q''|$ and are proportional to σ in the limit of equal radii $r_1 = r_2$ of the ions and for $\sigma \to 0$.

This finding is relevant for Sec. 5.2.3 and in particular for Eq. (5.25).

5.D   Asymptotic decay of the one-point direct correlation functions

Within this Appendix the asymptotic decay behavior of the one-point direct correlation functions (DCFs) $c_{0,1,2}^{hs}(\boldsymbol{r})$ and $c_{0,1,2}^{att}(\boldsymbol{r})$ is examined at positions far away from the wall. This behavior is related to the decay behavior of the number densities $\bar{\varrho}_0(\boldsymbol{r})$ and $\varrho_{1,2}(\boldsymbol{r})$ which fulfill the ELEs (5.23) and (5.12). Let us introduce the deviations of the number densities from their respective bulk values, $\Delta\varrho_0(\boldsymbol{r}) := \bar{\varrho}_0(\boldsymbol{r}) - \varrho_0^{b}$ and $\Delta\varrho_{1,2}(\boldsymbol{r}) := \varrho_{1,2}(\boldsymbol{r}) - \varrho_{1,2}^{b}$, and use the notation in Eqs. (5.47) – (5.49) in order to rewrite Eqs. (5.23) and (5.12) as

$$\ln\left[1 + \frac{\Delta\varrho_0(\boldsymbol{r})}{\varrho_0^{b}}\right] + \beta V_0(\boldsymbol{r}) - \Delta c_0^{hs,att}(\boldsymbol{r}) - \ln\left\{\frac{\sinh[\beta m \Delta E(\boldsymbol{r})]}{\beta m \Delta E(\boldsymbol{r})}\right\} = 0 \tag{5.88}$$

and, $i \in \{1, 2\}$,

$$\ln\left[1 + \frac{\Delta\varrho_i(\boldsymbol{r})}{\varrho_i^{b}}\right] + \beta V_i(\boldsymbol{r}) - \Delta c_i^{hs,att}(\boldsymbol{r}) + \beta q_i \Delta\Phi_i(\boldsymbol{r}) = 0. \tag{5.89}$$

Within this Appendix, a spherical wall is discussed, as in Appendix 5.C, and we consider the case that all particle species have the same radius: $r_0 = r_1 = r_2$. As a consequence the one-point direct correlation functions and the differences of the electrostatic potentials are the same for all species, i.e., $\Delta c_{0,1,2}^{hs,att}(\boldsymbol{r}) =: \Delta c^{hs,att}(\boldsymbol{r})$ and $\Delta\Phi_{1,2}(\boldsymbol{r}) =: \Delta\Phi(\boldsymbol{r})$. In the following the equation for the solvent [Eq. (5.88)] is discussed in detail so that the presented procedure can be applied analogously to the two equations for the ionic species in Eq. (5.89). The Fourier transform [Eq. (5.65)] of Eq. (5.88) is given by

$$\int_{\mathbb{R}^3} d^3r \, \exp(-i\boldsymbol{q} \cdot \boldsymbol{r})\left\{\ln\left[1 + \frac{\Delta\varrho_0(\boldsymbol{r})}{\varrho_0^{b}}\right] + \beta V_0(\boldsymbol{r})\right.$$
$$\left. - \Delta c^{hs,att}(\boldsymbol{r}) - \ln\left\{\frac{\sinh[\beta m \Delta E(\boldsymbol{r})]}{\beta m \Delta E(\boldsymbol{r})}\right\}\right\} = 0. \tag{5.90}$$

We introduce the length r_g large enough such that

$$\beta V_{0,1,2}(\boldsymbol{r})\big|_{|\boldsymbol{r}|>r_g} = 0, \tag{5.91}$$

$$\frac{\sinh[\beta m \Delta E(\boldsymbol{r})]}{\beta m \Delta E(\boldsymbol{r})}\bigg|_{|\boldsymbol{r}|>r_g} \simeq \frac{\beta m \Delta E(\boldsymbol{r})}{\beta m \Delta E(\boldsymbol{r})} = 1, \tag{5.92}$$

and, $i \in \{0, 1, 2\}$,

$$\ln \left[1 + \frac{\Delta \varrho_i(\boldsymbol{r})}{\varrho_i^{\mathrm{b}}}\right]\Bigg|_{|\boldsymbol{r}| > r_g} \simeq \frac{\Delta \varrho_i(\boldsymbol{r})}{\varrho_i^{\mathrm{b}}}. \tag{5.93}$$

The integration in Eq. (5.90) over the whole space can be split into two domains, one with $|\boldsymbol{r}| \leq r_g$, where the full ELE (5.88) is integrated, and another one with $|\boldsymbol{r}| > r_g$, where the ELE (5.88) is approximated according to Eqs. (5.91) – (5.93). We make use of the fact that the equilibrium density $\bar{\varrho}_0(\boldsymbol{r})$ fulfills the ELE (5.88) locally which is why the integral in the domain $|\boldsymbol{r}| \leq r_g$ vanishes. Therefore, with the approximations in Eqs. (5.91) – (5.93), the Fourier transform in Eq. (5.90) reads

$$\int\limits_{|\boldsymbol{r}| > r_g} \mathrm{d}^3 r \, \exp(-\mathrm{i}\boldsymbol{q} \cdot \boldsymbol{r}) \left[\frac{\Delta \varrho_0(\boldsymbol{r})}{\varrho_0^{\mathrm{b}}} - \Delta c^{\mathrm{hs,att}}(\boldsymbol{r})\right] = 0. \tag{5.94}$$

The one-point direct correlation function $\Delta c^{\mathrm{hs,att}}(\boldsymbol{r})$, which is a functional of the number densities $\varrho_{0,1,2}$ [see Eq. (5.13)], can be expressed in terms of a Taylor series expansion with respect to the bulk value:

$$\Delta c^{\mathrm{hs,att}}(\boldsymbol{r}) \simeq \int\limits_{\mathbb{R}^3} \mathrm{d}^3 r' \, c^{(2)\mathrm{hs,att,b}}(\boldsymbol{r} - \boldsymbol{r}')[\Delta \varrho_0(\boldsymbol{r}') + \Delta \varrho_1(\boldsymbol{r}') + \Delta \varrho_2(\boldsymbol{r}')]. \tag{5.95}$$

Since the integral in Eq. (5.94) is restricted to positions far away from the wall, i.e., $|\boldsymbol{r}| > r_g$, where the number densities are close to their respective bulk values and hence the deviations $|\Delta \varrho_{0,1,2}|$ are small, in Eq. (5.95) only terms up to and including linear order in $\Delta \varrho_{0,1,2}$ are taken into account. Note that $\Delta c^{\mathrm{hs,att}}$ [Eq. (5.49)] measures the difference of the one-point direct correlation functions from their respective bulk values. Therefore evaluation in the bulk leads to $\Delta c^{\mathrm{hs,att}} = 0$ which is the zeroth order of the expansion in Eq. (5.95). The quantity $c^{(2)\mathrm{hs,att,b}}$ denotes the bulk two-point direct correlation function governed by the hard spherical (hs) and the attractive (att) interaction, respectively. In Eq. (5.94) a conveniently chosen zero is added such that the original integration over $|\boldsymbol{r}| > r_g$ is written in terms of a Fourier integral and an integration over the domain $|\boldsymbol{r}| \leq r_g$ in order to obtain

$$\frac{\Delta \hat{\varrho}_0(\boldsymbol{q})}{\varrho_0^{\mathrm{b}}} - \hat{c}^{(2)\mathrm{hs,att,b}}(\boldsymbol{q})[\Delta \hat{\varrho}_0(\boldsymbol{q}) + \Delta \hat{\varrho}_1(\boldsymbol{q}) + \Delta \hat{\varrho}_2(\boldsymbol{q})] - F_0(\boldsymbol{q}) = 0,$$

$$F_0(\boldsymbol{q}) := \int\limits_{|\boldsymbol{r}| \leq r_g} \mathrm{d}^3 r \, \exp(-\mathrm{i}\boldsymbol{q} \cdot \boldsymbol{r}) \left\{\frac{\Delta \varrho_0(\boldsymbol{r})}{\varrho_0^{\mathrm{b}}} - \int\limits_{\mathbb{R}^3} \mathrm{d}^3 r' \, c^{(2)\mathrm{hs,att,b}}(\boldsymbol{r} - \boldsymbol{r}') \sum_{i=0}^{2} \Delta \varrho_i(\boldsymbol{r}')\right\}. \tag{5.96}$$

The same procedure can be applied to the sum of the two equations in Eq. (5.89). The contribution of the electric potential drops out of the sum because the ion species carry a charge of the same absolute value $q_1 = -q_2$, thus leading to

$$\frac{\Delta\hat{\varrho}_1(\boldsymbol{q}) + \Delta\hat{\varrho}_2(\boldsymbol{q})}{I} - 2\hat{c}^{(2)\mathrm{hs,att,b}}(\boldsymbol{q})[\Delta\hat{\varrho}_0(\boldsymbol{q}) + \Delta\hat{\varrho}_1(\boldsymbol{q}) + \Delta\hat{\varrho}_2(\boldsymbol{q})] - F_{1,2}(\boldsymbol{q}) = 0,$$

$$F_{1,2}(\boldsymbol{q}) := \int\limits_{|\boldsymbol{r}| \leq r_g} \mathrm{d}^3r \, \exp(-\mathrm{i}\boldsymbol{q} \cdot \boldsymbol{r}) \left\{ \frac{\Delta\varrho_1(\boldsymbol{r}) + \Delta\varrho_2(\boldsymbol{r})}{I} \right.$$
$$\left. - 2\int\limits_{\mathbb{R}^3} \mathrm{d}^3r' \, c^{(2)\mathrm{hs,att,b}}(\boldsymbol{r} - \boldsymbol{r}') \sum_{i=0}^{2} \Delta\varrho_i(\boldsymbol{r}') \right\}. \tag{5.97}$$

The functions $F_0(\boldsymbol{q})$ and $F_{1,2}(\boldsymbol{q})$ are entire, i.e., they do not possess any poles in $\boldsymbol{q} \in \mathbb{C}^3$, because the outer-most integrations in Eqs. (5.96) and (5.97) are those of continuous integrands which are entire in $\boldsymbol{q}$ over a compact domain. The sum of Eqs. (5.96) and (5.97),

$$\Delta\hat{\varrho}_0(\boldsymbol{q}) + \Delta\hat{\varrho}_1(\boldsymbol{q}) + \Delta\hat{\varrho}_2(\boldsymbol{q}) = \frac{\varrho_0^{\mathrm{b}} F_0(\boldsymbol{q}) + I F_{1,2}(\boldsymbol{q})}{1 - \hat{c}^{(2)\mathrm{hs,att,b}}(\boldsymbol{q})(\varrho_0^{\mathrm{b}} + 2I)}, \tag{5.98}$$

is an analogue of Yvon's equation in Fourier space [49] because it relates the number densities with an external perturbation given by the numerator on the right hand side of Eq. (5.98). The expression $S(\boldsymbol{q}) := [1 - \hat{c}^{(2)\mathrm{hs,att,b}}(\boldsymbol{q})(\varrho_0^{\mathrm{b}} + 2I)]^{-1}$ is the bulk structure factor [49]. Hence, following the line of argument in Appendix 5.C and recognizing that the numerator in Eq. (5.98) does not have poles, the asymptotic decay of the sum $\Delta\varrho_0(\boldsymbol{r}) + \Delta\varrho_1(\boldsymbol{r}) + \Delta\varrho_2(\boldsymbol{r})$ is given by the pole $q' + \mathrm{i}q''$ of $S(\boldsymbol{q})$ with the smallest imaginary part $|q''|$, which sets the length scale of the decay. Here the length scale can be identified as the bulk correlation length $\xi = 1/|q''|$ emerging from the hard spherical and attractive interactions. Far away from the wall, i.e., at positions $\boldsymbol{r}$ at which the approximations in Eqs. (5.91) – (5.93) can be applied, the ELE for the solvent Eq. (5.88) and the sum of the ELEs for the ions in Eq. (5.89) are given by

$$\frac{\Delta\varrho_0(\boldsymbol{r})}{\varrho_0^{\mathrm{b}}} = \Delta c^{\mathrm{hs,att}}(\boldsymbol{r}) \tag{5.99}$$

and

$$\frac{\Delta\varrho_1(\boldsymbol{r})}{\varrho_1^{\mathrm{b}}} + \frac{\Delta\varrho_2(\boldsymbol{r})}{\varrho_2^{\mathrm{b}}} = 2\Delta c^{\mathrm{hs,att}}(\boldsymbol{r}). \tag{5.100}$$

From Eqs. (5.99) and (5.100) it follows that the decay of the one-point direct correlation function difference $\Delta c^{\mathrm{hs,att}}(\boldsymbol{r})$ is given by the decay of the number densities $\Delta\varrho_{0,1,2}(\boldsymbol{r})$. That is, $\Delta c^{\mathrm{hs,att}}(\boldsymbol{r})$ decays on the length scale of the bulk correlation length ξ. This result

is used in Sec. 5.2.3 and in Appendix 5.C in order to justify the neglect of the one-point direct correlation function differences in Eqs. (5.52) and (5.53).

Chapter 6

Conclusions and outlook

The present dissertation has been dedicated to interfaces between *curved* solid walls and different kinds of fluids, in particular, simple fluids and electrolyte solutions. The dependence of interfacial quantities, like the interfacial tension γ and the differential capacitance C, on the geometry of the solid wall has been assessed by means of various theoretical approaches.

In Chaps. 2 and 3 density functional theory (DFT) has been applied in order to determine the interfacial tension γ of the interface between a simple fluid and a solid wall. The latter has been assumed to be of spherical or cylindrical shape with arbitrary radius R. The dependence of the interfacial tension $\gamma(R)$ on the radius has been assessed numerically in Chap. 2 and analytically in Chap. 3. Expansions in powers of the wall curvature $1/R$ have rendered curvature coefficients γ_{si}, $i \geq 1$, for the spherical and γ_{ci} for the cylindrical geometry. These exact results have been compared to the predictions of morphometric thermodynamics (MT) stating that $\gamma_{si} = 0$ for $i \geq 3$ and that $\gamma_{ci} = 0$ for $i \geq 2$. It has turned out that MT is not complete for all considered cases, i.e., for distinct interaction potentials for the fluid-fluid as well as for the fluid-wall interactions. This result is in line with studies in Refs. [19–24] which question the completeness of MT. Therefore MT has the status of an approximation. In Chaps. 2 and 3 it has become evident that the quality of the approximation depends to a large extent on the considered geometry and on the convention for the interfacial position parameterized by δ in Chap. 2; the results in Chap. 3 have been quoted with respect to $\delta = 0$. Up to γ_{s3} and γ_{c2} the coefficients exhibit a dependence on δ (see Figs. 2.5 – 2.9). This has the following consequence: In general by truncating the exact expansion in agreement with MT a certain remainder is neglected. Since most of the coefficients vary with δ, the relative magnitude of the remainder, as compared to the considered terms, depends on the chosen convention. In spherical geometries the MT approximation is in better agreement with the exact results than in cylindrical geometries. This has become particularly apparent in the discussion of Chap. 3 where the deviation between MT and the exact result is exponentially small at the spherical wall whereas it is algebraic at the cylindrical wall. For the latter, depending on

the convention, it may occur that $|\gamma_{c2}| > |\gamma_{c1}|$, i.e., the second coefficient, which should not be present according to MT, can be *larger* than the first coefficient. Possibly this inequality only holds for small number densities upon which the discussions in Chaps. 2 and 3 focus. In this limit such an inequality can also be inferred from the expressions for the curvature coefficients in Ref. [21]. Since the coefficients γ_{s3} and γ_{c2} are independent of the convention for the interface, a convenient choice for the convention might be helpful to obtain these coefficients from numerical results. In some conventions the coefficients in agreement with MT are much larger than the coefficients not in agreement so that within such conventions MT is a good approximation [see, e.g., Fig. 2.4(b)]. This might explain why MT has been found to perform well in several studies [8–18] despite of the aforementioned deficits. In the presence of an excess external potential, i.e., in excess to the hard wall potential, the agreement between the MT approximation and the exact result deteriorates. This is pointed out clearly by the analytic results in Chap. 3, where the coefficients not in agreement with MT become more and more dominant upon increasing the range or the strength of the excess external potential. In a sense Chaps. 2 and 3 specify the incompleteness of MT. The deviations between MT and the exact results range from exponentially small, through to algebraic with comparably small coefficient up to algebraic with comparably large coefficient. For applications based on MT these findings are problematic because the deviations depend, for instance, on the geometry. In case of arbitrary geometries, for which MT would be essentially powerful, the deviations probably cannot be estimated without the knowledge of the exact result. The ratio between the first curvature coefficients of the different geometries is given by $\gamma_{s1}/\gamma_{c1} = 2$ for all conventions. This ratio is in agreement with other studies [8, 19, 21, 23, 24, 93]. Interestingly, in the limit of small number densities and for $\delta = 0$, also the corresponding ratio for the second coefficients has been found to be given by a constant value $\gamma_{s2}/\gamma_{c2} = 8/3$; in this context *constant* means that this value has been found for all considered particle-particle interaction potentials as well as for an ideal gas in the limit of small excess external potentials and that this ratio has been confirmed in other studies [21, 23, 24]. These findings inspire confidence that this value is of general validity.

It would be interesting to verify the presented results by means of computer simulations. For this purpose in particular low density fluids surrounding a spherical or cylindrical hard wall seem to be promising configurations. If the interfacial tension is determined as a function of the wall radius in the convention $\delta = 0$, within the cylindrical geometry the coefficient γ_{c2}, which is not in agreement with MT, is expected to be comparably large. In that case the coefficient should be determinable with relative ease which would further substantiate the incompleteness of MT. The same procedure with respect to spherical geometries would enable to verify the aforementioned ratio of second order curvature coefficients, which, so far, has only been predicted theoretically.

In Chap. 4 the differential capacitance C of an electric double layer (EDL) between an

electrolyte solution and a solid charged electrode has been analyzed within the framework of the Poisson-Boltzmann (PB) equation. The focus has been on the dependence of the differential capacitance on the geometry of the electrode. To that end spherical or cylindrical electrodes of radius R have been under consideration. The impact of the geometry on the differential capacitance could be conveniently assessed by means of plots of C in dependence of the electrode curvature $1/R$ (see Figs. 4.3 and 4.4). There the size of the electrode has been varied quasi-continuously between the limiting cases of a planar electrode and an electrode of small radius as compared to the Debye length. Further dependencies, for instance on the surface charge density σ and the ionic strength, have been incorporated parametrically in these plots. In the limiting cases of the electrode curvature the graphs reveal different behavior which has been discussed in detail. For small curvatures a strong dependence on the surface charge density occurs. An expansion of C in powers of the curvature has led to expansion coefficients which depend on only one parameter. The curvature expansion in case of the cylindrical electrode has yielded that a prediction in agreement with MT would not be complete. For large curvatures the dependence of C on σ is reduced. This observation is in line with an analytical discussion which provides the insight that for small radii of the spherical electrode a description based on the linearized PB equation becomes reliable.

A system in the PB model is defined by a comparably small amount of parameters. Therefore the PB approach is well suited in order to estimate the basic structure of results in view of more sophisticated models. For instance, here the discussion of the PB model has been helpful in order to gauge the outcome of the microscopic model in Chap. 5. A common extension of the PB approach is usually referred to as the Gouy-Chapman-Stern model (see Chap. 1). There an additional Helmholtz layer is introduced in between the electrode surface and the electrolyte solution which takes into account the volume of the adsorbed ions. This modification is known to affect the differential capacitance at the planar wall. It would be enlightening to extent the present discussion in this context. Furthermore one could try to assess the implications of differently chosen boundary conditions. For instance, image charge effects would consider that the electrode behavior depends on the distribution of the ions. The present discussion has addressed convex electrodes which are surrounded by the electrolyte solution. The question arises, what is the corresponding outcome in the case of concave electrodes filled with electrolyte solution?

Also Chap. 5 has been dedicated to the analysis of EDLs. As compared to Chap. 4, in Chap. 5 a molecular model for the electrolyte solution has been applied in order to determine the structure of the EDL and the corresponding differential capacitance C at a spherical electrode of arbitrary radius R. The DFT implementation of the so-called civilized model is capable of taking into account microscopic details like the volumes of the particles in the electrolyte solution and dipole moments embedded in the solvent

particles. Consequently, for instance the profile of the charge density exhibits new features as compared to PB results, for example, layering close to the electrode. To a large extent the influences of microscopic and other parameters have been assessed by evaluating C as a function of the curvature $1/R$. The basic structure of this kind of plots is known from Chap. 4; these graphs enable to consider the impacts of different parameters in various (geometrical) configurations of the electrode. In Chap. 5 it has turned out that the electrode geometry determines the relevance of microscopic details. PB and the civilized model with equally chosen particle radii predict similar values for the differential capacitance at the planar wall. If the electrode is curved, the agreement deteriorates. However, for equal particle radii at least no qualitative differences occur. The results are only minorly affected by the strength of the dipole moment embedded in the solvent particles. Qualitative differences between the PB and the civilized model arise, if in the latter the particles have unequal radii. In that case these differences manifest at both planar and curved electrodes. In general, the limit of small curvatures is nontrivial and reveals a dependence on various parameters. However, in the limit of large curvatures the dependence on the surface charge density reduces, as in the case of PB. Additionally the results show a common behavior independent of the chosen values for the particle radii. Hence in the limit of large curvatures the linearized PB model might be a satisfactory approximation for the comparably sophisticated civilized model.

In future projects the presented results for the spherical electrode could be complemented by results for the cylindrical electrode. As compared to other geometries, the latter exhibits certain symmetries which allow to reduce the dimensionality of the generic civilized model and which therefore enable precise numeric calculations; this procedure has been discussed here for the spherical electrode and it should be applicable analogously for the cylindrical case. The same should be true for the corresponding complementary cases, i.e., the electrolyte solution surrounded by a spherical or cylindrical electrode. In view of porous electrode surfaces in terms of supercapacitors results for these geometries might be of technological interest. On the way towards a more realistic model one could think about implementing several modifications into the model in the present state; unfortunately these usually would be accompanied by an increase of the already large number of parameters. For instance, specific adsorption of ions at the electrode surface could be incorporated on the level of the external potential. Probably this would have a similar effect as the Helmholtz layer in the Stern model. In that case, the differential capacitance is expected to be affected by this modification. As mentioned before, by means of image charge effects another kind of wall-fluid interaction would be taken into account. Instead of choosing hard spherical particles one could assume the particle shapes to be more asymmetric. In particular, in case of the solvent particles this would couple steric effects with the anisotropic dipole interaction potential which might lead to interesting effects in dependence of the electrode curvature. In view of the explicit dipole description

within the presented model comparisons with simulations would be enlightening. The results have only been minorly affected by the strength of the dipole moment. Therefore the question arises, whether this is a model specific weakness or whether larger impacts cannot be expected principally. Moreover one could think about refining the so-called attractive interaction, which has been assumed to be the same for all particles in the present model. This might be a step towards a description of solvated ions accompanied by a solvation shell. The finding, that the differential capacitance of a small spherical electrode can be estimated rather accurately by the linearized PB equation, might guide the way towards the treatment of more complex surfaces, e.g., rough electrodes.

Summary

The present dissertation has been dedicated to the theoretical study of interfaces between *curved* solid walls and different kinds of fluids. Special attention has been paid to the dependence of interfacial quantities on the wall geometry. The insight gained in the course of this dissertation is contained in Chaps. 2 – 5; in part these have already been published in Refs. [22, 72, 94]. The present thesis can be roughly divided thematically into two parts. In Chaps. 2 and 3 interfaces in combination with various simple fluids have been under consideration. The dependence of the corresponding interfacial tension γ on the curvature of the wall has been assessed and compared with the predictions of the morphometric thermodynamics approach (see below). In Chaps. 4 and 5 electric double layers at interfaces between curved electrodes and electrolyte solutions have been discussed in terms of the differential capacitance C. The results of various models regarding the dependence of the differential capacitance on the electrode geometry have been compared with each other and the impact of several intrinsic parameters has been assessed.

In Chap. 2 the interface between a planar, spherical, or cylindrical wall and several model fluids with small number densities has been analyzed. Density functional theory (DFT) within the second virial approximation [Eq. (2.7)] has been applied in order to determine the interfacial tension γ in dependence of the radius R of the spherical and cylindrical wall. This approach gives accurate results for small number densities which has been confirmed by comparison with computer simulations (see Fig. 2.3). From the numerically acquired relation between γ and R the lowest order coefficients of the curvature expansion in Eq. (2.18) of the interfacial tension γ have been obtained by a fitting routine. These results have been compared with the expressions derived within morphometric thermodynamics (MT) [Eq. (2.3)]. According to the prediction of MT, the dependence of the interfacial tension on the wall curvature is given by a quadratic (linear) polynomial in the curvature in the case of a spherical (cylindrical) wall. Throughout the discussion particular attention has been paid to the implications of the choice of the position of the interface, which underlies the definition of the interfacial tension [see Eq. (2.16) and Fig. 2.1]. For none of the considered systems the expression for the interfacial tension in accordance with morphometric thermodynamics is exact, regardless of whether the particles interact with each other via a square-well or square-shoulder potential [Eq. (2.4)], a Yukawa potential [Eq. (2.5)], or a Lennard-Jones potential [Eq. (2.6)]. In general MT seems to be a

better approximation for spherical than for cylindrical walls. As shown in Figs. 2.5 – 2.8 the coefficients $\gamma_n(\delta)$ of the curvature expansion in Eq. (2.18) may depend sensitively on the chosen interface convention, which is expressed in terms of the shift parameter δ [see Eq. (2.16) and Fig. 2.1]. There are conventions for which the morphometrically allowed coefficients are much larger than the morphometrically forbidden ones so that within these conventions morphometric thermodynamics is a reliable approximation of the interfacial tension. However, the opposite situation can occur for other interface conventions, in which case morphometric thermodynamics has to be used with caution. In particular the reliability of morphometric thermodynamics as an approximation deteriorates in the presence of excess contributions to the hard wall potential (Fig. 2.9). The ratio of the leading coefficients for the spherical wall, $\gamma_{s1}(\delta)$, and for the cylindrical wall, $\gamma_{c1}(\delta)$, has been found to take the well-known value $\gamma_{s1}(\delta)/\gamma_{c1}(\delta) = 2$. Interestingly, in the limit of small number densities and excess external potentials, also the ratio of the corresponding next-to-leading coefficients has rendered the value $\gamma_{s2}(0)/\gamma_{c2}(0) = 8/3$ independent of the particle-particle interaction. This relation, which would not be defined according to MT, has been confirmed in Chap. 3 and in other studies. Based on these results, it turns out to be necessary in future applications of morphometric thermodynamics to clearly state which interface convention is chosen and why morphometric thermodynamics is expected to be a reliable approximation for that particular interface convention as compared with others.

In Chap. 3 the interface between a convex wall of planar, spherical, or cylindrical shape and a Yukawa fluid has been under consideration. To that end the fluid has been described within density functional theory by the functional in Eq. (3.9) which corresponds to a modified version of the functional Eq. (2.7) used in the preceding Chap. 2. The applied simplifications, which have led from the preceding model to the one in Chap. 3, have facilitated to obtain analytic expressions for the interfacial tension [Eqs. (3.34) and (3.35)] at a planar [γ_p, Eq. (3.47)], spherical [γ_s, Eq. (3.58)], and at a cylindrical [γ_c, Eq. (3.78)] wall. That is, within the considered approach the entire dependence of the interfacial tension on the wall radius R is known exactly and can be evaluated as a function of further intrinsic parameters: the strength of the fluid-fluid interaction, the bulk number density, the strength of the wall potential in excess to the hard interaction, and the range of this excess wall potential, which may be chosen independently from the range of the fluid-fluid interaction. In spite of the applied simplifications, the results of the model in Chap. 3 agree well with the ones corresponding to the preceding model in Chap. 2 (see Fig. 3.2). In contrast to the preceding approach, in Chap. 3 the coefficients of the curvature expansions are available analytically for both cases, a spherical wall [with the expansion in Eq. (3.65) and corresponding coefficients γ_{s1} and γ_{s2} in Eqs. (3.66) and (3.67)] and a cylindrical wall [with the expansion in Eq. (3.88) and corresponding coefficients $\gamma_{c1} - \gamma_{c3}$ in Eqs. (3.89) – (3.91)]. As compared to numerically determined curvature coefficients

these exactly known coefficients are not subject to inaccuracies in fitting procedures. Furthermore they allow one to scan the parameter space rapidly. The results in Chap. 3 could substantiate the findings of the preceding chapter. For instance, it has been possible to actually *prove*, that for the model under consideration the approach of morphometric thermodynamics is not complete. Therefore the morphometric approach has the status of an approximation. The quality of MT as an approximation has been discussed within the convention $\delta = 0$. For the cylindrical geometry the arbitrary criterion for a good approximation $|\gamma_p|, |\gamma_{c1}| > |\gamma_{c2}|, |\gamma_{c3}|, \dots$ has been introduced in order to judge the values of the coefficients relative to each other. With the aid of plots the dependence of the coefficients on various system parameters has been examined. In most cases the criterion has turned out to be not fulfilled mainly because $|\gamma_{c2}| > |\gamma_{c1}|$. This can be observed, e.g., in Figs. 3.3 and 3.4, where the bulk parameters packing fraction and strength of the fluid-fluid interaction potential are varied. An additional excess external potential, parameterized by its strength and range in Figs. 3.5 and 3.6, further deteriorates the applicability of MT because there the criterion is as well violated with respect to γ_{c3}. The results for the two types of curved geometries reveal qualitative differences. In the case of *cylindrical* walls the morphometric approach proposes to truncate the curvature expansion such that terms of significant magnitude may be neglected. However, for *spherical* geometries the MT expression equals the exact one up to exponentially small terms and, thus, it corresponds to an approximation of comparatively high quality. The aforementioned relations between curvature coefficients of different geometries [see Eqs. (3.92) and (3.95)] agree well with those found in the literature and in Chap. 2.

In Chap. 4 an interface between a charged electrode and an electrolyte solution has been examined. The structure of the accompanying electrical double layer (EDL) has been assessed in terms of the Poisson-Boltzmann (PB) equation [Eq. (4.1)]. Electrodes of planar ($d = 0$), cylindrical ($d = 1$), or spherical ($d = 2$) shape [Eq. (4.2)] have been analyzed. The differential capacitance C [Eq. (4.5)] has been calculated for various ionic strengths I, surface charge densities σ, and electrode radii R. The focus has been on examining the dependence of the differential capacitance on the curvature $1/R$ of the electrode as displayed in Figs. 4.3 and 4.4. In all cases the surface charge density has a strong effect on the capacitance for small curvatures whereas for large curvatures the behavior becomes independent of σ. These limits have been analyzed in detail. For small curvatures (see Sec. 4.3.3) a curvature expansion of the capacitance [Eq. (4.14)] has revealed the behavior in a very convenient way because the corresponding expansion coefficients C_n depend on the single parameter $t \in [-1, 1]$ [Eqs. (4.15) and (4.28)] and on the geometry $d \in \{0, 1, 2\}$ only. Therefore, within PB theory, the influence of any conceivable combination of system parameters on the lowest order coefficients C_n can be inferred from Fig. 4.5. For large curvatures (see Sec. 4.3.4) an analytic discussion has provided the insight that the linearized PB theory becomes reliable, if the radius of

the spherical wall is small enough; this explains the general behavior visible in Fig. 4.3. In Chap. 4 the mesoscopic structure of electrolyte solutions at curved electrodes has been discussed systematically in terms of the differential capacitance within PB theory. Within the latter a system is specified by a relatively small amount of parameters and the comparably simple description allows for detailed discussions. Therefore this approach is well suited for providing the basic structure of results for the considered kind of systems, i.e., electrolyte solutions at curved electrodes. That is, this approach offers to judge less integral, microscopic approaches such as the one presented in Chap. 5.

In Chap. 5 the electric double layer of an electrolyte solution in contact with an electrode of planar or spherical shape has been analyzed. The electrolyte solution has been described in terms of density functional theory based on the functional given in Eq. (5.3). This approach, which is a certain version of the so-called *civ*ilized model (CIV, see Sec. 5.2.4), takes into account all particle species on equal footing. All particles are modelled as hard spheres with non-vanishing volumes, embedded charges (in the cases of the monovalent anions or cations) or point-dipoles (in the case of the solvent molecules), and with an attractive interaction amongst all particles which enables one to discuss an electrolyte solution in the liquid state under realistic ambient conditions. This microscopic model is a possible extension of the mesoscopic Poisson-Boltzmann approach, which has been used in Chap. 4 in order to discuss EDLs at curved electrodes. Close to the wall the microscopic description gives rise to a layering behavior of the charge density and of the polarization (see Figs. 5.2 – 5.4) whereas the PB approach renders monotonic profiles only. As in Chap. 4 the structural features of the EDL enter into the differential capacitance C [Eq. (5.32)] which facilitates the comparison of various models or the evaluation of the influence of various system parameters such as particle radii, dipole moment of the solvent molecules, ionic strength, surface charge density, and electrode radius. At the planar wall and for equal radii of all particles, PB and CIV lead to similar values for the capacitance (see Fig. 5.5). Since in comparison with CIV (see Sec. 5.2.4) PB neglects many microscopic details, this finding is not obvious. Against this background, in its turn it is remarkable, that in the case of spherical electrodes of finite radii R the agreement between the predictions of the two models deteriorates (see Fig. 5.7), i.e., the relevance of microscopic details, captured by the CIV model, depends on the geometry of the electrode. The restricted primitive model (RPM), in which the particle species are not treated on equal footing, clearly exhibits a different trend in comparison with the other models (see Figs. 5.5 and 5.7). In the case of spherical electrodes the capacitance data obtained within CIV for equal particle radii are qualitatively similar to the PB results in Chap. 4 (compare Fig. 4.3 with Figs. 5.8 – 5.10). Nevertheless, there are quantitative differences (see Fig. 5.7). Considering the dipoles explicitly has no large effect (compare the two curves labelled with CIV in Figs. 5.5 and 5.7 or compare Fig. 5.8 with Fig. 5.10). Qualitative and relatively large quantitative differences occur if the particle radii of ions

and solvent molecules are unequal. This is the case for planar electrodes [see Fig. 5.6 where the PB result turns out to be close to the solid black curve (see Fig. 5.5)] as well as spherical electrodes (compare Fig. 5.8 with Figs. 5.11 – 5.14). However, the differences are borne out only for small and intermediate electrode curvatures $1/(\kappa R)$. For large curvatures the capacitance curves of all considered cases exhibit a common behavior and converge to the limiting graph valid for small surface charge densities $\sigma \rightarrow 0$, i.e., in this limit the behavior becomes independent of σ (see Figs. 5.8 – 5.14). Moreover, this behavior becomes also independent of the choice of the particle radii (see Fig. 5.15). For $1/(\kappa R) \gg 1$ the simple linearized PB model appears to be an adequate approximation of the relatively complex CIV. In summary it can be stated that the geometry of the electrode determines the relevance of microscopic details. Apart from the limit of small electrode radii, for which a general behavior is observed, PB provides acceptable estimates in the case of equal particle sizes and large electrode radii.

Zusammenfassung

Die vorliegende Dissertation wurde dem theoretischen Studium von Grenzflächen zwischen *gekrümmten* festen Wänden und verschiedenen Arten von Fluiden gewidmet. Besondere Aufmerksamkeit galt der Wandgeometrieabhängigkeit von Grenzflächengrößen. Die im Zuge dieser Dissertation erlangten Erkenntnisse sind in den Kapiteln 2 – 5 enthalten; zum Teil sind diese bereits unter den Referenzen [22, 72, 94] veröffentlicht worden. Die vorliegende Doktorarbeit kann thematisch grob in zwei Teile unterteilt werden. In den Kapiteln 2 und 3 wurden Grenzflächen in Kombination mit verschiedenen einfachen Fluiden betrachtet. Die Wandkrümmungsabhängigkeit der entsprechenden Grenzflächenspannung γ wurde bestimmt und mit den Vorhersagen des Ansatzes der morphometrischen Thermodynamik (siehe unten) verglichen. In den Kapiteln 4 und 5 wurden elektrische Doppelschichten an Grenzflächen zwischen gekrümmten Elektroden und Elektrolytlösungen hinsichtlich der differentiellen Kapazität C diskutiert. Die Ergebnisse verschiedener Modelle bezüglich der Elektrodengeometrieabhängigkeit der differentiellen Kapazität wurden miteinander verglichen und die Einflüsse unterschiedlicher inhärenter Parameter wurden bestimmt.

In Kapitel 2 wurde die Grenzfläche zwischen einer ebenen, kugel- oder zylinderförmigen Wand und verschiedenen Modellfluiden kleiner Anzahldichten analysiert. Dichtefunktionaltheorie (DFT) in zweiter Virialnäherung [Gl. (2.7)] wurde verwendet um die Grenzflächenspannung γ in Abhängigkeit des Radiuses R der kugel- oder zylinderförmigen Wand zu bestimmen. Dieser Ansatz erzielt genaue Ergebnisse bei kleinen Anzahldichten, was durch den Vergleich mit Computersimulationen bestätigt wurde (siehe Abb. 2.3). Aus dem numerisch erlangten Zusammenhang zwischen γ und R wurden die Koeffizienten kleinster Ordnung der Krümmungsentwicklung in Gl. (2.18) der Grenzflächenspannung γ durch Kurvenanpassung gewonnen. Diese Ergebnisse wurden mit den aus der morphometrischen Thermodynamik (MT) abgeleiteten Ausdrücken [Gl. (2.3)] verglichen. Gemäß der Vorhersage der MT ist die Wandkrümmungsabhängigkeit der Grenzflächenspannung im Fall einer kugelförmigen (zylinderförmigen) Wand durch ein quadratisches (lineares) Polynom in der Krümmung gegeben. Während der Diskussion wurde insbesondere auf die Auswirkungen der Wahl der Grenzflächenposition geachtet, die der Definition der Grenzflächenspannung zugrunde liegt [siehe Gl. (2.16) und Abb. 2.1]. Bei keinem der betrachteten Systeme ist der Ausdruck für die Grenzflächenspannung gemäß der morphome-

trischen Thermodynamik exakt, ungeachtet dessen, ob die Teilchen miteinander durch ein square-well oder square-shoulder Potential [Gl. (2.4)], ein Yukawa Potential [Gl. (2.5)] oder ein Lennard-Jones Potential [Gl. (2.6)] wechselwirken. Generell scheint MT eine bessere Approximation für kugelförmige als für zylinderförmige Wände zu sein. Wie in den Abb. 2.5 – 2.8 gezeigt können die Koeffizienten $\gamma_n(\delta)$ der Krümmungsentwicklung in Gl. (2.18) empfindlich von der gewählten Grenzflächenkonvention, die mithilfe des Verschiebeparameters δ [siehe Gl. (2.16) und Abb. 2.1] wiedergegeben wird, abhängen. Es gibt Konventionen, in denen die morphometrisch erlaubten Koeffizienten viel größer als die morphometrisch verbotenen sind, so dass innerhalb dieser Konventionen die morphometrische Thermodynamik eine zuverlässige Approximation der Grenzflächenspannung darstellt. In anderen Grenzflächenkonventionen kann sich jedoch auch die gegenteilige Situation einstellen, in welchem Fall die morphometrische Thermodynamik mit Vorsicht eingesetzt werden sollte. Insbesondere verschlechtert sich die Zuverlässigkeit der morphometrischen Thermodynamik als Approximation in Gegenwart von Zusatzbeiträgen zum harten Wandpotential (Abb. 2.9). Für das Verhältnis der führenden Koeffizienten der kugelförmigen Wand, $\gamma_{s1}(\delta)$, und der zylinderförmigen Wand, $\gamma_{c1}(\delta)$, wurde der bekannte Wert $\gamma_{s1}(\delta)/\gamma_{c1}(\delta) = 2$ festgestellt. Interessanterweise hat sich im Limes kleiner Anzahldichten und Zusatzbeiträge zum externen Potential auch für das Verhältnis der entsprechenden Koeffizienten zweiter Ordnung der Wert $\gamma_{s2}(0)/\gamma_{c2}(0) = 8/3$ unabhängig von der Teilchen-Teilchen Wechselwirkung ergeben. Dieser Zusammenhang, der gemäß MT nicht definiert wäre, wurde in Kapitel 3 und in anderen Studien bestätigt. Aufgrund dieser Ergebnisse stellt es sich für zukünftige Anwendungen von morphometrischer Thermodynamik als notwendig heraus, klar darzulegen, welche Grenzflächenkonvention gewählt wird und warum erwartet wird, dass durch die morphometrische Thermodynamik in dieser Grenzflächenkonvention eine vergleichsweise zuverlässige Approximation gegeben ist.

In Kapitel 3 wurde die Grenzfläche zwischen einer konvexen Wand von ebener, kugel- oder zylinderförmiger Gestalt und einem Yukawafluid betrachtet. Zu diesem Zweck wurde das Fluid mittels Dichtefunktionaltheorie durch das Funktional in Gl. (3.9) beschrieben, welches einer modifizierten Version des im vorangehenden Kapitel 2 verwendeten Funktionals in Gl. (2.7) entspricht. Die angewendeten Vereinfachungen, die vom vorangehenden Modell zu demjenigen in Kapitel 3 geführt haben, ermöglichten es analytische Ausdrücke für die Grenzflächenspannung [Gln. (3.34) und (3.35)] an einer ebenen [γ_p, Gl. (3.47)], kugelförmigen [γ_s, Gl. (3.58)] und an einer zylinderförmigen [γ_c, Gl. (3.78)] Wand zu erhalten. Das heißt, innerhalb des betrachteten Ansatzes ist die gesamte Abhängigkeit der Grenzflächenspannung vom Wandradius R bekannt und kann als Funktion weiterer inhärenter Parameter ausgewertet werden: die Stärke der Fluid-Fluid Wechselwirkung, die Anzahldichte im Bulk, die Stärke des Wandpotentials zusätzlich zur harten Wechselwirkung und die Reichweite ebendieses Wandpotentials, die unabhängig von der Reichwei-

te der Fluid-Fluid Wechselwirkung gewählt werden kann. Trotz der angewendeten Vereinfachungen stimmen die Ergebnisse des Modells in Kapitel 3 gut mit denjenigen aus dem vorangehenden Modell in Kapitel 2 überein (siehe Abb. 3.2). Im Gegensatz zum vorangehenden Ansatz sind in Kapitel 3 die Koeffizienten der Krümmungsentwicklungen sowohl für eine kugelförmige Wand [mit der Entwicklung in Gl. (3.65) und den entsprechenden Koeffizienten γ_{s1} und γ_{s2} in Gln. (3.66) und (3.67)] als auch für eine zylinderförmige Wand [mit der Entwicklung in Gl. (3.88) und den entsprechenden Koeffizienten γ_{c1} – γ_{c3} in Gln. (3.89) – (3.91)] analytisch zugänglich. Verglichen mit numerisch bestimmten Krümmungskoeffizienten unterliegen diese genau bekannten Koeffizienten keinerlei Ungenauigkeiten durch Kurvenanpassungen. Darüber hinaus ermöglichen sie den Parameterraum zügig abzutasten. Die Ergebnisse in Kapitel 3 konnten die Befunde des vorangehenden Kapitels untermauern. Zum Beispiel war es möglich zu *beweisen*, dass der Ansatz der morphometrischen Thermodynamik für das betrachtete Modell nicht vollständig ist. Aus diesem Grund ist der morphometrische Ansatz als Approximation einzuordnen. Die Qualität der MT als Approximation wurde bezüglich der Konvention $\delta = 0$ erörtert. Um die Beträge der Koeffizienten relativ zueinander zu beurteilen, wurde für die Zylindergeometrie das willkürliche Kriterium für eine gute Approximation $|\gamma_p|, |\gamma_{c1}| > |\gamma_{c2}|, |\gamma_{c3}|, \dots$ eingeführt. Unter Zuhilfenahme von Plots wurde die Abhängigkeit der Koeffizienten von verschiedenen Systemparametern untersucht. Hauptsächlich weil $|\gamma_{c2}| > |\gamma_{c1}|$ stellte sich das Kriterium in den meisten Fällen als nicht erfüllt heraus. Dies lässt sich z.B. in Abb. 3.3 und 3.4 feststellen, in denen Bulkparameter, namentlich die Packungsdichte und die Stärke des Fluid-Fluid Wechselwirkungspotentials, variiert werden. Durch ein zusätzliches äußeres Potential, das in Abb. 3.5 und 3.6 durch seine Stärke und Reichweite parametrisiert wird, verschlechtert sich die Anwendbarkeit der MT weiter, weil dann das Kriterium auch in Bezug auf γ_{c3} verletzt wird. Die Ergebnisse für die zwei Typen von gekrümmten Geometrien offenbaren qualitative Unterschiede. Im Fall *zylinderförmiger* Wände schlägt der morphometrische Ansatz vor, die Krümmungsentwicklung so abzubrechen, dass dabei Terme signifikanter Größe vernachlässigt werden können. Bei *kugelförmigen* Geometrien hingegen gleicht der MT Ausdruck dem exakten bis auf exponentiell kleine Terme und entspricht somit einer Approximation vergleichsweise hoher Qualität. Die oben angesprochenen Verhältnisse zwischen Krümmungskoeffizienten verschiedener Geometrien [siehe Gln. (3.92) und (3.95)] stimmen gut mit den entsprechenden in der Literatur und in Kapitel 2 überein.

In Kapitel 4 wurde eine Grenzfläche zwischen einer geladenen Elektrode und einer Elektrolytlösung untersucht. Die Struktur der damit einhergehenden elektrischen Doppelschicht (EDL, englisch: electric double layer) wurde auf Basis der Poisson-Boltzmann (PB) Gleichung [Gl. (4.1)] bestimmt. Elektroden ebener ($d = 0$), zylinderförmiger ($d = 1$) oder kugelförmiger ($d = 2$) Gestalt [Gl. (4.2)] wurden analysiert. Die differentielle Kapazität C [Gl. (4.5)] wurde für unterschiedliche Ionenstärken I, Oberflächenladungsdichten

σ und Elektrodenradien R berechnet. Der Schwerpunkt lag auf der Untersuchung der Abhängigkeit der differentiellen Kapazität von der Elektrodenkrümmung $1/R$ wie in Abb. 4.3 und 4.4 dargestellt. In allen Fällen hat die Oberflächenladungsdichte einen starken Effekt auf die Kapazität bei kleinen Krümmungen, während sich bei großen Krümmungen ein von σ unabhängiges Verhalten zeigt. Diese Grenzfälle wurden ausführlich untersucht. Für kleine Krümmungen (siehe Abschnitt 4.3.3) offenbarte eine Krümmungsentwicklung der Kapazität [Gl. (4.14)] das Verhalten auf praktische Weise, weil die entsprechenden Entwicklungskoeffizienten C_n nur von dem einen Parameter $t \in [-1, 1]$ [Gln. (4.15) und (4.28)] und von der Geometrie $d \in \{0, 1, 2\}$ abhängen. Daher kann aus Abb. 4.5 auf den Einfluss jeder denkbaren Kombination von Systemparametern innerhalb der PB Theorie auf die Koeffizienten C_n niedrigster Ordnung geschlossen werden. Für große Krümmungen (siehe Abschnitt 4.3.4) führte eine analytische Diskussion zu der Erkenntnis, dass die linearisierte PB Theorie zuverlässig wird, sofern der Radius der kugelförmigen Wand klein genug ist; dies erklärt das in Abb. 4.3 erkennbare generelle Verhalten. In Kapitel 4 wurde die mesoskopische Struktur von Elektrolytlösungen an gekrümmten Elektroden im Bezug auf die differentielle Kapazität im Rahmen der PB Theorie systematisch erörtert. Innerhalb letzterer wird ein System durch eine relativ kleine Anzahl an Parametern festgelegt und die vergleichsweise einfache Beschreibung ermöglicht detaillierte Diskussionen. Aus diesen Gründen eignet sich dieser Zugang gut um die Grundstruktur der Ergebnisse bezüglich der betrachteten Systeme, d.h. Elektrolytlösungen an gekrümmten Elektroden, bereitzustellen. Das heißt, dieser Ansatz ermöglicht es, weniger zugängliche, mikroskopische Ansätze einzuschätzen, wie z.B. denjenigen in Kapitel 5.

In Kapitel 5 wurde die elektrische Doppelschicht einer Elektrolytlösung in Kontakt mit einer Elektrode ebener oder kugelförmiger Gestalt analysiert. Die Elektrolytlösung wurde mittels Dichtefunktionaltheorie auf Basis des Funktionals in Gl. (5.3) beschrieben. Dieser Ansatz, eine Art des so genannten *civ*ilized model (CIV, siehe Abschnitt 5.2.4), berücksichtigt alle Teilchensorten auf gleiche Weise. Alle Teilchen werden als harte Kugeln modelliert mit nicht-verschwindenden Volumina, eingebetteten Ladungen (in den Fällen der monovalenten Anionen oder Kationen) oder Punkt-Dipolen (im Fall der Lösungsmittelmoleküle) und mit einer attraktiven Wechselwirkung zwischen allen Teilchen, die es ermöglicht, eine Elektrolytlösung im flüssigen Zustand unter realistischen Umgebungsbedingungen zu betrachten. Dieses mikroskopische Modell ist eine denkbare Erweiterung des mesoskopischen Poisson-Boltzmann Ansatzes, der in Kapitel 4 verwendet wurde um EDLs an gekrümmten Elektroden zu diskutieren. Durch die mikroskopische Beschreibung wird nahe der Wand Schichtbildung im Profil der Ladungsdichte und der Polarisation sichtbar (siehe Abb. 5.2 – 5.4) während der PB Ansatz lediglich monotone Profile wiedergibt. Wie in Kapitel 4 gehen die strukturellen Besonderheiten der EDL in die differentielle Kapazität C [Gl. (5.32)] ein, was den Vergleich verschiedener Modelle miteinander vereinfacht bzw. es ermöglicht, den Einfluss unterschiedlicher Systemparameter wie Teilchenradien, Dipol-

moment der Lösungsmittelmoleküle, Ionenstärke, Oberflächenladungsdichte und Elektrodenradius zu ermitteln. An der ebenen Wand und bei gleichen Teilchenradien führen PB und CIV auf ähnliche Werte für die Kapazität (siehe Abb. 5.5). Da PB, verglichen mit CIV (siehe Abschnitt 5.2.4), viele mikroskopische Details vernachlässigt, ist dieser Befund nicht selbstverständlich. Vor diesem Hintergrund ist es wiederum bemerkenswert, dass sich im Falle kugelförmiger Elektroden endlicher Radien R die Übereinstimmung zwischen den Vorhersagen der beiden Modelle verschlechtert (siehe Abb. 5.7), d.h. die Relevanz mikroskopischer Details, erfasst im CIV Modell, hängt von der Elektrodengeometrie ab. Das restricted primitive model (RPM), in welchem die Teilchensorten nicht alle auf die gleiche Weise berücksichtigt werden, weist im Vergleich mit den anderen Modellen klar einen abweichenden Verlauf auf (siehe Abb. 5.5 und 5.7). Im Falle kugelförmiger Elektroden sind die Kapazitätsdaten, die innerhalb CIV mit gleichen Teilchenradien berechnet wurden, qualitativ ähnlich zu den PB Resultaten in Kapitel 4 (vergleiche Abb. 4.3 mit Abb. 5.8 – 5.10). Dennoch sind quantitative Unterschiede vorhanden (siehe Abb. 5.7). Die explizite Betrachtung der Dipole hat keinen großen Effekt zur Folge (vergleiche die zwei mit CIV bezeichneten Kurven in Abb. 5.5 und 5.7 oder vergleiche Abb. 5.8 mit Abb. 5.10). Qualitative und relativ große quantitative Unterschiede tauchen auf, wenn die Teilchenradien der Ionen und Lösungsmittelmoleküle ungleich sind. Dies ist der Fall sowohl für ebene Elektroden [siehe Abb. 5.6, in welcher das PB Ergebnis nahe der durchgezogenen schwarzen Kurve wäre (siehe Abb. 5.5)] als auch für kugelförmige Elektroden (vergleiche Abb. 5.8 mit Abb. 5.11 – 5.14). Jedoch sind die Differenzen nur bei kleinen und mittleren Elektrodenkrümmungen $1/(\kappa R)$ ausgeprägt. Bei großen Krümmungen weisen die Kapazitätskurven aller betrachteter Fälle ein gemeinsames Verhalten auf und konvergieren gegen die Kurve, die dem Grenzfall kleiner Oberflächenladungsdichten $\sigma \to 0$ entspricht, d.h., in diesem Limes wird das Verhalten unabhängig von σ (siehe Abb. 5.8 – 5.14). Darüber hinaus wird das Verhalten auch unabhängig von der Wahl der Teilchenradien (siehe Abb. 5.15). Für $1/(\kappa R) \gg 1$ scheint das einfache linearisierte PB Modell eine angemessene Approximation für das relativ komplexe CIV zu sein. Zusammenfassend kann festgestellt werden, dass die Elektrodengeometrie die Relevanz mikroskopischer Details festlegt. Abgesehen vom Limes kleiner Elektrodenradien, in welchem ein generelles Verhalten beobachtet wird, bietet PB akzeptable Abschätzungen im Fall gleicher Teilchengrößen und großer Elektrodenradien.

Bibliography

[1] H.-D. Dörfler, *Grenzflächen und kolloid-disperse Systeme* (Springer, Berlin, 2002).

[2] H.-J. Butt, K. Graf, and M. Kappl, *Physics and chemistry of interfaces* (Wiley, Weinheim, 2003).

[3] J. S. Rowlinson and B. Widom, *Molecular theory of capillarity* (Dover Publications, New York, 2002).

[4] J. Lyklema, *Fundamentals of interface and colloid science, Vol. 1: Fundamentals* (Academic, London, 1993).

[5] R. C. Tolman, J. Chem. Phys. **17**, 333 (1949).

[6] D. Fennell Evans and H. Wennerström, *The colloidal domain — Where physics, chemistry, biology, and technology meet* (VCH, New York, 1994).

[7] M. Bachmann, *Thermodynamics and statistical mechanics of macromolecular systems* (Cambridge, Cambridge, 2014).

[8] P.-M. König, R. Roth, and K. R. Mecke, Phys. Rev. Lett. **93**, 160601 (2004).

[9] B. Groh and S. Dietrich, Phys. Rev. E **59**, 4216 (1999).

[10] P. Bryk, R. Roth, K. R. Mecke, and S. Dietrich, Phys. Rev. E **68**, 031602 (2003).

[11] P.-M. König, P. Bryk, K. Mecke, and R. Roth, Europhys. Lett. **69**, 832 (2005).

[12] R. Roth, J. Phys.: Condens. Matter **17**, S3463 (2005).

[13] H. Hansen-Goos and R. Roth, J. Phys.: Condens. Matter **18**, 8413 (2006).

[14] R. Roth, Y. Harano, and M. Kinoshita, Phys. Rev. Lett. **97**, 078101 (2006).

[15] H. Hansen-Goos, R. Roth, K. Mecke, and S. Dietrich, Phys. Rev. Lett. **99**, 128101 (2007).

[16] B. B. Laird, A. Hunter, and R. L. Davidchack, Phys. Rev. E **86**, 060602(R) (2012).

[17] Y. Harano, R. Roth, and S. Chiba, J. Comput. Chem. **34**, 1969 (2013).

[18] M. E. Evans and R. Roth, Phys. Rev. Lett. **112**, 038102 (2014).

[19] E. M. Blokhuis, Phys. Rev. E **87**, 022401 (2013).

[20] H. Hansen-Goos, J. Chem. Phys. **141**, 171101 (2014).

[21] I. Urrutia, Phys. Rev. E **89**, 032122 (2014).

[22] A. Reindl, M. Bier, and S. Dietrich, Phys. Rev. E **91**, 022406 (2015).

[23] I. Urrutia and I. E. Paganini, J. Chem. Phys. **144**, 174102 (2016).

[24] I. Urrutia, Phys. Rev. E **94**, 022149 (2016).

[25] D. C. Grahame, J. Am. Chem. Soc. **76**, 4819 (1954).

[26] R. Parsons and R. Payne, Z. Phys. Chem. **98**, 9 (1975).

[27] G. Valette, A. Hamelin, and R. Parsons, Z. Phys. Chem. **113**, 71 (1978).

[28] G. Valette, J. Electroanal. Chem. **122**, 285 (1981).

[29] M. M. Islam, M. T. Alam, and T. Ohsaka, J. Phys. Chem. C **112**, 16568 (2008).

[30] H. Helmholtz, Ann. Phys. **243**, 337 (1879).

[31] O. Stern, Zeitschrift für Elektrochemie **30**, 508 (1924).

[32] M. Gouy, J. Phys. Theor. Appl. **9**, 457 (1910).

[33] D. L. Chapman, Philos. Mag. **25**, 475 (1913).

[34] W. Schmickler and E. Santos, *Interfacial electrochemistry* (Springer, Berlin, 2010).

[35] D. C. Grahame, Chem. Rev. **41**, 441 (1947).

[36] D. N. Card and J. P. Valleau, J. Chem. Phys. **52**, 6232 (1970).

[37] D. M. Heyes, Chem. Phys. **69**, 155 (1982).

[38] G.-W. Wu, M. Lee, and K.-Y. Chan, Chem. Phys. Lett. **307**, 419 (1999).

[39] G. M. Torrie and J. P. Valleau, J. Chem. Phys. **73**, 5807 (1980).

[40] L. Degrève, M. Lozada-Cassou, E. Sánchez, and E. González-Tovar, J. Chem. Phys. **98**, 8905 (1993).

[41] C. N. Patra, J. Phys. Chem. B **113**, 13980 (2009).

[42] J. G. Kirkwood, J. Chem. Phys. **2**, 767 (1934).

[43] J. J. Bikerman, Phil. Mag. **33**, 384 (1942).

[44] S. Levine and G. M. Bell, J. Phys. Chem. **64**, 1188 (1960).

[45] L. B. Bhuiyan, C. W. Outhwaite, and S. Levine, Chem. Phys. Lett. **66**, 321 (1979).

[46] C. W. Outhwaite, L. B. Bhuiyan, and S. Levine, J. Chem. Soc.-Faraday Trans. II **76**, 1388 (1980).

[47] C. W. Outhwaite and L. B. Bhuiyan, J. Chem. Soc.-Faraday Trans. II **79**, 707 (1983).

[48] C. W. Outhwaite and L. B. Bhuiyan, J. Chem. Phys. **84**, 3461 (1986).

[49] J. P. Hansen and I. R. McDonald, *Theory of simple liquids* (Academic, London, 1976).

[50] J. C. Rasaiah, D. N. Card, and J. P. Valleau, J. Chem. Phys. **56**, 248 (1972).

[51] B. Larsen, J. Chem. Phys. **68**, 4511 (1978).

[52] E. Waisman and J. L. Lebowitz, J. Chem. Phys. **56**, 3086 (1972).

[53] E. Waisman and J. L. Lebowitz, J. Chem. Phys. **56**, 3093 (1972).

[54] S. L. Carnie and D. Y. C. Chan, J. Chem. Phys. **73**, 2949 (1980).

[55] L. Blum and D. Henderson, J. Chem. Phys. **74**, 1902 (1981).

[56] G. M. Torrie, P. G. Kusalik, and G. N. Patey, J. Chem. Phys. **90**, 4513 (1989).

[57] G. M. Torrie, P. G. Kusalik, and G. N. Patey, J. Chem. Phys. **91**, 6367 (1989).

[58] R. Evans, Adv. Phys. **28**, 143 (1979).

[59] Y. Rosenfeld, Phys. Rev. Lett. **63**, 980 (1989).

[60] R. Roth, R. Evans, A. Lang, and G. Kahl, J. Phys.: Condens. Matter **14**, 12063 (2002).

[61] R. Roth, J. Phys.: Condens. Matter **22**, 063102 (2010).

[62] A. Oleksy and J.-P. Hansen, Mol. Phys. **104**, 2871 (2006).

[63] B. Medasani, Z. Ovanesyan, D. G. Thomas, M. L. Sushko, and M. Marucho, J. Chem. Phys. **140**, 204510 (2014).

[64] Z. Ovanesyan, B. Medasani, M. O. Fenley, G. I. Guerrero-García, M. Olvera de la Cruz, and M. Marucho, J. Chem. Phys. **141**, 225103 (2014).

[65] R. Roth and D. Gillespie, J. Phys.: Condens. Matter **28**, 244006 (2016).

[66] T. Biben, J. P. Hansen, and Y. Rosenfeld, Phys. Rev. E **57**, R3727 (1998).

[67] S. Lamperski and C. W. Outhwaite, J. Electroanal. Chem. **460**, 135 (1999).

[68] A. Oleksy and J.-P. Hansen, J. Chem. Phys. **132**, 204702 (2010).

[69] D. Henderson, D. Jiang, Z. Jin, and J. Wu, J. Phys. Chem. B **116**, 11356 (2012).

[70] A. Härtel, S. Samin, and R. van Roij, J. Phys.: Condens. Matter **28**, 244007 (2016).

[71] V. Warshavsky and M. Marucho, Phys. Rev. E **93**, 042607 (2016).

[72] A. Reindl, M. Bier, and S. Dietrich, J. Chem. Phys. **146**, 154704 (2017).

[73] A. A. Kornyshev, J. Phys. Chem. B **111**, 5545 (2007).

[74] M. V. Fedorov and A. A. Kornyshev, Chem. Rev. **114**, 2978 (2014).

[75] M. Z. Bazant, B. D. Storey, and A. A. Kornyshev, Phys. Rev. Lett. **106**, 046102 (2011).

[76] M. Z. Bazant, B. D. Storey, and A. A. Kornyshev, Phys. Rev. Lett. **109**, 149903 (2012).

[77] C. Merlet, B. Rotenberg, P. A. Madden, and M. Salanne, Phys. Chem. Chem. Phys. **15**, 15781 (2013).

[78] H. Hadwiger, *Vorlesungen über Inhalt, Oberfläche und Isoperimetrie* (Springer, Berlin, 1957).

[79] K. R. Mecke, Int. J. Mod. Phys. B **12**, 861 (1998).

[80] G. Gompper and S. Zschocke, Phys. Rev. A **46**, 4836 (1992).

[81] E. M. Blokhuis and D. Bedeaux, Mol. Phys. **80**, 705 (1993).

[82] M. Schmidt, H. Löwen, J. M. Brader, and R. Evans, J. Phys. Condens. Matt. **14**, 9353 (2002).

[83] J. R. Henderson, J. Chem. Phys. **116**, 5039 (2002).

[84] M. Abramowitz and I. A. Stegun, *Handbook of mathematical functions with formulas, graphs, and mathematical tables* (U.S. Government Printing Office, Washington, DC, 1970).

[85] D. E. Sullivan, J. Chem. Phys. **74**, 2604 (1981).

[86] D. E. Sullivan, Phys. Rev. B **20**, 3991 (1979).

[87] I. Hadjiagapiou, J. Phys.: Condens. Matter **6**, 5303 (1994).

[88] I. A. Hadjiagapiou, J. Phys.: Condens. Matter **7**, 547 (1995).

[89] R. Hołyst and A. Poniewierski, Physica A **149**, 622 (1988).

[90] I. Hadjiagapiou, J. Chem. Phys. **105**, 2927 (1996).

[91] I. A. Hadjiagapiou, J. Phys. Chem. B **101**, 8990 (1997).

[92] A. D. Polyanin and A. V. Manzhirov, *Handbuch der Integralgleichungen* (Spektrum, Heidelberg, 1999).

[93] W. Helfrich, Z. Naturforsch. C **28**, 693 (1973).

[94] A. Reindl, M. Bier, and S. Dietrich, J. Chem. Phys. **146**, 154703 (2017).

[95] M. V. Kiamahalleh, S. H. S. Zein, G. Najafpour, S. A. Sata, and S. Buniran, Nano **7**, 1230002 (2012).

[96] E. T. Mombeshora and V. O. Nyamori, Int. J. Energy Res. **39**, 1955 (2015).

[97] G. Qu, J. Cheng, X. Li, D. Yuan, P. Chen, X. Chen, B. Wang, and H. Peng, Adv. Mater. **28**, 3646 (2016).

[98] L. Šamaj and E. Trizac, Phys. Rev. E **93**, 012601 (2016).

[99] L. Šamaj and E. Trizac, J. Phys. A: Math. Theor. **48**, 265003 (2015).

[100] R. Kant and M. B. Singh, Phys. Rev. E **88**, 052303 (2013).

[101] E. J. F. Dickinson and R. G. Compton, J. Phys. Chem. C **113**, 17585 (2009).

[102] M. C. Henstridge, E. J. F. Dickinson, and R. G. Compton, Chem. Phys. Lett. **485**, 167 (2010).

[103] J. Huang, R. Qiao, B. G. Sumpter, and V. Meunier, J. Mater. Res. **25**, 1469 (2010).

[104] R. E. Goldstein, A. I. Pesci, and V. Romero-Rochín, Phys. Rev. A **41**, 5504 (1990).

[105] B. Duplantier, R. E. Goldstein, V. Romero-Rochín, and A. I. Pesci, Phys. Rev. Lett. **65**, 508 (1990).

[106] E. Trizac and G. Téllez, Macromolecules **40**, 1305 (2007).

[107] H. N. W. Lekkerkerker, Physica A **159**, 319 (1989).

[108] D. J. Mitchell and B. W. Ninham, Langmuir **5**, 1121 (1989).

[109] W. J. Moore, *Physical chemistry* (Longman, London, 1976).

[110] W. M. Haynes (ed.), *CRC handbook of chemistry and physics* (CRC, Boca Raton, 2016).

[111] E. W. Lemmon, M. O. McLinden, and D. G. Friend, *Thermophysical properties of fluid systems*, in *NIST chemistry webbook, NIST standard reference database number 69*, edited by P. J. Linstrom and W. G. Mallard (National Institute of Standards and Technology, Gaithersburg MD, 2016); http://webbook.nist.gov (retrieved December 2, 2016).

[112] D. I. Page, in *Water — a comprehensive treatise*, Vol. 1, edited by F. Franks (Plenum, New York, 1972).

[113] H. Zhou, P. Ganesh, V. Presser, M. C. F. Wander, P. Fenter, P. R. C. Kent, D. Jiang, A. A. Chialvo, J. McDonough, K. L. Shuford, and Y. Gogotsi, Phys. Rev. B **85**, 035406 (2012).

[114] M. F. Toney, J. N. Howard, J. Richer, G. L. Borges, J. G. Gordon, O. R. Melroy, D. G. Wiesler, D. Yee, and L. B. Sorensen, Nature **368**, 444 (1994).

[115] D. Boda, K.-Y. Chan, and D. Henderson, J. Chem. Phys. **109**, 7362 (1998).

[116] L. Pegado, B. Jönsson, and H. Wennerström, Adv. Colloid Interface Sci. **232**, 1 (2016).

[117] R. Evans, J. R. Henderson, D. C. Hoyle, A. O. Parry, and Z. A. Sabeur, Mol. Phys. **80**, 755 (1993).

[118] R. Evans, R. J. F. Leote de Carvalho, J. R. Henderson, and D. C. Hoyle, J. Chem. Phys. **100**, 591 (1994).

Danksagung

Ich bedanke mich bei Ihnen, Prof. Dr. Siegfried Dietrich, dass Sie mir die Möglichkeit gegeben haben, diese Doktorarbeit in Ihrer Abteilung anzufertigen. Ihre inspirierenden Vorschläge und konstruktiven Einwände waren unschätzbar für dieses Projekt genauso wie die Freiräume, die Sie eingeräumt haben, um diversen Einfällen nachzugehen. Vielen Dank, dass ich an zahlreichen Konferenzen teilnehmen durfte.

Vielen Dank Ihnen, Prof. Dr. Christian Holm und Prof. Dr. Peter Michler, für Ihre Zeit und Mühen als Mitberichter bzw. als Vorsitzender des Prüfungsausschusses.

Ich danke Dir, Priv.-Doz. Dr. Markus Bier, für die Betreuung im Laufe dieses Projektes. Es tat gut zu wissen, dass Deine Tür buchstäblich immer offen stand und dass ich ohne große Umstände um Rat fragen konnte. Danke für Deine hilfreichen Anregungen technischer und konzeptioneller Art und dafür, dass Du Dir für unsere Diskussionen so viel Zeit genommen hast.

Vielen Dank Dir, Anke Geigle, für Deine engagierte Hilfe bei administrativen Angelegenheiten, ganz besonders in Bezug auf Dienstreisen.

Ich danke Dir, Marcel Labbé-Laurent, für die freundliche Atmosphäre in unserem gemeinsamen Büro und für die anregenden Gespräche während unserer Kaffeepausen.

Vielen Dank Dir, Dr. Nima Farahmand Bafi, für Deine Unterstützung und Ratschläge.

Danke an alle gegenwärtigen und ehemaligen Mitglieder der Abteilung Dietrich für die angenehme Atmosphäre und Hilfsbereitschaft. Ich wünsche Euch alles Gute für die Zukunft!

Zu guter Letzt danke ich Euch, meinen Eltern Norbert und Martina und meiner Schwester Isabel, für Eure Unterstützung und Eure Begleitung auf meinem bisherigen Lebensweg.